Contribution expérimentale à l'amélioration des modèles de transition de régime en écoulement diphasique horizontal.

Onur Can Ozturk

UNIVERSITÉ DE GRENOBLE

THÈSE

Pour obtenir le grade de

DOCTEUR DE L'UNIVERSITÉ DE GRENOBLE

Spécialité : **Mécanique des fluides, Procédés, Energétique**

Arrêté ministériel : 7 août 2006

Présentée par

Onur Can ÖZTÜRK

Thèse dirigée par **Pr. Michel LANCE** et
codirigée par **Dr. Muriel MARCHAND** et **Dr. Guillaume Serre**

préparée au sein du **Laboratoire DEN/DANS/DM2S/STMF/LIEFT**
au **CEA Grenoble**

Contribution expérimentale à l'amélioration des modèles de transition de régime en écoulement diphasique horizontal

Thèse soutenue publiquement le **5 décembre 2013**,
devant le jury composé de :

M Christophe CORRE
Professeur au LEGI, Président
M Frédéric RISSO
Directeur de recherche à l'IMFT, Rapporteur
M Horst-Michael PRASSER
Professeur à l'ETH Zurich-Suisse, Rapporteur
M Michel LANCE
Professeur à l'Ecole Centrale de Lyon, Directeur de thèse
M Romain VOLK
MCF à l'Ecole Normale Supérieure de Lyon, Membre
Mme Muriel MARCHAND
Docteur au CEA Grenoble, Membre et Encadrant de thèse
M Guillaume SERRE
Docteur au CEA Grenoble, Invité et Encadrant de thèse

Acknowledgement

First, I would like to thank my supervisors, Muriel MARCHAND and Guillaume SERRE, who were always supportive and helpful during my thesis and my life in France. A special thanks to the magical technician Jean Pierre BERLANDIS who had to be retired due to unfortunate circumstances. Thanks to these three nice people, I have gone further in my scientific carrier. In addition, thanks to their confidence on me, I have worked autonomous and self-independent during my thesis. This helped me to improve my skills and knowledge.

Another special thanks to my thesis director Michel LANCE who always introduced new and brilliant ideas for the problems experienced during my thesis. Furthermore, I am more than glad to work with Eric HERVIEU, Isabelle TKATSCHENKO, Bernard FAYDIDE and Jean Paul GARANDET who were and are the directors of my laboratory at CEA Grenoble. I specially thank to all staff of DEN Grenoble and LIEFT for their lovely friendship and support.

I would like to thank all the members of my jury Christophe CORRE, Frédéric RISSO, Horst-Michael PRASSER and Romain VOLK. Thanks to their remarks and feedbacks, this thesis report has reached its final version.

Before finishing, I would like to thank to my lovely family members who always trust and support me even I live far away from them. A very special and unique thanks to the love of my life (l'amour de ma vie), my "Kuzu Eda", who is always supporting my carrier and decisions during this thesis. Thank you for your patience and understanding during this difficult period of my life.

Finally, I thank all the people whose names are not mentioned above.

TABLE OF CONTENTS

TABLE OF FIGURES

NOMENCLATURE

Latin letters

$\tilde{A}$	Dimensionless flow cross-section (-)
$\tilde{A}_G$	Dimensionless flow cross-section of gas phase (-)
A_i	Interfacial area concentration (m^{-1})
A_k	Area of horizontal layers (m^2)
$\tilde{A}_L$	Dimensionless flow cross-section of liquid phase (-)
A_T	Total cross-sectional area (m^2)
A_{wire}	Area of wire (m^2)
CT	Transition criteria (-)
D	Internal diameter of the test section (m)
d_{32}	Sauter mean diameter (m)
Δd_{0i}	Distance between probe tips (m)
$\tilde{D}_L$	Dimensionless hydraulic diameter (-)
d_{pq}	Average diameter at the moments p and q
Δt_{0i}	Time lag (time-of-flight) between probe tips (s)
d_{wire}	Diameter of wire (m)
e	Voltage across film/wire (V)
E_{wire}	Energy stored on wire (J)
$\tilde{h}$	Dimensionless liquid height (-)
$h_C(l)$	Chord length distribution function (-)
$h_{Convection}$	Heat transfer coefficient / Newton convection coefficient ($W/(m^2.K)$)
$h_D(l)$	Bubble diameter distribution function (-)
h_{Liq}	Liquid height (m)
$h_L(l)$	Distribution function (-)
I	Current passing through film/wire (A)
J_L, J_G	Superficial velocity of liquid and gas phases (m/s)
K	Turbulent kinetic energy (m^2/s^2)
l	Length (m)
l_{wire}	Length of wire (m)
N	Correction coefficient for turbulent kinetic energy (-)
N_b	Number of bubbles (-)
Nu	Nusselt number (-)
P_{Joule}	Power due to Joule effect (W)
Pr	Prandtl number (-)
$q_{w\to o}$	Heat transferred from wire to outside (J)
r	Radial position in the test section (m)
R	Internal radius of the test section (m)
Re	Reynolds number (-)
Re_{film}	Reynolds number of film (-)
R_{wire}	Resistance of wire (Ω)

$\tilde{S}_i$	Dimensionless perimeter of liquid-gas interface (-)
$\tilde{S}_L$	Dimensionless perimeter of liquid phase (-)
S_p	The moment of p order (-)
T	Dimensionless dispersed bubble flow parameter (-)
T_a	Ambient temperature (°C)
t_{Gas}	Total time of gas phase presence (s)
T_{ref}	Reference temperature (°C)
t_{Total}	Total acquisition time (s)
T_{wire}	Temperature of film/wire (°C)
u	Fluctuating component of axial liquid velocity (m/s)
u', v', w'	Standard deviation of fluctuating component of axial, radial and orthoradial liquid velocity (m/s)
U_{axe}	Maximum average axial liquid velocity (m/s)
U_B	Bubble velocity (m/s)
U_{eff}	Effective cooling velocity (m/s)
U_L	Average Axial component of liquid velocity (m/s)
$\tilde{U}_L$	Dimensionless axial liquid velocity (-)
U_L^{inst}	Instantaneous axial liquid velocity (m/s)
u_{LS}, u_{GS}	Superficial velocity of liquid and gas phases (m/s)
U_τ	Friction velocity (m/s)
V_{deb}	Axial average liquid superficial velocity (m/s)
V_{Gas}	Velocity of gas phase (m/s)
V_L	Radial component of liquid velocity (m/s)
V_{liq}	Velocity of liquid phase (m/s)
X	Lockhart-Martinelli parameter (-)

Greek letters

α	Void fraction (-)
β	Inclination angle (°)
κ	Slope factor of hot-film anemometry probes (-)
λ	Thermal conduction coefficient of water (W/(m.K))
ρ_L, ρ_G	Density of liquid and gas (kg/m^3)
σ	Surface tension (mN/m)
υ	Kinematic viscosity (m^2/s)

Remarks:

- Spatial averaging operator: The spatial value of variable *f* is written as <*f*> (averaging methods are described in Appendix 3)
- Graphical representation: Unless it is stated, *r/R=0* represents the center of the pipe and *r/R=1* & *r/R=-1* represent the upper and lower walls respectively.
- The lines connecting the experimental points of axial or radial profiles are tendencies.

CHAPTER 1

INTRODUCTION

1 INTRODUCTION

The aim of this thesis work is to study horizontal flow regimes and their evolution. There are two main reasons of this work: new experimental technics are now mature to profoundly the physical mechanisms involved in the evolution of these flows and numerical tools used in safety studies should be improved continuously.

The two-phase flow simulation tool, CATHARE, used in the nuclear industry for the safety of nuclear power plants, has been improved by the French Alternative Energies and Atomic Energy Commission (CEA). In the frame of the NEPTUNE project (collaboration of EDF, CEA, AREVA-NP and IRSN), the physical models of this code are validated thanks to various experimental works such as those performed on METERO.

This experimental setup is devoted to the study of horizontal two-phase flows and their axial evolution. As explained further, the knowledge of horizontal flow regimes can be critical for the calculation of an accidental situation such as a break on the horizontal leg of the primary circuit. Although such flows have already been studied and modeled, it is important to measure previously inaccessible physical quantities that play an important role in the evolution of flow regimes by the help of new experimental technics and local probes. The evolution of a bubbly flow toward a stratified one depends strongly on two main forces acting on liquid and gas phases: turbulence, which is responsible for the break-up and dispersion of bubbles, and buoyancy, which results in the rise of bubbles toward the top of the pipe where they can coalesce eventually until phase separation is reached. Even though these forces cannot be measured directly, their consequences on the flow can be.

The research efforts on this topic should focus on the following areas:

- **Comprehension and explanation of the physical mechanisms which drive flow regime transitions in horizontal pipe.** Although the studies in the literature bring fundamental results for horizontal flows and the study of Bottin (2010) has introduced some detailed results in dispersed bubbly flows in horizontal pipe, it is necessary to gather more data and understand the flow regimes (increase the spatial resolution of measurements for various flow rates, etc.). For this reason, some questions should be answered such as:
    - "What is the spatial distribution of the phases?"
    - "Does coalescence or break-up of bubbles take place in flows?"
    - "What are the effects of liquid and gas flow rates?"
    - "What is the nature of the interactions between liquid and gas phases?"
    - "How could the competition between turbulent and buoyancy forces be described?"
    - "Is it possible to obtain a simple and natural flow regime transition indicator which can be used in the simulation tools and industrial codes?"

- **Description, analysis and modeling of the axial development of horizontal two-phase flow focusing particularly on the evolution of the interfacial area concentration and the turbulent kinetic energy.** Two-phase flows occurring in a hot/cold leg of a nuclear reactor are developing flows since their lengths are in the order of few diameters. Analyzing and modeling of these flows and their transitions is one challenge in multiphase research and development (R&D). Although, the industrial case points out developing two-phase flows in the pipes, the studies in the literature were focused on developed two-phase flows which are established at great distances from the entrance (lengths in the order of 200-300 diameters).

In the light of this information, turbulent and buoyancy forces can be considered as the two main phenomena whose competition determine the horizontal two-phase flow regime. For better understanding of two-phase flow and better modeling, particular attention should be paid to the interfacial area concentration (the area of the bubble surfaces per unit volume) and turbulent kinetic energy in the flows. There are two main reasons why the interfacial area concentration is one of the quantities of interest. Firstly, the interfacial area is involved explicitly in many interfacial exchange models (phase change, friction between phases). Secondly, its order of magnitude is an indicator of flow regimes (low in stratified flows and high in dispersed bubbly flows). Concurrently, turbulence has an important role in two-phase flow regime transitions by mixing the phases and leading to break-up of the bubbles in the flow. As a result, the turbulent kinetic energy is a quantity that can help to characterize the flow regime.

1.1 Industrial Context

Two-phase flows occur in many industrial sectors such as chemistry, petroleum, automotive, nuclear, etc. In the nuclear sector context, most of the studied hypothetical accidents are the consequence of a break on a pipe of the primary circuit leading to a loss of water. Since the water in this circuit is at high pressure (150 bar) and temperature (300 °C), the depressurization of water results in important vaporization. Thus, two-phase flow appears near the break and propagates in the entire circuit and in the reactor core.

Safety criteria concerning the temperature evolution of fuel clad depend on the remaining water mass inside the core and on what appends in all the circuit during the generation of two-phase flow. The ratio of liquid to steam flowing out at the break determines the evolution of the accident. When it is high, the pressure decreases slowly which is disadvantageous since the safety injections are automatically activated at medium pressure. In addition, core mass inventory decreases rapidly. On the other hand, for a low value of this ratio, pressure decreases rapidly and the liquid mass decreases slowly. Consequently, great amount of core energy is evacuated via steam enthalpy and this is a favorable situation in the nuclear safety. The ratio of liquid to steam near the break is determined by the local flow regime. As an example, the quantity of liquid flowing at a pressurizer discharge valve (TMI accident, 1979) (see Figure 1.1) depends on the flow regime at the junction between the hot leg and the pressurizer (see Figure 1.2): in case of stratified flow, the flowing fluid will be essentially steam while it will be essentially water in case of bubbly flow.

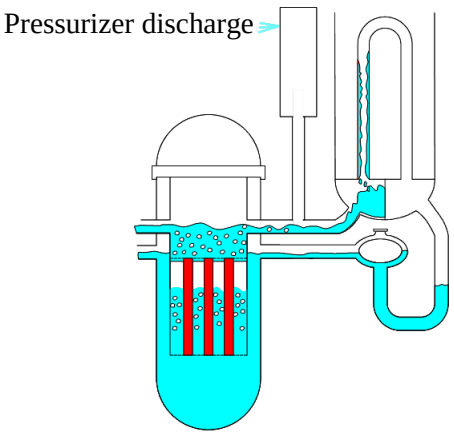

Figure 1.1 - Accidental situation due to loss of coolant at pressurizer

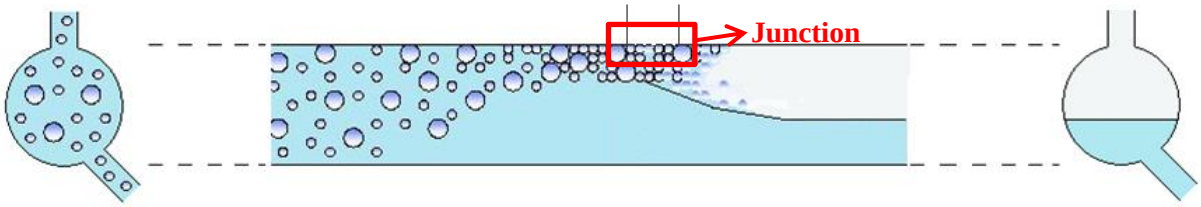

Figure 1.2 - Illustration of the importance of bubble-stratified transition to predict correctly the mass and energy lost in a break or discharge valve of the pressurizer

In this context of the improvement of safety numerical tools, the NEPTUNE project was initiated by CEA, EDF, AREVA-NP and IRSN at the end of 2001. The purposes of this project are to build a new software platform for advanced two-phase flow thermal-hydraulics allowing easy multi-scale and multi-disciplinary calculations and develop new physical models and numerical methods for each simulation scale as well as their coupling in order to meet the industrial needs. As a result, the NEPTUNE research program covers all levels of modeling (from the nucleation scale to the reactor scale) and focuses on different areas as software development, modeling and experimental studies.

In order to study, understand and model occurrence of stratification in horizontal two-phase flows, METERO (Maquette d'Etude des Transitions d'Ecoulements air/eau) has been designed as a part of the NEPTUNE project.

The experimental results obtained in the METERO experiment will support the validation and improvement of the existing models in the CATHARE code. The current industrial version of the code, CATHARE 2, is based on the two-fluid model with 2x3 equations: balance of mass, momentum and energy for liquid and gas phases. Thanks to the recent measurement technics that give access to physical quantities playing an important role in the flow evolution such as turbulent kinetic energy or interfacial area; it makes sense to add new equations for the transport of these quantities since direct validation is now possible. Therefore, a new version of the code, CATHARE 3, is under development. This new version includes a multi-field approach (splitting of the liquid phase into film and droplet fields that behave separately), transport equations for interfacial area concentration and turbulent kinetic energy. Moreover, the simplified flow map used in CATHARE 2 (as well as those found in the literature) is based on developed flows while it is never the case in nuclear power circuits. Thus, results of the METERO experiment allow checking if developed flow models have to be corrected or not for developing flows.

1.2 State of Art

Two-phase air/water flows have been investigated in the light of measured typical flow parameters such as void fraction, bubble size, interfacial area, velocity and turbulent quantities. In the literature, there exist many publications about vertical two-phase flows; however, the studies about horizontal flows are very limited compared to the studies on vertical flows.

The quantities concerning horizontal two-phase flow (dispersed bubbly and intermittent flows) have been measured and modeled by a few authors in the literature.

Kocamustafaogullari & Wang (1991) presented local distributions of void fraction, interfacial area concentration, mean bubble diameter, bubble interface velocity, chord-length (intercept length) and bubble frequency in horizontal air-water bubbly flow. The authors measured local quantities in a transparent circular pipe line which has a 50.3 mm internal diameter and is 15.4 m in length. In their

measurements, a double-sensor resistivity probe was used with a sampling frequency of 20 kHz and sampling time of 1s. Concerning the test conditions, the water superficial velocity ranged from 3.74 to 5.71 m/s while the air superficial velocity varied from 0.25 to 1.37 m/s. In addition, the range of average void fraction was from 0.043 to 0.225 during the tests. The experimental results showed that void fraction, interfacial area and bubble frequency values increase by decreasing the liquid flow at constant gas flow or increasing gas flow at fixed liquid flow. In addition, local maxima near upper wall have been observed in the distribution profiles of these flow quantities. The bubble interface velocity has a relatively uniform distribution except near upper wall where a sharp decrease of velocity was observed. Furthermore, the authors stated that the average interface velocity and turbulent fluctuations are increasing with an increase in the gas flow. Mean bubble diameter was calculated by using the relationship between void fraction, interfacial area concentration and mean bubble diameter. It was observed that the mean bubble diameter generally increases with an increase in gas flow rate at fixed liquid flow rate; however, this effect is not significant. In conclusion, the effects of inlet and boundary conditions on the distribution of local flow quantities (void fraction, interfacial area, etc.) were investigated in this study. Moreover, the authors recommended that further studies are essential to understand the effects of inlet conditions and wall on the distribution of the flow quantities in horizontal flows.

Similar to the study mentioned above, Kocamustafaogullari et al. (1994) studied local distributions of void fraction, interfacial area concentration and Sauter mean diameter in air-water horizontal bubbly flows. In addition, area averaged values of these flow quantities were also investigated in this study. The measurements have been performed on an experimental setup which consists of a transparent circular pipe with 50.3 mm internal diameter and is 15.4 m in length. In addition, water was circulated in a closed loop and air is circulated in an open loop in which the air was released to the atmosphere at the outlet of the test section. The local flow quantities have been acquired at 253 diameters downstream of the air-water mixing chamber by using double-sensor resistivity probe for various test conditions such as liquid superficial velocity ranging from 3.74 to 6.59 m/s, gas superficial velocity ranging from 0.21 to 1.34 m/s and average void fraction ranging from 0.037 to 0.214. The results showed that the inlet conditions have significant effects on the local and area-averaged values of the flow quantities. Decrease in liquid flow rate for constant gas flow or increase in gas flow rate for fixed liquid flow rate results in an increase in the local and area-averaged values of void fraction and interfacial area concentration. Moreover, the effect of liquid flow on these values is not as significant as that of gas flow. On the other hand, change in liquid flow has more significant effect on Sauter mean diameter values compared to effect of gas flow. Furthermore, area averaged interfacial area concentration values have been compared with those calculated by using different models existing in the literature for vertical flows. This comparison showed that the models for the vertical flows are not applicable for the horizontal flows. Thus, the authors introduced new mathematical models based on mechanistic modeling of the bubble break-up process to predict the area averaged values of interfacial area concentration and Sauter mean diameter for horizontal flows by using. The predicted values by the models were in good agreement with ones measured by a double-sensor resistivity probe.

Lewis et al. (1996) published their study about time averaged local values of void fraction due to small and large bubbles, mean liquid velocity and liquid turbulence fluctuations in horizontal air-water slug flow. The measurements have been performed on a circular transparent pipe (50.3 mm internal diameter, 15.4 m in length) by using hot-film anemometry and conical shaped (TSI 1231-W) hot-film probes which were located 253 diameters downstream of the inlet. The tests have been carried out for various liquid and gas superficial velocities (range from 1.10 to 2.20 m/s for water and range from 0.27 to 2.20 m/s for gas) at an operating temperature about 20-22 °C. The void fraction profiles

showed that the void fraction due to large bubbles decreases toward the upper wall while total void fraction increases slightly in this part. This slight increase indicates the contribution of small bubbles to the total void fraction due to the strong migration of small bubbles to the upper part of the pipe. In addition, either decreasing water flow rate for fixed gas flow rate or increasing gas flow rate for a given liquid flow rate results in an increase in the void fraction. Furthermore, it was observed that the liquid velocity distribution is asymmetrical and the degree of asymmetry increases with a decrease in liquid flow rate or an increase in gas flow rate. In addition, the velocity profile results show that there exists a strong shear layer starting at the top of the bottom liquid layer. In addition, velocity profiles similar to the ones observed at a fully developed turbulent pipe flows have been acquired at the bottom liquid layer and the top portion of liquid slug. The effect of inlet conditions on turbulence, namely flow rates, has been clearly seen in the results. An increase in liquid and/or gas flow rates results in an increase of both the absolute value of turbulence and the turbulence intensity. In addition, the effects of flow rates are greater within the liquid slug. The authors concluded that their results are a starting point to understand the horizontal intermittent two-phase flow and additional data is essential to understand these flows in details. Moreover, time averaged results limits to study structures of liquid slugs and the liquid layer below the gas slugs separately. Thus, instantaneous velocity measurements are necessary.

Riznic & Kojasoy (1997) have investigated local interfacial area concentration, void fraction, interfacial velocity and slug bubble frequency in horizontal air-water slug flows. The tests were carried out on a transparent circular pipe which has 50.3 mm internal diameter and is 15.4 m in length. In addition, slug flows were generated with various liquid and gas superficial velocities (ranging from 0.55 to 2.20 m/s for water and from 0.27 to 2.20 m/s for air) and void fraction between 0.1 to 0.7. The measurements were performed at an axial location of 253 diameters downstream of inlet by using four-sensor resistivity probe (for instantaneous phase velocity and interfacial concentration area due to large air slug bubbles) and two-sensor resistivity probe (for interfacial area concentration due to small bubbles). The interested quantities, except the slug bubble frequency, were measured not only at radial profiles (two-dimensional representation) but also across the pipe cross section (three-dimensional representation). Void fraction results show that void fraction increase while decreasing the liquid flow rate or increasing the gas flow rate. The authors stated that the total interfacial area concentration measured in slug flows is determined by the air slug and small bubbles. Void fraction and interfacial area concentration profiles showed that these flow quantities are distributed asymmetrically indicating non-symmetrical transport in a horizontal intermittent two-phase flow. Furthermore, slug frequency results indicate the effects of inlet conditions such that increasing liquid flow rate raises the slug frequency. On the other hand, slug frequency has a different trend with an increase in gas flow rate: it first increases and then decreases. The authors concluded that more detailed study is essential to understand the influence of inlet conditions on the slug frequency.

Bertola (2002) has studied the slug velocity and gas-liquid interface velocities for horizontal air-water two phase flows in a 12-meter-long circular transparent pipe with 80 mm internal diameter. Air-water two-phase flows were generated for liquid superficial velocities ranging from 0.6 to 2 m/s and gas superficial velocities ranging from 0.3 to 8 m/s at atmospheric pressure and temperature. The acquisitions were performed at axial locations of 96, 101 and 104 diameters from the inlet of pipe. In this study, gas-liquid interface velocities were calculating by cross-correlating phase density function time series obtained by a pair of single-fiber optical probes. The duration of the acquisitions is 400 seconds with a sampling frequency of 2 kHz. Slug velocities acquired in the tests have been compared to the slug velocities calculated by a model introduced by Dukler & Fabre (1994). This comparison showed that the model can predict the slug velocity for the mixture flows which have a Froude number

smaller than 3.5. For the flows with greater Froude number, the model overestimates the slug velocity. Thus, it is essential to introduce a different slug velocity correlation for these flows.

Iskandrani & Kojasoy (2001) presented their experimental results in terms of time averaged local values of void fraction, bubble-passing frequency, axial mean liquid velocity and the liquid turbulence fluctuations in horizontal air-water bubbly flows. These flow quantities were measured, in a transparent circular pipe (50.3 mm internal diameter and 15.4 m in length) by using a conical shape (TSI 1231-W) hot-film probes located at 253 diameters downstream with constant temperature anemometry system. The test were performed with various liquid and gas superficial velocities (from 3.8 to 5.0 m/s for water and from 0.25 to 0.8 m/s for air) at atmospheric pressure and temperature about 20-22 °C. Void fraction and bubble-passing frequency results showed that the profiles of both flow quantities have local maxima near the upper wall. In addition, the profiles become more flat when the liquid flow rate is increased. An increase of gas flow rate at fixed liquid flow rate also affects the flow quantities such that both void fraction and bubble passing frequency are increased. Axial mean liquid velocity is distributed uniformly except near the upper pipe wall where a sharp decrease in velocity is observed. Increasing gas flow rate results in an increase in mean velocity and turbulent fluctuations. Furthermore, the turbulent intensity at very low void fractions is slightly lower than the one in single phase flows. In addition, the turbulent intensity is increased with respect to an increase in the void fraction. Thus, the authors concluded that the local turbulence intensity is mainly a function of the local void fraction.

Yang et al. (2004) presented their study about turbulent structure in horizontal air-water bubbly flow. The turbulence structure was measured by using two X type (1246-60W) hot-film probes operated with an over heat ratio of 1.08. In addition, the measurements were taken in 1s with a sampling frequency 20 kHz. The probes were installed at 172 diameters downstream and on a horizontal transparent tube (10 m in length) with a 35 mm internal diameter. Horizontal bubbly flows were generated liquid and gas superficial velocities ranged from 3.5 to 4.5 m/s and from 0.00 to 0.44 m/s respectively. The operating pressure is 214-319 kPa and the working temperature is about 28 °C. The experimental results showed that mean axial liquid velocity, turbulent fluctuations and turbulent intensity have asymmetric distributions at measuring angles 0° and 45°. On the other hand, they are symmetric when the measuring angle is 90°. In the lower part of the tube, the mean axial liquid velocity profiles have a similar trend of what is observed in single phase flows. In the upper part where the bubbles are accumulated, the velocity decreases sharply. By increasing gas flow rate, mean velocity increases in the lower part. On the other hand, a decrease in mean velocity in the upper part was observed for the same condition. In the lower part, the turbulence structure is similar to that observed in fully developed single phase flows. The turbulence increases in the upper portion and reaches a maximum point. After this maximum, it decreases in the region near upper tube wall. The authors concluded that there is a strong momentum exchange in the circumferential direction that may be induced by the bubble immigration. In our point of view, the experimental results of Yang et al. (2004) are significantly contributive to the error calculation of spatial averaging methods for turbulent kinetic energy since the turbulence structure was measured in three different angles.

As a general trend in literature, flow regime maps are generated by the help of the visual observations. However, these maps could not represent the flow regime transitions universally due to the dependence of experimental facility conditions and properties. In addition, the lack of precision in describing these visual observations brings problems to the classification of flow regimes and their transitions. At this point, Taitel & Dukler (1976) introduced a mechanistic model which predicts the relationship between operation conditions (gas and liquid flow rates, properties of fluids, pipe diameter and angle of inclination) and flow regime transitions in horizontal and near horizontal flows. This

model is based on physical concepts and it is very successful to predict flow regimes and transitions. By using this model, the authors created a generalized dimensionless flow regime map for horizontal flows. This flow regime map was in a good agreement with the experimental data collected from the literature. The model and the flow regime map introduced by the authors motivate us to generate a dimensionless flow regime map for the METERO experiment and to develop analytical criteria for flow regime transitions.

Ekambara et al. (2008) presented a CFD simulation study on the internal phase distribution of co-current, air-water bubbly flow in a horizontal pipeline which has a 50.3 mm internal diameter. Liquid and gas superficial velocities varied from 3.8 to 5.1 m/s and from 0.2 to 1.0 m/s respectively. In addition, average void fraction was ranging from 0.04 to 0.16. The results of the predicted void fraction and the mean liquid velocity were compared to the experimental data taken from the literature. There exists a good agreement between the predicted and experimental results. In the study of Ekambara et al. (2008), it is more delightful to note that horizontal gas-liquid two phase flows were classified with respect to the dominant mechanism in the flows. The authors organized the flows in three groups: gas dominant, liquid dominant and gas-liquid coordinated. In gas dominant flows, the flow is controlled by gas phase and the liquid phase exists in droplets (for instance, mist flow). If the liquid flow rate reaches a certain level where the flow is driven by liquid phase, this flow is called liquid dominant flow. Dispersed bubbly flow is a representative example of liquid dominant flows. In the case of gas-liquid coordinated flows, neither gas phase nor liquid phase can control the flow. Buoyant bubbly, plug, slug and wave flows are in this group. This flow regime classes have already been used in the METERO experiment to define the generated flow regimes.

Bottin (2010) presented a PhD thesis which was focused on local distribution and axial evolution of flow quantities in horizontal single phase and two-phase flows (void fraction, bubble size, interfacial area, velocities of liquid and gas phases and turbulence) and modeling of turbulence and interfacial area in horizontal dispersed bubbly flows. The author performed tests in the METERO experiment (details will be given in Chapter 2) at three different axial locations: 5, 20 and 40 diameters downstream of the inlet. Furthermore, as a part of the thesis, the author defined flow regimes by the help of high speed camera visualizations and presented a flow regime map for the METERO experiment, as seen in Figure 1.8. These flow regimes were defined in 5 major groups such as Buoyant Bubbly Flow (BBF), Stratified Bubbly Flow (SBF), Plug Flow (PF), Slug Flow (SF) and Stratified Flow. The descriptions of these flow regimes are given in the following paragraphs.

Buoyant Bubbly Flow (BFF) is a flow regime where the bubbles are dispersed in liquid phase. The bubbles are not in contact with other bubbles, as seen in Figure 1.3. The bubbles are not distributed uniformly in the test section compared to fully dispersed flows since buoyancy force results in the migration of the bubbles to the upper part. The effects of non-uniform bubble distribution can be observed in the flow quantity profiles. Bottin (2010) stated that fully dispersed bubbly flows cannot be achieved in the METERO experiment since the liquid flow rates cannot reach certain values to establish full dispersion.

In Stratified Bubbly Flow (SBF), as seen in Figure 1.4, the bubbles start to accumulate at the upper part of the test section and form a mattress of bubbles. The motion of the bubble mattress is different from the liquid phase which determines the motion of the bubbles at the lower part. It can be conclude that there exist two different flows in the test section which are gas dominant at the upper part and liquid dominant at the lower part. Thus, this flow is a clear example of gas-liquid coordinated flow defined by Ekambara et al. (2008).

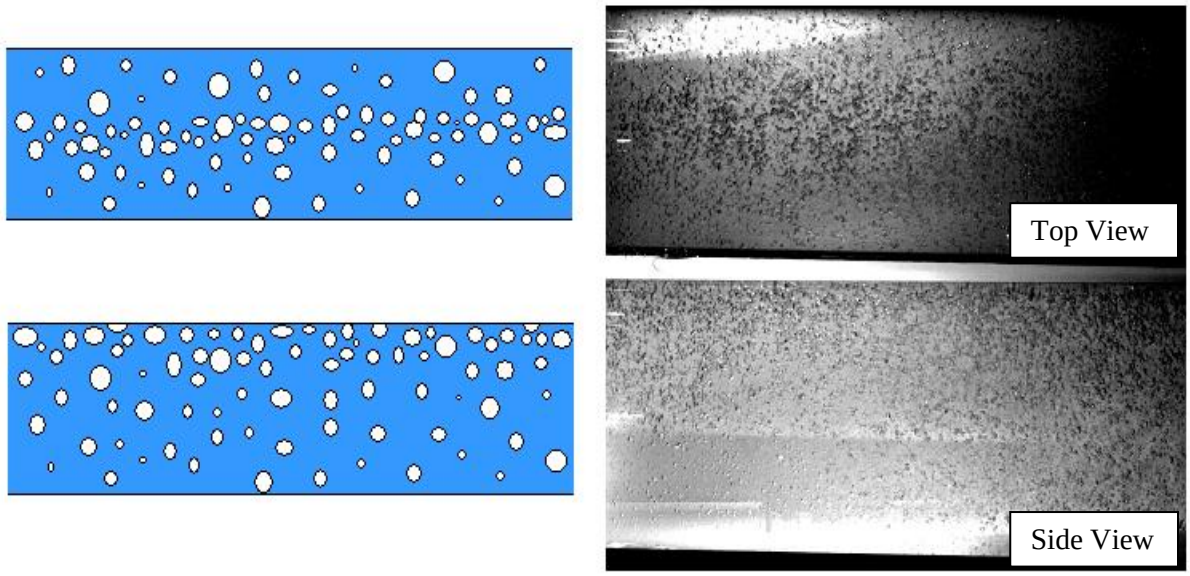

Figure 1.3 - Buoyant bubbly flow for J_L=5.31 m/s and J_G=0.0255 m/s (Bottin, 2010)

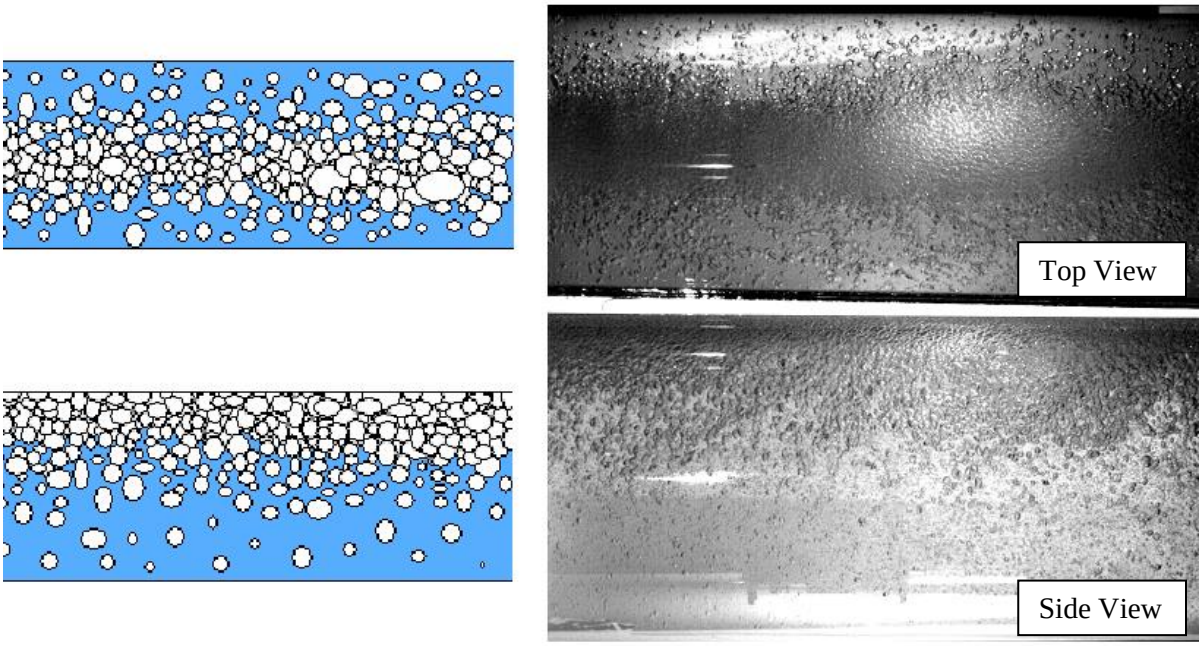

Figure 1.4 - Stratified bubbly flow for J_L=4.42 m/s and J_G=0.1273 m/s (Bottin, 2010)

Plug Flow (PF) is described such that air plugs are generated and the number of air plugs increases while decreasing liquid flow rate. As seen in Figure 1.5, there exist small bubbles in the lower part of the test section and bigger bubbles around the air plugs.

In Slug Flow (SF), slugs are generated by decreasing the liquid flow rate at a constant gas flow rate. In addition, the coalescence of the small bubbles and air plugs occur in the turbulence since turbulence, which is the main source of bubble break-up, is decreased. As a result, Taylor bubbles are observed in the upper part and small bubble take place in liquid slugs as seen in Figure 1.6.

In Stratified Flow, there exist two separated phases flowing parallel to each other. Although there is a velocity difference across the phase interface, it is not sufficient to establish air pockets in the flow, but the waves occur on the interface as seen in Figure 1.7.

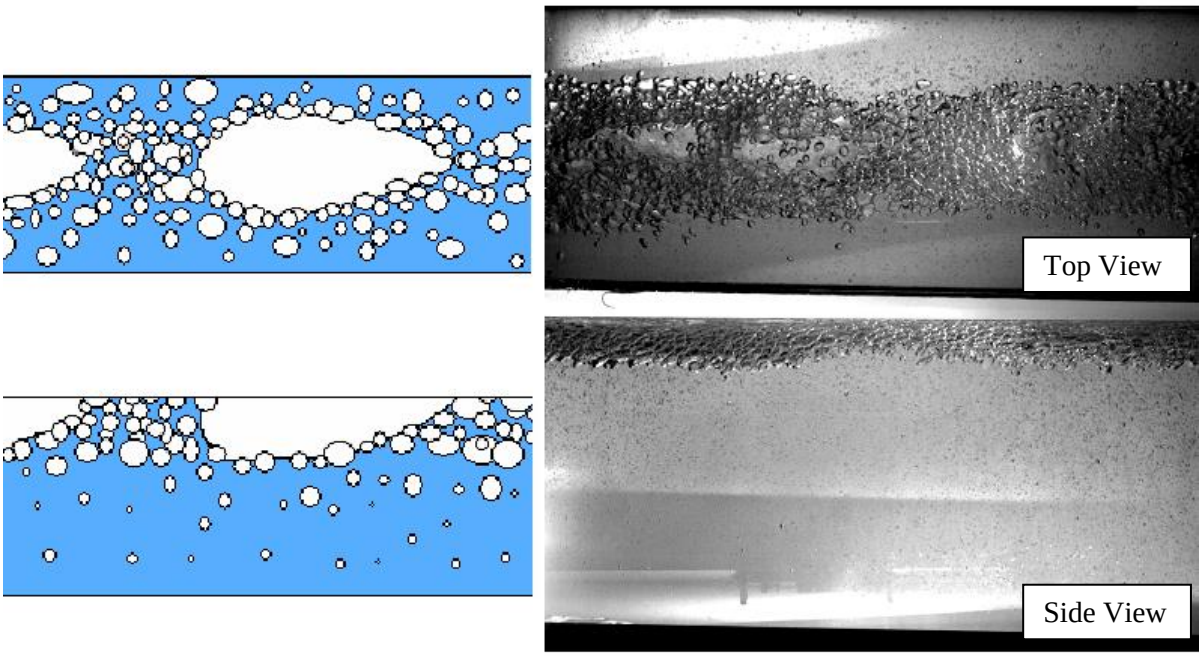

Figure 1.5 - Plug flow for J_L=2.19 m/s and J_G=0.0637 m/s (Bottin, 2010)

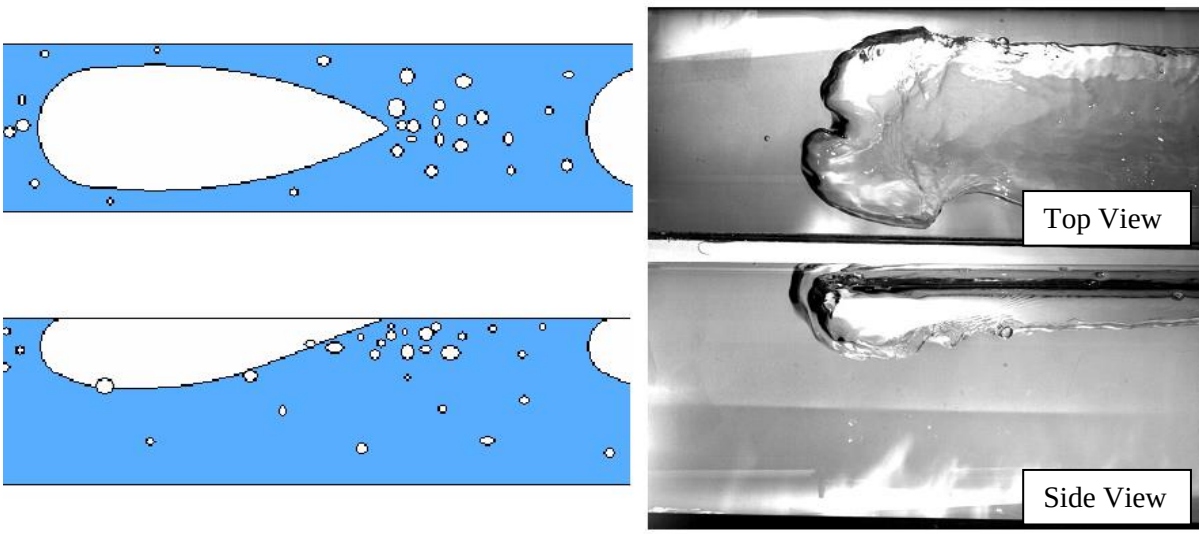

Figure 1.6 - Slug flow for J_L=0.53 m/s and J_G=0.0637 m/s (Bottin, 2010)

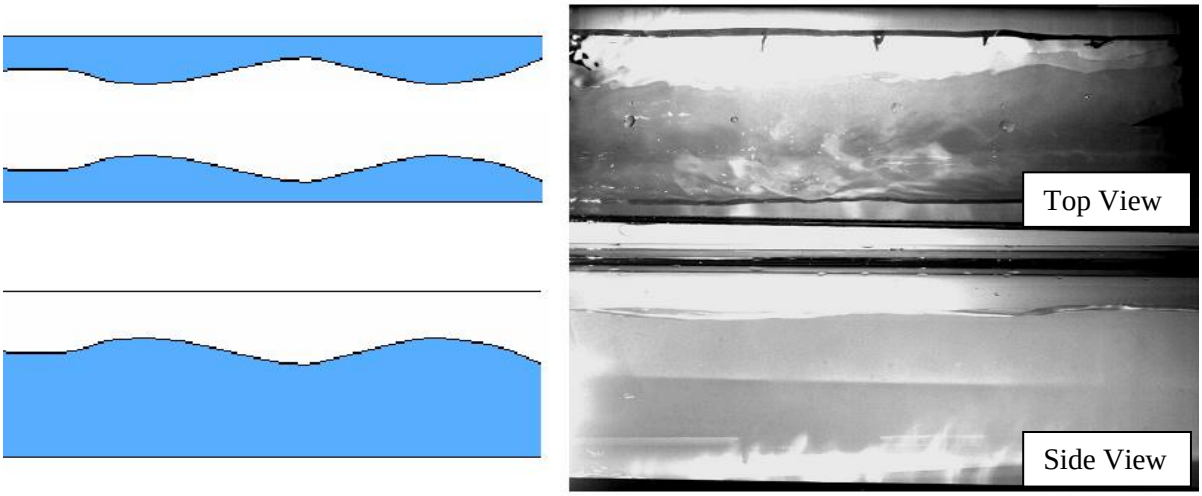

Figure 1.7 - Stratified flow for J_L=0.39 m/s and J_G=0.0955 m/s (Bottin, 2010)

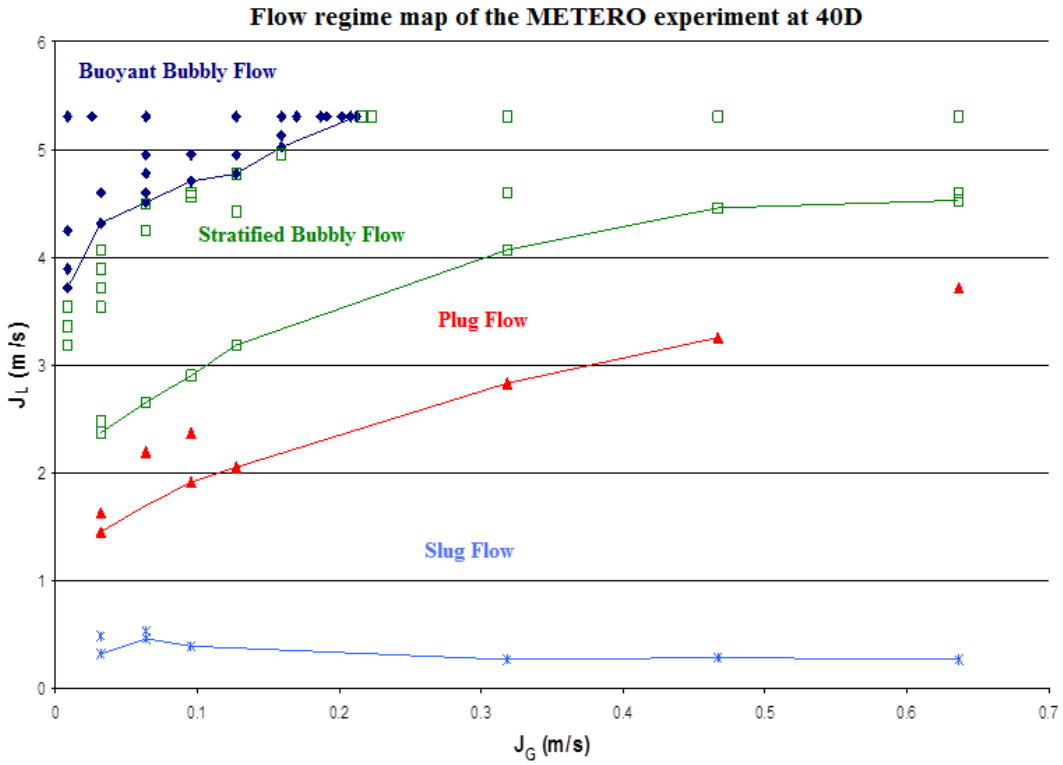

Figure 1.8 - METERO flow regime map at 40D

As mentioned before, the flow quantities were measured at three axial locations by Bottin (2010). For this purpose, X shaped hot-film probes with a constant temperature anemometry (CTA) system has been used in single phase flows. In two-phase flows, two-point optical fiber probes and conical hot-film probes with CTA have been used for the measurements. The details of these probes are given in Chapter 3.

The results of Bottin (2010) showed that the distribution of gas phase results from the competition between buoyancy force which tends to migrate bubbles to the top of the test section and turbulent force which promotes the homogenization of the phases. Thus, spatial distribution of the bubbles depends on the bubble size and flow variations. The effects of spatial distribution were observed in the radial profiles of flow quantities such as Sauter mean diameter, interfacial area concentration and void fraction. In addition, the author stated that the evolution of average interfacial area shows a linear

dependence as a function of gas superficial velocity. In addition, the presence of bubbles was also observed in velocity and turbulence profiles. For instance, the liquid velocity decreases sharply at the top of the pipe where the bubbles are accumulated. This velocity decreases results from the additional turbulence introduced by bubbles. Moreover, presence of bubbles brings out an asymmetrical distribution of velocity and turbulence profiles. The axial evolution of the flow quantities gives access to observe sedimentation or coalescence of bubbles. The author also presented mathematical models of average turbulent kinetic energy and interfacial area transport. The comparison of experimental results and turbulent kinetic energy model showed that the model shows a good estimation of average kinetic energy at 40 diameters; however, the estimation of axial evolution is poor. The results of the interfacial area transport model are a good agreement with the experimental results obtained for low gas flow rates. For higher flow rates, the model does not represent the physics of the flow due to the lack of data. Thus, further investigation is essential to develop the models.

As seen from the studies mentioned above, most of them, except the one of Bottin (2010), were performed to measure the flow quantities of developed flows at locations relatively far from the inlet of the test section (from 172 to 253 diameters from the inlet which are longer than the lengths in the PWRs, around 10 diameters) and the axial evolution of the flow quantities are not in the focus of these studies. The experimental study on developing dispersed bubbly and intermittent flows is necessary to model correctly the transport of interfacial area and mean turbulent kinetic energy. Thus, this study is devoted to the experimental investigation on the flow quantities of developing flows and their modeling.

1.3 Report Plan

This thesis report consists of 7 chapters and is organized as:

Chapter 1 introduces the start point of this thesis by presenting the industrial and scientific context and gives some example studies on horizontal two-phase flows from literature.

In Chapter 2, the experimental setup (METERO) is presented. Chapter 3 gives detailed information about the measurement techniques (optical fiber probes, hot-film anemometry and high-speed camera), instrumentation, acquisition and post-processing procedures (programs, routines, analysis, averaging methods and uncertainties).

In chapters 4 and 5, local and axial studies of the flow quantities (void fraction, Sauter mean diameter, interfacial area concentration, phase velocities, etc.) in dispersed bubbly and intermittent flows are presented. Chapter 6 is dedicated to dimensionless flow regime maps generated for the METERO experiment.

Chapter 7 concludes the thesis and presents the outlook that highlights the originality of the present work and contributions of this thesis.

There exist 6 appendices in this thesis. The first four appendices give detailed information about methods and techniques used in the present work. In addition, appendices 5 and 6 present all experimental results acquired in the METERO experiment during the present work.

CHAPTER 2

EXPERIMENTAL SETUP

2 EXPERIMENTAL SETUP

2.1 Objectives and Challenges

METERO (Maquette d'Etude des Transitions d'Ecoulement air/eau) (Figure 2.1), designed in 2004 and operated first in 2006) is the first experiment of the co-developed CEA-EDF NEPTUNE project.

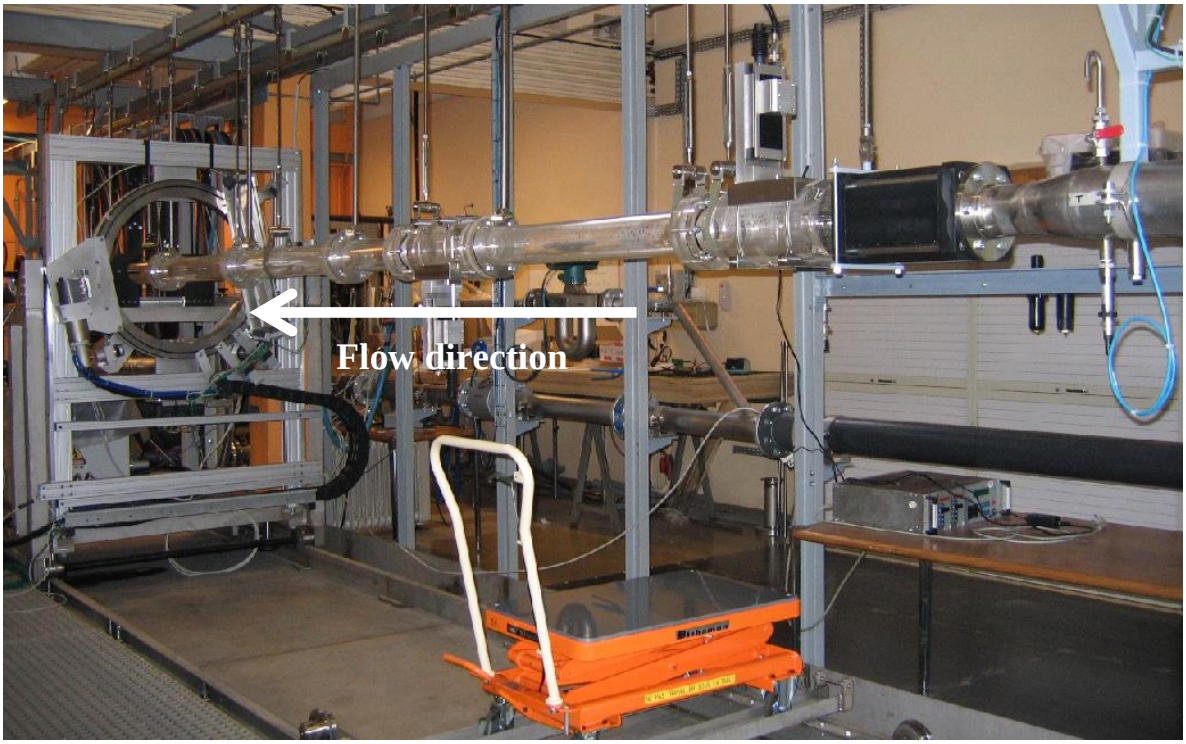

Figure 2.1 - The METERO experiment

As mentioned previously, the METERO experiment is dedicated to understand the responsible mechanisms of the transition between bubbly and stratified two-phase flows in a horizontal pipe. This experiment is also used to create experimental databases for thermal-hydraulics simulation code CATHARE (Code Avancé en ThermoHydraulique pour les Accidents dans les Réacteurs à Eau) and to validate 1D (size averaged) models for interfacial area concentration transport and turbulent kinetic energy in CATHARE code. This experiment may also be used to create future models for NEPTUNE CFD codes.

The METERO experiment allows measuring various two-phase air/water flow quantities, such as void fraction, interfacial area, bubble sizes, velocity of the gas phase, liquid height, turbulence level, mean and fluctuating velocity of the liquid phase, etc., in order to analyze two-phase flows in details. This chapter is devoted to describe the METERO experiment.

2.2 Description of the Experimental Setup

The schematic of the experimental setup is presented in Figure 2.2.

The air/water flow is generated in a transparent 5.4-meter-long horizontal circular pipe which is made of Plexiglas with an internal diameter of 100 mm and a wall thickness of 10 mm. In the METERO experiment, air/water two-phase flows can be generated with various air and water flow rates such as:

- from 1 to 150 m^3/h for water flow

– and from 1 to 60 m^3/h (or 1000 Nl[1]/min) for air flow (used up to 350 Nl/min due to pressure drops).

These flow rates generate various single phase axial velocities of 0.5 to 5.31 m/s for water and 0.5 to 0.8 m/s for air. The method to obtain phasic velocities from the gas flow rates is summarized in Appendix 1.

2.2.1 Water and air circuits

The water circuit consists in:

– a non-pressurized water storage tank with 1500-liter-capacity supplied with city water (tap water). There exists heat exchange circuit and water level sensor inside the tank. In the beginning, the water was initially distilled through a demineralization system to prevent the contamination of water by minerals and particles that might damage the anemometer probes. The use of the demineralization system has been abandoned with the appearance of triboelectric phenomena strongly arisen with demineralization.
  The temperature variations of water can significantly affect the measurements. These variations are limited to 0.1 °C and 0.5 °C for hot-film anemometry and optical fiber probe measurements respectively. Thus, the storage tank is equipped with a heat exchanger circulating industrial water to control temperature variations of the water.
  A filter with 5 µm mesh size is installed on a by-pass to filter water to prevent the contamination of water by particles which may damage the probes.

– a water circulation system (pump provided by Finder with 2.8 bar discharge pressure, 150 m^3/h maximum flow rate and 18.5 kW electrical power) connected to the test section via two flow measurement lines:
  - a line with a nominal diameter of 25 mm for 0-to-15 m^3/h range associated with a Coriolis mass-flow meter,
  - a line with a nominal diameter of 100 mm for 15-to-150 m^3/h range associated with a volumetric electromagnetic flow meter.

The water is circulated in a closed circuit such that the water flows through the test section and returns to storage tank which acts as a cyclone separator at the tangential inlet. A grid system, seen in Figure 2.3, is installed in the storage tank to eliminate the bubbles in the water circuit.

[1]A normoliter (Nl) represents a liter under normal conditions (temperature of 273.15 K and pressure of 101325 Pa).

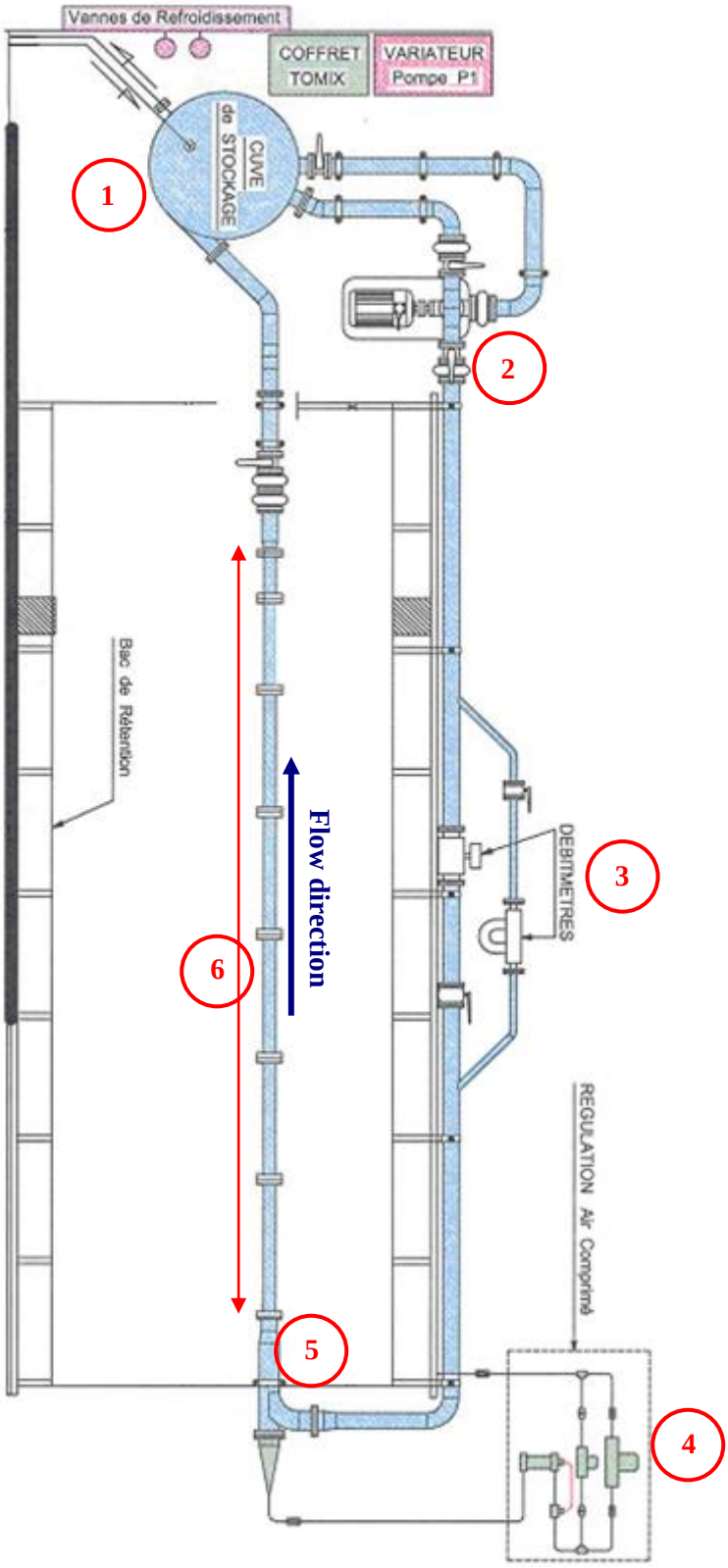

Figure 2.2 - Schematic of the experimental setup: (1) Water storage tank, (2) pomp, by-pass and filter, (3) water flow rate measurement system, (4) air filtration and flow rate measurement system, (5) fluid injection, (6) test section

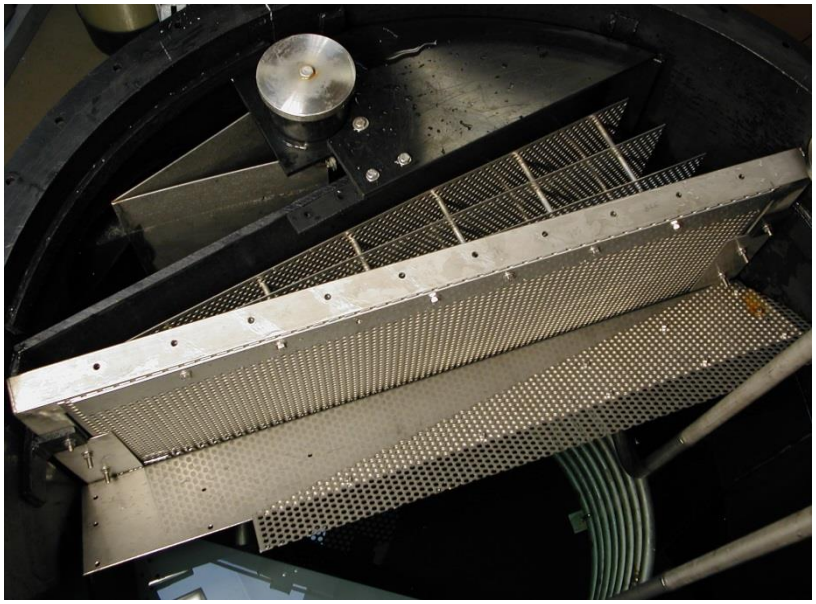

Figure 2.3 - Grid system in the storage tank for bubble elimination

The air circulation system consists in:

- a line for air supply coming from bonded network of the building (7 bars) via expansion/filtration station,
- two lines to measure and control the flow:
  - a line for 0-to-40 Nl/min range,
  - a line for 40-to-350 Nl/min range.

The air flowing in the test section is released to the atmosphere in the room after the separation in the water storage tank. Thus, the air circuit becomes open. Air and water are mixed in the inlet of test section via a system of 320 water tubes and 37 air injection tubes.

A test series with hot-film anemometry probes were conducted by Bottin (2010) to observe the effects of the upstream conditions. Although a settling system is installed, the velocity profiles showed the effect of the elbow in which the water is flowing. In addition, the existence of air injectors causes a wake and its effects can be observed from velocity profiles and void fraction profiles measured by optical fiber probes. In order to eliminate the effects of upstream conditions, grids with different mesh sizes were installed in the inlet of the test section and several tests were carried out. Consequently, a system of three grids with decreasing mesh size in the direction of the flow (see details in Table 2.1) was chosen and installed at the air injectors after the settling system. The grid system and air injectors held together with a strapping system and spacers.

Grid Number	Pitch (mm)	Wire diameter (mm)	Porosity[2]
1	2.71	0.71	0.545
2	1.475	0.35	0.582
3	1.391	0.221	0.7075

Table 2.1 - Characteristics of the grids at the inlet

Bottin (2010) stated that the homogenization of the flow was improved and the influence of upstream conditions (elbow and wakes due to air injectors) was significantly reduced after the installation of

[2] Porosity: Ratio of empty surface to total surface

three-grid system. In addition, three-grid system resulted in a better bubble dispersion in two-phase flows.

Although the three-grid system improved the dispersion of the bubbles, it was observed that the bubbles were fragmented with various sizes after the injectors in the case of low liquid flow rates, as seen in Figure 2.4. Thus, another grid (the fourth grid) was installed after the three-grid system to improve the homogenization of the bubbles. In addition, a fifth grid was installed at twenty centimeters upstream of the settling system. A schematic of injection/settling/homogenization system is given in Figure 2.5.

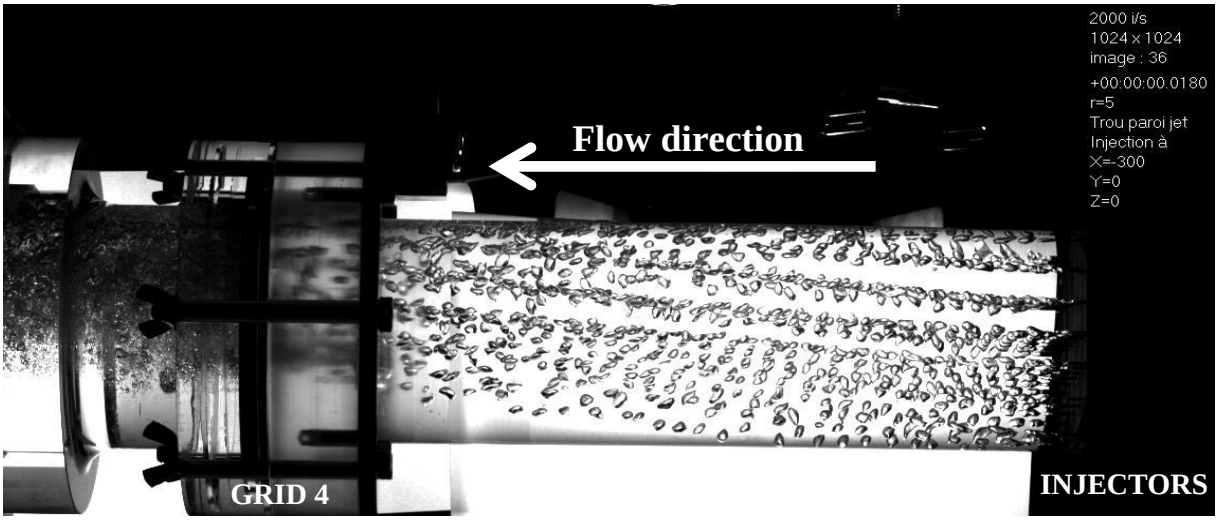

Figure 2.4 - Fragmentation of the bubbles on the mixing grid (grid 4) for J_L=2.12 m/s and J_G=0.064 m/s

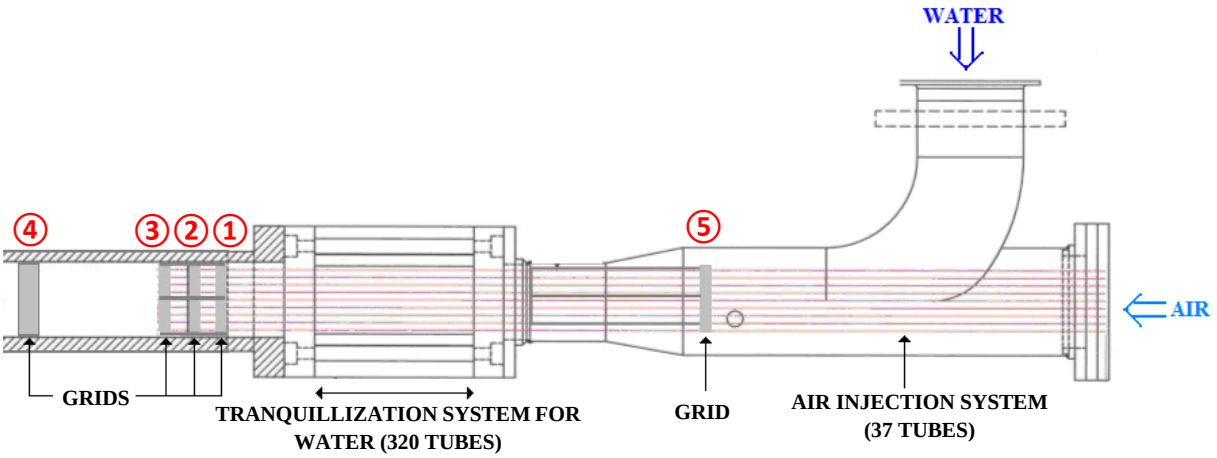

Figure 2.5 - Schematic of tranquillization/homogenization system

Bottin (2010) measured intercept length distribution profiles at 5 diameters downstream of the inlet and for various air/water superficial velocities (J_G and J_L) and presented the results in terms of probability density functions, as seen in Figure 2.6. The results showed that the bubbles have considerably the same size after the grid system and required homogenization of bubbles was established.

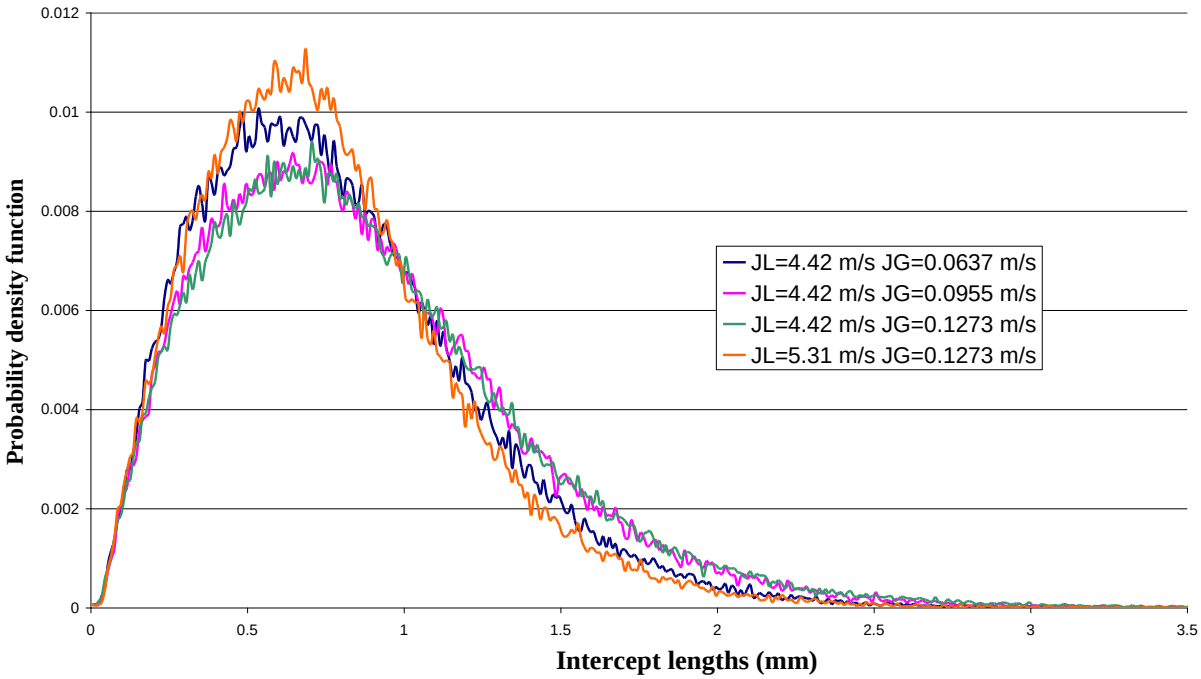

Figure 2.6 - Probability density function of intercept lengths, averaged in the section, at 5 diameters (Bottin, 2010)

2.2.2 Instrumentation

There exist two types of instrumentation on the METERO experiment. The first group (two water flow meters, two air flow meters, two pressure sensors, two temperature sensors) is used to measure the flow conditions. Their characteristics are:

- *Krohne water flow meter*: 15-to-150 m^3/h range with ±2% accuracy of measurement point,
- *Brooks Emerson gas flow meter for smaller flow rates*: 2-to-50 Nl/min range with ±0.07% accuracy of measurement point,
- *Books Emerson gas flow meter for greater flow rates*: 40-to-1000 Nl/min range with ±0.07% accuracy of measurement point,
- *K-type thermocouples*: 0-to-50 °C range with ±0.5% accuracy of measurement point.

The second group of instrumentation is dedicated to the study of the flow regime characteristics. The instrumentations in this group are:

- *optical fiber probes* measuring the local phase indicator functions and providing information about main characteristic parameters of two-phase flows such as void fraction, interfacial area concentration, bubble velocity, etc.,
- *hot-film anemometry probes*, after the discrimination of liquid and gas phases, providing access to the axial and radial components of the instantaneous liquid velocity vector,
- *high-speed camera* which can acquire images with very high frequency to observe two-phase flows and short-lived phenomena that may occur.

Optical fiber and hot-film anemometry probes are installed on portable-rotatable sections and connected to a traversing system as seen in Figure 2.7. The traversing system is driven by a stepper motor with a micrometric precision and is operated by a Microcontrôle ITL09 control element. This traversing system moves the probes along vertical axis in the test section.

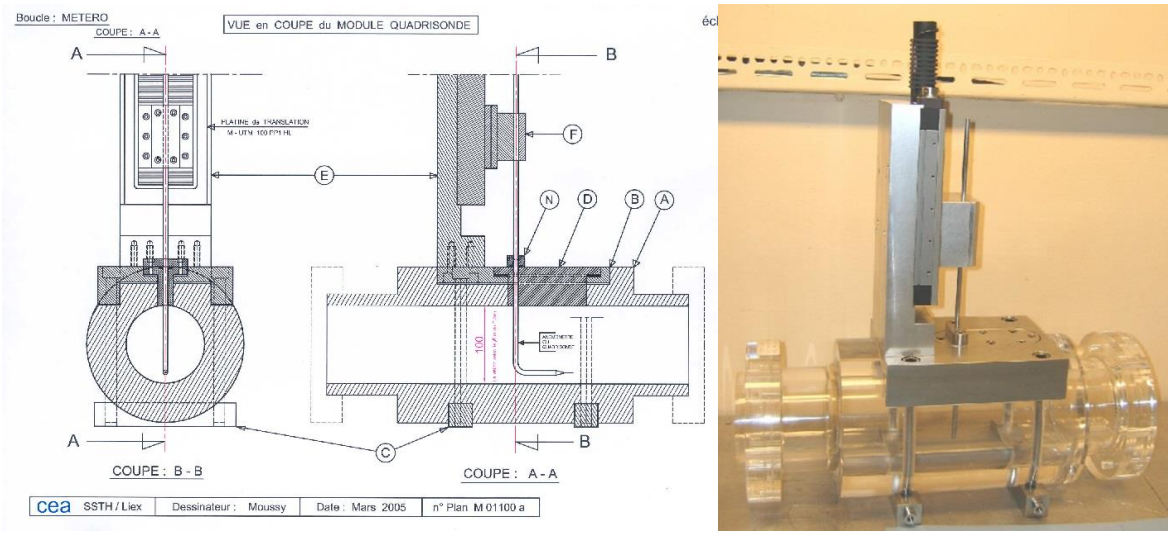

Figure 2.7 - Instrumentation module

2.3 Operation of the Experimental Setup

The entire system is controlled remotely from the control room and National Instruments PCI-6229 and PCI-6143 acquisition cards can acquire the loop conditions and the measurements. The air and water flow rates are controlled manually from the control room via a control board which displays the flow conditions (flow rates, temperatures, pressures).

All the measurement instrumentations, except high-speed camera, are also controlled remotely from the control room by personal computer via controlling programs written in Labview or VI (Virtual Instrument) computer languages. The main control program, *pilotage-metero.vi* whose user interface is shown in Figure 2.8, can control instrumentation by sending commands to a stepper motor for vertical movement of probes and acquire measurements.

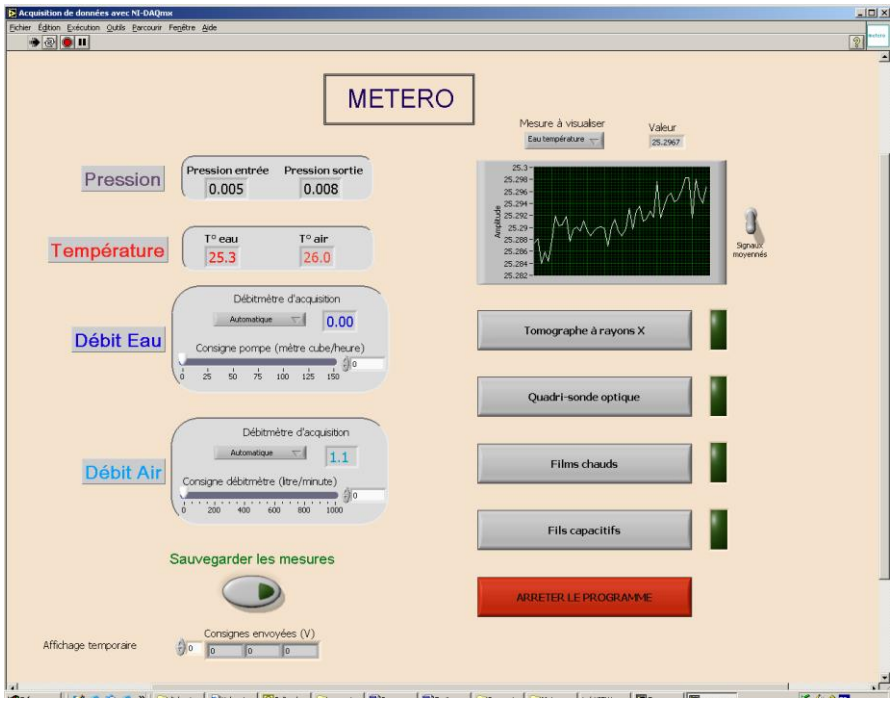

Figure 2.8 - User interface of *pilotage-metero.vi*

The importance of the water temperature influence on the measured voltages across the hot-film probes was observed in the test carried out in single phase water flow. The water temperature is significantly important for the hot-film anemometer acquisitions due to:

- the temperature dependence of the wire resistances,
- the low overheating factor used for the measurements in the water to avoid parasite boiling problems and accelerated aging of the probes,
- very high convective heat transfer coefficient of water.

Several tests showed that a variation of a few tenth degrees in water temperature results in an error of several percent on the measured instantaneous velocity. Thus, Bottin (2010) used a correction factor for the temperature data (see Appendix 2) which is valid for small changes in the water temperature. Consequently, it is crucially important to carry on the acquisitions for stable temperature conditions.

For the stabilization of the water temperature, a heat exchanger consisting of small tubes is installed in the storage tank. Industrial water is circulated in this heat exchanger and the flow rate of the industrial water is controlled by an automatic differential valve which compares the water temperature and set temperature entered by user. Although there are several factors affecting the water temperature (industrial water temperature, ambient temperature, heat generated by the pump), it is easy to control the temperature of water circulated in the METERO experiment by the help of the automatic valve.

In order to reduce the uncertainty in the temperature measurements, the thermocouples installed on the experimental setup were calibrated by using a calibration bath whose temperature is controlled and measured by a platinum precision probe PT100. Bottin (2010) also verified that the temperature upstream of the test section (reference temperature of the acquisitions) and liquid temperature at the anemometer probe are equivalent. As a final step to reduce the uncertainty, a calibration before and after each hot-film anemometer acquisition are performed to optimize the voltage/velocity conversion and temperature correction coefficient for hot-film anemometry measurements (see section 4.2.4.2).

It is essentially important to utilize the METERO experiment with particle free water, since the probes are significantly fragile and even a slight shock with any particle results in the destruction of the probes. In addition, any dirt on the probes causes a change on the voltage across the films of the probe due the deterioration of the heat transfer. Thus, the water circulated in the experiment is changed and filtered periodically with the installed filters (5 μm filters). The entire installation is also cleaned with a dry cloth without any chemicals.

Bottin (2010) also measured the surface tension of water, taken from tap water and used in the METERO experiment, under static conditions for several samples. The surface tension was measured at 18 °C by an interfacial tension meter K8 provided by KRUSS® and the results were compared to the surface tensions of other water samples. This comparison, given in Table 2.2, showed that the static surface tension of water from METERO (58.5 mN/m) is very close to that of tap water (61.5 mN/m).

Analyzed Sample	**Superficial tension (mN/m)**
METERO sample n^{o} 1	58
METERO sample n^{o} 2	59
Demineralized water	66
Tap water	61.5
Doubly distilled water	72.6

Table 2.2 - Comparison of surface tensions for various water samples (Bottin, 2010)

CHAPTER 3

THE MEASUREMENT TECHNIQUES

3 THE MEASUREMENT TECHNIQUES

3.1 Optical Fiber Probes

Optical fiber probe is a measurement technique which is based on Snell's law of diffraction mentioned by Danel and Delhaye (1971), Abuaf et al. (1978), and Moujaes (1990) to determine the different phases in multiphase flows discretely by the help of the different refraction index of each phase. This probe type is preferred among other probe types because of its various advantages: shorter response times compared to electrical probes, possibility to operate even in mineralized water while electrical probes operate in demineralized water and better flow characteristics measurements due to reduced dimensions (a few microns).

The probe is connected to RBI™ optoelectronic system which emits a laser beam at the probe tip via an emission/reception box. As seen in Figure 3.1, the laser beam is totally reflected when the probe tip is in the gas phase. On the other hand, the refraction index of water causes the penetration of the laser beam from the probe tip into the liquid phase. In the reception box, a photodetector determines the presence of the reflected laser beam and generates an analog electrical signal with high and low levels due to the presence of gas and liquid phases respectively. This analog signal is converted into a binary signal which is called Phase Indicator Function (PIF). The characteristic quantities of two-phase flows, namely void fraction, interfacial area concentration, velocity, frequency and average bubble diameter, are calculated by analyzing phase indicator functions.

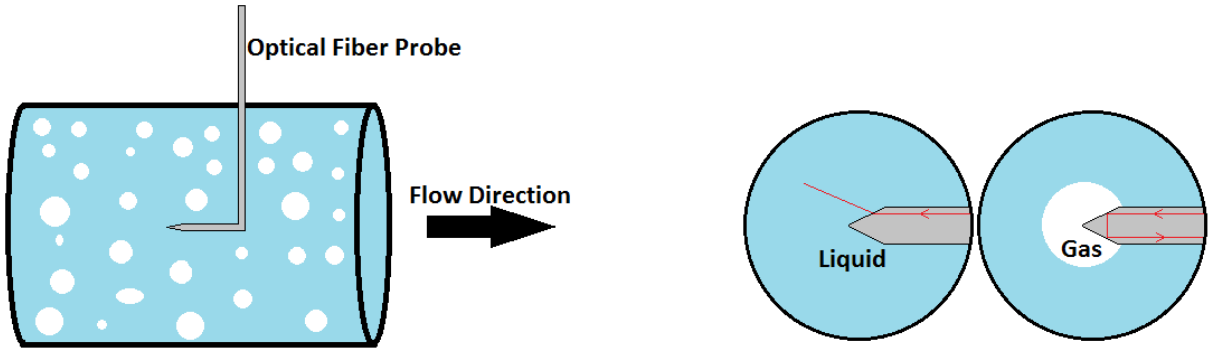

Figure 3.1 - Operation principle of optical fiber probes

3.1.1 Material and production process

The optical fiber probes were produced from conventional optical fiber cables. In order to have a sharp and precisely small probe tip, the fibers were cut by P 2000 SUTTER device. Once the probe was produced, the probe geometry (Figure 3.2) was measured by a Nikon™ Profile Projector to prepare the three dimensional geometrical information of the probe for the data acquisition software. As seen from Figure 3.3, the axial distance between the central tip and rear tips is around 500 microns. The radial distance is around 200 microns which determines the minimum measured bubble size by this probe.

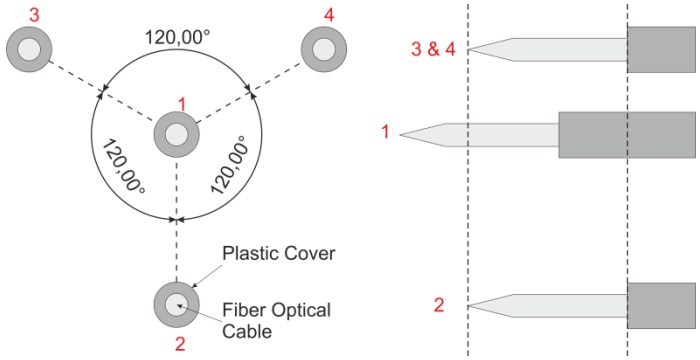

(a) Front View (b) Side View

Figure 3.2 - Schematic diagram of a four-tip optical fiber probe

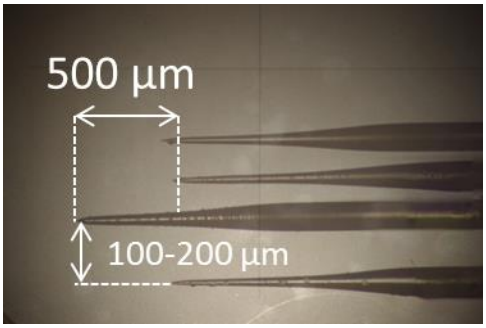

Figure 3.3 - Dimensions of a four-tip optical probe

In the previous studies, two-point optical fiber probes were utilized with an assumption such that only spherical bubbles take place in the dispersed bubbly flows. However, it was observed by high-speed camera visualizations that the bubbles are deformed after contact with probe, as seen in Figure 3.4. In addition, bubbles are also deformed in intermittent flow regimes such as plug and slug flows. Thus, the use of four-point optical probes which can provide more detailed information about the flow characteristics (presented in Figure 3.2) is necessary. In this report, the optical probe measurements were acquired by four-point optical fiber probes.

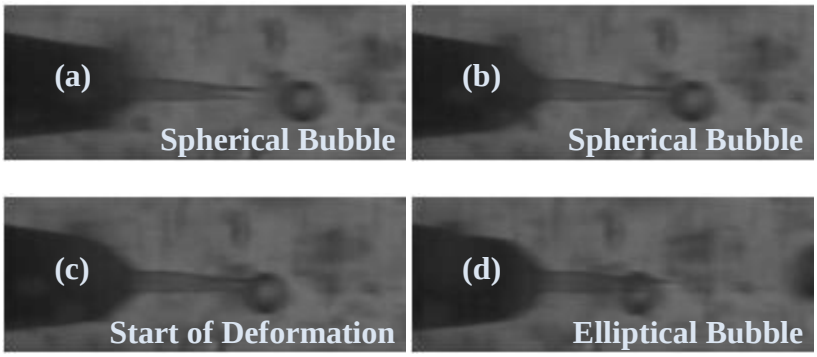

Figure 3.4 - Interaction of a spherical bubble with optical fiber probe

3.1.2 Generation of PIFs

As mentioned before, an analog electrical signal is created by the optoelectronic system due to the reflection or refraction of the laser beam. Double thresholding is applied to this analog signal in order to generate a digital signal (PIF). Analog-to-Digital (A/D) signal transformation is represented in Figure 3.5.

The parameters of A/D signal transformation (for instance, the threshold voltages) can be adjusted by utilizing potentiometers on the optoelectronic system. The adjustment of the threshold voltages is not an automatic process, thus the level of the threshold voltages is set closer to the minimum and maximum signal voltage levels. As a final remark, the PIF, generated after A/D signal transformation, is acquired with a high sampling frequency of 2 MHz.

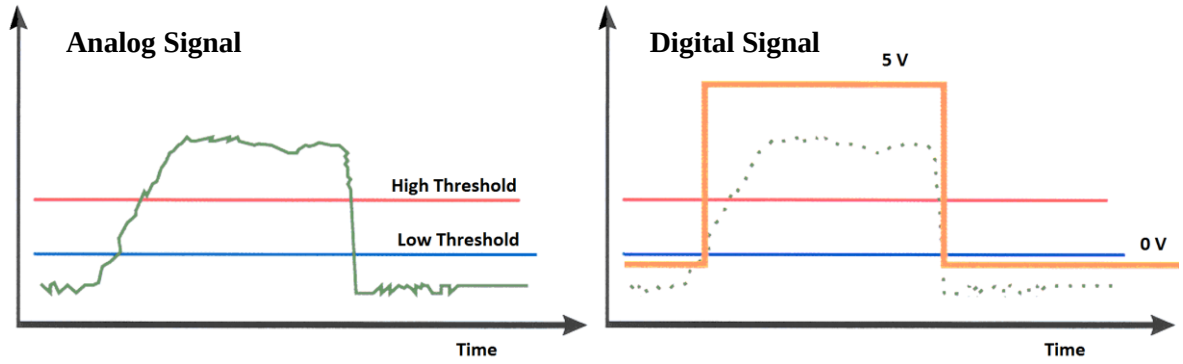

Figure 3.5 - A/D signal transformation (Bottin, 2010)

3.1.3 Analysis of PIFs

In this study, the analysis of PIFs is based on two following assumptions:

1. The concentration of the bubbles is homogenous in the volume where the probe located,
2. The flow of the particles is unidirectional

3.1.3.1 Void fraction

The void fraction (α) is measured by comparing the total time of the gas phase presence (t_{Gas}) in contact with the probe tips and the total time of the acquisition (t_{Total}) such as:

$$\alpha = \frac{\sum t_{Gas}}{\frac{N_b \in t_{Total}}{t_{Total}}} \quad (1)$$

N_b is the number of bubbles pierced by the probe tip during the acquisition. Void fraction is a result of a time average and it is critically important that the flow conditions are stable during the acquisitions.

3.1.3.2 Gas phase velocity

The average gas velocity is calculated by cross-correlating PIFs measured by each probe tip. In the analysis process, it is assumed that the measured PIFs are identical with a short time lag between the PIFs if the gas phase is pierced by all probe tips without any disturbance.

An example of cross-correlation analysis for the gas phase velocity is given in Figure 3.6. PIFs are coupled as 0-1, 0-2 and 0-3 and the "0" represents the PIF measured by the central tip. The time lag between each couple is determined by cross-correlation analysis. In the analysis, "PIF 0" is chosen as reference and the second PIF of each couple is shifted and multiplied with the reference PIF. This process creates a peak point, as in Figure 3.6 (b), when the best overlap occurs. In other words, if the shift of the second PIF equals the time lag between the couples, the multiplication of reference PIF and shifted PIF brings a peak point.

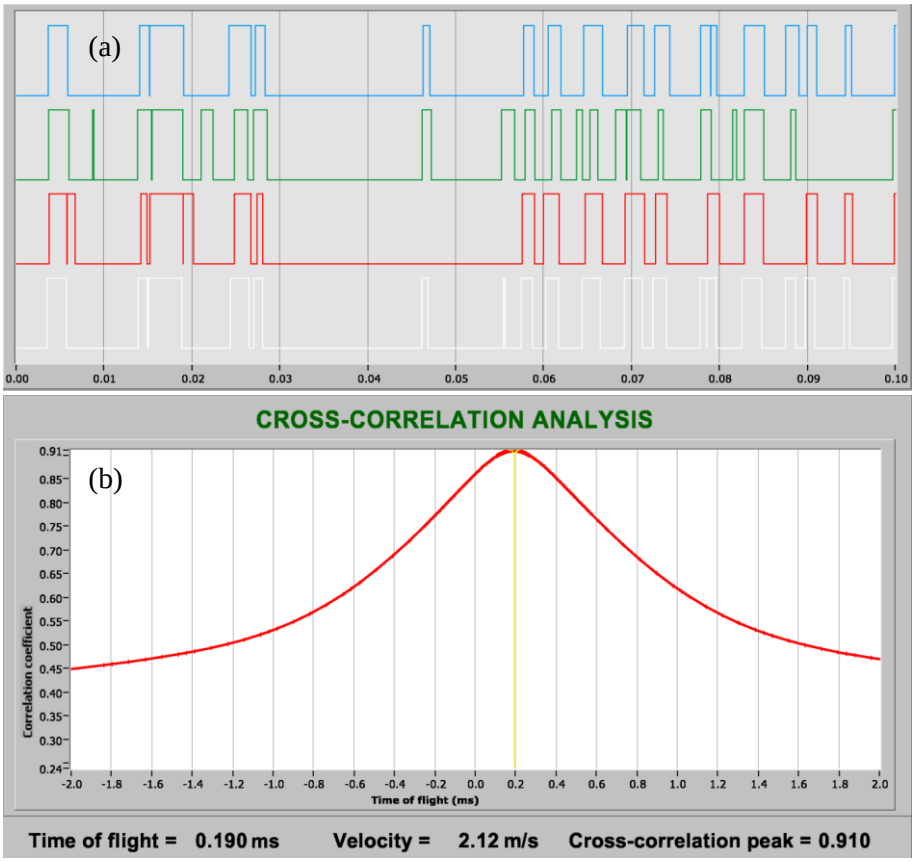

Figure 3.6 - (a) Phase indicator functions, (b) Cross-correlation analysis

The peak point of the cross-correlation function represents the most frequently measured time lag between PIF couples and it gives an average time of flight between PIFs. Moreover, the average gas phase velocity is calculated from the average time of flight and distances between the probe tips. In our case, there exists 3 PIF couples, thus this brings three independent gas phase velocities calculated by the analysis. These three velocities are used to calculate the average velocity by using the following formula:

$$V_{Gas} = \frac{1}{N}\sum_{i=1}^{N}\frac{\Delta d_{0i}}{\Delta t_{0i}} \tag{2}$$

In Equation (2), Δd_{0i} represents the distance between the probe tip couples and Δt_{0i} is the time lag between PIF couples calculated by cross-correlation analysis.

The peak value of the cross-correlation function is an indicator of the calculation and acquisition quality such that the larger the value of the peak, the more bubbles pierced by the optical fiber probe and the more precise information from the signal processing.

3.1.3.3 Granulometry

Granulometry is the study of the bubble size distribution in the flow. The intercept lengths of gas phase are calculated by using the gas phase velocity and the duration of the gas phase occurrence. The histogram of the intercept lengths gives the distribution function h_L as a function of intercept length l. For the bubble size calculation, several methods based on Bayes' theorem (Langston et al., 2001) which is the application in the case of bubbles can be used. In addition, the studies of Herringe & Davis (1976) and Suzanne et al. (1998) on the bubble sizes can also be taken into account. In this study

and in the study of Bottin (2010), stereological and statistical processing allows to access to the bubble diameter distribution function $h_D(l)$ from the histogram of the intercept lengths by using differential expression introduced by Gundersen & Jensen (1983):

$$h_D(l) = \frac{1}{2}\left[h_c(l) - l\frac{d(h_c(l))}{dl} \right] \tag{3}$$

The average bubble diameter can be calculated from the diameter distribution function in a statistical way. The moment of order p is obtained by integrating the bubble diameter histogram with the following formula:

$$S_p = \int_0^\infty d^p \cdot h_D(d) \cdot dd = N_b \int_0^\infty d^p \cdot p_D(d) \cdot dd \tag{4}$$

, where $p(d) = \frac{h_D(d)}{N_b}$ and N_b is the number of bubbles.

The bubble size can be characterized by calculating an average diameter d_{pq} for moments p and q such as:

$$d_{pq} = \left(\frac{S_p}{S_q} \right)^{\frac{1}{p-q}} \tag{5}$$

Thus, Sauter mean diameter (d_{32}), most commonly used term to represent the average bubble size, can be calculated as (Kamp et al., 2001):

$$d_{32} = \left(\frac{S_3}{S_2} \right)^{\frac{1}{3-2}} = \frac{\int_0^\infty d^3 \cdot f(d) \cdot dd}{\int_0^\infty d^2 \cdot f(d) \cdot dd} \tag{6}$$

3.1.3.4 Interfacial area

Acquiring the void fraction and Sauter mean diameter leads to the calculation of the interfacial area such as:

$$Ai = \frac{6\alpha}{d_{32}} \tag{7}$$

3.1.4 Acquisition and analysis software

The control and the acquisition of the optical probes are operated by a Labview™ routine (details are given in Appendix 4). In this routine, the measurement locations along the test section axis are imposed by the user. Afterwards, the probe is moved to each measurement location, and the signals are acquired and saved in a binary file. For each measurement location, a binary file is recorded to a

directory; moreover, a log file of the acquisition which contains operating conditions during acquisitions (namely temperature, pressure, flow rates, etc.) is also recorded in the same directory.

For the analysis of the measurements, a home-developed software called ISO (Interface pour Sondes Optique in French) is utilized to record the probe geometry and perform post-processing. Before starting the acquisitions, the probe geometry (i.e. the relative position of each tip with respect to the central tip) and acquisition parameters (maximum acquisition period and maximum bubble number) should be registered in ISO. In the METERO experiment, maximum acquisition period is set to 15 minutes and the bubble number parameter is 200000 for each probe tip. These two parameters are sufficient to ensure statistical convergence of the results due to the lack of the bubbles in certain areas of the test section (for example in the lower part of the test section, the bubble are rare). The time-averaged the flow quantities, mentioned before, are obtained by processing PIFs for each measurement location and these results are recorded in a file which also contains all the acquisition conditions (flow rates, temperatures, etc.).

Void fraction for each measurement location is calculated from the PIF of central probe tip by ratio of the total duration of gas phase to the total acquisition period (Equation (1)). By applying cross-correlation to PIFs, the velocity is calculated for each PIF couple and the overall velocity is calculated by averaging the individual velocities (Equation (2)). Sauter mean diameter and interfacial area are calculated from the histograms of the bubble diameter by using Equations (6) and (7). Distribution of intercept lengths is also calculated by ISO. The details are given in Appendix 4.

3.1.5 Measurement uncertainties

There are various sources of uncertainties on the measured quantities by the optical fiber probes as shown in Figure 3.7. In the figure, the uncertainty factors are represented in red and these factors can introduce error at each step, given in black frames, while obtaining average interfacial area values.

Estimation of the measurement uncertainties is difficult and depends on various factors, i.e. the way a bubble is pierced by an optical probe, the characteristics of a bubble (shape, size, velocity, etc.) and the location of the optical probe in the test section. Bottin (2010) investigated the gas temperature effect on the probe sensitivity and the results showed that temperature variations have a negligible effect on the measurements. Moreover, Cubizolles (1996) carried out a detailed study about the measurement errors of the optical fiber probes. The maximum error of the local void fraction was estimated as ±5% and the errors on the local quantities derived from PIF couples, e.g. velocity, Sauter mean diameter, are approximately ±10%. For the local interfacial area measurements, the estimated error is proportional to the ratio of the void fraction and Sauter mean diameter errors and it is about ±15%.

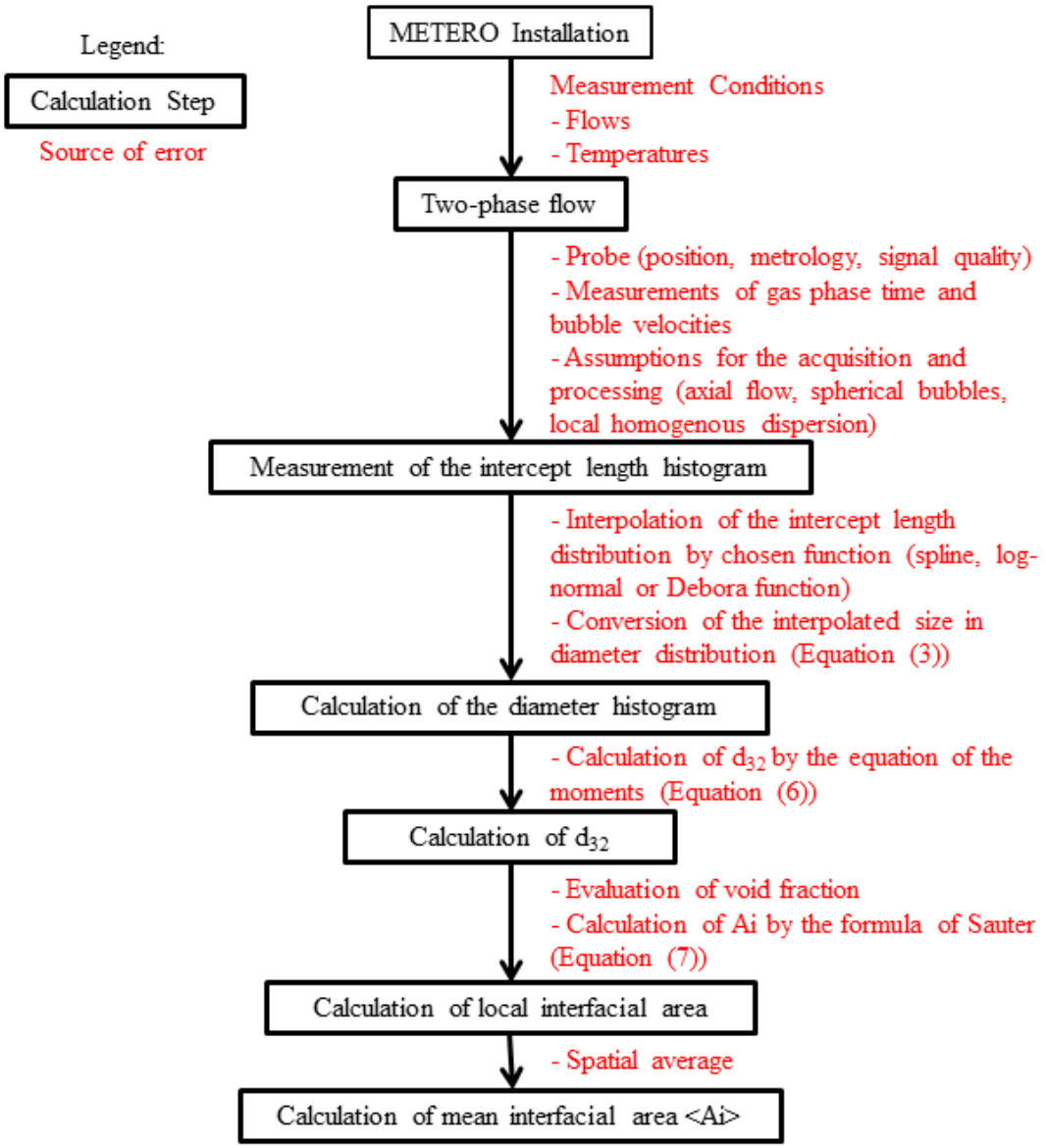

Figure 3.7 - Flow chart of steps leading to the calculation of <Ai> and associated error sources (Bottin, 2010)

While obtaining averaged quantities from the local quantities, the integration process of local measurements can introduce an error. Indeed, the measurements were conducted on the radial (vertical axis) profile and it is assumed that the distribution of the quantities is homogenous in the orthoradial axis. Andreussi et al. (1999) studied the distribution of the void fraction with different inclinations over a test section, as represented in Figure 3.8. For the profile at 0^o (along the vertical axis, represented in red), the void fraction increases with increasing r (altitude in the test section). On the other hand the distribution of the void fraction is nearly homogenous and constant at 90^o profile (along the orthoradial axis, represented in blue). These results show that the distribution of the flow quantities along the orthoradial axis is homogenous and constant, thus the assumption for our optical fiber probe measurements is justified.

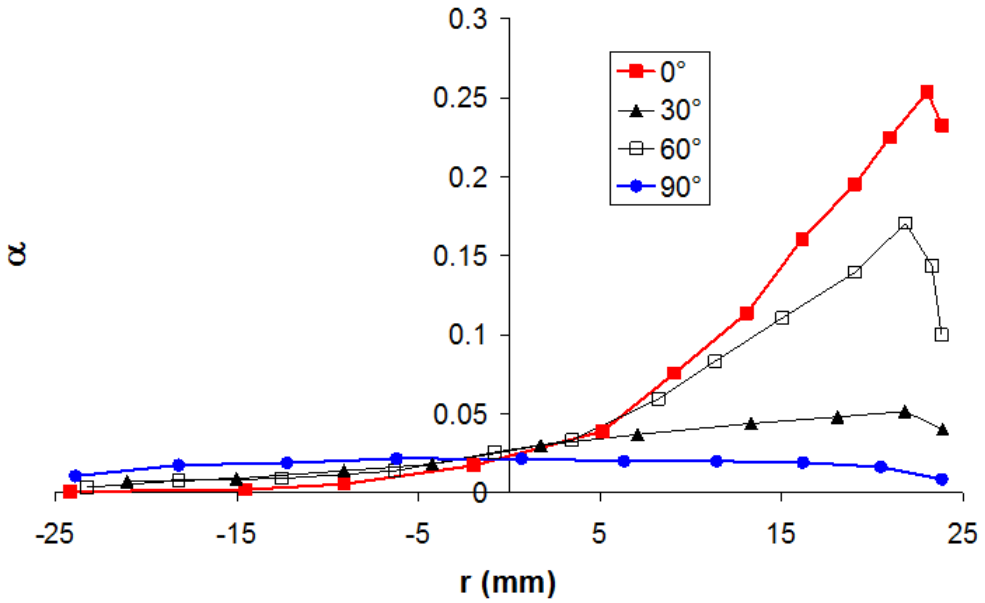

Figure 3.8 - Void fraction profiles with different inclinations (Andreussi et al., 1999)

Uncertainties due to the spatial averaging of local flow quantities were studied by Bottin (2010). The details of this study are given in Appendix 4. The results of this study showed that the estimated maximum uncertainty of the integration is around ±10%. When the integration and measurement uncertainties are combined, the maximum uncertainties in average void fraction and average interfacial are around ±15% and ±25% respectively.

3.2 Hot-Film Anemometry

Hot-film anemometry is a well-known and convenient velocity measurement technique especially for the single phase flows. In CEA, this measurement technique has been utilized for a long time and a well knowledge about this technique has been established. Moreover, hot-film anemometry was used in the studies of Bottin (2010), thus the equipment is already present in the laboratory. As a result, this measurement technique was preferred to measure the liquid velocity instead of other techniques such as Laser Dopler Velocimery (LDV) and Particle Image Velocimetry (PIV), etc. The advantage of this technique is the operation availability in the multiphase flows even with high void fractions and providing instantaneous liquid velocity measurements. On the other hand, the presence of the bubbles in multiphase flows is a disadvantage for this technique which results in the underestimation of the liquid velocity. However, this disadvantage can be neglected with an intelligent phase discrimination process which will be explained in Section 3.2.3.4.

3.2.1 Operation principle

The operation principle of the hot-film anemometry is based on the heat exchange rate which is measured by the sensing element of the probe located in the flow. The film is heated by Joule effect ($P_{Joule} = R_{wire}.I^2$ where I is the current on the film) and it is cooled by the liquid flow. As a result, the measured liquid velocity is a function of the heat removed from the film. In other words, the higher velocity of the flow results in the higher heat removed from the film.

In this study, a constant temperature anemometry has been used. As seen in Figure 3.9, the film (R_S) is a part of a Wheatstone bridge which provides the constant temperature on the film. In the case of a sudden change of the heat flow on the film (film resistance variation), Wheatstone bridge is out of balance and a current is returned to the bridge to restore the film temperature to the adjusted constant

value and the probe resistance to its initial value. These current fluctuations due to the imbalance of the bridge represent the heat flux fluctuations on the film, consequently, the liquid velocity fluctuations.

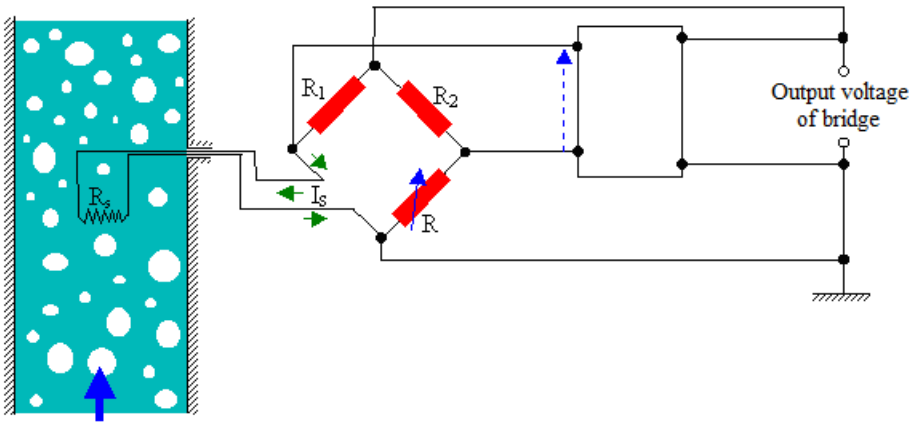

Figure 3.9 - Operation principle of a constant temperature anemometer (Bottin, 2010)

The heat removed from the film is dependent on the Reynolds number of the flow and the Nusselt number which is a function of the Reynolds and Prandtl numbers. In the literature, there are several correlations to calculate the Nusselt number. In this study, Nusselt number correlation for forced convection flows introduced by King (1914) and cited in Collis & Williams (1959) and Bottin (2010) is taken into account such as:

$$Nu = A_{Nu}(\mathrm{Pr}) + B_{Nu}(\mathrm{Pr}) \cdot \mathrm{Re}_{film}^{\,n_K} \tag{8}$$

In Equation (8), *Nu*, *Pr* and Re_{film} are the Nusselt, Prandtl and Reynolds numbers of the flow based on the hot-film diameter and $A_{Nu}(Pr)$ and $B_{Nu}(Pr)$ are constants depending on the Prandtl number. In general the power n_K is approximately 0.5.

The voltage on the film is a function of the balance between the power produced by Joule effect and the heat transferred from the film to the liquid which brings the Nusselt number. At this point, the implementation of King's correlation of Nusselt number into the power balance equation results in a relation between the Reynolds number of the flow and the current passing through the film. Once the resistance of the film is known, this relation can be transformed into a relation between the Reynolds number, which is a function of liquid velocity, and the voltage across the film by the help of the Ohm's law ($e = R_{film} \,.\, I$). Finally, the voltage across the film can be formulized as a function of the ambient temperature (T_a) and the liquid velocity (V_{liq}) as in Equation (9). The details of this relation are given in Appendix 2.

$$e^2(T_a) = A'(T_a) + B'(T_a) \cdot V_{liq}^{\,n_K} \tag{9}$$

The power n_K in Equation (9) has been investigated by various authors. For example, Comte-Bellot & Corrsin (1966) suggested this term ranging from 0.45 to 0.5 for thermal anemometry in air and for probe diameter based Reynolds number which is ranging from 0.02 to 44. However, Bottin (2010) showed that the probe diameter based number in the METERO experiment is around 200 and it is not possible to apply the n_K of Comte-Bellot & Corrsin (1966) in the METERO experiments. Thus, the author optimized the power n_K as 0.15 and this power is also used in this study.

As seen in Equation (9), the measured voltage across the film is highly sensitive to the ambient temperature (T_a) and this brings a necessity of temperature correction with respect to a reference temperature. In this study, the classical temperature correction formula has been used and the details are given in Appendix 2. The voltage measured at an ambient temperature (T_a) different from a reference temperature (T_{ref}) is given by Bearman (1971) and Brunn (1995) such as:

$$e(T_a) \approx \left(\frac{T_{wire} - T_a}{T_{wire} - T_{ref}} \right)^{0.5} \cdot e(T_{ref}) \tag{10}$$

In Equation (10), T_{wire} represents the temperature of the sensing element of the probe, film in our case. By the help of Equations (8), (9) and (10), and calibration (see Section 3.2.4.2) the relation between the voltage across the probe and the liquid flow velocity is determined.

In multiphase flows, the application of hot-film anemometry to measure liquid velocity is more difficult due to the different characteristics of the fluids. In other words, the heat transfer coefficients of the fluids can be very different. For instance, the heat transfer coefficient of water is greater than that of air in air-water two-phase flows. As a result, the measured voltage in the case of probe-water interaction is greater. In addition, lower heat transfer coefficient of air results in lower levels of measured voltages which do not represent actual liquid velocities in the flow. Furthermore, high velocity fluctuations in highly turbulent flows bring the difficulty to discriminate the velocity fluctuations and fluctuations due to probe-air interaction. Thus, these facts bring the necessity of a reliable phase discrimination process for voltage signals of hot-film anemometry. A discrimination method was already introduced by Bottin (2010) for the measured signals by single component hot-film anemometry probes. This method was improved for the signals measured by two-component hot-film anemometry probes in the framework of the present study. The details of the improved discrimination process are given in Section 3.2.3.4.

3.2.2 System

3.2.2.1 Two component probe

There are two main parts for the hot film anemometry probes. The first part is the probe support on which the probe is placed and a thin film of platinum or nickel is the second part of the probe. The film is covered with a thin layer which provides sufficient insulation of the probe from the ambient liquid.

In the present study, a DANTEC™ 55R61 two-component X shape probe, Figure 3.10 (b), is utilized. This probe is composed of two crossed films in X shape at 45 degrees angle and each film is composed of a quartz layer (3 mm in length with 1.25 mm sensible part and 70 μm of diameter), a thin nickel coating layer and another layer of quartz insulator (2 μm). The films are connected to the probe support via a platinum plate. The dimensions of the probe prevents probe to be significantly close to the wall, thus the closest measurement location to the test section wall is 3 mm from the wall.

In the tests with two-component X shape probes, it has been observed that there exist intermittent gas pockets behind the hot-film probe for liquid superficial velocities greater than or equal to J_L = 3.90 m/s, as seen in Figure 3.11. The effect of air pockets was seen as an intermediate probe voltage level which represents the voltage level of neither probe-water interaction nor probe-air interaction (Figure 3.12). This phenomenon was studied by Bottin (2010) for various liquid and gas flow rates. The results

showed that this phenomenon is a result of the wake behind the film which creates a low pressure zone and traps the bubbles in this zone.

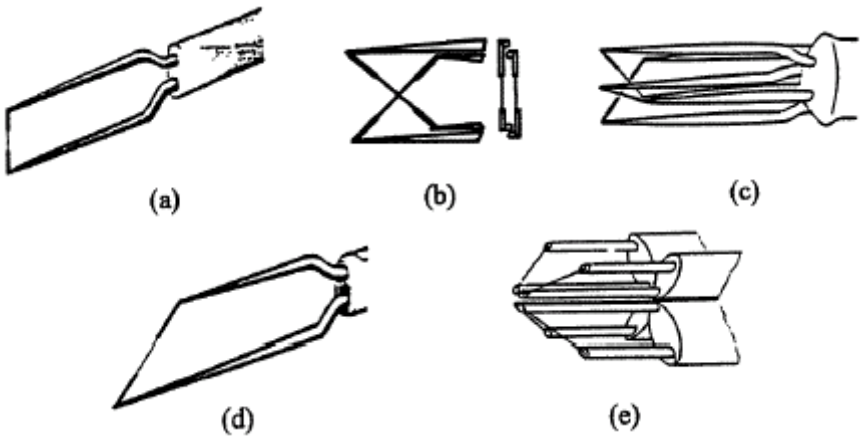

Figure 3.10 - Different configurations of hot-wire/hot-film probes
(a) single normal wire (DANTEC) ; (b) X shape wires ; (c) triple hot film (TSI-1299) ;
(d) inclined wire (DANTEC) ; (e) quad wires (Döbbeling et al., 1990)

Figure 3.11 - Air pockets behind the two-component hot-film probes

As mentioned before, the presence of bubbles in the flow complicates the discrimination process. In addition, the air pockets behind the film bring another difficulty for this sophisticated process. Thus, X shape probes should be used in the tests with liquid velocities lower than 3.90 m/s in two phase flows which is the concern of this study.

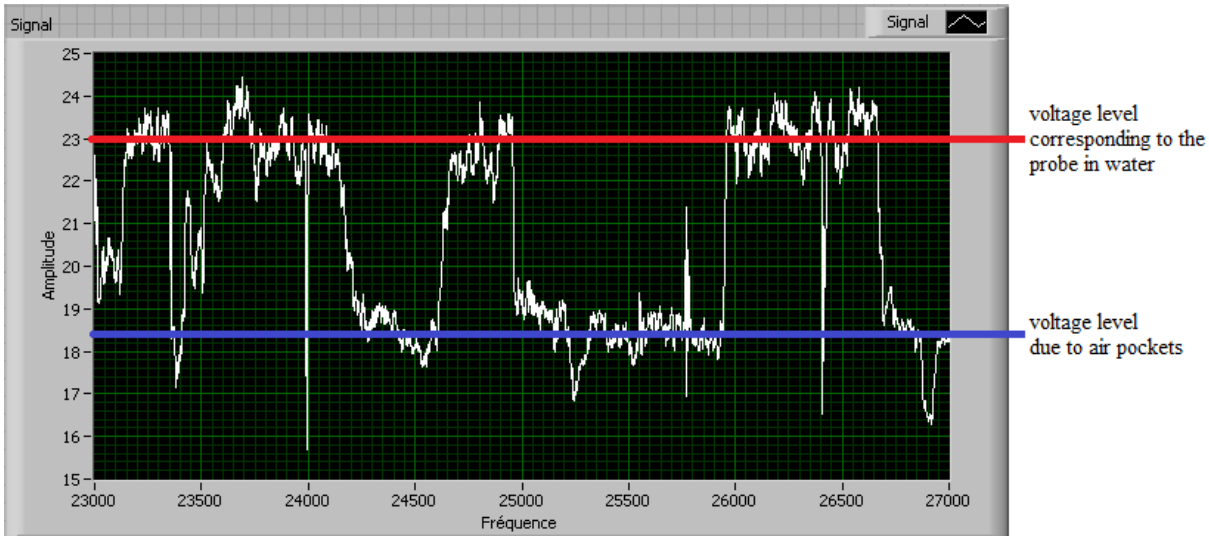

Figure 3.12 - Visualization of a voltage signal presenting clashes due to air pockets

3.2.2.2 Measurement system

The hot-film anemometer probes are connected to a constant temperature anemometry system, DANTEC® CTA Streamline®. This system acquires the analog signals coming from the probes, converts into digital signals, linearizes and stores the final digital signals as seen in Figure 3.13.

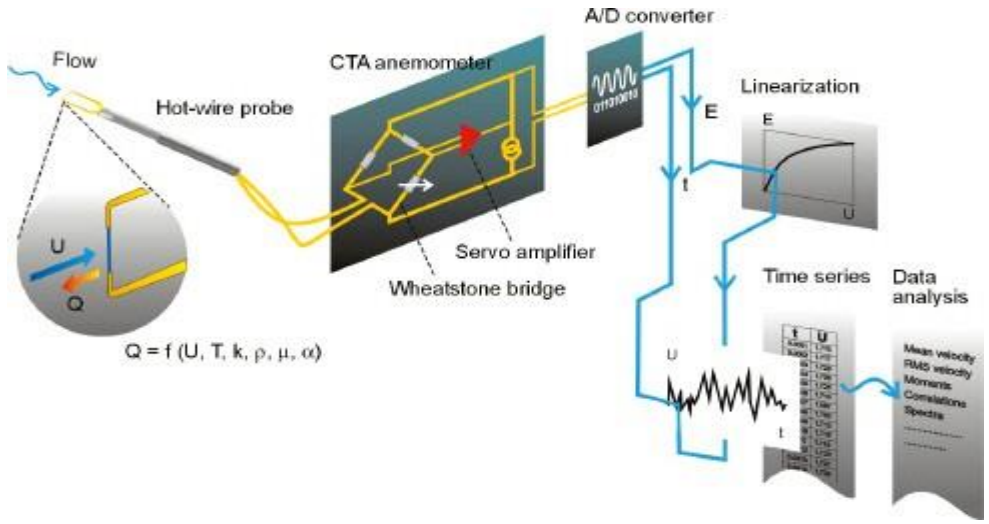

Figure 3.13 - Measurement chain diagram (Source: Dantec Dynamics®)

The parameters of Wheatstone bridge (measurement of the resistance of the probe and the cables, calculation and application of the overheating coefficient on the probe, response setting of servo-amplifier, signal conditioning, etc.) are adjusted on the Streamware software provided by Dantec™.

The acquisition of the output voltage signals is performed by a Labview™ acquisition routine which is prepared in the laboratory (see Section 3.2.3.2.2 for details) and the signals are acquired via a BNC2110 terminal and two channels of NI PCI 6143S card. This Labview™ routine generates and stores two binary files containing instantaneous voltage signals for each measurement location.

3.2.2.3 Fragility of hot-film anemometry probes

One of the main problems observed in the use of hot-film anemometry probes is the destruction due to very high fragility. This problem was also highlighted by Bottin (2010). There are two major reasons causing this problem: 1) Small particles in flows and 2) Triboelectricity effect.

In the METERO experiment, it was reported that particles which are colliding the probes can cause a fracture on the quartz coating. This fracture can lead to the destruction of hot-film probes even with very low liquid velocities. This problem was solved implementing a simple water filtration system with two particle sizes 5 and 25 microns (see Section 2.2.1) which can extract particles from the liquid.

In high liquid flow rates, the quartz coating is positively charged while the test section walls are positively charged. These electrical charges generate an electrical field in the liquid which creates an electrical potential around the coating. This electrical potential can damage the coating and the platinum/nickel part of the film can have a direct electrical contact with liquid. Once the electrical contact is established, the measured voltages are deteriorated and probe destruction occurs. In order to avoid this problem, three solutions were suggested. The first solution is the use of mineralized water which promotes the electrical charges and minimizes the electrical potential around the probe. Grounded electrodes equipped around the probe (as seen in Figure 3.14) are the second solution. By the help of the grounded electrode, the discharges damaging the quartz coating can be eliminated. The final solution is to adjust the gain of CTA servo amplifier to an intermediate value which avoid the effect of the electrostatic discharges on the output voltages and lead to a good response frequency in the measurements.

Figure 3.14 - An electrode system to protect hot-film anemometer probes

3.2.3 Data processing

3.2.3.1 Measurement system parameters

The measurement system parameters are adjusted on Dantec© Streamware software. The characteristics of the measurement system (e.g. probe type, probe support, probe terminals, cables and Wheatstone bridge information) and acquisition parameters (filters, gains and offset values) should be entered in the software, as seen in Figure 3.15. As seen in Figure 3.16, the probe parameters (e.g. reference temperatures for each film, overheat ratios which are chosen as 0.08 or 0.09 in the METERO experiments) should be adjusted for each experiment before the acquisitions. Afterwards, the software enables the settings of the bridge parameters and the power for the probe.

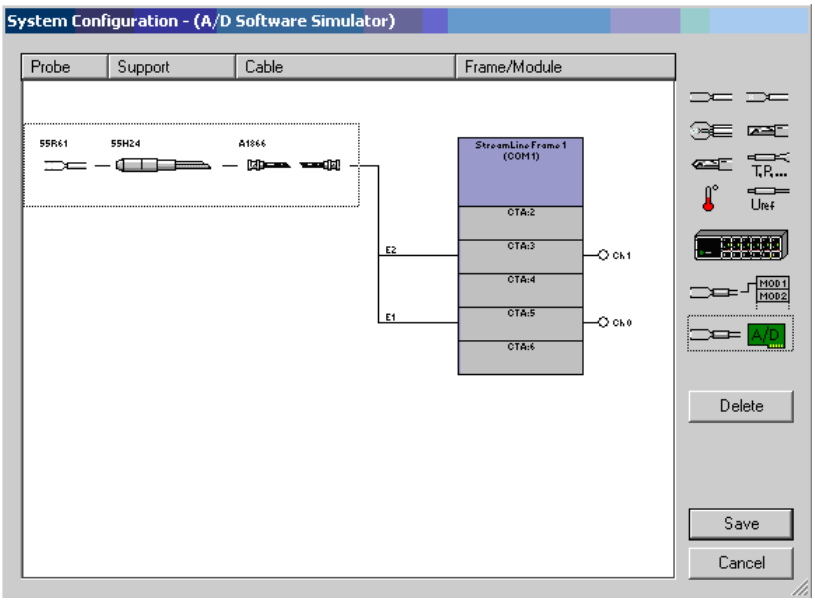

Figure 3.15 - Measurement system chain in Streamware

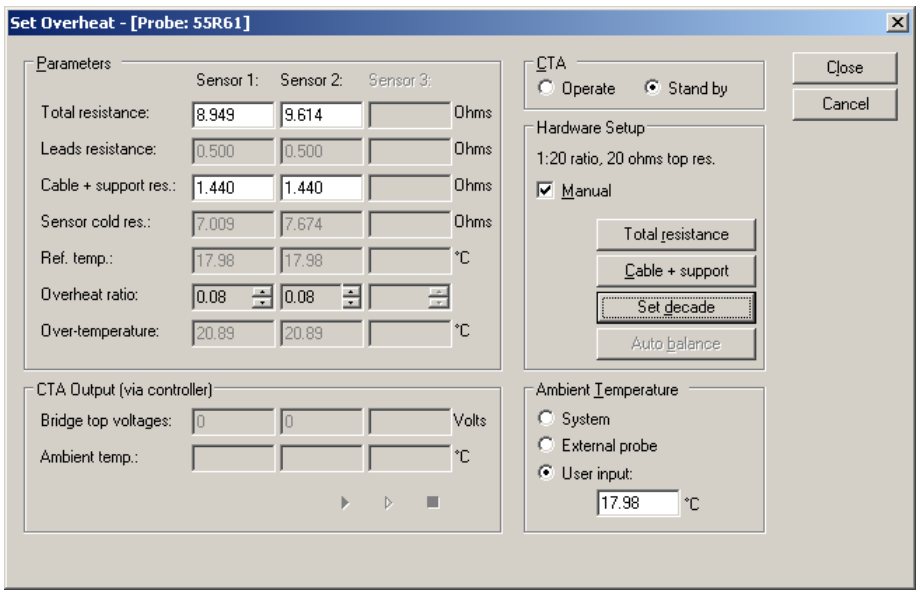

Figure 3.16 - An example of hardware configuration

Dantec© Streamware software can perform data processing of the hot-film anemometry. In addition, this software applies an automatic temperature correction on the voltage signals. Although this data processing feature of the software is very helpful, it limits the data processing accuracy. Thus, manual temperature correction and data processing procedure are preferred in the METERO experiment.

3.2.3.2 Acquisition software

3.2.3.2.1 Preliminary geometric treatment

The axial component U_L and the radial component V_L of the instantaneous liquid velocity are calculated from the effective cooling velocities of the hot films (U_{eff1} and U_{eff2}). Since the films are inclined at 45 degrees relative to the vertical axis, the geometrical treatment to calculate U_L and V_L can be formulized as:

$$\begin{cases} U_L = \dfrac{\sqrt{2}}{2}\sqrt{\dfrac{1}{1-\kappa^4}\left(U_{eff\,1}{}^2 - \kappa^2 U_{eff\,2}{}^2\right)} + \dfrac{\sqrt{2}}{2}\sqrt{\dfrac{1}{1-\kappa^4}\left(U_{eff\,2}{}^2 - \kappa^2 U_{eff\,1}{}^2\right)} \\ V_L = \dfrac{\sqrt{2}}{2}\sqrt{\dfrac{1}{1-\kappa^4}\left(U_{eff\,1}{}^2 - \kappa^2 U_{eff\,2}{}^2\right)} - \dfrac{\sqrt{2}}{2}\sqrt{\dfrac{1}{1-\kappa^4}\left(U_{eff\,2}{}^2 - \kappa^2 U_{eff\,1}{}^2\right)} \end{cases} \quad (11)$$

Where, the characteristic slope factor (κ) is typically 0.04 for the hot-film probes. Equation (12) is taken into account in the treatment of the acquired voltage signals and the details are given in Appendix 2.

3.2.3.2.2 Acquisition software

The control, displacement and acquisition of the hot-film probes are performed by the Labview™ routine "pilotage-metero.vi". Before the start of the data acquisition, the measurement locations of the probe should be entered in this routine. Afterwards, the probe is moved to the first measurement location by the routine and the acquisition starts. For each measurement point, the routine generates two binary files which contain raw voltage signals due to the instantaneous local liquid velocities. At the end of the acquisitions, a text file containing the measurement conditions during the acquisitions and another text file containing the probe characteristics (coefficients of the King's law, reference temperatures of the film, etc.) is generated in the folder of the acquisition files.

3.2.3.3 Conversion of voltages into velocities

The conversion of the raw voltages into velocities consists of two steps. The first step is calculation of calibration coefficients which is derived from the voltage signals during calibration acquisitions. These coefficients will be used in the conversion of voltages into velocities which is the second step. For this conversion, a Labview™ routine (see details in Appendix 4) had been developed in the laboratory which requires calibration coefficients, voltage signals, reference temperature and acquisition temperature. Once all these variables are obtained, the routine uses Equations (9) and (10) to convert voltage signals into velocities.

This conversion process works perfectly for the voltage signals acquired in the single phase flow. Concerning two-phase flows, voltage signals include signal portions corresponding to the gas phase which result in the underestimation of liquid velocities. Thus, it is essential to apply phase discrimination on voltage signals before the conversion process.

3.2.3.4 Phase Discrimination

As mentioned before, the presence of the bubbles in the two-phase flows creates difficulties in the liquid velocity measurements. Thus, proper phase discrimination should be applied on the raw voltage signals generated by the measurement system after investigating the raw voltage signals in details.

3.2.3.4.1 Voltage signals of hot-film anemometry in two-phase flows

In two-phase flows, the voltage signals due to the presence of the bubbles should be removed in order to obtain true liquid velocity. However, this process constitutes the main difficult part of the phase discrimination. A sample voltage signal of the interaction between X shape hot-film probe and a bubble is given in Figure 3.17. It shows that the voltage signal across the films drops in the presence of a bubble since the heat transfer coefficient of the gas phase is much lower than the one of the liquid

phase. Thus, the phase discrimination process can be based on the heat transfer difference of the phases, in other words, the voltage signal response due to each phase.

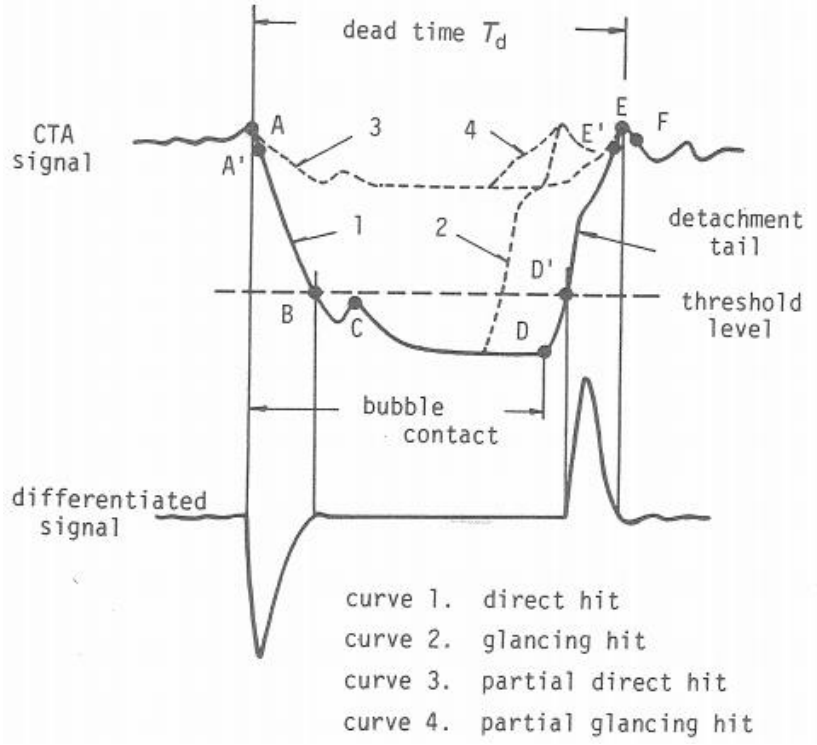

Figure 3.17 - Change in X shape hot-wire probe signal due to bubble interaction (Brunn, 1995)

In the literature, Brunn (1995) claimed that the shape change of the X shape hot-film probe signal for several types of bubble hits is similar to those of the cylindrical hot-film probes due to the probe-bubble interaction in a vertical test section, as seen in Figure 3.18.

When a bubble is approaching the probe (Point A), the probe voltage will increase due to the greater bubble velocity than the average liquid velocity until there is a contact between the bubble and the probe (Point B). After the contact, a meniscus is formed around the probe (Point C) and it continues to cover the probe. This causes a sharp decrease in the probe voltage. At Point D, two menisci will merge behind the probe and a small water film is formed between the probe and the bubble (Point E). Moreover, the probe causes a slow evaporation of the water film while the shape of the meniscus around the probe remains virtually constant. Thus, this slow evaporation decreases the probe voltage as in Point F. In most of the cases, the film remains until the back part of the bubble arrives to the probe. When the back part reaches to the probe (Point G), water starts to cover the probe and forms a liquid meniscus around the probe. The probe voltage increases rapidly and reaches a peak after the contact between the water and probe occurs (Point 3). After the peak point, the voltage decreases slowly to a certain level which represents the average liquid velocity.

Raw voltage signal obtained by hot-film anemometry is represented in Figure 3.19 with its discriminated form. The discriminated signal is generated by deleting the voltage signal portions corresponding to the gas phase and it is consisted of only the voltage signal portions belonging to the liquid phase. The liquid phase velocity is calculated from the discriminated signal by applying calibration coefficients obtained in single phase flows. The details of the phase discrimination process will be given in the next section.

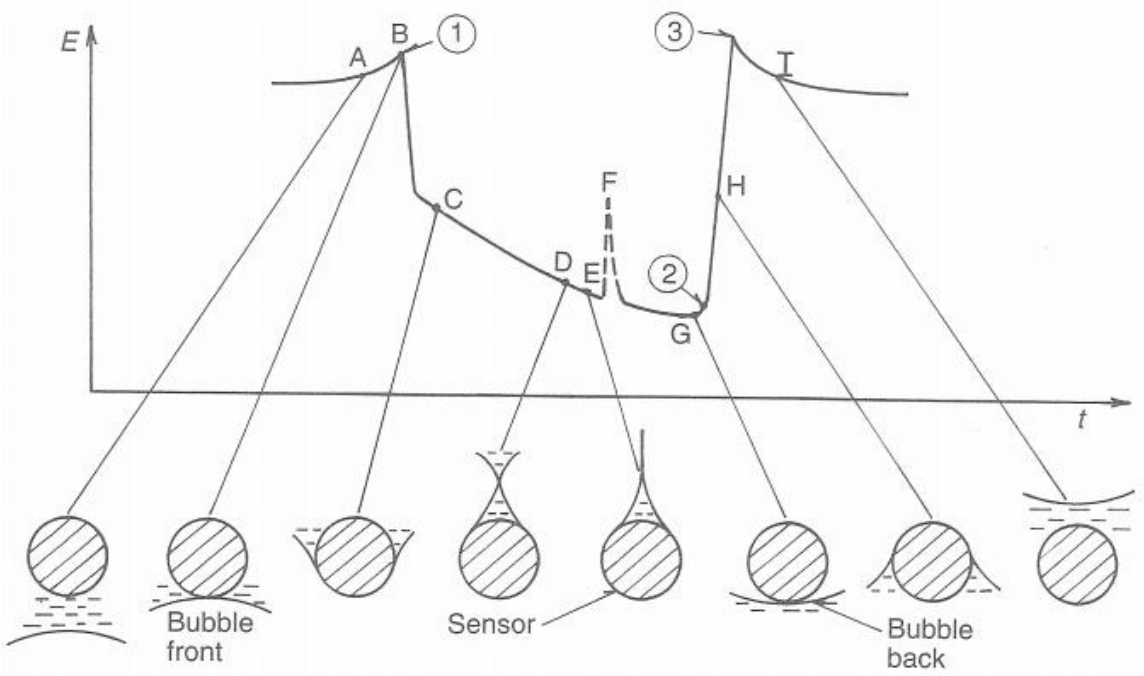

Figure 3.18 - Interaction between cylindrical hot-film probe and a bubble (Brunn, 1995)

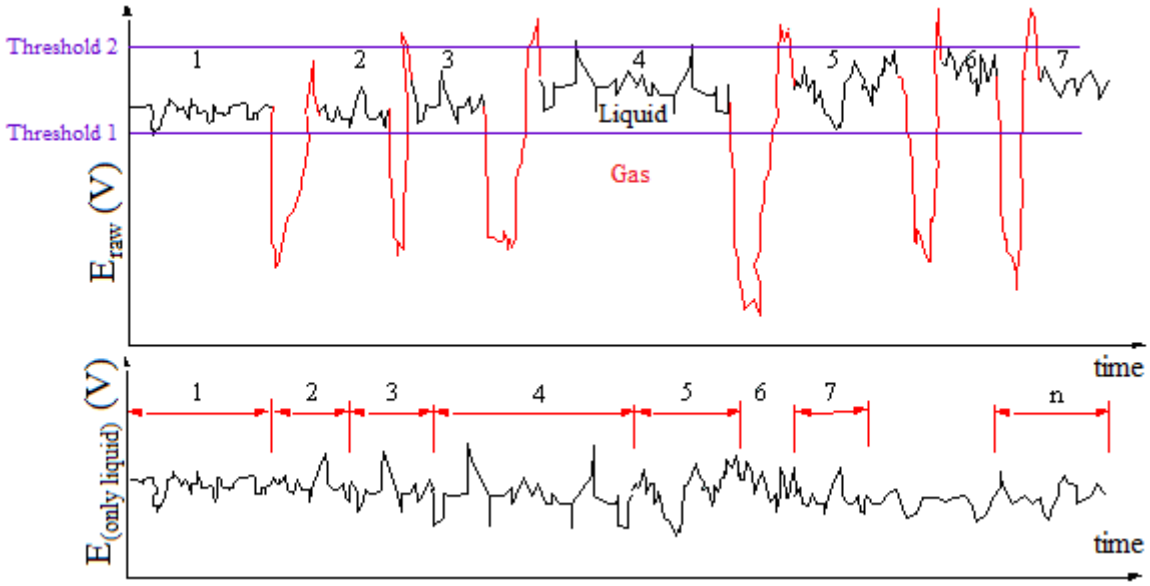

Figure 3.19 - Extraction of signal due to liquid from two-phase raw signal (Bottin, 2010)

3.2.3.4.2 Phase discrimination process

The phase discrimination process of the hot-film anemometry voltage signals can be based on thresholding, derivative of the signal, etc. In this study, as a heritage from the study of Bottin (2010), thresholding principle was used in the discrimination process. This principle is based on the studies of the IMFT (Bel Fdhila et al. (1993)), Suzanne et al. (1998) and LMFA (Garnier, 1998).

The first version of phase discrimination program created by Bottin (2010) identifies the bubbles one by one by using threshold voltages. The points defined as bubbles are removed from the raw voltage signals. The efficiency of this program was significant; however, it is not applicable for the signals of multi-component probes since it was created for the signals of the single component probes (conical hot-film anemometry probes). Thus, the original program is now improved for the signals of the X

shape hot-film probes. The user interface of the new program developed for this study is given in Figure 3.20.

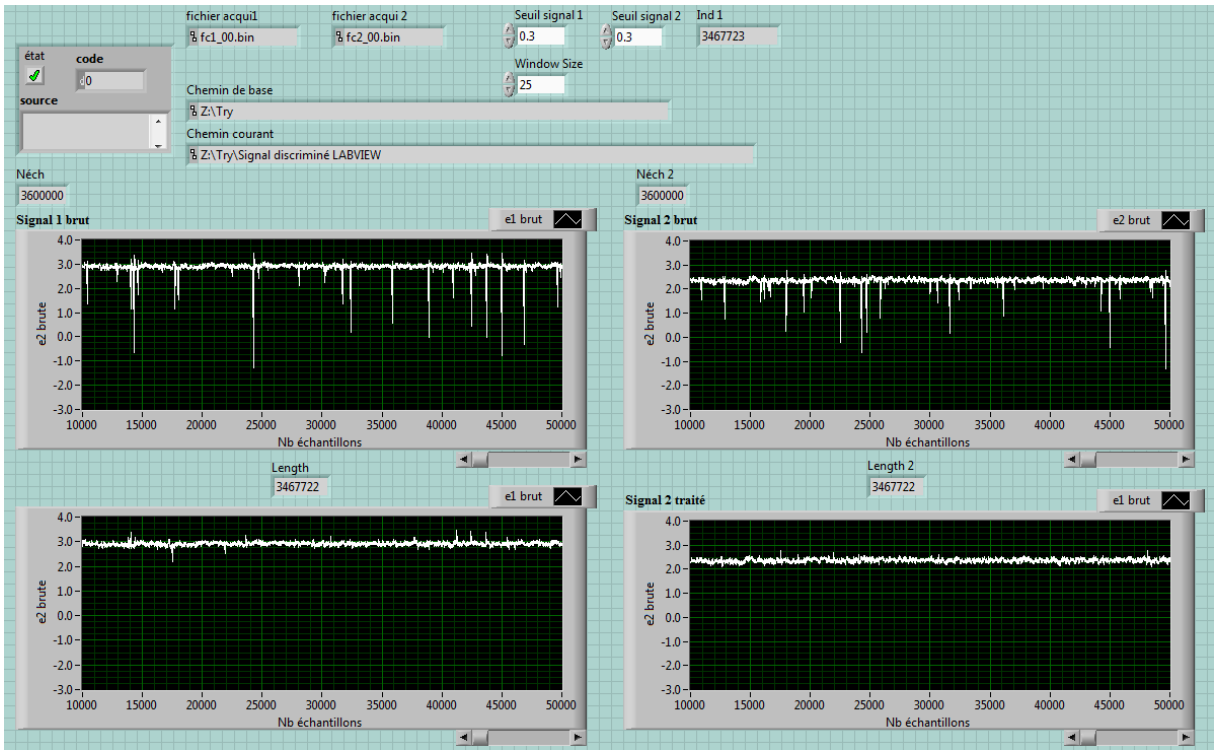

Figure 3.20 - The user interface of phase discrimination program for X shape probes

Similar to the first version, the voltage signals are controlled sample by sample simultaneously and the maximums on the left side and the right side of the each signal sample are determined in a predefined window. As seen in Figure 3.21, if the voltage difference between the maximum and the signal samples is large enough at least for one signal sample, then the samples are considered as bubbles and the signal portions on both signals due to the bubbles are removed. At the end of this process, the signals corresponding to only the liquid phase are recorded, but temporal information is lost. In addition, the files of probe settings and acquisition conditions are recorded in the folder of the discriminated raw voltage signals. The operation principle of the program is illustrated in Figure 3.22.

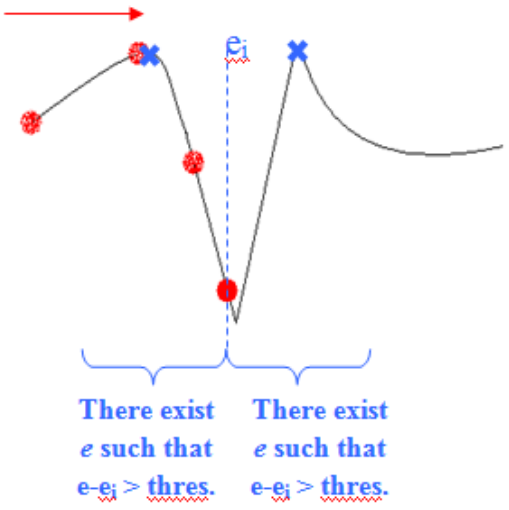

Figure 3.21 - Illustration of the chosen discrimination method (Bottin, 2010)

The signals are scanned point by point (red points represent the voltages e_{i1} and e_{i2}. Then, the program identifies the maximums on the left ($e_{max\text{-}left1}$ and $e_{max\text{-}left2}$) and right ($e_{max\text{-}right1}$ and $e_{max\text{-}right2}$) of the points e_{i1} and e_{i2} on a window of constant size represented by two lines [i-25; i+25]. Afterwards, the program compares ($e_{max\text{-}left1}$- e_{i1}), ($e_{max\text{-}right1}$- e_{i1}), ($e_{max\text{-}left2}$- e_{i2}) and ($e_{max\text{-}right2}$- e_{i2}) to a threshold value.

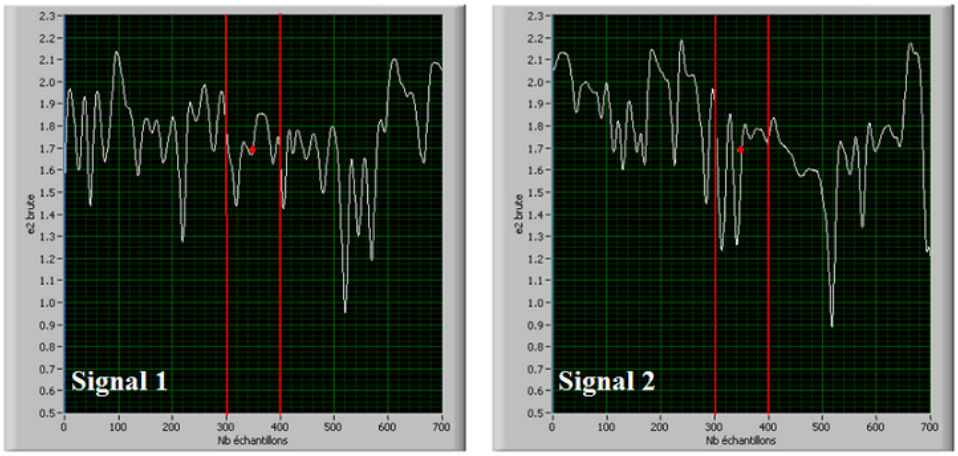

The signal decreases and then increases sharply, that is to say:

$e_{max\text{-}left1}$- e_{i1} > Threshold
C1 AND
$e_{max\text{-}right1}$- e_{i1} > Threshold

AND/OR

$e_{max\text{-}left2}$- e_{i2} > Threshold
C2 AND
$e_{max\text{-}right2}$- e_{i2} > Threshold

It is considered that the point(s) correspond(s) to a bubble. In order to remove the signal due to bubble, the size of the portion is determined according to the conditions C1 and C2.

If only "C1" is valid, remove from both signals between:
$i_{max\text{-}left1}$ and $i_{max\text{-}right1}$
If only "C2" is valid, remove from both signals between:
$i_{max\text{-}left2}$ and $i_{max\text{-}right2}$
If "C1" and "C2" are valid, remove from both signals between:
$Min(i_{max\text{-}left1}, i_{max\text{-}left2})$ and
$Max(i_{max\text{-}right1}, i_{max\text{-}right2})$

At least one of the conditions is not satisfied, that is to say:
$e_{max\text{-}left1}$- e_{i1} < Threshold
OR
$e_{max\text{-}right1}$- e_{i1} < Threshold
OR
$e_{max\text{-}left2}$- e_{i2} < Threshold
OR
$e_{max\text{-}right2}$- e_{i2} < Threshold

It is considered that there is no bubble and the index i is increased

Figure 3.22 - Schematization of the discrimination principle

The width of the predefined window should be determined carefully such that the width is sufficient to evaluate just one bubble in each step. The amplitude of threshold voltage is also important for the discrimination process. The larger the bubble size, the greater threshold voltage is required. For instance, if there are large bubbles in the measurement position, greater threshold voltage should be chosen in the process. In the case of small bubbles, threshold voltage is not as great as the ones for bigger bubbles. In our measurements, it was observed that very large bubbles in the upper part of the test section disturb the balance of Wheatstone bridge and anemometer electronics cannot establish a balance in the bridge. The detailed investigation on the signals in which very large bubbles do not take place showed that a common threshold voltage in the order of 0.3 V is necessary to have a successful discrimination process.

After a successful discrimination process, the signal portions corresponding to the presence of the gas phase are removed completely and the remaining of the signal is representing only the liquid phase. Moreover, the number of samples in the final signals is less than the one of the original signals because of deleted portions. If the number of samples in the final signal is not sufficient to have high quality statistical information, the acquisition is redone to improve the number of samples.

3.2.4 Acquisition

3.2.4.1 Principle and measurements

For velocity measurements in liquids, overheat ratio of hot-film anemometry systems is set to lower values. As a result, the change in liquid temperature has a significant influence on the measurements. Thus, the liquid temperature should be stabilized around a certain value before the acquisitions and this stabilized temperature in the METERO experiment is chosen as 18 °C. Once the liquid temperature is stable, the acquisition is started by setting the reference temperatures for the films and adjusting the resistance values for Wheatstone bridge on Streamware software. Before each acquisition, an initial calibration is performed (see Section 3.2.4.2) to obtain the first set of coefficients. Afterwards, the acquisition is performed along the vertical axis of the test section with a 5 mm displacement between each measurement location. When the acquisition is finished, a second calibration is performed for the second set of the calibration coefficients. The conversion of the voltages into the velocity values is done with the final coefficients which are the average of the first and the second calibration coefficient sets.

Concerning the measurement convergence, Bottin (2010) performed a statistical test (see Appendix 4) for conical hot-film probes. The results showed that 2000000 samples are sufficient to obtain reliable statistical calculations in single phase flow. In two-phase flows, more samples are required since some signal portions representing the gas phase are removed after the discrimination process. Thus, in order to assure statistical convergence, the number of samples taken in two-phase flows has been chosen as 3.6 million with 20 kHz sampling frequency.

3.2.4.2 Calibration

The calibration measurements are always performed in the single phase flow before the acquisitions. The probe is located in the center of the test section where mean axial component (U_{axe}) of liquid velocity is maximum. This maximum velocity value is known thanks to the correlations which are generated by the help of Pitot tube measurements and presented by Bottin (2010). These correlations are given in Appendix 4. Calibration acquisitions are done for various liquid velocities. Afterwards, the voltages across the films (e_i) can be plotted as functions of effective cooling velocities (U_{eff1} and

U_{eff2}) and the coefficients of the King's law can be calculated by using linear interpolation. By applying two calibration acquisitions (before and after each complete profile acquisitions), average voltage-to-velocity coefficients are derived in order to minimize the influence of the acquisition condition variations. The details of calibration process are given in Appendix 4.

3.2.4.3 Calculation of the spatial average of the turbulent kinetic energy <K>

In turbulent flows, the instantaneous liquid velocity is composed of an average velocity component U_L and a fluctuating component u, as seen in Equation (12). The turbulent kinetic energy for a certain measurement location along the vertical axis is calculated by using the standard deviations of the fluctuating velocities (axial (u), radial (v) and orthoradial (w) components) as in Equation (13).

$$U_L^{inst} = U_L + u \tag{12}$$

$$K = \frac{1}{2}\left(u'^2 + v'^2 + w'^2\right) \tag{13}$$

Thanks to the X shape hot-film probe, the axial and the radial velocity components can be measured directly in the METERO experiments. However, the third component cannot be measured directly, thus, an assumption about the third component is necessary to calculate the turbulent kinetic energy.

In the literature, Laufer (1953) has studied the distribution of these three velocity components in single phase flows for two values of Reynolds numbers ($Re_{Laufer} \approx 40000$ and 430000) in a circular pipe configuration. The author provided the standard deviations of dimensionless fluctuating velocities calculated with the friction velocity U_τ, as seen in Figure 3.23. The values of the three fluctuating components are approximately the same in the center of the test section (*r/R=0*) and they differ significantly while approaching the wall of the test section (*r/R=-1* and *r/R=+1*). Moreover, a relationship between the standard deviations of fluctuating velocities can be derived by averaging the values over the test section such that:

$$\langle u' \rangle > \langle w' \rangle > \langle v' \rangle \tag{14}$$

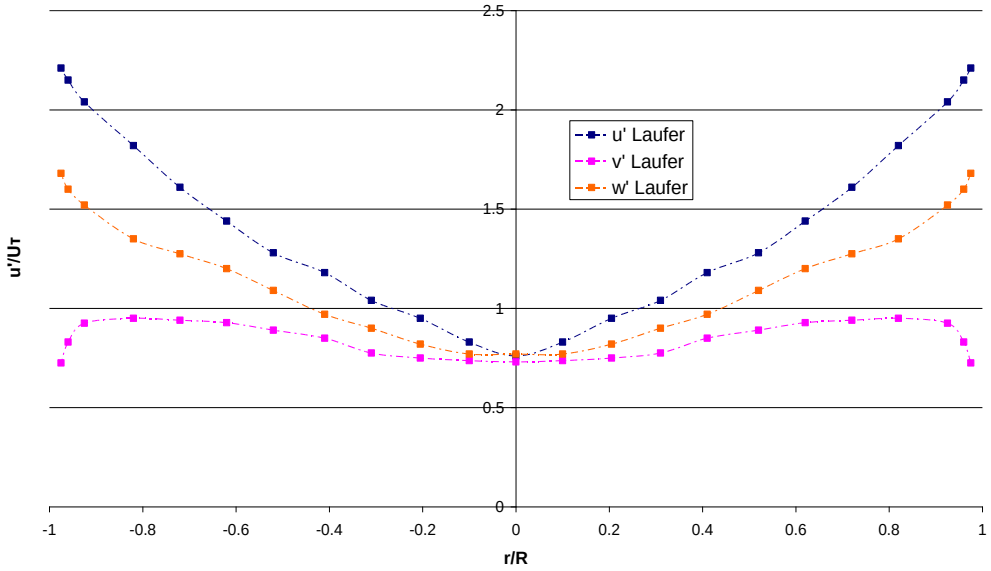

Figure 3.23 - Standard deviations of the dimensionless fluctuating velocities calculated with the friction velocity for the data of Laufer (Re≈430000) (Bottin, 2010)

As mentioned before, the axial and radial components of the liquid velocity are measured by the hot-film probes and a modified turbulent kinetic energy calculation can be written by using only these two components as in Equation (15). In Equation (15), it is assumed that the standard deviations of the radial and orthoradial components are equal. However, the distributions provided by Laufer (1953) and the relation (Equation (14)) derived from these distributions show that the orthoradial component is greater than the radial component. This fact results in the underestimation of the turbulent kinetic energy in Equation (15). Thus, it is obvious that a correlation to determine the third component is necessary in order to calculate the proper turbulent kinetic energy.

$$K = \frac{1}{2}\left(u'^2 + 2v'^2\right) \tag{15}$$

Bottin (2010) studied the different kinetic energy formulas by averaging the fluctuating velocities over the test section with an integration method (details are given in Appendix 3) and the associated errors for the formulas. The results show that there is an underestimation of the turbulent kinetic energy, as expected, by using Equation (15). The difference between the three-component equation (Equation (13)) and two-component equation (Equation (15)) is around 16%. In order to reduce the error in the turbulent kinetic energy calculation, a correction factor in the turbulent kinetic energy formula has been suggested by the author such as:

$$\langle K \rangle = \frac{\langle u'^2 \rangle}{2}\left(1 + N(\mathrm{Re})\right) + \frac{\langle v'^2 \rangle}{2} \tag{16}$$

where, *N(Re)* can be calculated with Equation (17).

$$N(\mathrm{Re}) = 1{,}537 \cdot 10^{-7} \cdot \mathrm{Re} + 0{,}526 \tag{17}$$

Hereinafter, the averaged turbulent kinetic energy presented in this study will be corrected to restore the anisotropy of the flow by using Equations (16) and (17) which are derived from the data, presented by Laufer (1953) and measured in single phase flows.

3.2.5 Measurement uncertainties

The sources of measurement uncertainties in hot-film anemometry are various and these sources should be determined carefully. The calculation of the average turbulent kinetic energy <K> brings out the maximum error since it requires many processing steps for the calculation. Thus, the uncertainty sources for the turbulent kinetic energy calculations are good examples to determine the errors. As seen in Figure 3.24, the sources can be listed as the followings:

- The uncertainties in the measurement system which is given by Dantec™
- The acquisition procedure which includes probe conditioning, calibration and temperature stability: For minimum error, a stable water temperature is required in the measurements. In addition, the correlations used in the calibration process (see Section 3.2.4.2) and flow rate variations during calibrations can also introduce an error.
- Phase discrimination process: The size of predefined window and threshold voltages can bring out an error in the measurements.
- The assumption about the distribution of the fluctuating velocities in the test section: In the test series, the liquid velocity has been measured on the vertical axis of the test section. Due to the lack of data, it is assumed that the distribution of liquid velocity is axisymmetrical and the

velocities are integrated by half-crowns with this assumption. In fact, the presence of the gas phase deteriorates this axisymmetry and introduces an error.

– The averaged turbulent kinetic energy is calculated by the axial and radial component (u' and v') with a correction factor ($N(Re)$) instead of using three fluctuating velocities. This results in an uncertainty in the calculation.

According to the information mentioned above, the uncertainties on the local quantities (local velocities) have been estimated as:

– ±3% on the axial and the radial component of the average liquid velocity with two component probe
– ±5% on the standard deviation of the velocity fluctuations.

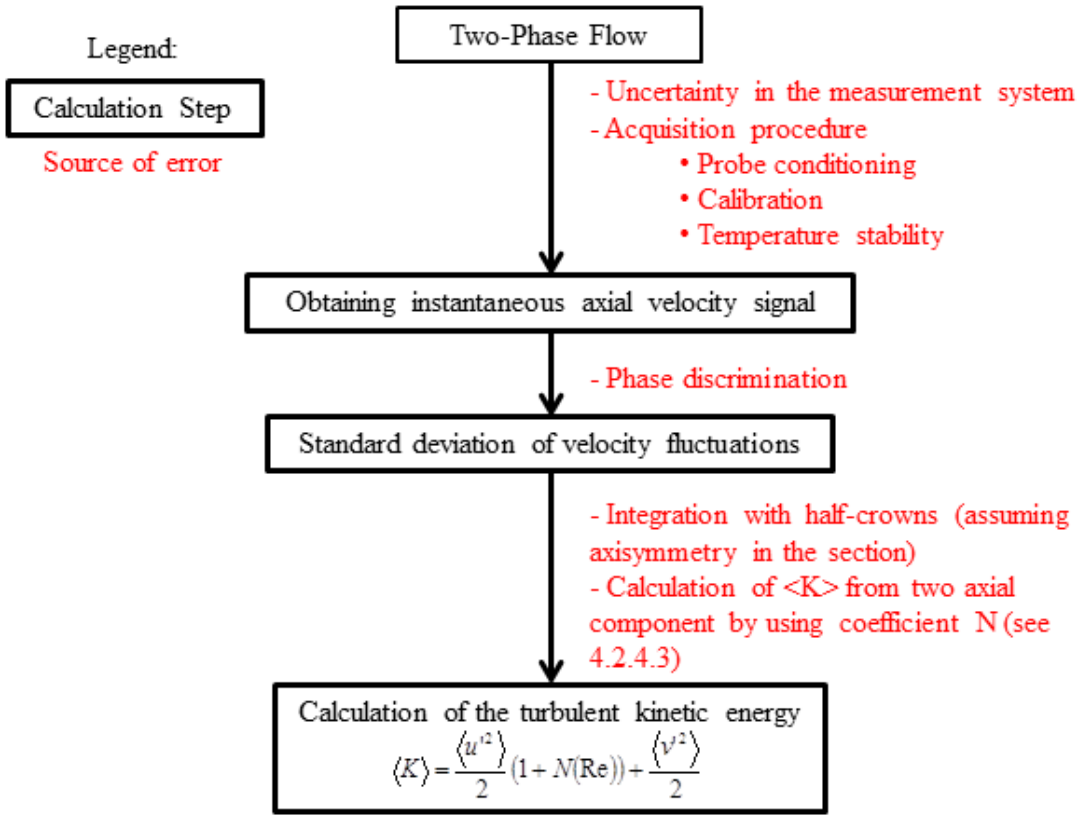

Figure 3.24 - Steps to obtain the average turbulent kinetic energy and associated error sources

Uncertainty calculation of spatial averaged turbulent kinetic energy is even more complicated due to the lack of data in the METERO experiment. Bottin (2010) studied this uncertainty for conical (single component) hot-film probes by using the data presented by Yang et al. (2004). Yang et al. (2004) measured standard deviations of axial, radial and orthoradial fluctuating velocities along profiles oriented at 0^o (radially), 45^o (diagonally) and 90^o (orthoradially) as shown in Figure 3.25. The measurements were acquired for J_L=4 m/s and J_G=0, 0.07 and 0.14 m/s which are similar conditions generated in the METERO experiment. Similar to the study of Bottin (2010), an uncertainty study has been performed in the present paper for X shape (two-component) hot-film probes.

In the uncertainty calculations, three methods of spatial averaging have used with the measured velocity profiles of Yang et al. (2004). As seen in Figure 3.26, these methods are:

- In the first method, the variances of the axial and radial fluctuating velocities u'^2 and v'^2 are spatially averaged along the vertical axis of the test section through discrimination in half-crowns, and the coefficient *N(Re)* is used for the calculation of the average turbulent kinetic energy: $<K>_1$
- The second method is the spatial averaging of local turbulent kinetic energies calculated from the variances of the three fluctuating velocities through half-crowns: $<K>_2$
- As the final method, spatial averaged turbulent kinetic energy $<K>_3$ is calculated from three fluctuating velocities for the profiles at 0°, 45° and 90° with an assumption of symmetrical distribution of the flow with respect to the vertical axis of the test section by averaging through angular sectors (portions of crowns). This method is expected to result in a more realistic value.

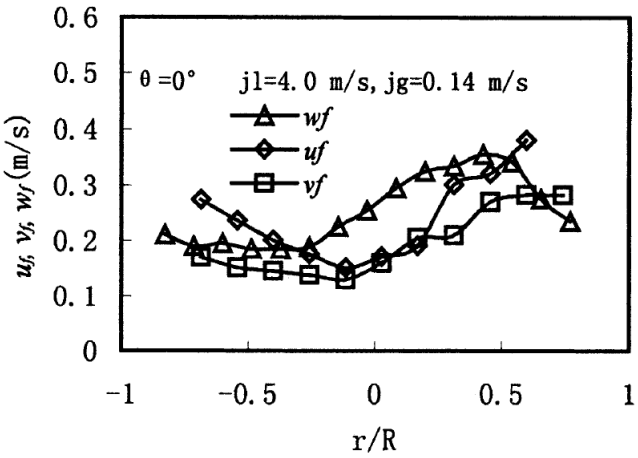

Figure 3.25 - Standard deviations of axial, radial and orthoradial fluctuating velocities in dispersed bubbly flow (Yang et al., 2004)

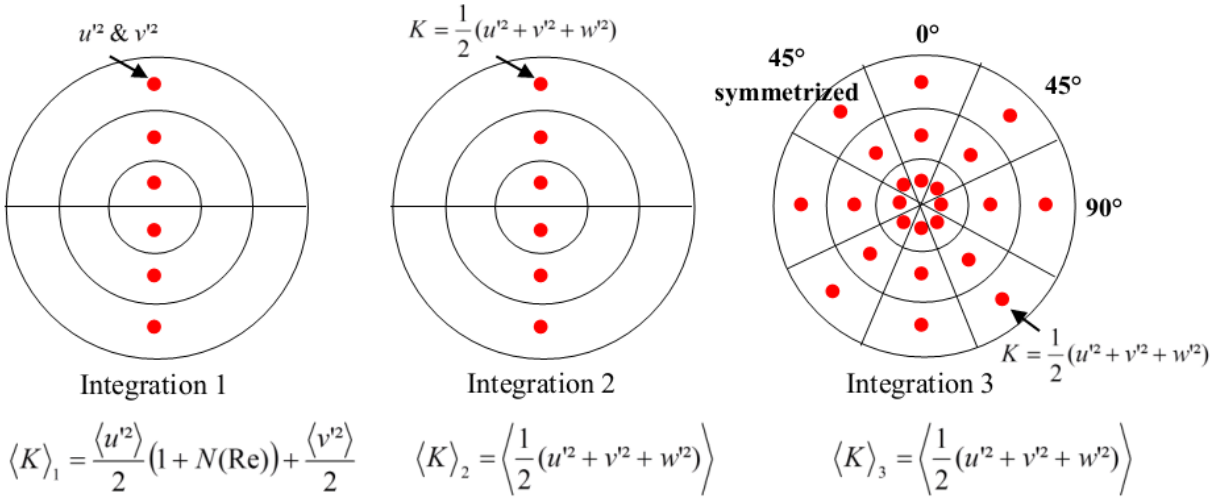

Figure 3.26 - Illustration of the integration procedures to estimate the uncertainties in the calculation of $<K>$

The results of the uncertainty study (in percentages) for J_L=4.00 m/s by comparing the average turbulent kinetic energy values obtained from different integration methods are represented in Table 3.3.

	J_G = 0.00 m/s	J_G = 0.07 m/s	J_G = 0.14 m/s
Error of $\langle K \rangle_1$ with respect to $\langle K \rangle_2$ (%)	4.68	4.68	5.39
Error of $\langle K \rangle_1$ with respect to $\langle K \rangle_3$ (%)	5.99	6.83	1.85
Error of $\langle K \rangle_2$ with respect to $\langle K \rangle_3$ (%)	1.26	12.07	7.65

Table 3.3 - Errors between different values of $\langle K \rangle$ depending on the type of integration based on the data of Yang et al. (2004)

The results in Table 3.3 show that the maximum uncertainty of the first integration method is around 15%. By combining the uncertainty of the fluctuating velocity measurements (around 5% for each fluctuating component), the maximum uncertainty in the spatial averaged kinetic energy can be estimated 25%. Although the uncertainty value is great, this value is smaller than the uncertainty in the study of Bottin (2010) which is 35%. In the study of Bottin (2010), the author claimed that this 35% of uncertainty is sufficient for one-dimensional two-phase flow modeling which is expected to have less precision compared to the traditional CFD codes. Thus, the turbulent kinetic energy calculated by our first method with less uncertainty can provide better information for one-dimensional two-phase flow modeling.

3.3 High-Speed Video Camera

High speed video cameras are one of the most commonly used instrumentations in ballistics, aerospace, fluid dynamics, etc. In fluid dynamics, this instrumentation has been utilized to visualize single phase and multiphase flows with various applications (Bröder and Sommerfeld (2002), Lindken and Merzkirch (2002), Kitagawa, et al. (2003), and Sathe, et al. (2010)). Since the METERO experiment is constructed from transparent pipes which gives the opportunity to visualize the flow inside the test section, high speed video cameras are applicable in the METERO experiment.

There exist various types of high speed video cameras with different specifications. In this study, a Photron Fastcam SA1.1 high speed video camera has been used for flow visualizations and the details of this camera are given in the following section.

3.3.1 Camera

An example picture of the camera is given in Figure 3.27. The camera is installed with a mega pixel resolution CMOS sensor which is capable of clear recording in low-light with an ultra-high speed frame rate (Photron Fastcam SA1.1 Hardware Manual). Moreover, this sensor is a 12-bit ADC (Bayer system color, single sensor) with 20 μm pixel size. Moreover, the camera has an internal memory with 3 different sizes such as 8, 16 and 32 GB. In this study, a camera with 16 GB memory has been used.

Figure 3.27 - Photron Fastcam SA1.1 camera (Source : Photron)

The camera can be operated with various resolutions and sampling frequencies. Example operation parameters are given in Table 3.4. In addition, the shutter speed of the high speed video camera is also variable (from 16.7 ms to 1 μs) and it can be adjusted on the related software (Photron FASTCAM View) which is described in Section 3.3.2.2.1. In this study, the camera has been operated at 5400 fps (frame per second) of sampling frequency with 1024 x 1024 pixel resolution and a 1/104000 seconds shutter speed.

Resolution (Pixels)	Sampling Frequency (fps)
1024 x 1024	5400
832 x 608	10800
640 x 480	18000
512 x 512	20000
256 x 256	67500
256 x 16	500000
64 x 16	675000

Table 3.4 - Example operation parameters of Photron Fastcam SA1.1

Different types and brands of camera lenses can be mounted on the camera via an interchangeable lens mount according to the measurement purposes, as seen in Figure 3.28. In the METERO experiment, a camera lens with a focal length of 180 mm (f180 mm) has been mounted on the camera which ensures a narrow depth of focus in the measurements. It is also possible to increase the focal length of this lens by adding extension rings on the lens in order to zoom the measurement area; however, the f180 mm lens is sufficient for the measurement purposes in this study.

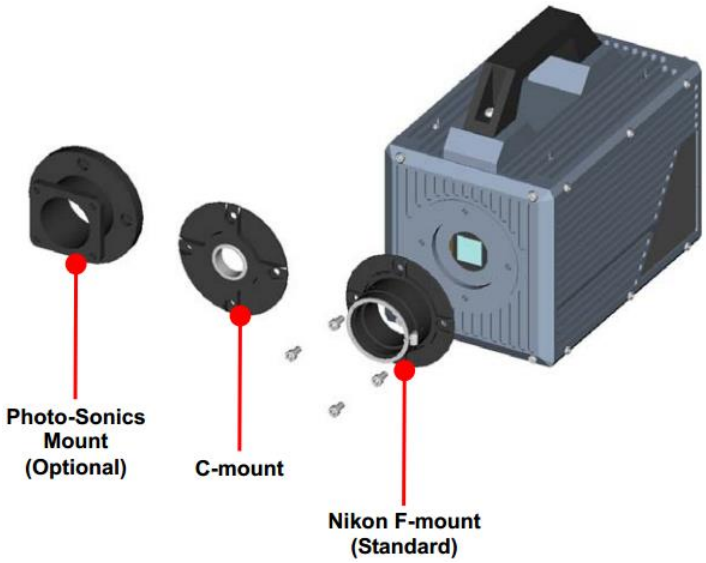

Figure 3.28 - Photron Fastcam SA1.1 camera with interchangeable lens mounts (Source: Photron)

Photron Fastcam SA1.1 has a hybrid design to allow operation via a LCD monitor keypad provided by Photron and operation from Photron FASTCAM Viewer via a gigabit Ethernet connection (Photron Fastcam SA1.1 Hardware Manual), as seen in Figure 3.29. In the METERO experiment, the camera is operated by PC via Ethernet connection due to its easy implementation. In addition, the camera can be triggered via the PC software manually or by a synchronizer which is utilized in the PIV measurements to synchronize the laser system and the camera. In this study, shadowgraphy system (details given in Section 3.3.2.1) applied in the tests does not need synchronization or automatic triggering. Thus, the camera has been operated with manual trigger via the software.

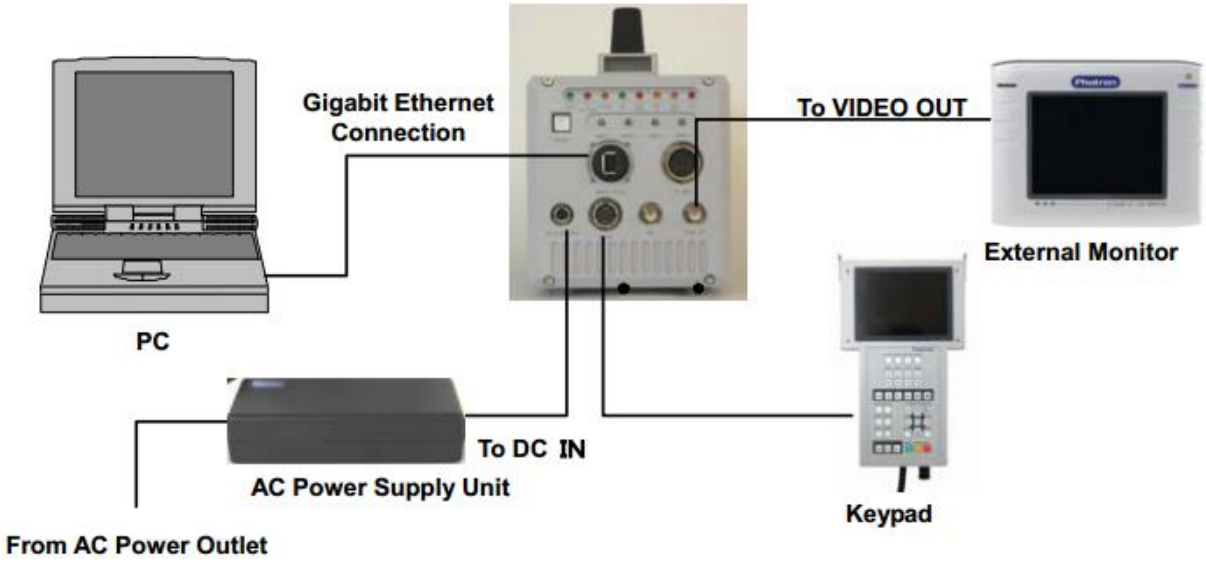

Figure 3.29 - Example cable/device connections (Source: Photron)

3.3.2 Measurement system

3.3.2.1 System configuration

In the METERO experiments, the high speed video camera has been used to measure the gas phase, specifically bubble, velocity in the center of the test section by applying shadowgraphy technique whose details are given in section 3.3.3.1. The schematic of the measurement system configuration is given in Figure 3.30. The system consists of a high speed video camera, a light source and a computer. The test section is illuminated by a strong light source which enables to obtain the shadow images of the bubbles. For this purpose, two DEDOLIGHT 575 W spotlights have been utilized in the measurement system. Furthermore, the images are recorded by the high speed video camera which is connected to a laptop PC via gigabit Ethernet connection. The camera has been fixed in a location in order to acquire the images of the bubbles which are at the center of the test section and 40D axial location from the injectors by the help of aluminum camera support produced in-situ.

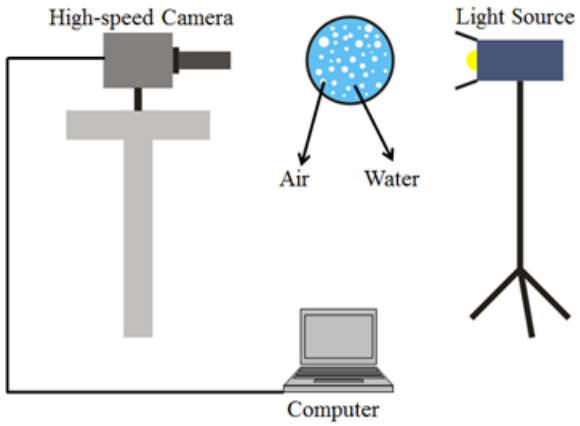

Figure 3.30 - Schematic of the measurement system

3.3.2.2 Data acquisition

3.3.2.2.1 Acquisition software

In the measurements, the camera is operated and the bubble images are acquired by the acquisition software Photron FASTCAM Viewer provided by Photron. This software allows us to change the display parameters of the images (i.e. zoom, brightness, gamma parameters, etc.) and camera settings (sampling frequency, shutter speed, resolution, etc.), and to playback the recorded images.

Before the start of the acquisitions, the camera parameters should be set in the software. Afterwards, the acquisitions of the images can be started manually or automatically. The acquisitions are completed automatically when the internal memory of the camera is full. In this study, 1024 x 1024 pixels resolution has been chosen for the acquisitions and the size of single image is 1 MB. Thus, the camera completes the acquisitions after capturing 16384 images. By the help of acquisition software, the images can be recorded with various file types.

3.3.2.2.2 Calibration

Before the measurements, a calibration acquisition has been performed in the METERO experiment to convert the distances from pixels into meters. For the calibration, a calibration plate has been placed in the center of the test section, as seen in Figure 3.31 (a) and (b). On the calibration plate, there exist points and crosses (white points and crosses in Figure 3.31 (a)). The white crosses represent the axial central axis where the camera is focused for the measurements. The distance between two crosses is 5 cm exactly. Moreover, the white points are distributed along the plate and the distance between two points is 1 cm precisely.

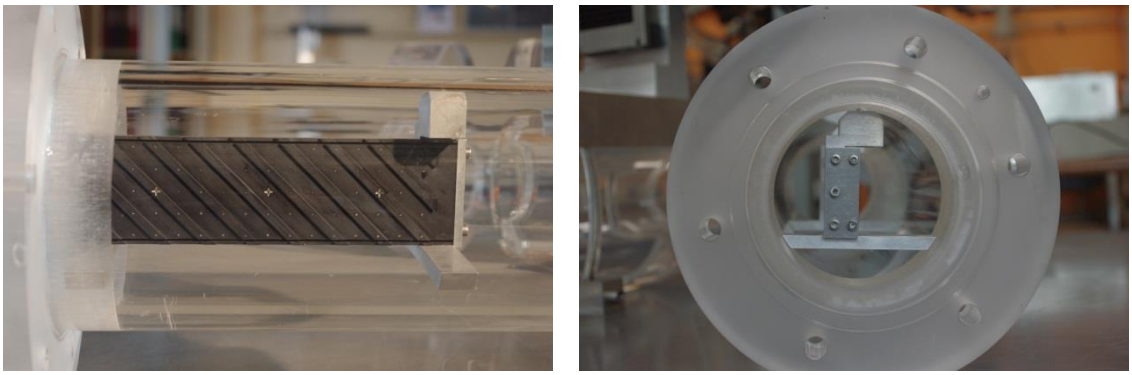

(a) Front view (b) Side view

Figure 3.31 - Calibration plate

After placing the calibration plate in the test section as seen from Figure 3.32, 100 images of the test section (an example image is given in Figure 3.33) have been acquired by the high speed video camera and the software while the test section was filled with water. Afterwards, the 100 calibration images are averaged and the calibration of the distance between pixels has been performed by using the averaged calibration image. In principle, the distance between two white points in meters is known and that one in pixels can be measured by using either Photron FASTCAM View or MATLAB manually. Since these two distances (in meters and pixels) represent the same quantity, they can be converted into each other easily. As an example, the distance between each point in Figure 3.33 is 0.01 m or 263 pixels. Thus, 1 pixel on the images is 0.04×10^{-3} in meters. Since the distances between pixels and the sampling frequency are known after calibration, the measured velocity of the gas phase in *pixel/frame* can be converted into *m/s* easily.

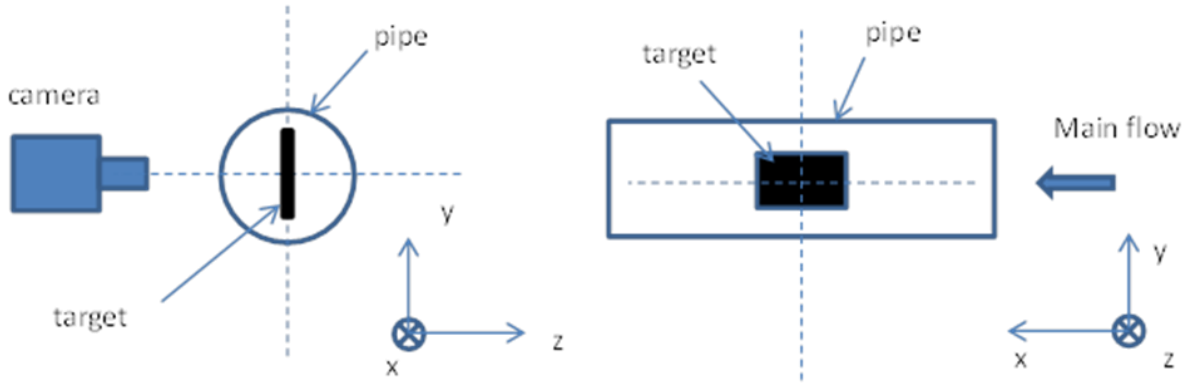

Figure 3.32 - Schematic of the calibration plate position in the test section

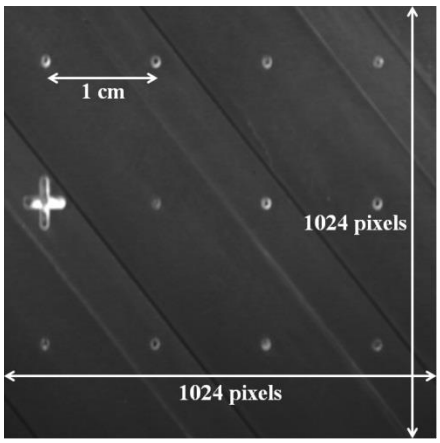

Figure 3.33 - Calibration image with calibration plate

Once the calibration has been performed successfully, the calibration plate is removed from the test section and the experimental setup has been prepared for the data acquisition of the bubble velocities.

3.3.2.2.3 Acquisition

The acquisitions take place just after the calibration acquisitions. The acquisitions parameters are exactly the same as the parameter of the calibration (5400 fps sampling frequency, 1/104000 seconds of shutter speed). In the beginning, 100 images have been acquired without any gas phase to eliminate the noise due the background and these images are averaged. The averaged background image is subtracted from the acquired images with gas phase for the fact that only bubbles will remain in the images afterwards. The details of this procedure will be given in Section 3.3.3.2. For the bubble velocity measurements, the acquisitions for each test have been completed when the internal memory of the camera is full (16384 recorded images). However, only 10400 images representing 2 seconds of acquisition for each test have been saved on the computer due to the memory limits of the laptop PC.

3.3.3 Data processing

In order to apply shadowgraphy technique, the images acquired by the high speed video camera should be converted into shadow images. These images are processed in a PIV software to obtain the bubble velocities. The details of the data processing procedure are given in the following sections.

3.3.3.1 Shadowgraphy

In the single phase flows, the PIV technique has significant success to measure the liquid velocity. However, this technique has some major disadvantages in multiphase flows due to the presence of the gas phase. The gas phase, more specifically bubbles, brings difficulties in the velocity measurements since the bubbles can reflect the laser beams and this phenomenon results in a saturation of the camera sensor. As a result, it is not possible to detect the tracer particles in the flow.

For this reason, another technique, shadowgraphy, has been developed to eliminate the problems caused by the presence of bubbles. In principle, shadowgraphy is a measurement technique such that shadow images of the bubbles, created by a strong light source coming from the back side of the bubbles, are recorded by a high speed video camera and shadow images of the bubbles are used as tracer particles, like in PIV technique, in order to calculate the bubble velocities (Lindken & Merzkirch (2002), Sathe et al. (2010)). In multiphase flows, this technique has been used for two main purposes. The first one is that shadowgraphy technique can create masks in the flow visualization which are used to eliminate the laser beam reflections and ensures the measurement of the liquid velocities. Secondly, this technique allows measuring the bubble velocity independently from PIV technique.

In the literature (Bröder and Sommerfeld (2002), Lindken and Merzkirch (2002), Kitagawa, et al. (2003), and Sathe, et al. (2010)), shadowgraphy technique has been combined with PIV technique in multiphase flow. In details, there exists a high speed video camera with a specific optical filter for each technique and two synchronized light sources (laser for PIV and LED array for shadowgraphy). PIV and shadow images are recorded separately to measure liquid and bubble velocities respectively. Since only bubble velocity is focused in this study, a single and simple shadowgraphy system has been utilized to validate the axial bubble velocity measurements by optical fiber probes.

3.3.3.2 Generation of shadow images

By using a high speed camera, only grayscale images of the bubbles have been acquired in the tests. Thus, it is necessary to generate shadow images by applying several procedures on the grayscale images.

The shadow image generation procedure starts with the subtraction of the averaged background image (Figure 3.34 (b)) from the original grayscale image of the bubble (Figure 3.34 (a)). By the help of the background subtraction, the noise generated by the background is eliminated. Afterwards, the subtracted image is converted into a binary image (Black and White (BW), Figure 3.34 (c)). In the final step, a median filter is applied to the BW image in order to retain the clearest bubble image. The size of the filter has been chosen as 7 x 7 pixels which is smaller than the minimum bubble size that has been focused in this study. The median filter ensures to retain only the bubbles which are located in the center of the test section. In other words, the filter eliminates the bubbles which are in the foreground and the background of the focused area in the test section.

(a) Grayscale (b) Subtracted (c) BW without filter (d) Filtered BW

Figure 3.34 - Shadow image generation steps

Once the shadow images are generated for each test, the bubble velocities are calculated from the shadow images by a free PIV software in MATLAB (PIVlab) which is described in the following section.

3.3.3.3 Calculation of bubble velocity

The shadow images are processed in a free PIV software (PIVlab, example user interface image given in Figure 3.35) implemented in MATLAB to determine the velocities. This software provides an access to statistical quantities of velocities such as mean and standard deviation of velocity fluctuations. The software implements advanced processing methods developed and published for several years (Keane & Adrian (1990), Westerweel et al. (1997), Scarano & Riethmuller (1999), Nogueira et al. (1999), Prasad et al. (1992)).

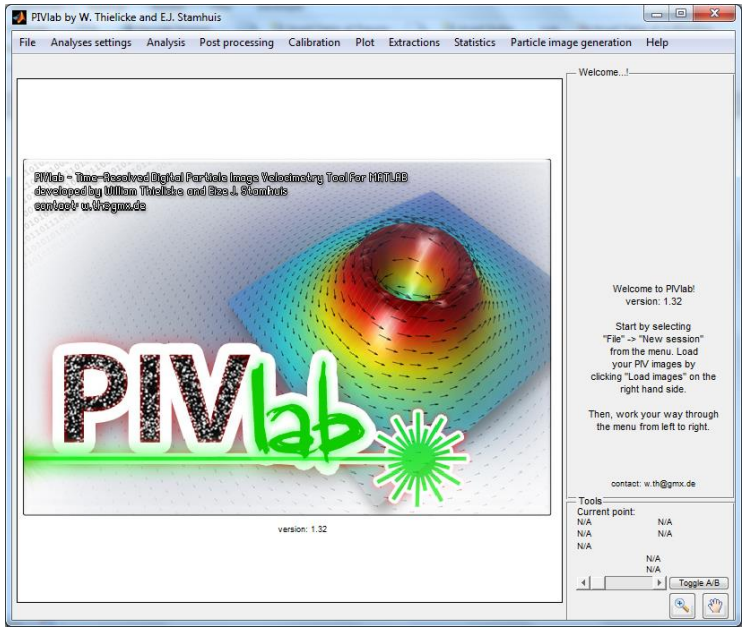

Figure 3.35 - PIVLab graphical user interface

In the post-processing, a ±64 pixels region of interest around the central axis which represents the center of the test section is defined. Similar to PIV post-processing rules, the size of analysis window should be chosen properly to ensure an accurate measurement and the displacement of a bubble between two shadow images cannot be greater than the quarter of the analysis window span. Thus, the analysis window size has been chosen equal to 128 pixels. In the studies, the results show that choosing smaller analysis windows results in the underestimation of the bubble velocities. As a final parameter for the post-processing, a 50% overlapping (64 pixels) between two analysis windows has been chosen.

Once the parameters are entered in the software, post-processing starts with the command of the user and bubble velocity is obtained by applying cross correlation on the shadow image couples. The results of the post-processing can be exported as text files. The software creates a unique text file for each shadow image couple and these files includes the information of radial and axial location of the velocity vectors in pixels and the radial and axial velocity values of each vector in pixel/frame corresponding the bubble velocity. Since the distance between each pixel and the sampling frequency of the measurements are known, actual bubble velocities in m/s are calculated by calibrating the bubble velocities, in pixel/frame, obtained by PIVlab software.

3.3.4 Measurement uncertainties

There exist various uncertainty sources in the measurements of high-speed video camera and shadowgraphy technique. These sources are represented in Figure 3.36. These uncertainties can be listed as:

- The uncertainties of the high speed video camera (sampling frequency, distortion of the sensor) given by Photron (negligible)
- The uncertainties in the measurements due to the refraction of the light. By focusing the camera lens in the center of the test section and using a calibration plate in the test section which is filled with water, the error due to refraction can be minimized.
- Background noise. The bubbles located in the background of the focused area can contribute to the uncertainty in the measurements. Thus, this can be eliminated by well-focused camera lens. In addition, the irregularity of the light source is another term which should be taken into account in the uncertainty study. The effect of the irregularity can be minimized by subtracting the background image from the grayscale bubble images.
- A size of median filter should be chosen carefully such that the filter should not disturb the image of the bubbles in the focused area.
- The calculation of the velocities in pixels/frame can be another factor for the uncertainty.
- The uncertainty in the calibration which is around 0.8%. This uncertainty of the calibration is calculated from the measured distance between white points which is 263 pixels (See section 3.3.2.2.2) and an assumed error of measurement as 1 pixel. Thus, $\varepsilon = [(263+1)-(263-1)]/263 = 2/263 = 0.008 = 0.8\%$.

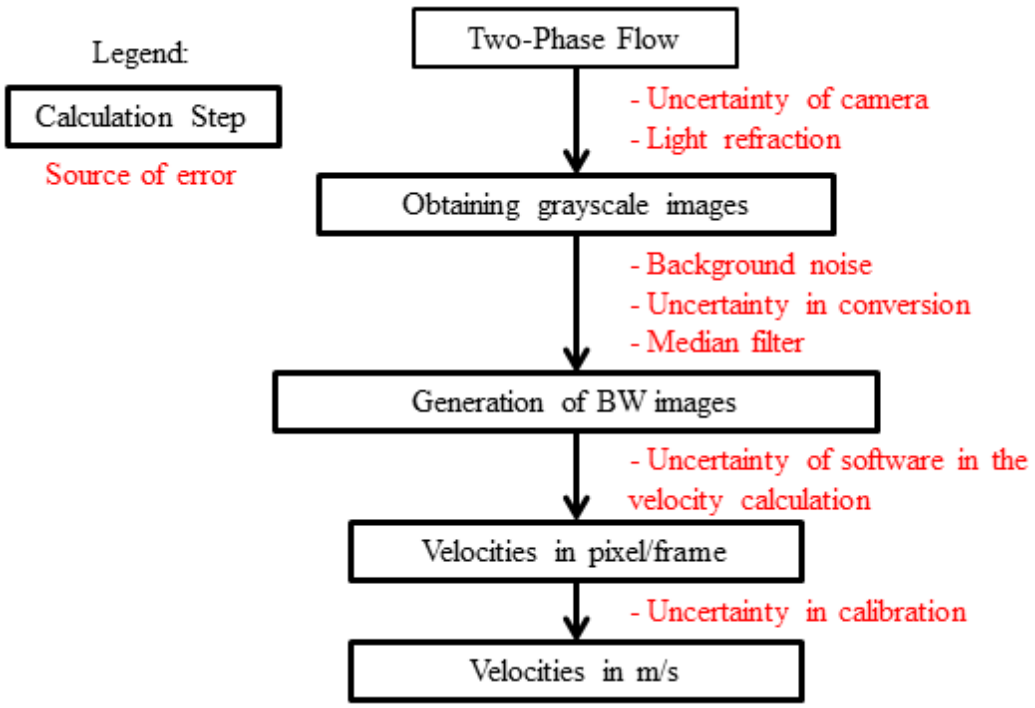

Figure 3.36 - Calculation steps of bubble velocity in m/s and associated error sources

Although the uncertainty sources have been defined very carefully for the high speed video camera and shadowgraphy system, it is difficult to estimate the total uncertainty of the measurement system which also depends on the number of the samples acquired for each acquisition. By using so-called

“Student’s t-distribution” with 99% confidence, the total maximum uncertainties could be estimated as:

- ±1.8% on the axial component of the bubble velocity
- ±19.1% on the radial component of the bubble velocity

CHAPTER 4

STUDY OF DISPERSED BUBBLY FLOWS

4 STUDY OF DISPERSED BUBBLY FLOWS

In this chapter, flow quantities in dispersed bubbly flows will be investigated. First, the local quantities measured at 40 diameters downstream of the inlet will be given in the first section. The second section of this chapter is focused on the axial evolution of flow quantities. Finally, a conclusion will sum up this chapter.

4.1 Local Studies on Flow Quantities

Dispersed bubbly flows can be generated with high liquid flow rates and low gas flow rates and they are free of gas pockets. Although the study of Bottin (2010) was dedicated on the dispersed bubbly flow regime, it was limited within certain flow rates (i.e. J_L from 4.42 to 5.31 m/s and J_G from 0.064 to 0.127 m/s). Thus, further studies on dispersed bubbly flow regimes with different flow rates are essential for completing those of Bottin in order to cover the full domain of this regime.

For these new studies, the following measurement and observation methods have been utilized in the METERO experiment:

- 4-tip optical fiber probes (see Section 3.1) to measure the all characteristics of bubbles such as void fraction, Sauter mean diameters, interfacial area, axial bubble velocities.
- Constant temperature hot-film anemometry (see Section 3.2) for the measurement of mean and fluctuating velocities of the liquid phase and estimation of the turbulence magnitude (turbulent kinetic energy).
- High-speed camera and shadowgraphy techniques (see Section 3.3) dedicated to the measurement of axial bubble velocity in the center of the test section.

Similarly to the measurements of Bottin (2010) performed with 2-tip optical fiber probes, the use of 4-tip optical fiber probe and post processing system require the following assumptions:

- Bubbles are uniformly distributed in the space near the probe.
- The motion of bubbles is collinear to the axis of the probe.

An important advantage of 4-tip optical fiber probe is that the spherical bubble assumption is not required.

In the case of hot-film anemometry, the measurements have been conducted for 3 minutes at a stable liquid temperature (18 °C) (see Section 3.2.4.1). As mentioned in Section 3.2.2.1, the existence of a wake behind the hot-film anemometry probe results in the limitation of the test conditions: the measurements in the liquid phase are possible only for liquid rates lower than 3.90 m/s. At this point, the hot-film anemometry measurements of Bottin (2010) for higher flow rates are relied on in this study.

The test conditions for each measurement method are given in Table 4.1.

Hot-film anemometry (mean and fluctuating velocity, magnitude of turbulence)				
J_L (m/s)	4.42[♣]	4.42[♣]	3.00	3.00
J_G (m/s)	0.064[♣]	0.127[♣]	0.064	0.127

Optical fiber probes (void fraction, chord length, interfacial area, axial velocity)										
J_L (m/s)	4.42	4.42	4.07	4.07	3.71	3.71	3.36	3.36	3.00	3.00
J_G (m/s)	0.064	0.127	0.064	0.127	0.064	0.127	0.064	0.127	0.064	0.127

High-speed camera and shadowgraphy (axial bubble velocity)							
J_L (m/s)	4.42	4.42	4.42	4.42	4.42	4.42	4.42
J_G (m/s)	0.011	0.025	0.042	0.064	0.085	0.110	0.120

Table 4.1 - Acquisition conditions for dispersed bubbly flows

In Figure 4.1, the test conditions for each measurement method given in Table 4.1 are represented on the flow regime map plotted for the axial location of 40D. As seen from the figure, these test conditions corresponds to Buoyant Bubbly Flow (BBF) and Stratified Bubbly Flow (SBF) which are the sub-regimes included in dispersed bubbly flow regime.

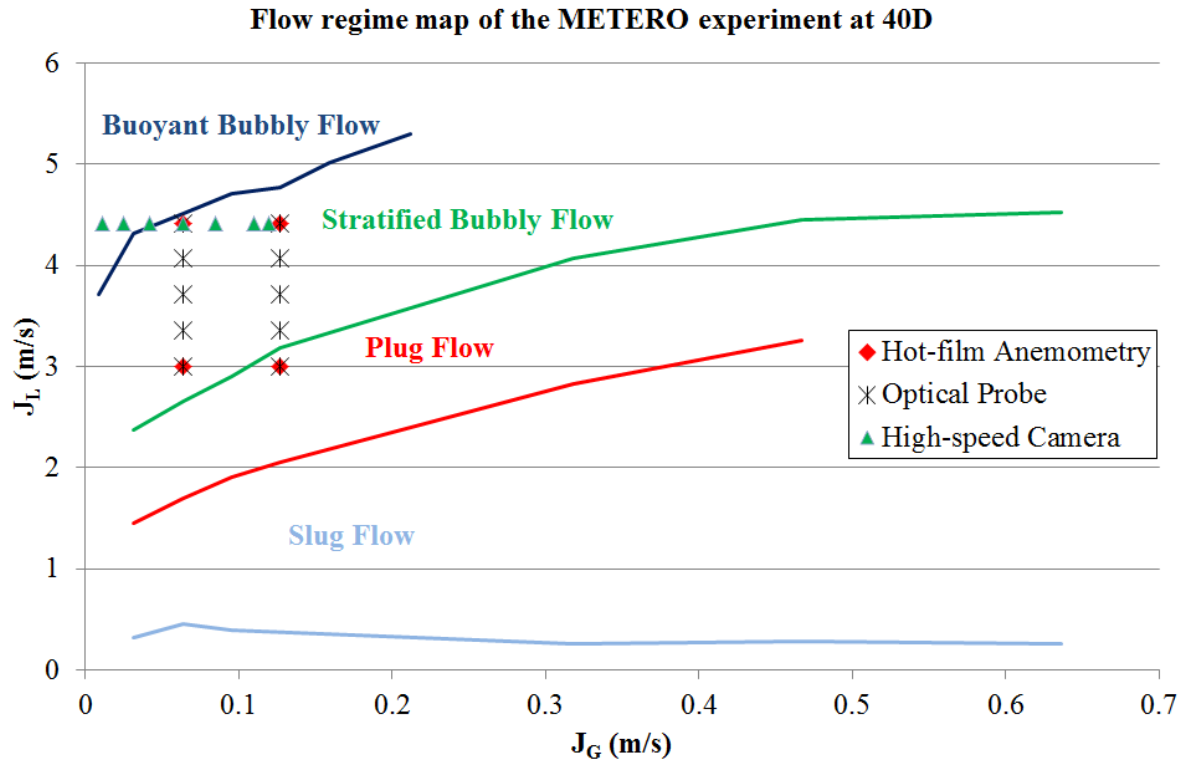

Figure 4.1 - Representation of the test conditions for dispersed bubbly flows on the flow regime map

The optical fiber probe and hot-film anemometry measurements have been carried out along vertical profiles at a constant temperature of 18 °C and axial locations of 5D, 20D and 40D far from the gas injectors. However, we focused on the measurements performed at 40D, a localization where the flow characteristics are not too much dependent on the inlet conditions.

As a final remark, the results of test conditions J_L=4.42 & 3.00 m/s and J_G=0.064 & 0.127 m/s (representing 4 test conditions) have been selected for this chapter. The results of the other test conditions are given in Appendix 5.

[♣] Measurements of Bottin (2010)

4.1.1 Void fraction

In the literature, several studies describing the void fraction distributions of dispersed bubbly flows in horizontal configurations have been presented: Kocamustafaogullari & Wang (1991), Kocamustafaogullari et al. (1994), Andreussi et al. (1998), Iskandrani & Kojasoy (2001), Yang et al. (2003) and Bottin (2010). The void fraction profiles of Kocamustafaogullari et al. (1994) and Iskandrani & Kojasoy (2001) have been reported in Figure 4.2. For comparison with these literature results, Figure 4.3 shows the void fraction profile obtained at an axial location of 40D in the METERO experiment.

As seen from the graphs, the void fraction profiles acquired in the METERO experiment are comparable with the literature ones. As a first remark, the void fraction for all test conditions starts to increase from the lower part of the test section (*r/R = -1*) to the upper part (*r/R = 1*) due to the effect of buoyancy force on the bubbles. Buoyancy drives the bubbles to the upper part of the test section where they form a visible layer. In addition, as a result of buoyancy, the void fraction reaches to zero in the lower part.

In the literature data (Figure 4.2), there are peaks in the void fraction profiles (red symbols) near the upper wall. Bottin (2010) has reported the existence of similar peaks in the METERO experiment for high liquid flow rates (J_L=5.31 m/s). Although the mechanism generating these peak points is complicated, from the curves, some conclusions can be drawn: the position of the peaks moves away from the wall when "*J_G is decreased for constant J_L* (as in Figure 4.2 (a))" or "*J_L is increased for constant J_G* (as in Figure 4.2 (b))" (i.e. increasing the relative effect of turbulence in the flow). Thus, for certain values of J_L and J_G, the position of the peak point could be very close to the wall where it is not possible to observe it due to the probe size. Since the flow rates focused in this study are lower than the ones in the literature (and so is the relative effect of the turbulence since it is an increasing function of the mean velocity), these peaks in the void fraction profiles have not been observed (Figure 4.3). In addition, the represented void fraction profiles in this study have a similar tendency of the one presented by Iskandrani & Kojasoy (2001) for J_L= 3.8 m/s and J_G=0.25 m/s (profile marked with circles in Figure 4.2): void fraction decreases sharply while moving away from the upper wall until *r/R = 0.3* and it does not change significantly after this position.

The void fraction profiles at 40D are sensitive to the flow rates in such way: increasing J_G for constant J_L results in sharpening the upper part of the void fraction profile (Figure 4.3). On the other hand, as seen in Figure 4.4, the same change in the flow rates leads to an attenuation of the void fraction in the lower part (*-1<r/R<0*). These two effects come from the relative decreasing effect of the turbulent mixing, which becomes dominated by buoyancy when gas flow rate is increased. If J_G is kept constant and J_L is increased, the turbulent mixing increases making the flow more uniformly dispersed. As a result, the void fraction profiles tend to flatten for higher liquid flow rates when the gas flow rates are constant.

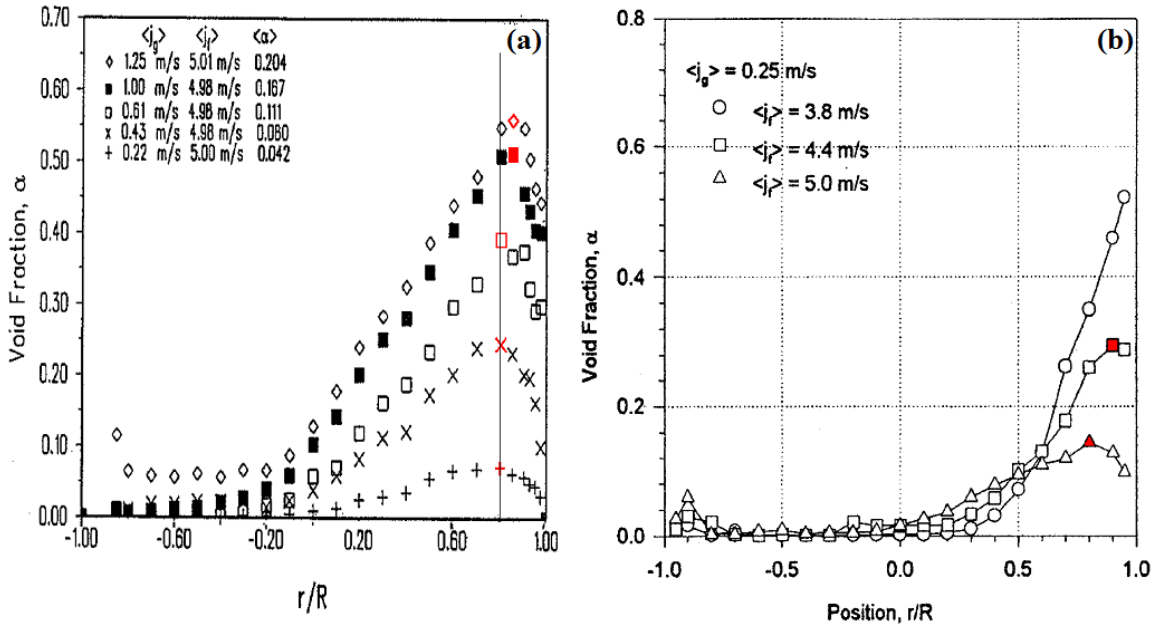

Figure 4.2 - Void fraction profiles, (a) constant J_L (Kocamustafaogullari et al., 1994) and (b) constant J_G (Iskandrani & Kojasoy, 2001)

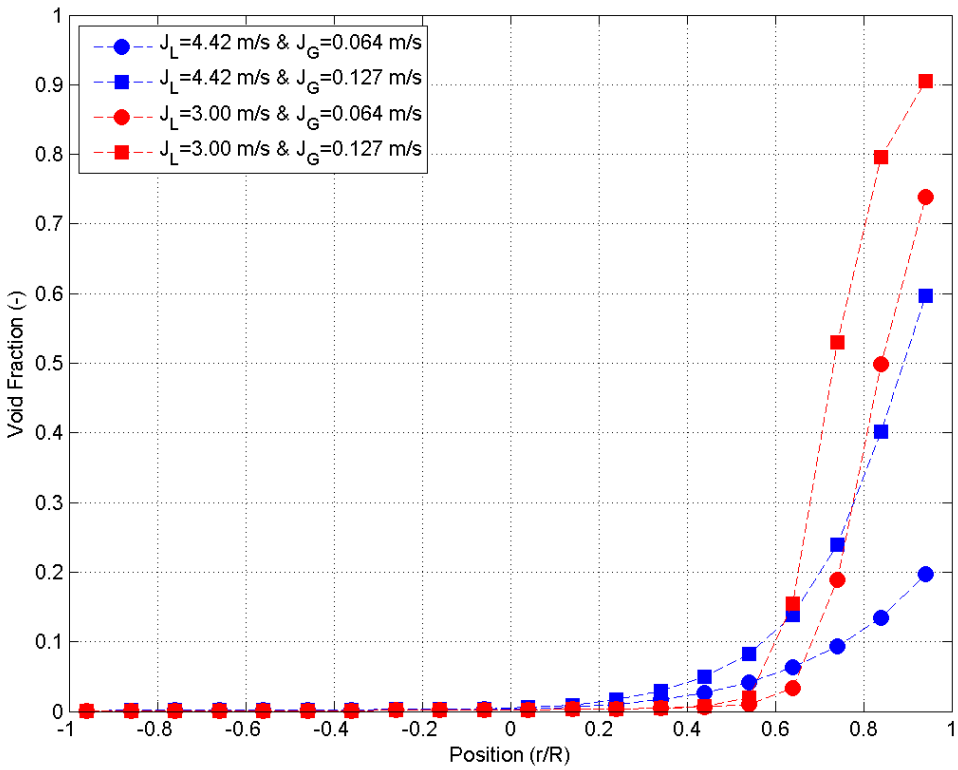

Figure 4.3 - Void fraction profiles of the METERO experiment for dispersed bubbly flows at 40D

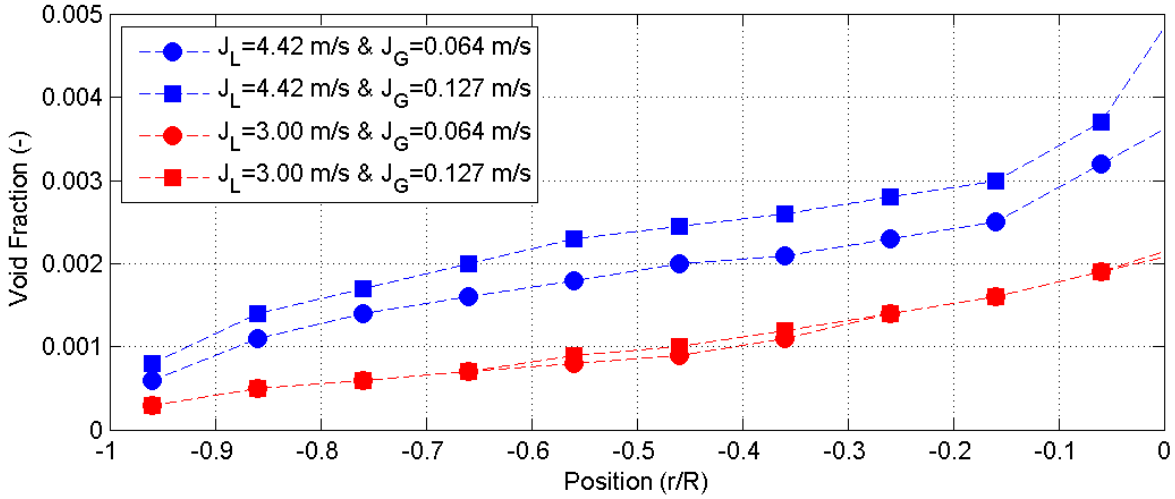

Figure 4.4 - Zoom of Figure 4.3 for *-1<r/R<0*

4.1.2 Bubble size

Bubble size plays an important role in two-phase flows and their distribution along a vertical axis could point out the competition of turbulent mixing and buoyancy. Thus, in order to determine the bubble size distributions, chord length distributions are investigated in the present study. An example of probability density function (PDF) of chord length histograms measured on a vertical axis is given in Figure 4.5. As seen from the curves, the chord length changes along the vertical axis. Furthermore, at *r/R=0.54*, there are two peaks on PDF representing two different chord lengths taking place in this position. It could be concluded that a PDF function with 2 peaks represent the boundary between the bubble layer located at the top of the test section and liquid phase carrying very small bubbles.

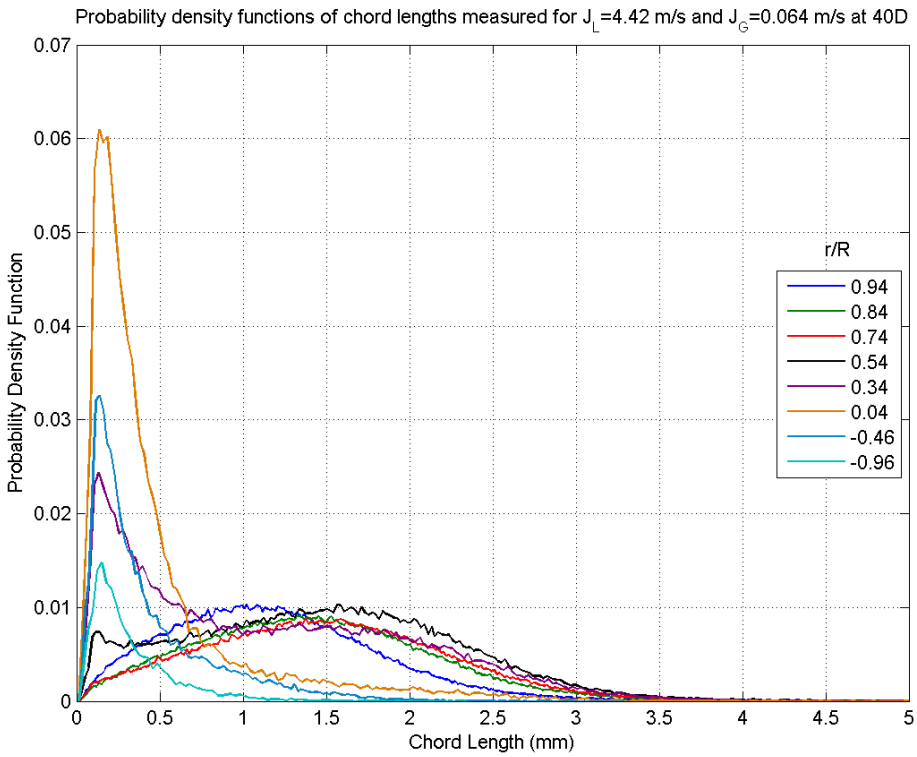

Figure 4.5 - Probability density function of chord lengths measured at 40 D for J_L=4.42 m/s and J_G=0.064 m/s

Chord length distribution profiles are created by selecting the chord length which has the highest probability in the measurement position. Therefore, these distribution profiles measured at 40D for various J_L and J_G are given in Figure 4.6.

It is observed that the profiles for higher J_L are significantly different from the ones measured for lower J_L. From the curves, it could be concluded that the bubbles are distributed along the vertical axis according to the chord lengths in all tests. The bubbles with large chord lengths will take place on the upper part of the test section since the buoyancy force is proportional to the bubble volume. Conversly, bubbles with small chord lengths (smaller bubbles) are located in the lower part ($r/R<0$) since the buoyancy force is dominated by the turbulent one (mixing) that prevents bubble migration. The clear difference between the profiles shows that different mechanisms take place in the chord length distribution. It is clearly observed that there exist two different regions in the chord length distribution profiles corresponding to two dominant mechanisms: the lower region ($-1<r/R<0$) where small bubbles, represented by small chord lengths, are dispersed by turbulence and the upper region ($0<r/R<1$) where the buoyancy drives the larger bubbles (greater chord lengths) toward the top.

In tests for higher J_L, the chord length distribution profiles are more homogenous due to relatively greater turbulent forces than in the profiles acquired for lower J_L. The average chord length in the lower region is around 0.12 mm while the one in the upper region it is about 1.45 mm. It is also obvious that the chord length profiles could be divided into three zones such as two zones with homogenous distributions and one transition zone between these two parts where the chord length decreases sharply.

Once the liquid flow rate is decreased, the effect of the buoyancy force starts to increase as seen on the chord length profiles for lower J_L. As a result, the homogeneity of the chord length distribution vanishes except in the lower region where the small bubbles are trapped by turbulence. It is observed that the maximum chord length in the flows for the lower J_L is increased to 2.28 and 2.96 mm while it is 1.45 mm on average for higher J_L. The profiles for the lower J_L could be categorized into two zones as: upper zone ($0<r/R<1$) with a linear decrease of the bubble diameter while moving away from the wall and lower zone ($-1<r/R<0$) where the chord length is constant around 0.12 mm.

Even though changing J_L for constant J_G generates different chord length distribution profiles, the change in J_G at constant J_L has same effect in both flow regimes. Once the J_G is increased, chord length values for the upper region increase. This is an obvious consequence of the greater J_G which generates larger bubbles. On the contrary to what happens in the upper region, the chord length does not change in the lower region while increasing J_G. This could lead to draw the conclusion that the effect of turbulent forces in the lower region is not affected or slightly affected by the change in J_G. The reason could be that wall induced turbulence remains constant at given liquid flow rate and bubbles induced turbulence is weal because only small bubbles are present here whatever is the gas flow rate.

In conclusion, on the one hand, the increase of liquid flow rate and thus turbulence mixing flattens the chord length profiles in the whole section. On the other hand, the increase of gas flow rate is responsible for the creation of larger bubbles that rise easily toward the top making these profiles more sharpened on the upper part of the test section.

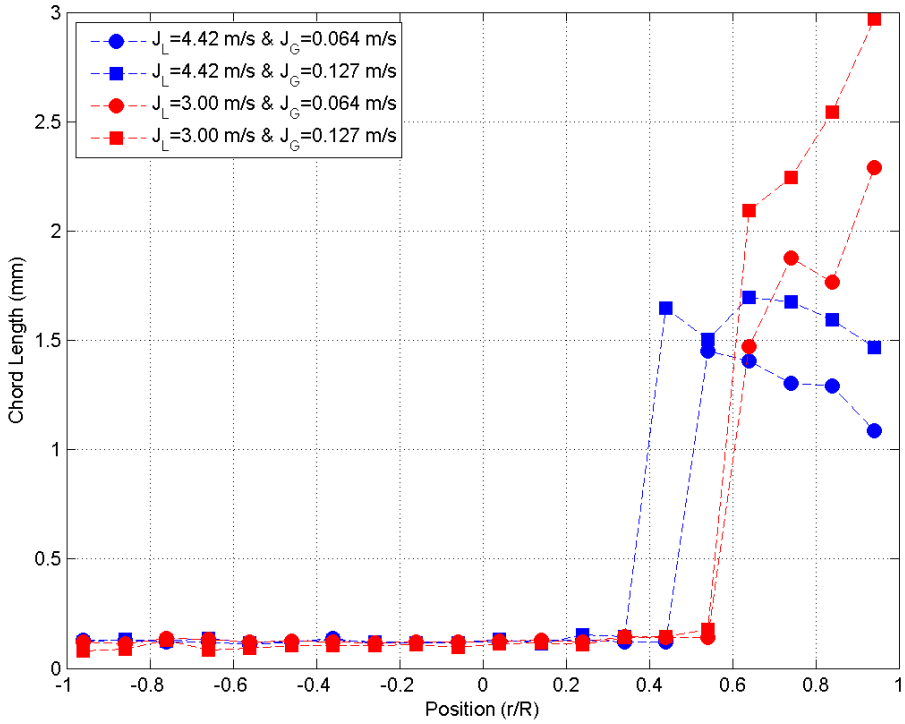

Figure 4.6 - Chord length distribution profiles of the METERO experiment for dispersed bubbly flows at 40D

4.1.3 Interfacial area

The interfacial area concentration profiles acquired at 40 diameters downstream from the inlet are given on Figure 4.7. In addition, zoomed profiles for the lower part of the test section are shown in Figure 4.8.

The results show that all the profiles can be split into two regions. The upper region (*0<r/R<1*) could be considered as the place where the interfacial area increases while approaching to the upper part of test section. The second one is the lower region (*-1<r/R<0*) where the interfacial area is constant. It should be remarked that the test condition J_L=3.00 m/s & J_G=0.127 m/s corresponds to a flow which is in the transition between dispersed bubbly and intermittent flows (Figure 4.1). Thus, the interfacial area profile of this test conditions have a similar trend with other test conditions until *r/R*=0.8. Beyond this position, elongated bubbles corresponding to plug flow have been observed.

In the upper part of the test section, for test conditions with the lower J_G, the interfacial area decreases by increasing J_L. This behavior could point out the existence of highly dispersed flows in the upper part due to increased turbulence mixing. In the case of constant J_L (J_L=4.42 m/s), there exists a decrease in the interfacial area when J_G is decreased. This is a result of decreased amount of gas phase in the test section. Since the chord lengths do not vary significantly with J_G, by checking void fraction values, it can be concluded that the number of the bubbles in the test section decreases with decreasing J_G. This leads to the decrease of the interfacial area.

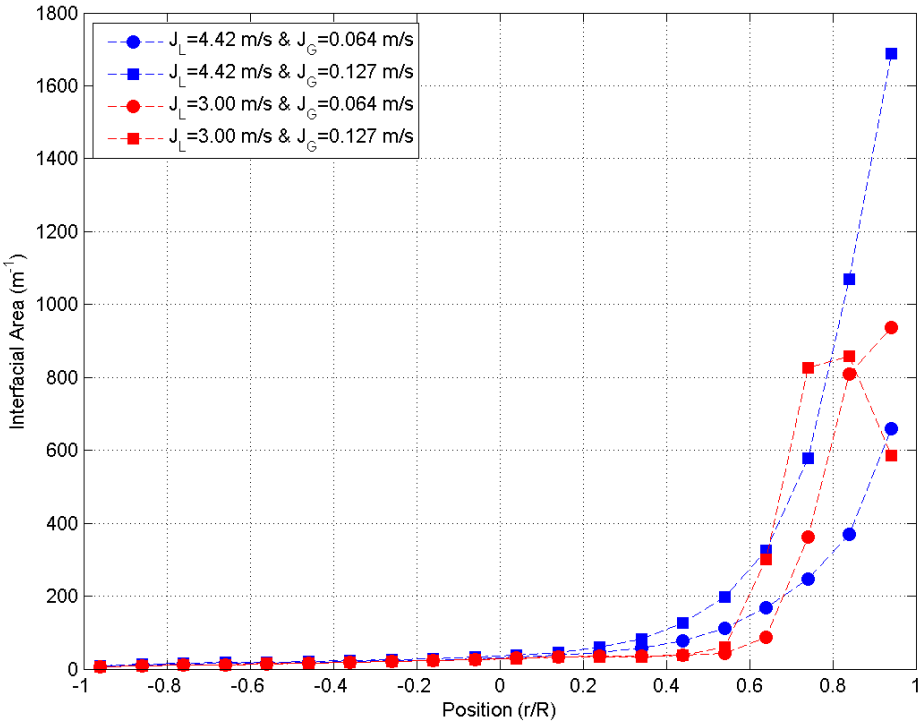

Figure 4.7 -Interfacial area profiles of the METERO experiment for dispersed bubbly flows at 40D

In the lower part of the test section, once J_L is increased at fixed J_G, an increase in interfacial area is observed. This increase is due to the fact that small bubbles cannot migrate to the upper part due to increased turbulence and the population of the bubbles increases in the lower part. For constant J_L, the increase of J_G results in an increase in the interfacial area because of the increase in bubble population with increased J_G.

In the literature, several authors (Kocamustafaogullari & Wang (1991), Kocamustafaogullari et al. (1994) and Bottin (2010)) observed peaks in the interfacial area profiles similar to the ones observed on the void fraction profiles. However, these peaks have not been observed in this study due to the same reason which was explained in Section 4.1.1.

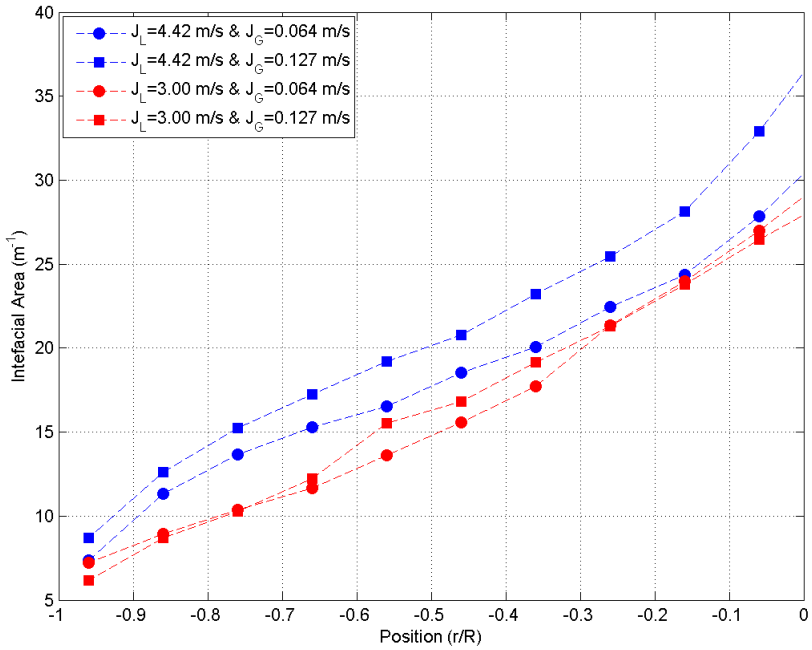

Figure 4.8 - Zoom of Figure 4.7 for *-1<r/R<0*

4.1.4 Axial bubble and liquid velocities

In this section, the average axial velocities of bubbles and liquid phase are measured together (but not simultaneously) since they are expected to be rather similar in horizontal dispersed bubbly flows. Therefore, the velocity profiles of bubbles and liquid phase have similar shapes.

As mentioned in Chapter 3, the liquid velocity is measured using hot-film anemometry probes while bubble velocity is measured using optical fiber probes. For optical probe technique, different configurations of probes (2-tip and 4-tip probes) have been used: firstly the simplest one (2-tip) but since it is known to be valid only for spherical bubbles, the 4-tip one was also used. 4-tip probe is also suspected to introduce errors by missing the smallest bubbles. Therefore, in order to check the validity of the two optical fiber probe results, several tests have been conducted using high-speed camera and shadowgraphy technique to measure bubble velocity. The measurements have been performed at the center of the test section and an axial location of 40D for J_L=4.42 m/s and various J_G.

For results validation, a bubble velocity database has been generated by using shadowgraphy technique which is considered the reference due to the following reasons: increasing the number of tips (4-tip probes) or changing the measurement medium (shadowgraphy) brings out similar results in the bubble velocities. On the one hand, optical fiber probe does require piercing of interface which can influence the measured velocity. On the other hand, shadowgraphy technique measures the velocity without any interaction with bubbles. Thus, shadowgraphy has been taken as the reference measurement technique.

The test conditions of high-speed camera and shadowgraphy technique and the measured average axial bubble velocities for each test are given in Table 5.2. Moreover, the measured velocities with error bars are presented in Figure 4.9.

High-speed camera and shadowgraphy system (bubble velocity measurements)							
J_L (m/s)	4.42	4.42	4.42	4.42	4.42	4.42	4.42
J_G (m/s)	0.011	0.025	0.042	0.064	0.085	0.110	0.120
U_B (m/s)	5.33	5.40	5.39	5.40	5.38	5.39	5.39

Table 4.2 - Test conditions and measurements results of high-speed camera and shadowgraphy technique

Once the reference velocity database was established, the average axial bubble velocity at the center of the test section and 40D was also measured for constant J_L (4.42 m/s) and various J_G (0.064 & 0.127 m/s with 4-tip probe and 0.064, 0.095 & 0.127 m/s with 2-tip probe). The comparison of the bubble velocity measurements by different techniques and liquid velocities is represented in Figure 4.10.

The comparison results show that the axial bubble velocity is systematically underestimated by 2-tip optical fiber probe, approximately 10%, compared to the measured velocities by shadowgraphy technique. This underestimation could be a result of bubble deformation after contact with the first tip of the probe which could increase the transit time of a bubble between the tips, thus the measured velocity is decreased. On the other hand, the results of 4-tip probe measurements have good agreement with our reference velocities. This result is due to the fact that the effect of bubble deformation on the velocity measurement is minimized by increasing number of probe tips. To sum up, increasing the number of probe tips results in better estimation of the bubble velocities. Thus, 4-tip optical fiber probes have been used in this study.

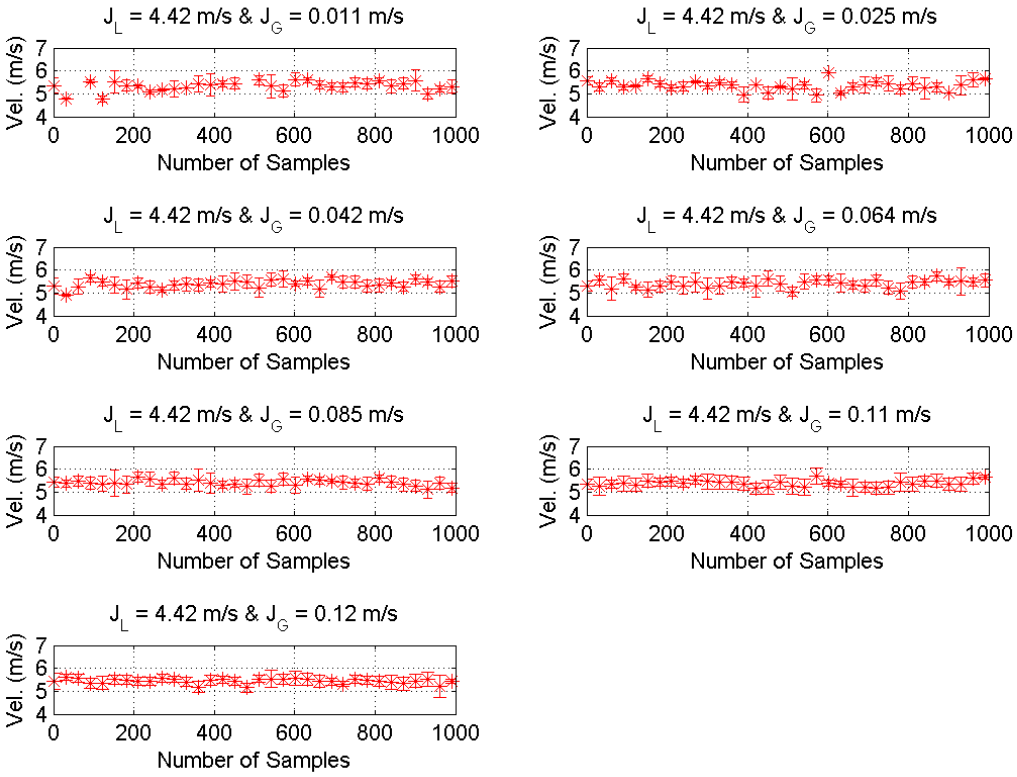

Figure 4.9 - Axial bubble velocity for various J_G at the center of the test section and 40D

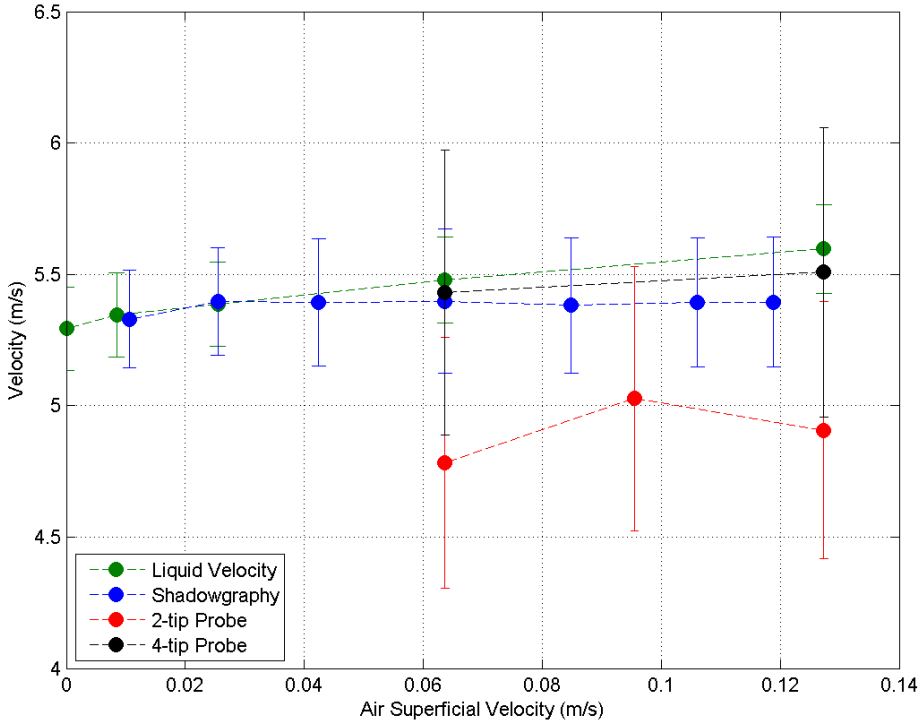

Figure 4.10 - Axial bubble velocity for J_L=4.42 m/s and various J_G at the center of the test section and 40D

Average axial velocity profiles of bubbles (U_B) and liquid phase (U_L), measured at 40D downstream, are given in Figure 4.11. The results show that the presence of bubbles makes asymmetrical the distribution of bubble and liquid phase velocity profiles. Moreover, this asymmetry increases with increasing J_G. This behavior has already reported by several authors in the literature

(Kocamustagaogullari & Wang (1991), Iskandrani & Kojasoy (2001), Yang et al. (2004), Ekambara et al. (2008), Bottin (2010)). As a consequence of this asymmetry, the maximum velocity measured in each test is decentered in the region: *-0.2<r/R<0* unlike in single phase flow. The shift of maximum velocity position comes from the gas layer in the top of the pipe that reduces and shifts downward the liquid flow cross section (Bottin, 2010). The position of the maximum velocity moves further downward of the test section when J_G is increased.

The loss of symmetry is also seen (Figure 4.11) on the velocity gradients in the near wall regions. The upper region gradient is quite higher than the lower one. This phenomenon has also reported by Bottin (2010). Iskandrani& Kojasoy (2001) have explained these differences by an increase of the wall friction on the upper wall induced by an additional turbulence due to the bubble layer.

Concerning average axial liquid velocities (U_Ls), it is observed that the magnitude of the liquid velocity is of course strongly dependent on J_L and quite less on J_G. The dependence on JG comes from the reduction of the liquid flow cross section induced by the presence of gas in the flow.

For the bubble velocity profiles, trends are similar to the liquid ones. The velocity gradients are asymmetric in the upper/lower wall regions. In addition, the position of the maximum velocity is shifted from the center to a zone of *-0.2<r/R<0*. It should be noted that the shift in the test J_L=3.00 m/s & J_G=0.127 m/s is greater than the others due the effect of the elongated bubbles formed in this test (see Section 5.1.3). Furthermore, when J_L is kept constant and J_G is increased, U_B is increased slightly as same trend as U_L. Keeping J_G constant and decreasing J_L results in a sharp decrease in the bubble velocity similar to the liquid velocity profiles. In the light of these similarities of the velocity profiles, it could be concluded that the bubbles are transported by the liquid phase and therefore U_B is strongly dependent on J_L.

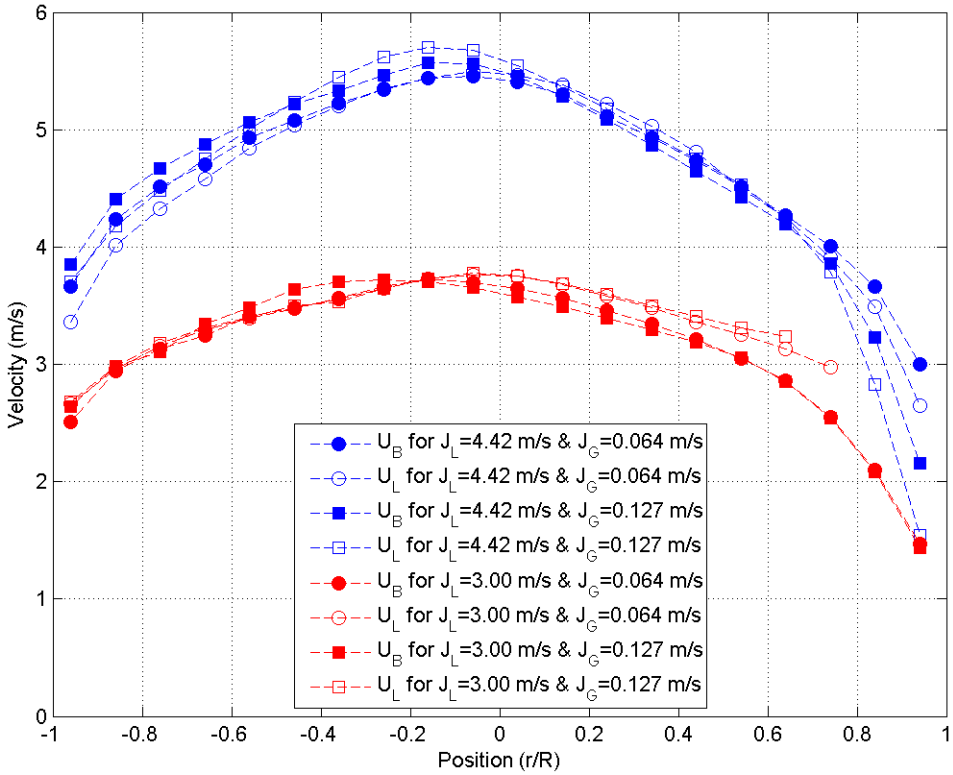

Figure 4.11 - Axial mean velocity profiles of the METERO experiment for dispersed bubbly flows at 40D

4.1.5 Turbulent kinetic energy of liquid

The liquid turbulent kinetic energy (TKE) profiles for various J_L and J_G are given in Figure 4.12. As seen in the figure, the profiles in two-phase flows have asymmetrical distributions, similar to the mean velocity profiles, due to the presence of the gas phase. It is also observed that the minimum of TKE takes place where the axial mean liquid velocity gradient is minimum which corresponds to the decentered position of the maximum liquid velocity. In addition, the TKE increases for all test conditions in the upper and lower walls where the velocity gradients are the maximum. These results are not surprising since turbulent production is proportional to these gradients.

It is observed that once J_G is kept constant and J_L is increased, TKE values in the lower part of the test section ($-1<r/R<0$) and the zone near the upper wall increase. These increases are due to the presence of gas phase; however, the mechanisms in the lower part and the near-upper-wall zone are different. Kocamustafaogullari & Wang (1991) has explained the mechanism in the lower part: once the gas phase is introduced, the bubble layer decelerates the main flow in the upper region. Thus, the flow velocity is increased in the lower part in order to ensure the continuity of the flow. Consequently, the velocity gradient is increased in the lower part which promotes TKE in this region. In addition, the increase of TKE in the near-upper-wall zone could be explained by additional effect of bubble induced turbulence. The effects of these two mechanisms can be seen in Figure 4.13 where TKE and roughly calculated velocity gradient are given with the boundary of bubble layer taken from void fraction measurements.

The change in the liquid velocity (J_L) at a fixed J_G has a strong influence on TKE. As seen from the results, TKE decreases with a decreasing (ask!!)

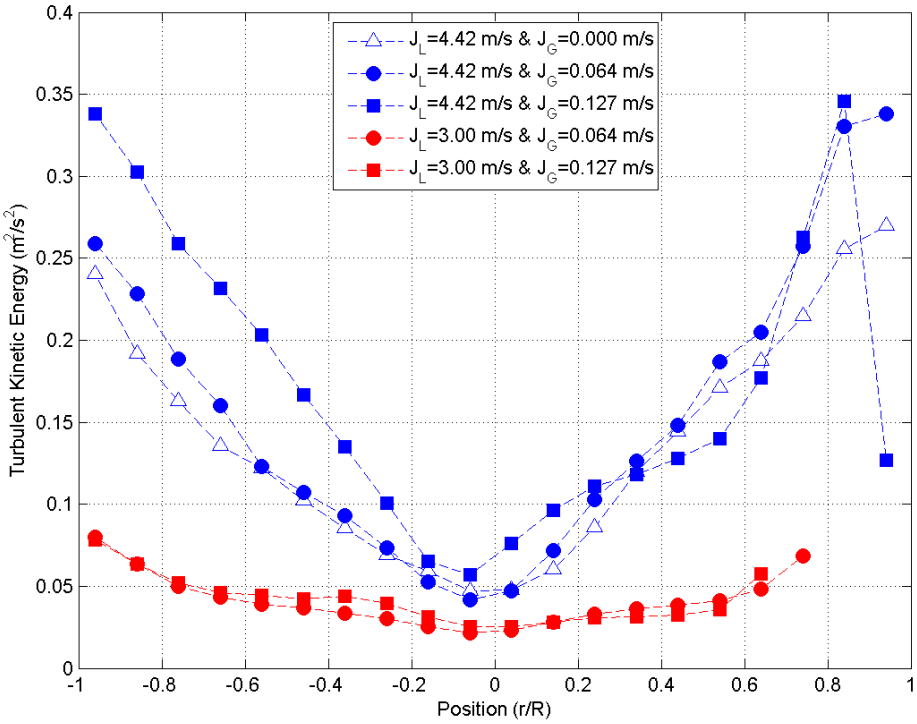

Figure 4.12 - Turbulent kinetic energy profiles of the METERO experiment for dispersed bubbly flows at 40D

The sharp decrease at r/R=0.94 for the test J_L=4.42 m/s & J_G=0.127 m/s has been reported by Bottin (2010) and the author stated that there exist numerous bubbles in this region for this test condition, thus discrimination process of the gas and liquid phases in the hot-film anemometry signals is

significantly difficult for this measurement point. Therefore, the reason of this sharp decrease could be a physical phenomenon or lack of discrimination process.

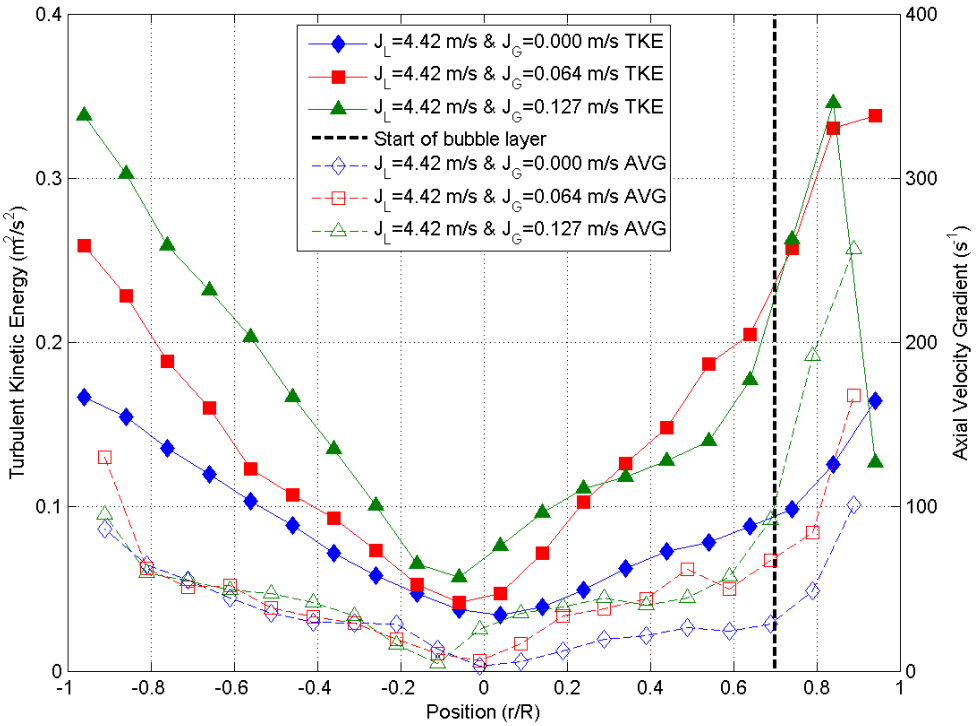

Figure 4.13 - Turbulent kinetic energy and axial velocity gradient profiles at 40D for J_L=4.42 m/s and various J_G

4.2 Axial Evolution of Flow Quantities

In this section, the axial evolution of the local flow characteristics (mentioned in Section 5.1) will be analyzed for understanding the development of dispersed bubbly flow along a horizontal pipe. For this purpose, the acquisitions of local flow characteristics for the tests conditions given in Table 4.1 for hot-film anemometry and optical probe acquisitions have been carried out at three axial locations of 5, 20 and 40 diameters downstream from the gas injection tubes.

4.2.1 Void fraction

The axial evolutions of the void fraction profiles for various J_L and J_G are given in Figure 4.14. The profiles are in linear-logarithmic scale for having a better presentation of very low void fraction values in the lower part of the test section.

As seen from Figure 4.14, the void fraction increases continuously at the upper part of the test section ($0<r/R<1$) while moving from 5D to 40D for higher J_L. On the other hand, the void fraction regularly decreases in the lower part ($0<r/R<1$) between 5D and 40D. These behaviors observed for higher J_L points out that the migration of the bubbles is still in process between 20D and 40D. Thus, it can be concluded that the turbulent mixing dominates the buoyancy and thus, the migration of bubbles is slowed down. As a consequence, bubble migration cannot be completed until at least 40D.

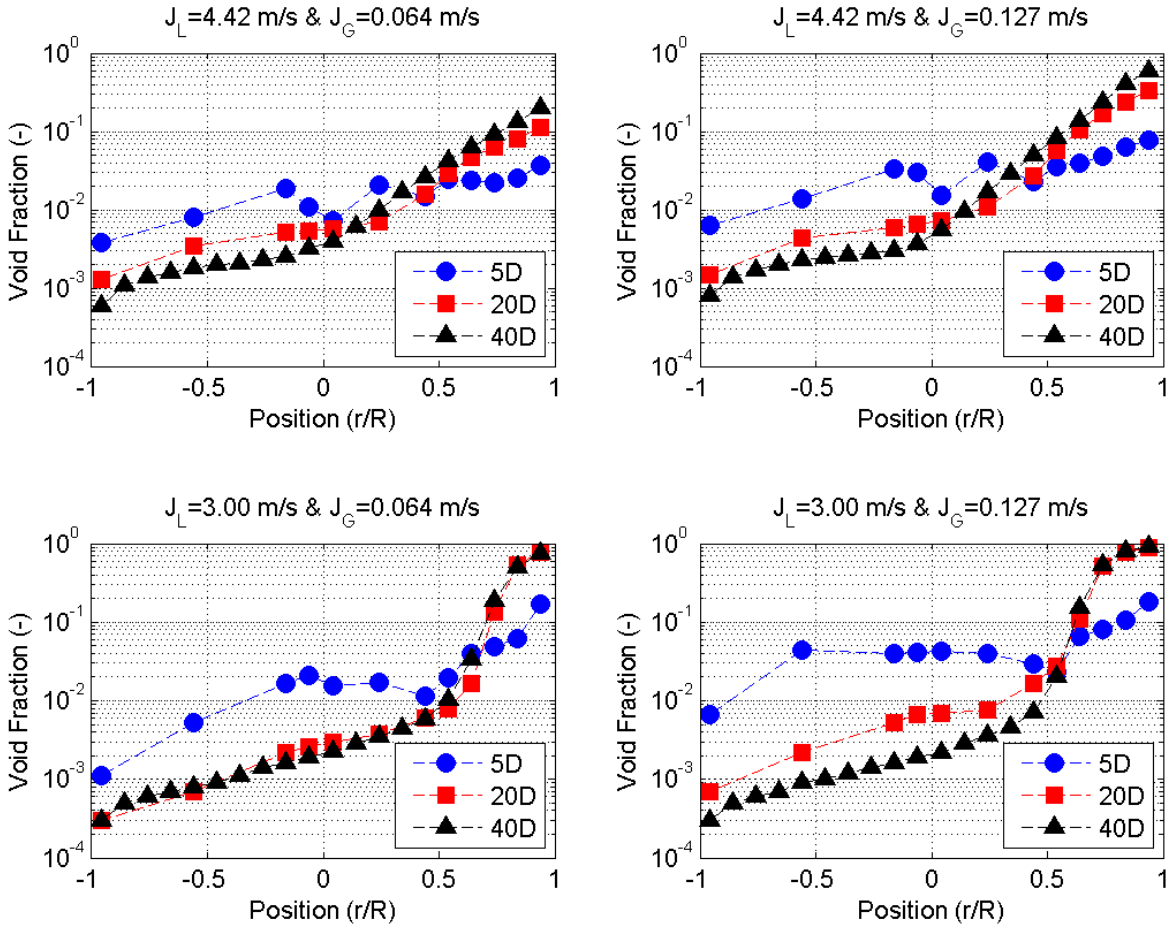

Figure 4.14 - Axial evolution of void fraction profiles for dispersed bubbly flows

The evolution of the void fraction profiles for lower J_L is different from the ones at lower J_L. The results for lower J_L show that the void fraction at the upper part (*0<r/R<1*) first increases while moving from 5D to 20D. Afterwards, the changes in the void fraction profiles at 40D are insignificant. This behavior demonstrates that the bubble migration is finished at 20D. Thus, it could be concluded that the relative effect of turbulent mixing (compared to buoyancy) is decreased when J_L is decreased. This results in the complete migration of the bubbles before 20D.

4.2.2 Bubble Size

Chord length profiles measured at three different axial locations (5D, 20D and 40D) for various J_L and J_G are given in Figure 4.15. The profiles are presented with linear-logarithmic scale for a better observation of small values in the lower part of the test section (*-1<r/R<0*). For all test conditions, it is observed that the chord lengths globally increase along the test section. At location 5D, chord lengths are distributed homogeneously. This could be explained by the test location just after the last grid (see Section 2.2.1) which determines the bubble sizes and chord lengths. When moving from 5D to 40D, the increases of chord lengths on the upper part of the test section are remarkable. It could be a result of the vertical migration of the bubbles toward the top and of coalescence; however, coalescence has never been visualized in the present study.

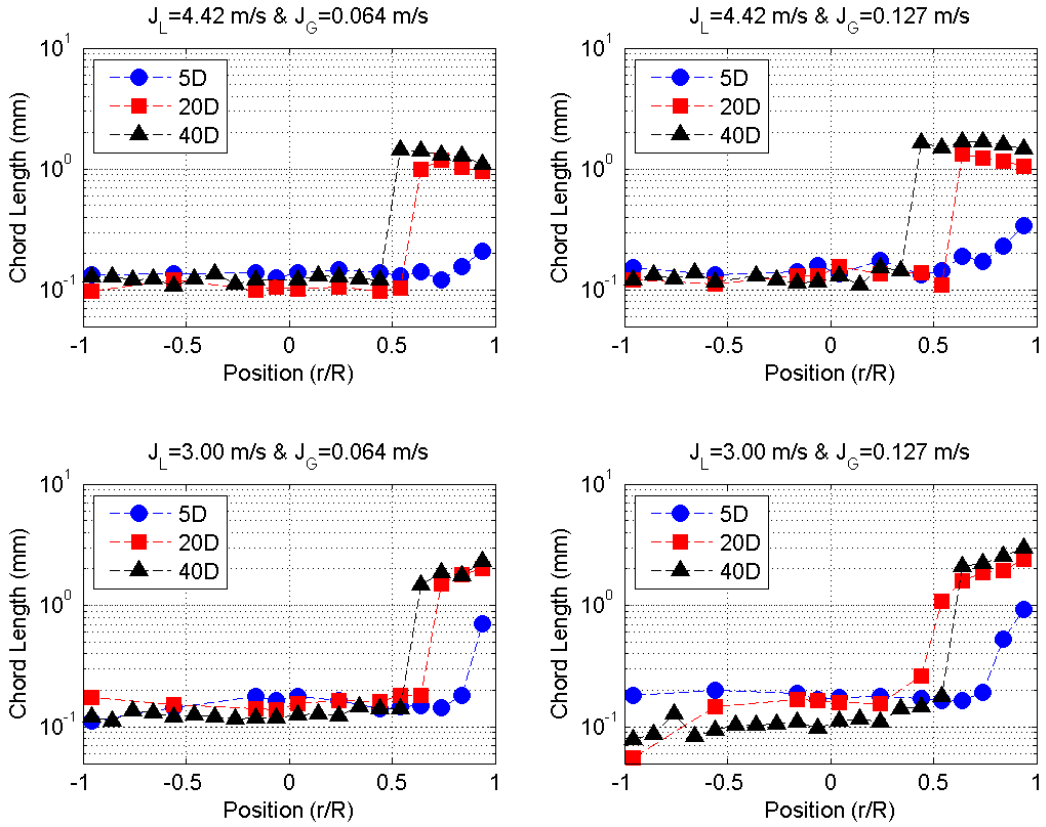

Figure 4.15 - Axial evolution of chord length profiles for dispersed bubbly flows

Once J_L is decreased, chord length profiles have different shapes. For instance, the bigger bubbles start to rise toward the upper part of the test section from 5D since the buoyancy force becomes relatively stronger due to the decrease of the turbulent force linked to the decrease of J_L. Similarly to the axial evolution of void fraction profiles for lower J_L, the change in chord length values is insignificant along the test section after 20D since the migration of the bubbles is completed with the biggest bubbles are located on the top. Furthermore, this small increase in chord lengths, while the void fraction is constant from 20D to 40D, could be a proof of sedimentation and coalescence of the bubbles at the top of the test section.

4.2.3 Interfacial area

In order to analyze the coalescence, the sedimentation and the evolution of the bubble population along the pipe, interfacial area concentration profiles are studied at different axial locations.

Interfacial area concentration profiles measured at 5, 20 and 40D for higher J_L are given in Figure 4.16. In order to observe the changes in both lower part ($-1<r/R<0$) and upper part ($0<r/R<1$), the profiles are presented in linear-logarithmic scale. As seen on the figure, the interfacial area concentration has a saw tooth shape whatever is the liquid velocity. This behavior was observed by Bottin (2010) and the author reported that it is a result of the localized and non-homogeneous air injection (37 mini tubes). On the other hand, the effect of these injectors is not observed at 20 and 40D.

By increasing gas flow rate (J_G) at a constant J_L, the interfacial area concentration increases in the upper part of the pipe ($0<r/R<1$) along the test section (from 5D to 40D). Simultaneously, the interfacial area decreases in the lower part of the test section ($-1<r/R<0$). These behaviors of the profiles are the consequences of the bubble migration toward the top. Furthermore, it is important to note that the increase in the interfacial area and void fraction at $0<r/R<1$ while chord lengths varies

slightly is the consequence of the bubble sedimentation. This could lead to the conclusion that coalescence does not take place. This conclusion is not surprising since the relative effect of turbulent mixing (compared to buoyancy) do not change significantly by increasing J_G from 0.064 m/s to 0.127 m/s at a fixed J_L (4.42 m/s). Thus, very high turbulent mixing does not allow the coalescence take place in the flow.

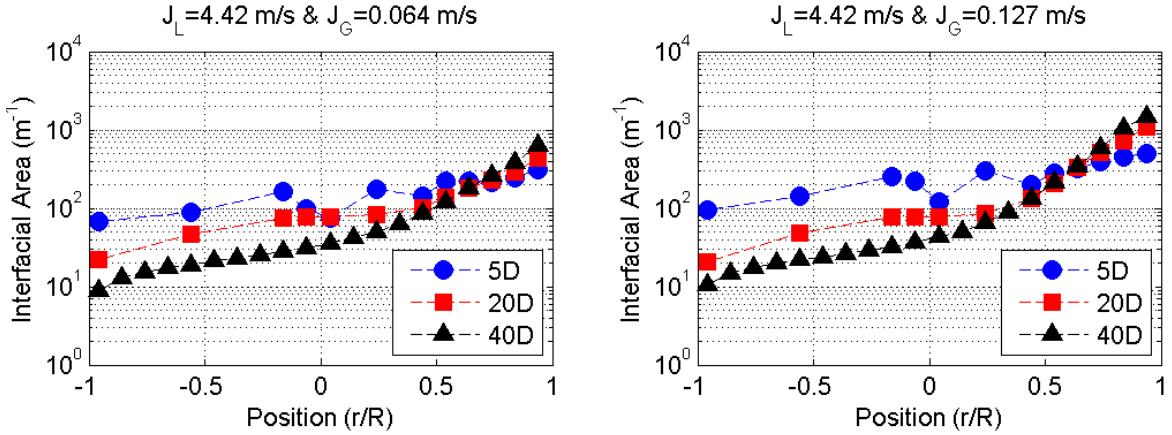

Figure 4.16 - Axial evolution of interfacial area profiles for dispersed bubbly flows at constant J_L

In order to observe the influence of J_L on the interfacial area, J_L is decreased from 4.42 m/s to 3.00 m/s while J_G is kept constant at 0.064 m/s. The results show that behavior of axial evolution in the lower part of the test section (*-1<r/R<0*) does not change significantly even liquid flow rate is decreased. On the other hand, the behavior observed in the upper part (*0<r/R<1*) differs by decreasing J_L and the axial evolution in this region should be investigated. Thus, axial evolutions of interfacial area concentrations acquired the upper part of the test section are given in Figure 4.17. As different from Figure 4.16, the results are represented in linear-linear scale in Figure 4.17 in order to observe the small variations.

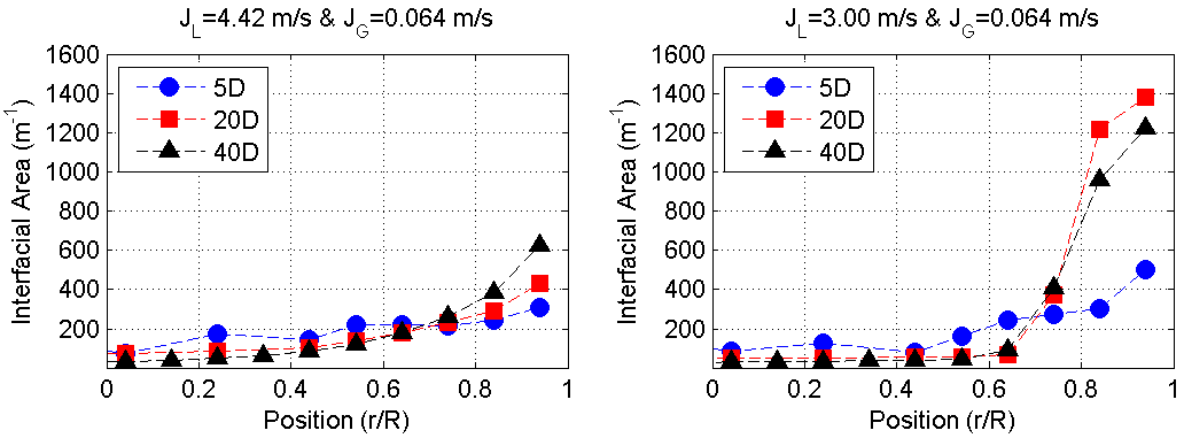

Figure 4.17 - Axial evolution of interfacial area profiles acquired at *0<r/R<1* for dispersed bubbly flows at constant J_G

As seen on the figure, after decreasing J_L, the interfacial area concentration is still increasing in the upper part (*0<r/R<1*) until 20D due to the rising bubbles. When the flow is approaching 40D, the interfacial area concentration decreases in the upper part, but not void fraction (between 20D and 40D). Thus, it could be concluded that the coalescence of bubbles takes place on the top of the test section.

4.2.4 Axial bubble and liquid velocities

The evolution of the axial mean bubble and liquid velocities along the test section are given in Figure 4.18 and Figure 4.19, respectively. As seen from the figures, the velocity of the bubbles is lower than the velocity of the liquid phase for the axial locations 5 and 20D. At 40D, liquid phase and bubbles have nearly the same average axial velocities.

At 5D, the velocity profiles of liquid phase and bubbles are nearly flat since the boundary layers are not developed. However, the velocities close to the upper wall are greater than the rest of the profile. Although a settling system is used upstream air injectors, the effect of the elbow located upstream this system (see Figure 2.2) is clearly observed on the increase of the velocity close to upper wall for all test conditions. The boundary layer starts to develop from the grid/injectors position and has not completely reached equilibrium before 20D as seen from the figures. As observed, the velocity increases from the wall to the center of the test section where both liquid and bubble velocities are constant. In addition, the velocity close to upper wall is decreasing sharper than the one close to the lower wall due to the presence of bubbles on the top (see section 5.1.4). At 40D, the velocity profiles show that the boundary layer is completely developed. In addition, the velocities close to wall for the flows with higher J_L decrease again due to the continuous migration of the bubbles to the top of the test section. On the other hand, for lower J_L, the velocity profiles close to the upper wall remain the same as the ones acquired at 20D since the migration of the bubbles was complete before this location.

As seen from the results, the flow rate conditions have different effects on the velocity profiles. For constant J_L, changing J_G has a slight influence on the velocity profiles. Moreover, the effect of J_G could be considered negligible on the velocity profiles acquired at 5 and 20D. On the other hand, not only liquid velocity but also bubble velocity is strongly dependent on J_L. Thus, it is concluded that the bubbles are transported by the liquid phase in dispersed bubbly flows.

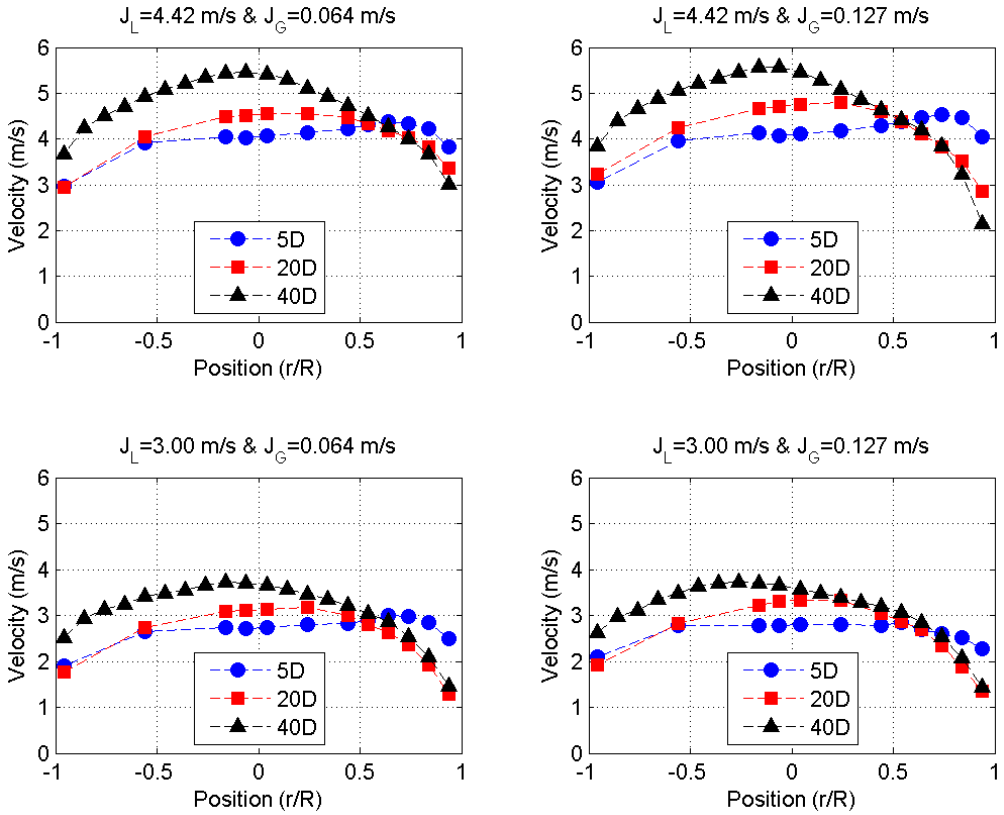

Figure 4.18 - Axial evolution of axial mean bubble velocity profiles for dispersed bubbly flows

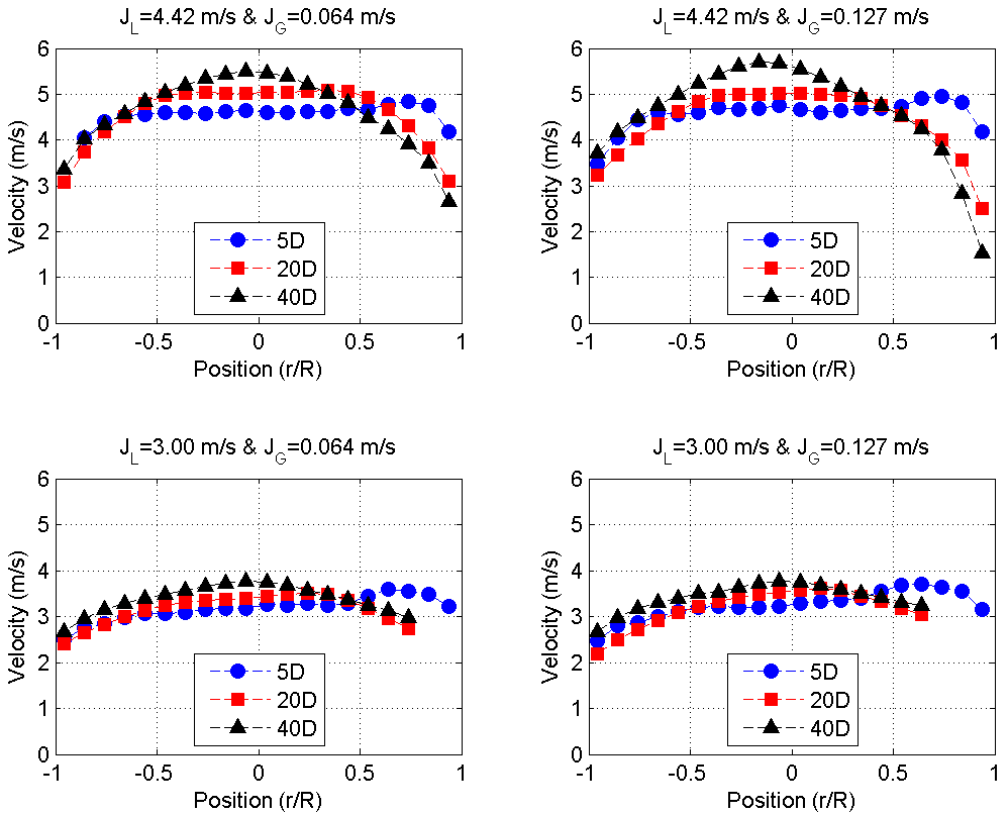

Figure 4.19 - Axial evolution of axial mean liquid velocity profiles for dispersed bubbly flows

4.2.5 Turbulent kinetic energy

Turbulent kinetic energy profiles acquired at different axial locations for various J_L and J_G are presented in Figure 4.20. It is observed that the profiles is asymmetric (minimum energy occurs at *-0.2<r/R<0*) after 20D due to presence of the bubbles and forms a V-shaped profile which is a trace of developed flows. Moreover, as mentioned in Section 4.1.5, the bubbles introduce additional turbulence to the wall shear turbulence at the top of the pipe. Consequently, the increase of the turbulent kinetic energy is sharper at the upper part than the increase at the bottom part. The turbulent kinetic energy profiles are more flat at 5 and 20D because of undeveloped boundary layers in the flow. It is also important to mention that the turbulent kinetic energy measured at the center of the test section at 5D is greater than the one measured at 20D. This is the consequence of the additional turbulence generated by the 4th grid placed in the test section.

As mentioned before, the changes in J_L (for fixed J_G) have a significant effect on turbulent kinetic energy measured at all axial locations. Although the effect of J_G (for constant J_L) on the magnitude of turbulent kinetic energy is slight, the asymmetry of the profiles is strongly dependent on the changes in J_G.

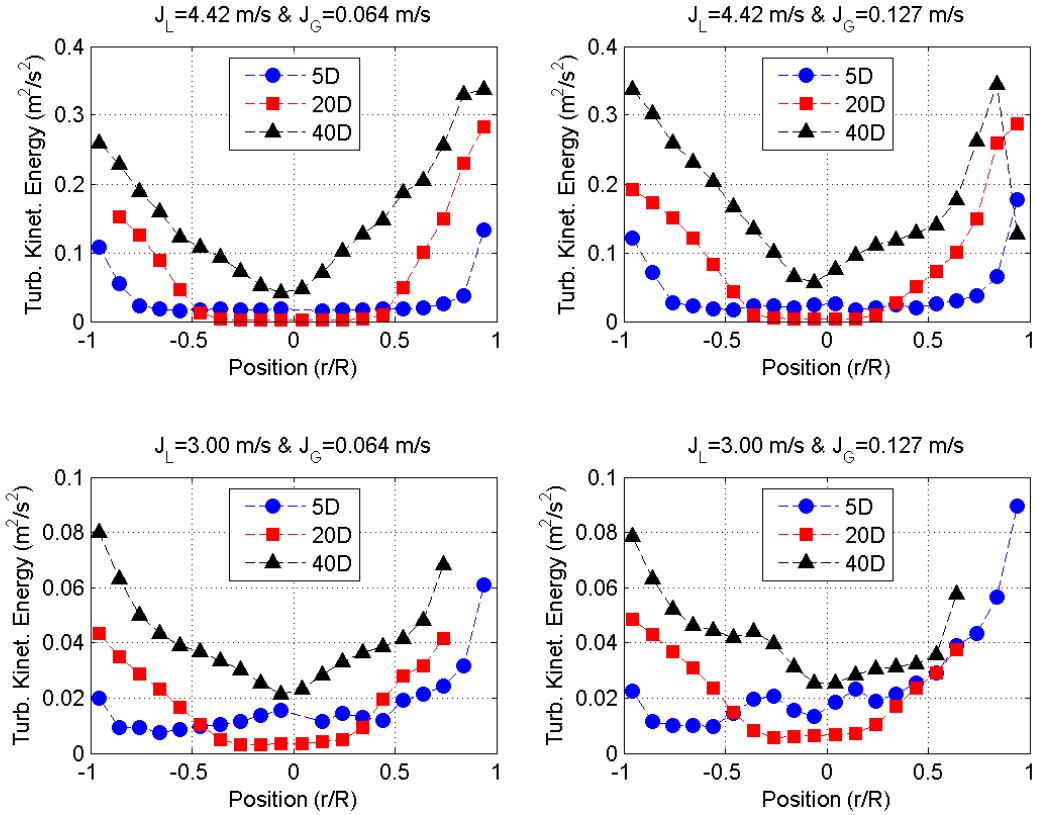

Figure 4.20 - Axial evolution of turbulent kinetic energy profiles for dispersed bubbly flows

4.3 Conclusion

In this chapter, flow quantities (namely void fraction, bubble size, interfacial area concentration, axial velocities of gas and liquid phases, and turbulent kinetic energy of liquid phase) are studied locally. In addition, their axial evolutions are also presented. As a general remark, it was observed that there two important forces determining the distribution of the flow quantities: turbulence and buoyancy. The consequences of turbulence-buoyancy competition are studied by changing liquid and gas flow rates (J_L and J_G, respectively). When J_L is increased, the turbulence is also increased. As a result, void fraction, chord length and interfacial area profiles become more flat due to increased turbulent mixing.

The effects of changing J_G are different from what is observed for J_L. If J_G is raised at a constant J_L, consequently, void fraction and bubble size increase because more gas phase is introduced in the flow. Once the bubble size is increased, the bubbles are exposed to greater buoyancy forces and they accumulate at the top of the pipe. As a result, the increase of void fraction in the upper part is greater than the one observed in the lower part. The influence of changing J_G on velocity and turbulent kinetic energy is insignificant.

The axial evolutions of void fraction, chord length and interfacial area concentration point out the bubble migration toward top and accumulation/sedimentation of the bubble at the top of the pipe. Although coalescence of bubbles is not visualized in the present study, the axial evolutions of flow quantities lead us to draw the conclusion that coalescence of the bubbles takes place in the flow.

The comparison of liquid and bubble velocities at 40D shows that the bubbles are transported by the liquid phase in the dispersed bubbly flows.

CHAPTER 5

STUDY OF INTERMITTENT FLOWS

5 STUDY OF INTERMITTENT FLOWS

5.1 Local Studies on Flow Quantities

Once the liquid flow rate is decreased, the buoyancy force is superior to the turbulent one and the intermittent flow regime is reached. The rising velocities of bubbles (gas phase) are no more decreased by mixing compared unlike in the dispersed bubbly flow. Although the nature of intermittent flow is more complicated, detailed studies are necessary to understand this flow regime.

To study intermittent flow, 4-tip optical fiber probes and constant temperature hot-film anemometry have been used for several test conditions (Table 5.1). In addition, the test conditions are also illustrated on the flow regime map (Figure 5.1). The operating conditions of these measurement techniques are the same as those of the dispersed bubbly flow measurements. The results given and analyzed in this section correspond to the values that are highlighted in yellow (representing Plug Flow (PF) and Slug Flow (SF)). The other results are given in Appendix 5.

Hot-film anemometry (mean and fluctuating velocity, magnitude of turbulence)						
J_L (m/s)	2.65	2.65	2.12	2.12	1.59	1.59
J_G (m/s)	0.064	0.127	0.064	0.127	0.064	0.127

Optical fiber probes (void fraction, chord length, interfacial area, axial velocity)						
J_L (m/s)	2.65	2.65	2.12	2.12	1.59	1.59
J_G (m/s)	0.064	0.127	0.064	0.127	0.064	0.127

Table 5.1 - Acquisition conditions for intermittent flows

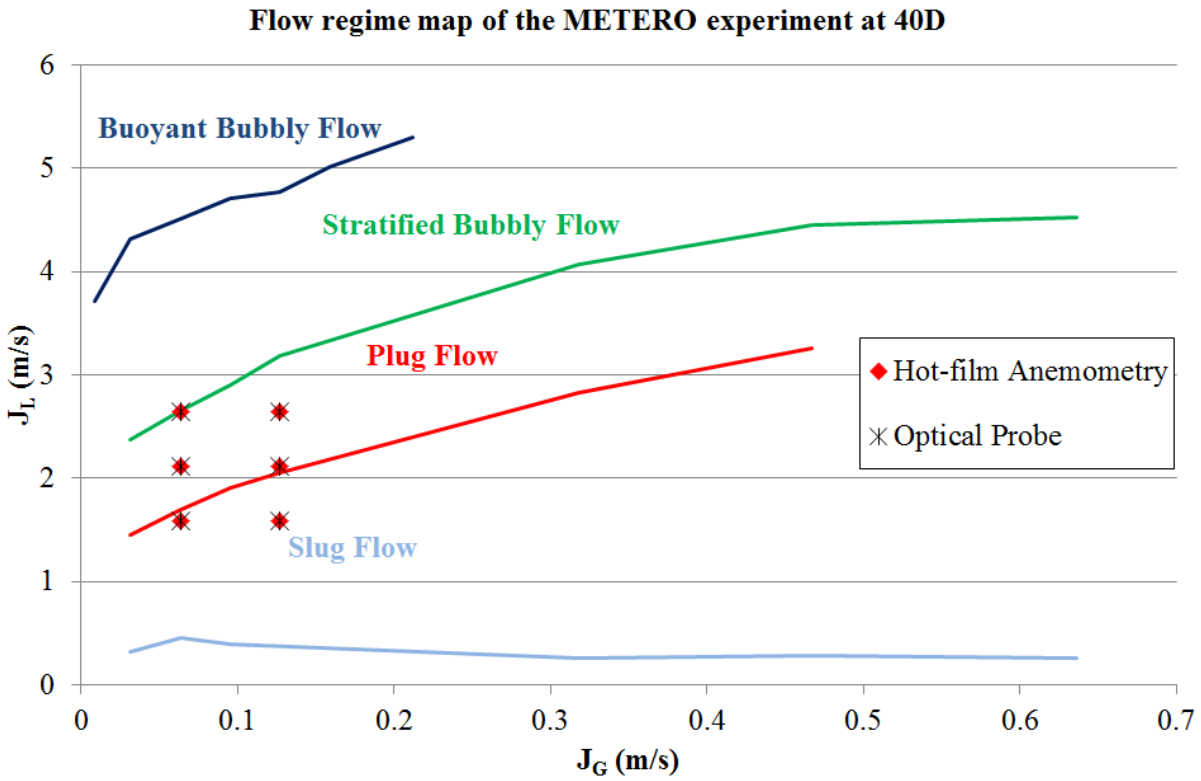

Figure 5.1 - Representation of the test conditions for intermittent flows on the flow regime map

5.1.1 Void fraction

Several authors (Lewis et al. (1996), Riznic & Kojasoy (1997) and Lewis et al. (2002)) have investigated void fraction distribution in intermittent flows, especially in slug flow. Some examples of void fraction distributions for horizontal intermittent flows are represented in Figure 5.2 and Figure 5.3. As seen from these figures, the void fraction profiles can be cut into three regions such as:

- A plateau in the upper part of the test section where the void fraction is very high due to the big slug bubbles,
- A sharp and short transition,
- Another plateau in the lower part where void fraction is close to zero (almost no bubbles).

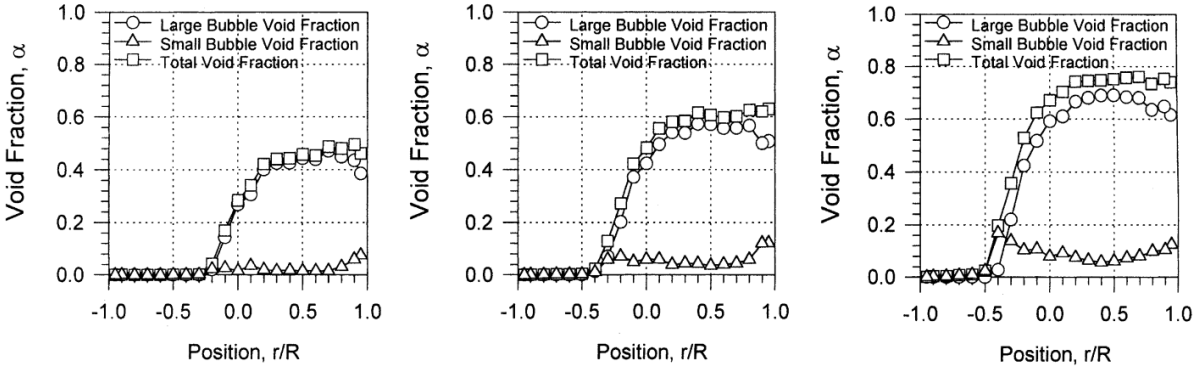

Figure 5.2 - Local void fraction distributions measured at 253D for J_L=1.65 m/s & J_G=0.55, 1.1 and 2.2 m/s (Lewis et al., 2002)

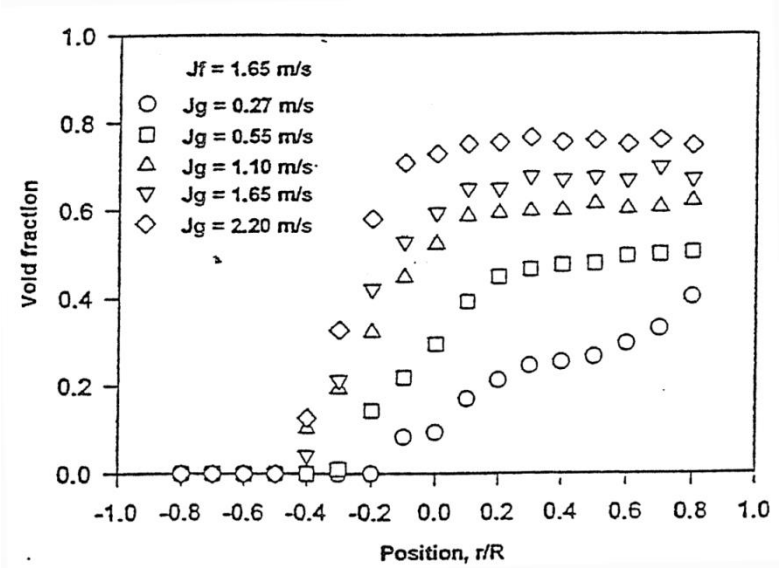

Figure 5.3 - Void fraction distribution measured at 253D for J_L=1.65 m/s and various J_G (Riznic & Kojasoy, 1997)

These contributions from the literature are significant; however, they correspond to data acquired far from the inlet (measurement location of 253 diameters). As already mentioned, the knowledge of the developing flows near the inlet is important in the nuclear field. Therefore, the void fraction profiles of intermittent flows have been measured at several axial locations in the METERO experiment. The results obtained at 40D from the inlet are given in Figure 5.4 and Figure 5.5.

In METERO experiment, a high void fraction zone exists near the upper wall but does not develop enough to make a plateau unlike literature studies since slug and plug bubbles generated in the present

study are smaller than the ones in the literature. It comes from the fact that our gas flow rates are quite lower. However, the transition zone and zero-void-fraction plateau have been observed. Regardless of the width of the high void fraction zone, it is important to state that the void fraction profiles in the METERO experiment and in the literature have similar trends.

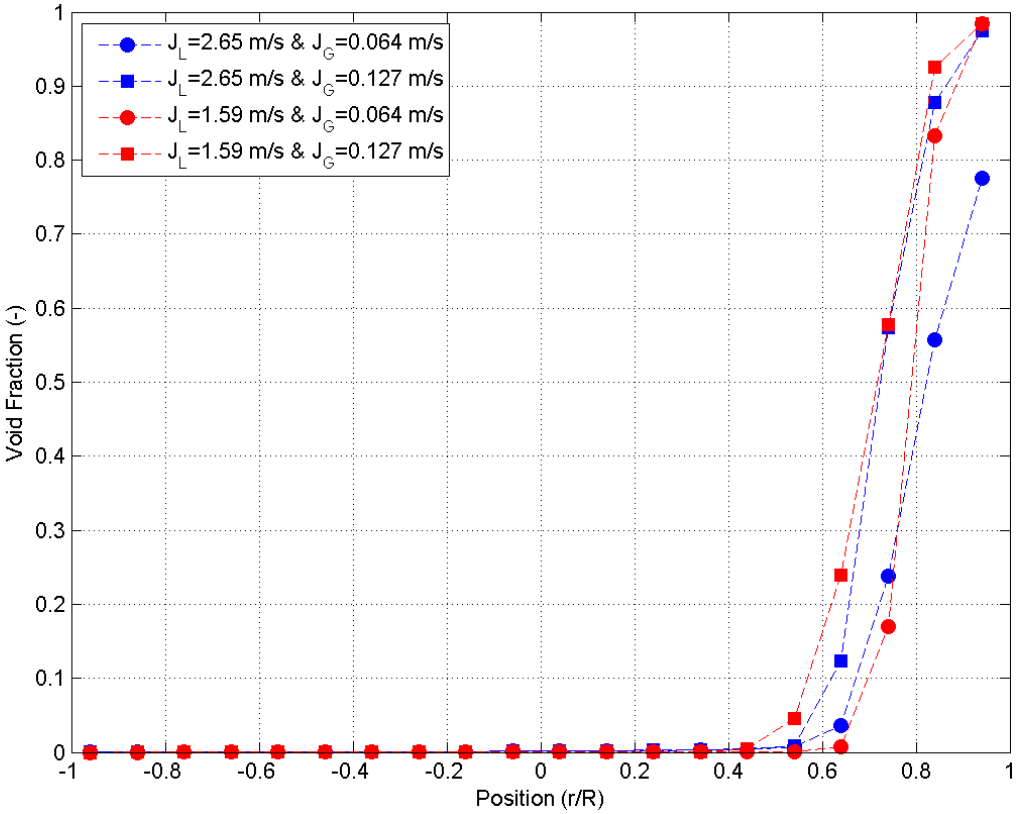

Figure 5.4 - Void fraction profiles of the METERO experiment for intermittent flows at 40D

As seen from the results (Figure 5.4), an increase in the J_G for fixed J_L increases the void fraction in the upper part of the test section. In the lower part, as seen in Figure 5.5, namely zero-void-fraction zone, the effect of J_G is very slight or negligible. In addition, increasing J_G also decreases the thickness of the zero-void-fraction zone since more bubbles rise to the upper part.

Once J_G is kept constant and J_L is changed, it is observed that the void fraction decreases with an increased J_L in the upper part. The opposite effect is observed in the lower part such that the void fraction increases in the lower part as seen in Figure 5.5. This effect can be explained by the increase of turbulence which homogenizes the gas phase in the section.

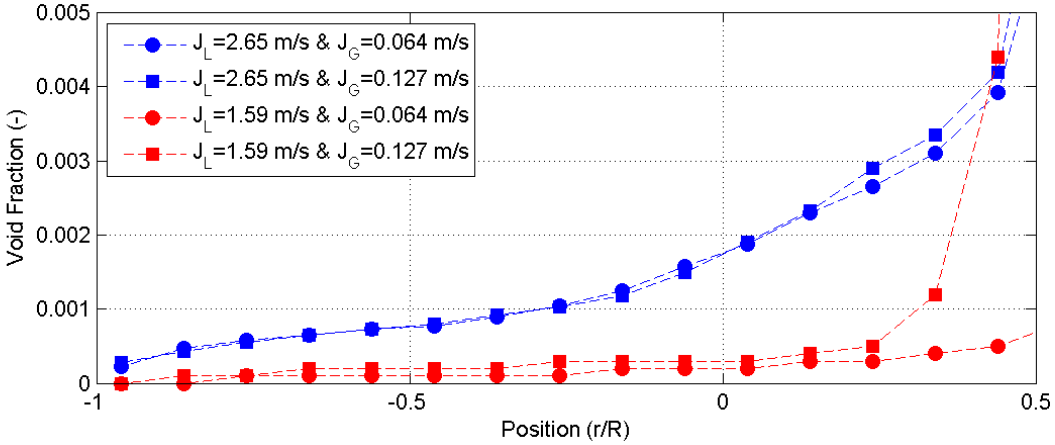

Figure 5.5 - Zoom of Figure 5.4 for *-1<r/R<0.5*

5.1.2 Bubble size

The chord length profiles acquired at 40 diameters downstream for various J_L and J_G generating intermittent flows are represented in Figure 5.6. The profiles are given in linear-logarithmic scale in order to observe the changes in the lower part of the test section.

As seen from Figure 5.6, in the upper part, the chord length values are increasing when J_G is increased at a fixed J_L. On the other hand, when J_L is increased at constant J_G, the turbulence is increased in the flow. As a result, the chord length values start to decrease because of turbulent break-up enhancement. These results show that the chord length, consequently bubble size, increases rapidly at the upper part of the test section when the flow becomes intermittent.

In the lower part of the test section, the chord length profiles have homogenous distribution which is actually observed in the fully developed turbulent flows such as dispersed bubbly flow. In addition, it is observed that J_L has a significant effect on the chord length while the influence of J_G is negligible in this region, $-1<r/R<0$. Thus, the greater the liquid flow rate is, the greater values chord lengths have. This behavior was also observed in dispersed bubbly flow and it is a result of the increased turbulence which prevents sedimentation process of the small bubbles.

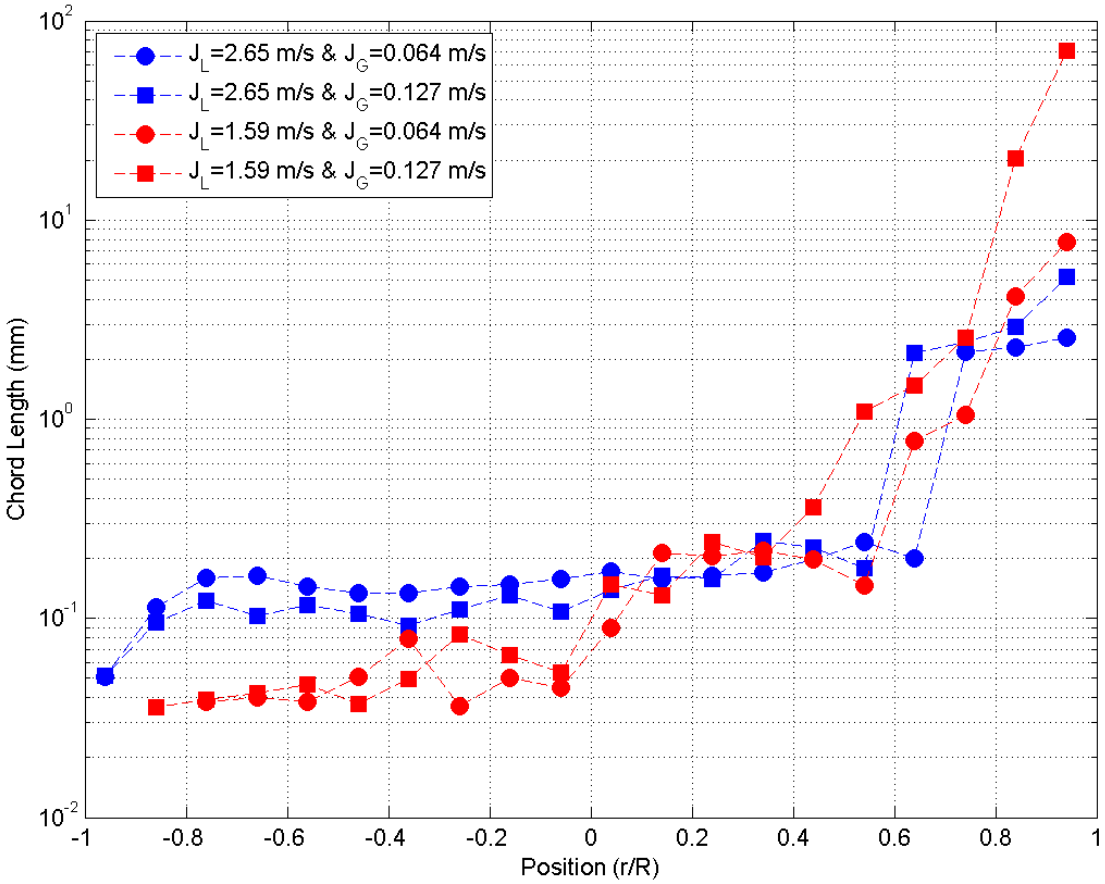

Figure 5.6 - Chord length profiles of the METERO experiment for intermittent flows at 40D

In conclusion, we have noted that a significant proportion of the bubbles migrate to the upper part of the test section because the buoyancy force is dominant in intermittent flows. Consequently, the bubbles accumulate in the upper part and since the turbulent forces are lower, coalescence of the bubbles takes place and elongated bubbles or air plugs are generated. This brings out the greater chord length values observed in the upper part. Furthermore, very small bubbles which are captured in the lower part due to the turbulent forces generate similar profiles that observed in the dispersed bubbly

flows. Thus, the flow could be split into two parts such as buoyancy dominant zone and turbulent dominant area which has been defined as gas-liquid coordinated flow introduced by Ekambara et al. (2008). This behavior was also reported by Lewis et al. (2002).

5.1.3 Interfacial area

Interfacial area concentration in horizontal intermittent flows has been described in the literature. In our study, we rely on the studies of Riznic & Kojasoy (1997) which is focused on the local interfacial parameters in horizontal slug flow. The interfacial area concentration profile measured by the authors for J_L=1.65 m/s and J_G=1.10 m/s and at an axial location of 253 diameters is given in Figure 5.7. As seen in the figure, the interfacial area concentration on the upper part of the test section (*0<r/R<1*) is constant and forms a plateau in this region which represents slug bubble. In addition, it is observed that interfacial area concentration is increasing at the left of the plateau since small bubbles take place below the slug bubble increasing the interfacial area concentration. Furthermore, left to the peak, the interfacial area concentration decreases rapidly along the lower part of the test section.

The tendency given in the literature has also been observed in the METERO experiment. The measured interfacial area concentration at 40 diameters for various flow rates is given in Figure 5.8. Moreover, the zoomed results for *-1<r/R<1* are given in Figure 5.9. It is observed that the trends are similar to those described in the literature, except for J_L=2.65 m/s and J_G=0.064 m/s which correspond to the transition between dispersed bubbly and intermittent flow. A peak value in each interfacial area profile is present for each test conditions. As explained before, these peak values represent the small bubble layer located below the slug or plug bubble. Since the air flow rates in our study are lower than the ones in the literature, the thickness of the slug or plug bubble layers are lower. Subsequently, the position of the peak is also shifted to the upper part of the test section.

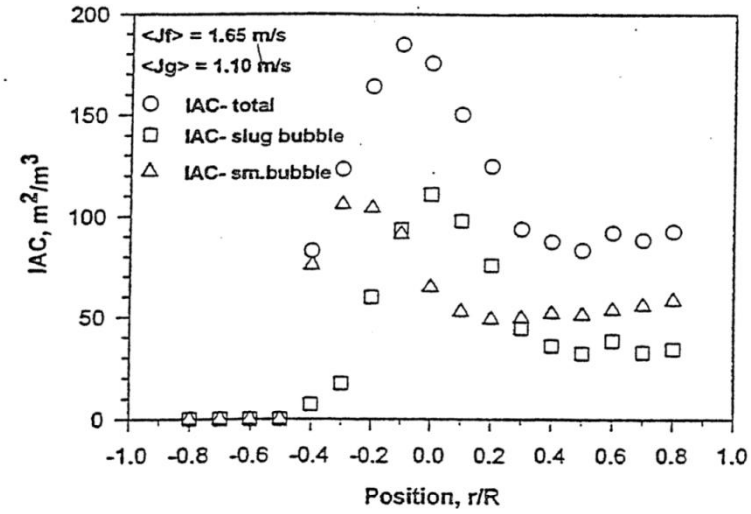

Figure 5.7 - Interfacial area concentration distribution measured at 253D for J_L=1.65 m/s and J_G=1.10 m/s (Riznic & Kojasoy, 1997)

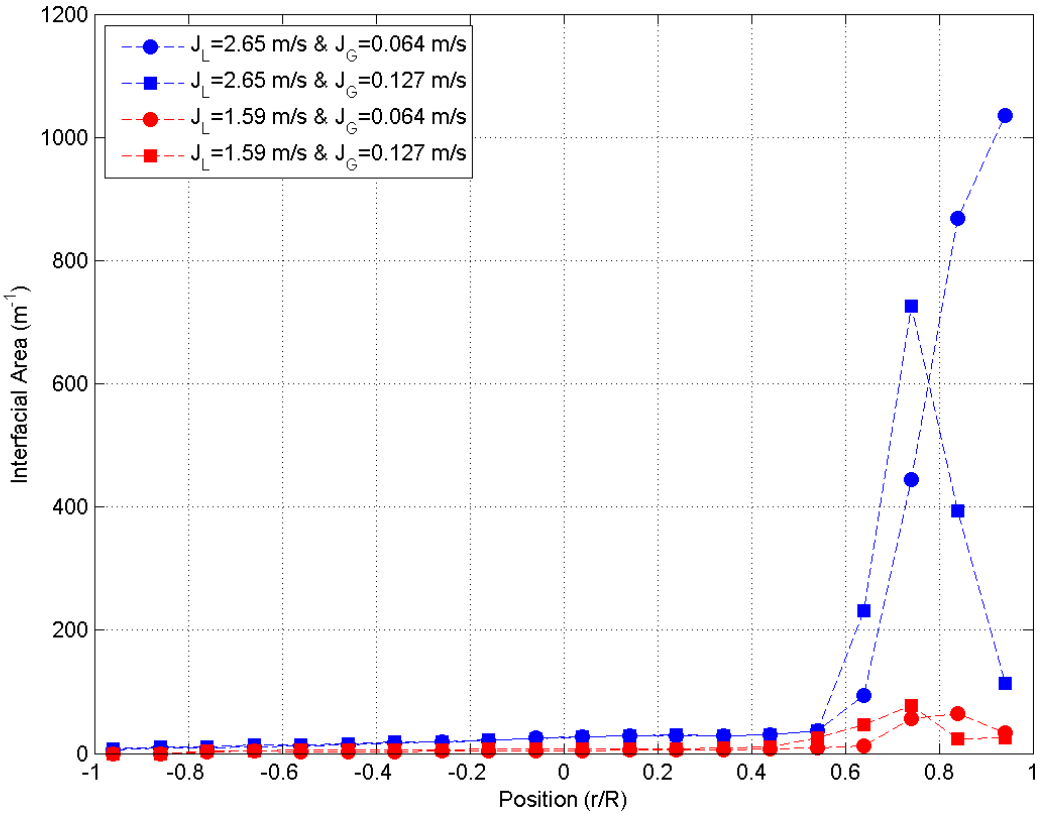

Figure 5.8 - Interfacial area profiles of the METERO experiment for intermittent flows at 40D

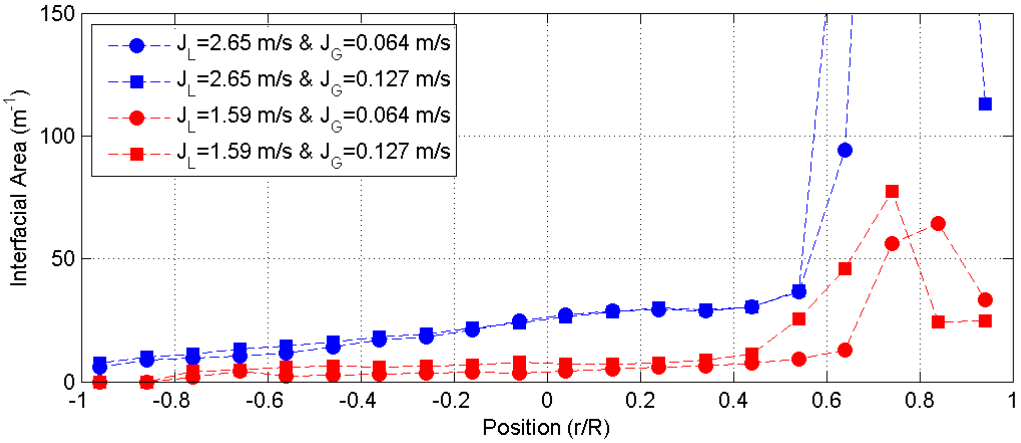

Figure 5.9 - Zoom of Figure 5.8 for *-1<r/R<1*

In our results, it is observed that interfacial area is increasing with increased J_L while J_G is kept fixed. This is due to the break-up of the bubbles resulted from increased effect of turbulent forces. In addition, the thickness of the slug or plug bubble layer (plateau) is also decreased with an increase in J_L. In the case of fixed J_L and an increase in J_G, the position of the peak shifts towards the center. The plateau mentioned in the literature is clearly observed for the test condition J_L=1.59 m/s and J_G=0.127 m/s. However, the thickness of this plateau is lower than the one in the literature due to the lower gas flow rates, as mentioned before.

Left (below) the interfacial area peak, the profiles decrease sharply toward zero since only few small bubbles remain in the lower part. The zoomed profiles show that the interfacial area concentration varies from 0 m^{-1} to 30 m^{-1} in the lower part. These values are in the same order of magnitude than those measured for dispersed bubbly flows (See Section 4.1.3). Furthermore, the tendencies are also

similar to the ones of dispersed bubbly flows: the influence of J_G is very slight (maybe negligible) while J_L affects the interfacial area values in the lower part of the test section. These results support the gas-liquid coordinated flow definition introduced by Ekambara et al. (2008).

5.1.4 Axial bubble and liquid velocities

In the literature, the vertical profiles of velocity in intermittent flows have been studied by several authors. These studies can be categorized into two groups: instantaneous velocity distributions during the passage of a slug or plug (Sharma et al., 1998) (Figure 5.10) and time averaged velocity distributions in slug flows (Lewis et al., 2002) (Figure 5.11). These two types of studies have contributed significantly to understand the velocity distribution mechanism in intermittent flows. Instantaneous velocity profiles show that the velocity distribution in intermittent flows is strongly dependent on the slug passage. In other words, the profiles are different before, after and during the slug passage. On the other hand, time averaged velocity profiles draw attention to two different zones in the velocity profiles whose tendencies are similar to those observed in fully developed turbulent flows.

The time averaged axial velocity profiles of bubbles and liquid phase measured at 40D in the METERO experiment are presented in Figure 5.12. The results show that the bubble velocities are close but not equal to the liquid ones for all test conditions in intermittent regime. The differences between velocity profiles indicate that the small bubbles are slower than the liquid. This behavior is also reported by Nydal & Andreussi (1993) and Al-Turaihi (2013): the liquid in a water slug moves faster than the bubbles and the bubbles will be caught by the next elongated bubble.

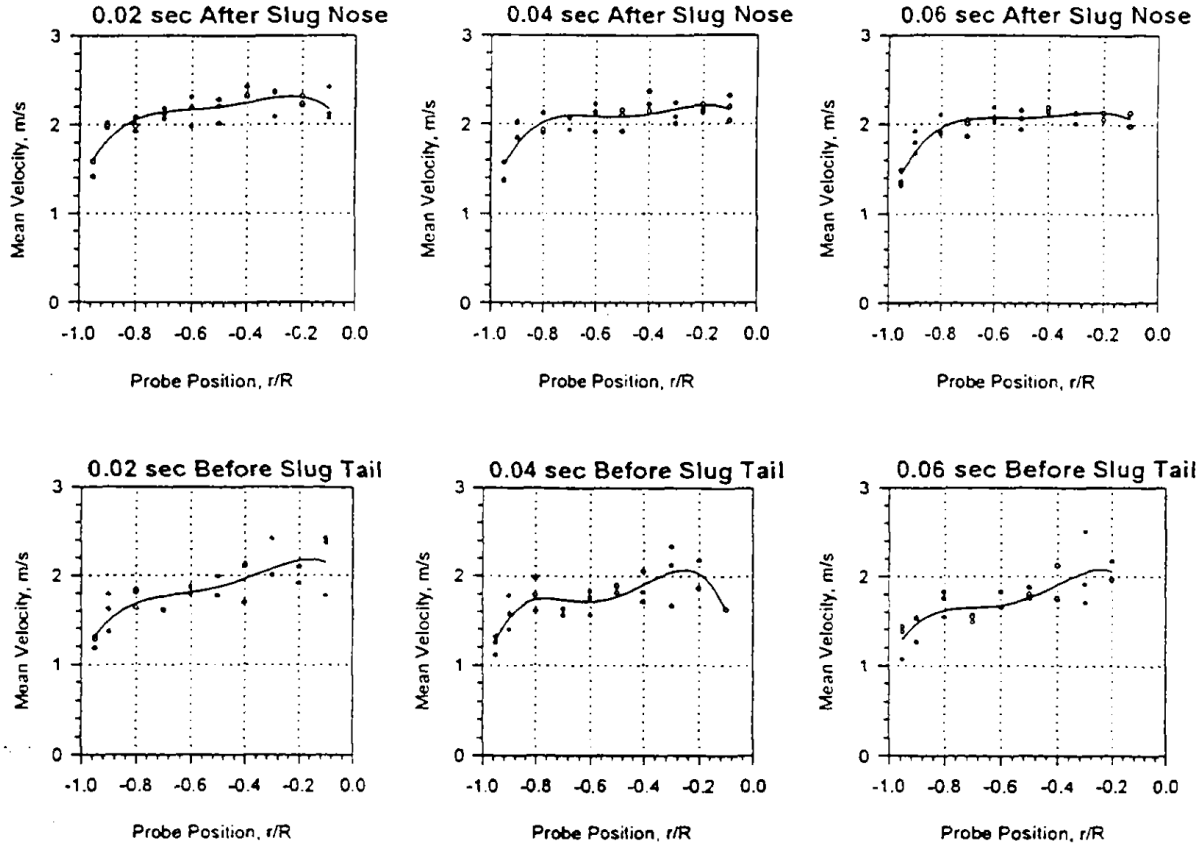

Figure 5.10 - A typical liquid velocity profile development in liquid layer below the gas slug (Sharma et al., 1998)

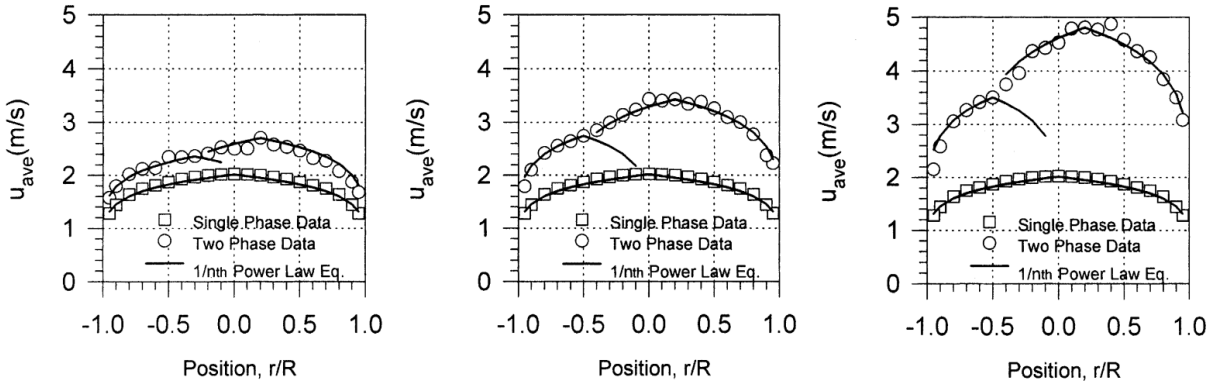

Figure 5.11 - Local axial mean velocity distributions measured at 253D for J_L=1.65 m/s & J_G=0.55, 1.10 and 2.20 m/s (Lewis et al., 2002)

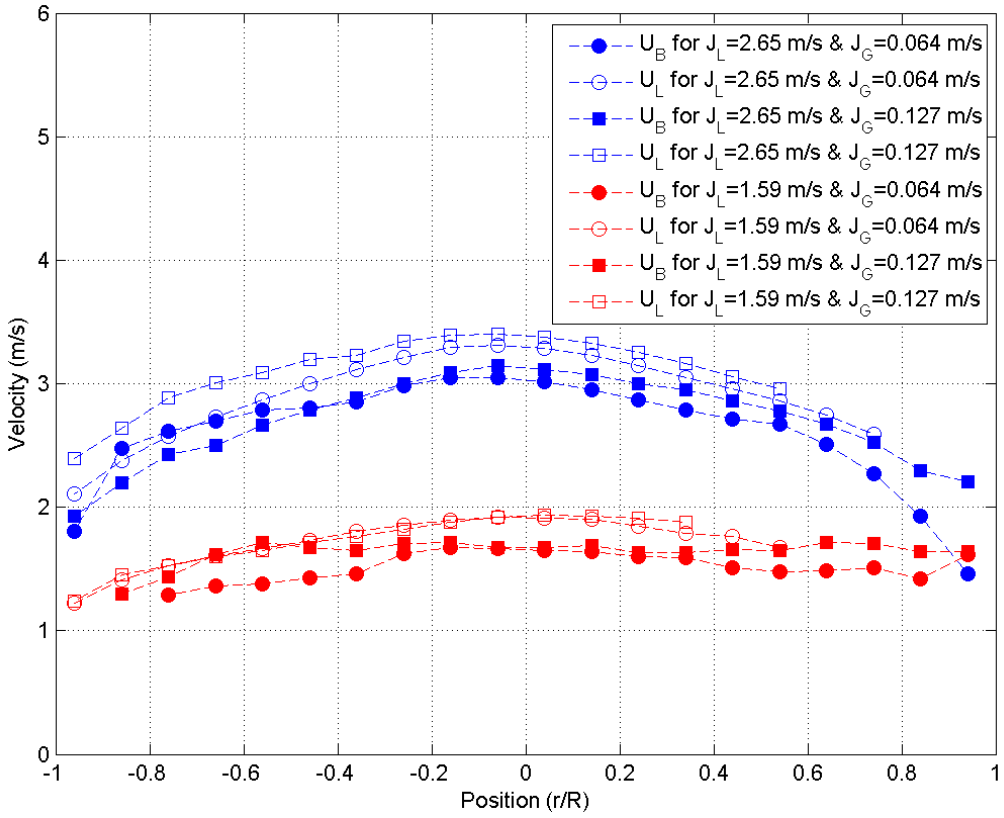

Figure 5.12 - Axial mean velocity profiles of the METERO experiment for intermittent flows at 40D

The position of the maximum velocity is close to the center of the test section in the intermittent flows while it is located in *-0.2<r/R<0* in dispersed bubbly flows (see Section 4.1.4). This behavior was observed Riznic & Kojasoy (1997) and Lewis et al. (2002). In order to understand this shift of the maximum velocity position, velocity profiles in liquid slugs (Figure 5.13) should be investigated. In horizontal slug flow, elongated bubbles which are located at the top of the pipe move faster than the liquid phase. Consequently, these bubbles accelerate the liquid phase in front of them and the velocity profiles have a maximum value at the upper part of the test section. This behavior is not observed only in the velocity profiles which are located in front of the elongated bubbles. Since the velocity is generally higher in the upper part of the test section, it is not surprising to observe time averaged mean velocity profiles with the maximum velocities located at the upper part of the pipe.

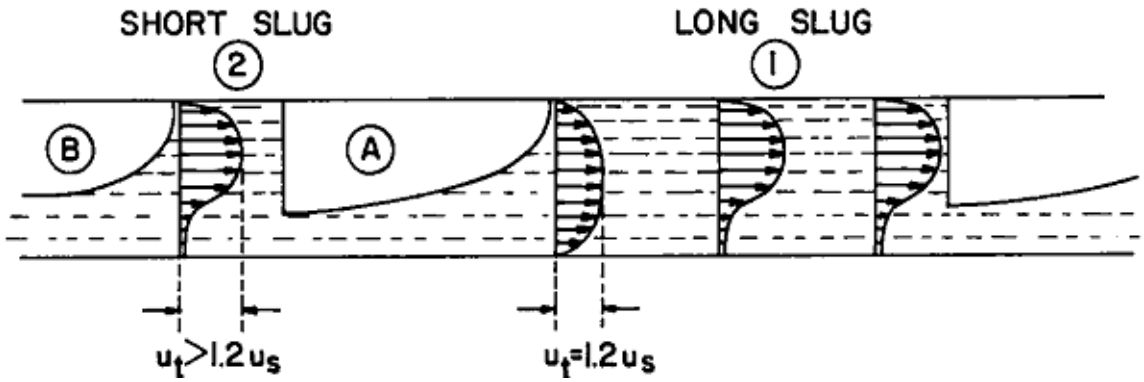

Figure 5.13 - Velocity profiles in liquid slugs (Taitel & Barnea, 1990)

The effect of J_L is significant on the bubble velocity profiles since liquid carries the bubbles. For J_L=2.65 m/s, the profiles are similar to the ones observed in dispersed bubbly flows (curved profile with a maximum near the center around *-0.2<r/R<0*). The profiles are more flat in the tests with J_L=1.59 m/s since the boundary layer is not well developed due to a lower liquid flow rate. The increase in J_G induces a bubble velocity increase essentially in the upper region where most of the gas migrates.

5.1.5 Turbulent kinetic energy

Turbulent kinetic energy profiles for various J_L and J_G representing intermittent flows are given in Figure 5.14. Similar to the profiles obtained in dispersed bubbly flows, the profiles also have a V-shaped distribution. However, the magnitude of the turbulent kinetic energy is less important in intermittent flows due to smaller liquid velocities and therefore velocity gradients.

The profiles obtained for J_L=2.65 m/s are the most interesting ones and are discussed here after. They all correspond to the plug flow regime. As a first remark, the change in J_G does not affect the turbulent kinetic energy in the central region (*-0.4<r/R<0.6*) but it does strongly in the bottom of the test section, near the wall. This influence is the consequence of the enhanced velocity gradient in this lower part. It comes from the reduction of the liquid flow cross section induced by the gas development. Furthermore, the profile increase sharply in the upper part because of the additional bubbles (plug) turbulence. As a final remark, the position of minimum turbulent kinetic energy is slightly decentered (*-0.1<r/R<0*).

The profiles associated with the lower liquid flow rate (J_L=1.59 m/s) correspond to slug flows. The sensitivity of the turbulent kinetic energy to J_G is observed only in the center of the pipe unlike the previous results (plug flow). We have no explanation for this deviation since the void fraction and the mean velocity profiles are both similar in the center of the test section. This deviation could be a measurement uncertainty.

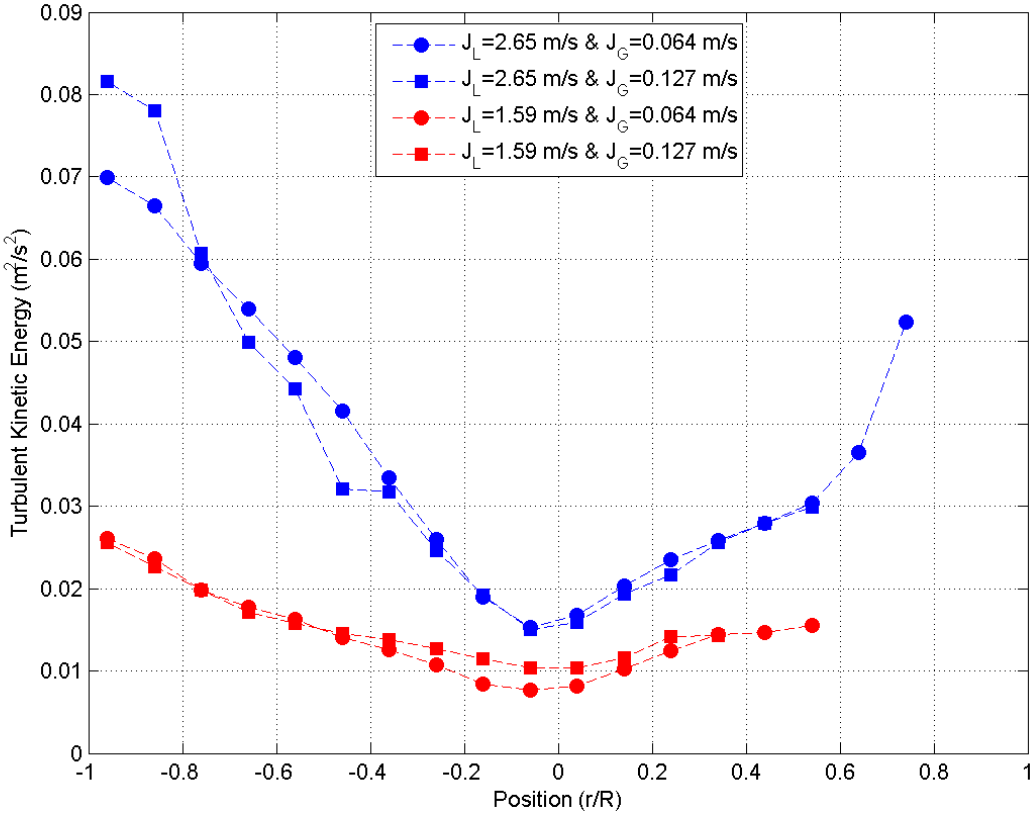

Figure 5.14 - Turbulent kinetic energy profiles of the METERO experiment for intermittent flows at 40D

5.2 Axial Evolution of Flow Quantities

The axial evolution of the intermittent flow characteristics for the test conditions given in the previous section (Table 5.1) will be studied in this chapter. Similar to the axial evolution for dispersed bubbly flows, the local characteristics have been measured at three axial locations, namely 5, 20 and 40 diameters downstream by using optical fiber probes and hot-film anemometry probes.

5.2.1 Void fraction

The axial evolutions of the void fraction profiles (in linear-logarithmic scale) measured for various J_L and J_G are given in Figure 5.15.

As seen from the results for J_L=2.65 m/s (plug flow), the void fraction distributions are homogenous at 5D, except near the upper wall where the bubbles migrate. While moving downstream, it is observed that the migration of bubbles has been almost completed around 20D since the void fraction profiles do not change between 20D and 40D. Most of the gas is then concentrated in the upper part, giving sharpened profiles.

The void fraction profile for slug flows (J_L=1.59 m/s) differs from the plug flow one essentially at 5D since the gas has already reached the upper part of the test section. This can be explained by the smaller turbulent mixing due to lower liquid flow rates in slug flow. Furthermore, the void fraction in the upper part of the pipe first increases until 20D and then decreases (Figure 5.16). In order to explain this phenomenon, several high-speed camera visualizations have been conducted at 20 and 40 diameters. Although an increase in the bubble size in the upper part of test section from 20D to 40D is

observed (Figure 5.17), the decrease of void fraction measured by the optical fiber probe is surprising. This can be explained by the definition of void fraction for optical probes.

The void fraction measured by the optical fiber probes is the temporal void fraction (based on the passage time of bubbles and so on bubble velocity), as formulated in Equation (1). In addition, it is strongly dependent on the flow topology: a small bubble occupies a small place and moves slowly while an elongated bubble occupies a wide space in the pipe but moves rapidly. At 20D, the optical probe gives a high void fraction corresponding to a mixture of numerous slow small bubbles and fast elongated ones. At 40D, the lower temporal void fraction corresponds mainly to elongated bubbles since lots of small ones have coalesced with the elongated ones. This may explain why the void fraction decreases from 20D to 40D.

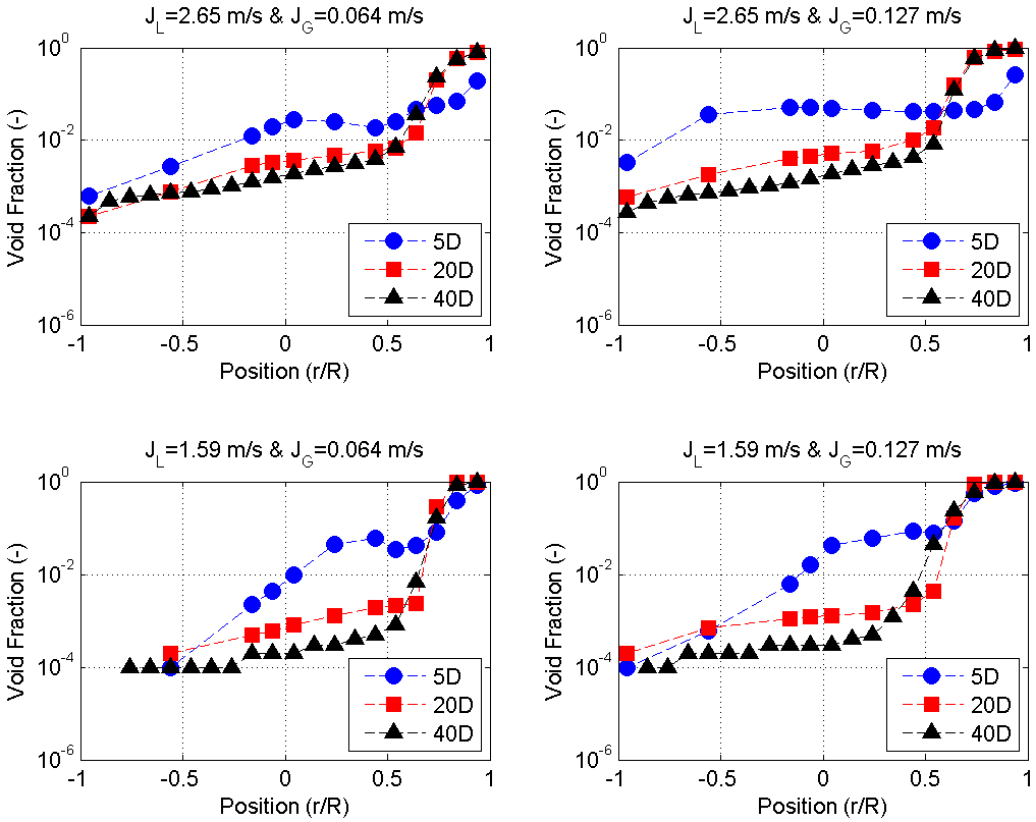

Figure 5.15 - Axial evolution of void fraction profiles for intermittent flows

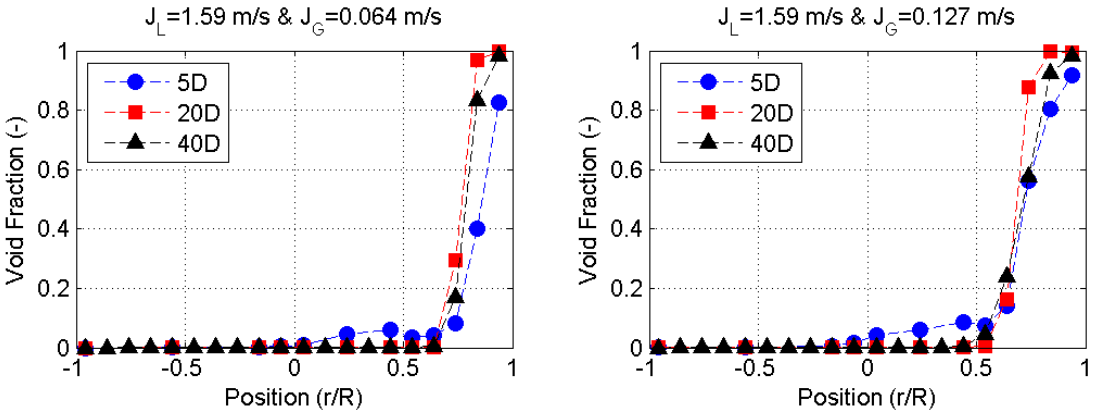

Figure 5.16 - Linear-linear representation of void fraction profile evolutions for J_L=1.59 m/s

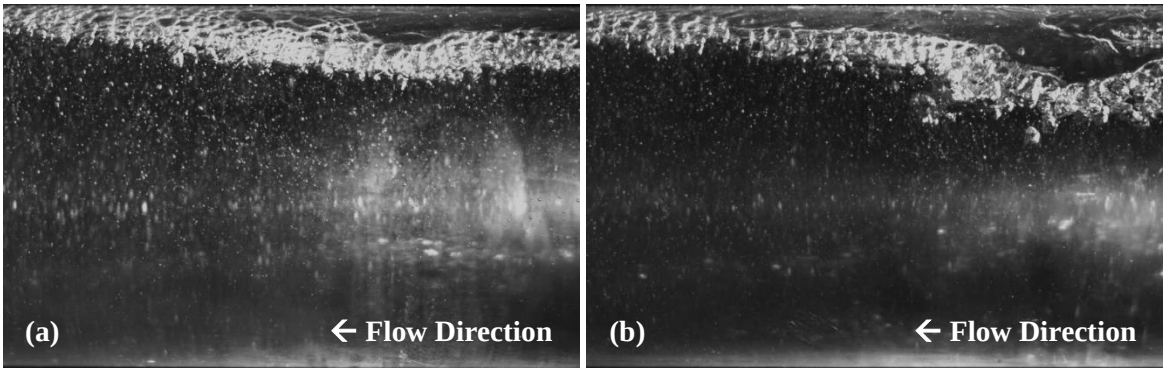

Figure 5.17 - Passage of a slug for J_L=1.59 m/s and J_G=0.127 m/s at axial locations 20D (a) and 40D (b)

5.2.2 Bubble size

The axial evolution of chord length profiles (represented in linear-logarithmic scale) measured for various J_L and J_G are given in Figure 5.18.

Depending on the liquid flow rate, two different tendencies are observed.

For the highest values of J_L, it is observed that the chord length values are increasing along the upper part of the pipe even more when the gas flow rate is important. This growth can be the result of the coalescence of the bubbles in this region. In the rest of the test section, the chord lengths do not change significantly. Probably, the bubbles very small enough to be able to migrate to the upper wall upon entry are captured in the liquid phase by the turbulence and remain at the same elevation. Moreover, the chord length distribution in this region is homogenous and the flow in this lower part can be considered as dispersed bubbly flow.

For the lowest values of J_L, the chord length is quite bigger than in the high J_L case, since the turbulence is reduced and so is the break-up while coalescence is promoted. In the lower part of the pipe, the chord length remains nearly constant like the previous case. In the upper part, the chord length evolves in a different way along the pipe. First, it increases until 20D and then it decreases. This tendency contradicts what is observed by high-speed camera visualizations (Figure 5.17): the bubble size at 40D at the top of the pipe is greater than the one observed at 20D.

In order to explain this contradiction, high-speed camera observations at 20D for J_L=1.59 m/s and J_G=0.127 m/s have been investigated in details. As seen in Figure 5.19, it is observed that a thick bubble layer has been located between two elongated bubbles and it has a structure similar to foam. In addition, there exist thin liquid films between the bubbles of this layer. Since the liquid film is very thin, it is not sufficient to wet the optical probe tips. As a result, our probes could not detect the end of an elongated bubble and consider the bubble layer as the continuation of elongated bubbles. This process continues until a liquid film which can wet the tips sufficiently is in contact with probe. Thus, this could explain the reason why the chord length values measured at 20D near the upper wall are greater than the ones observed at 40D.

In both high and low J_L cases, the flow can be divided into 2 parts: the lower one (¾ of the height approximately) where the turbulence is strong enough to "freeze" the chord length (mixing) and the higher one where the largest bubbles migrate all along the pipe and coalescence whatever the turbulence is.

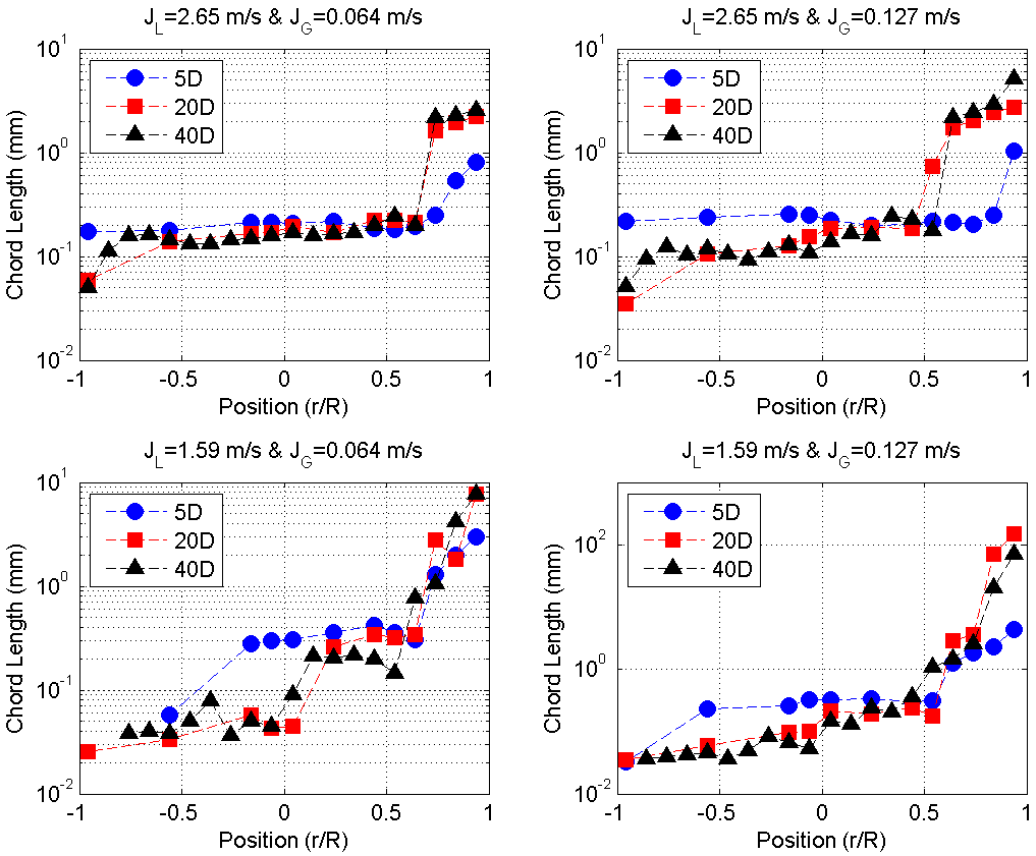

Figure 5.18 - Axial evolution of chord length profiles for intermittent flows

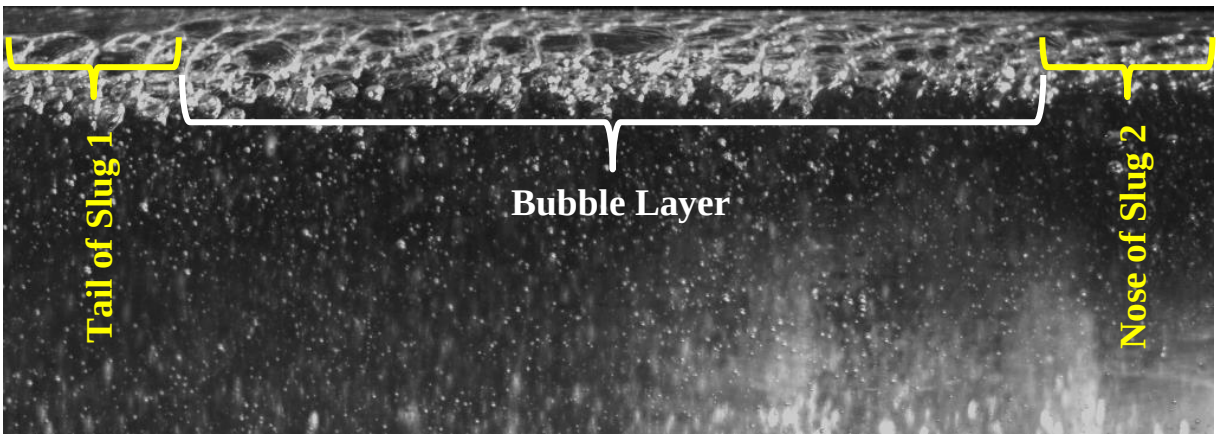

Figure 5.19 - Bubble layer between two slugs observed at 20D for J_L=1.59 m/s and J_G=0.127 m/s

5.2.3 Interfacial area

Interfacial area concentration profiles measured at 3 axial location for various liquid and gas flow rates are given in Figure 5.20. The profiles are represented in linear-logarithmic scale in order to have a better observation at the lower part of the pipe.

Likely in the chord length analysis, the flow can be split into two parts: the bottom one corresponding to at least ¾ of the pipe height and the rest above. In the bottom part, the interfacial area concentration (IAC) is very low and decreases slightly from 5D to 40D since bubbles rise and maybe some coalescence take place (we have no evidence of coalescence in the high-speed camera observations). In the upper part, IAC is very high, drawing a peak, and evolve differently depending on the liquid flow rate. For high ones, the peak first increases from 5D to 20D due to the rising bubbles and then

decreases due to coalescence process. Depending on the gas flow rate, the peak can be more or less close to the upper wall. The peak moves down when gas presence is increased since larger bubbles are created near the upper wall. For low liquid flow rate case, the peak disconnects from the upper wall and decreases rapidly until vanishing at 40D since turbulence is less important and buoyancy with coalescence is thus more efficient.

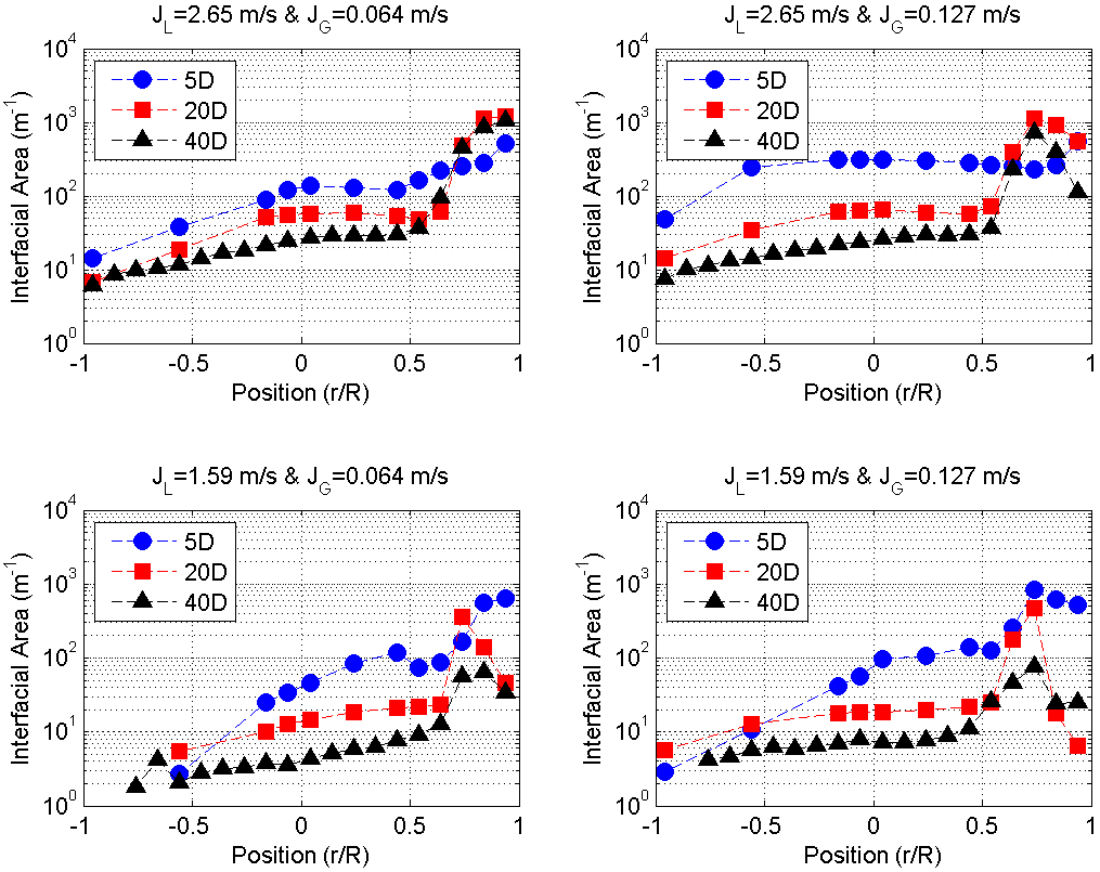

Figure 5.20 - Axial evolution of interfacial area profiles for intermittent flows

5.2.4 Axial bubble and liquid velocities

Evolution of the mean bubble and liquid velocity profiles measured at three different axial locations (5, 20 and 40D) are given in Figure 5.21 and Figure 5.22, respectively.

As seen from the results, the velocity profiles of bubbles and liquid phase measured for J_L=2.65 m/s have similar tendencies to what is observed for dispersed bubbly flows. At 5D, the effect of elbow on bubble and liquid phase velocities is observed clearly for J_G=0.064 m/s. Although this effect could not be observed for J_G=0.127 m/s, the velocity distributions at 5D are flat in both tests and this shows that the boundary conditions are not developed at 5D.

The results at 20D point out that the boundary conditions are developing at this location. As a result, the velocity is higher in the center of the test section and it decreases by approaching to the walls. The velocity profiles acquired at 40D have a reverse U-shape which has been also observed for dispersed bubbly flows; however, the profiles are more flat compared to the ones of dispersed bubbly flows. In both bubble and liquid phase velocity profiles, the position of the maximum average velocity is shifted to the center of the test section which has been mentioned in Section 5.1.4. In all profiles for J_L=2.65 m/s, it is observed that the velocity of the bubbles are slower than the liquid phase velocities. In addition, it is obvious that the axial velocity of the bubbles is determined by the liquid velocity.

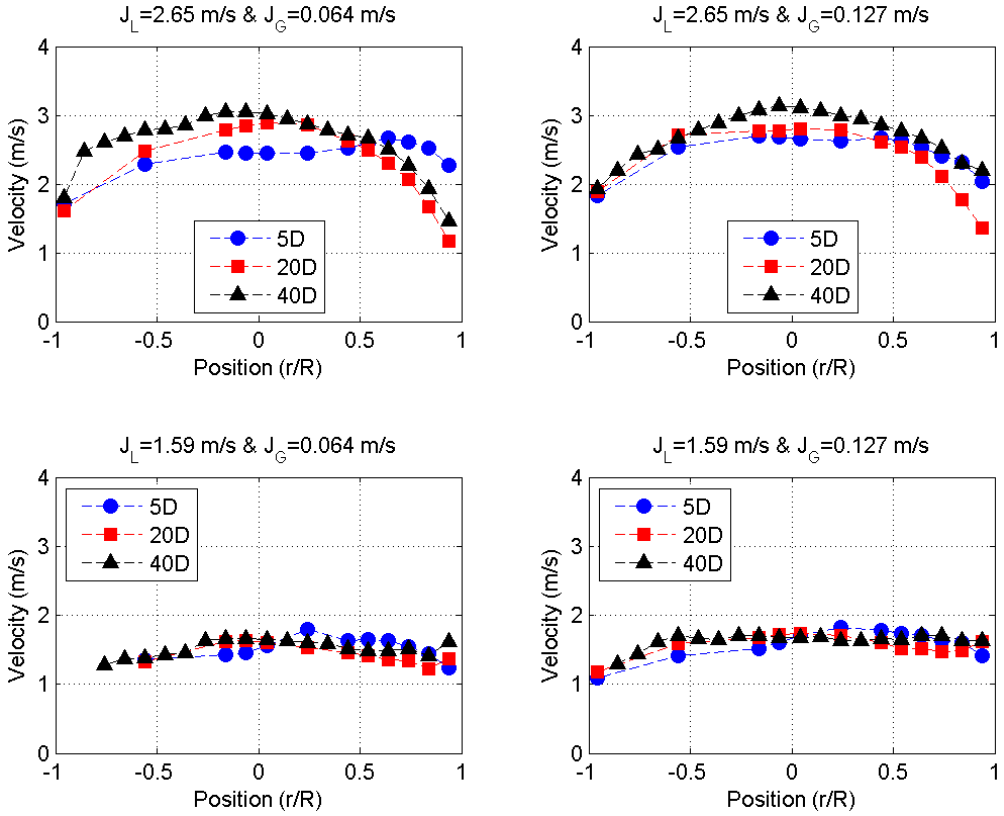

Figure 5.21 - Axial evolution of axial mean bubble velocity profiles for intermittent flows

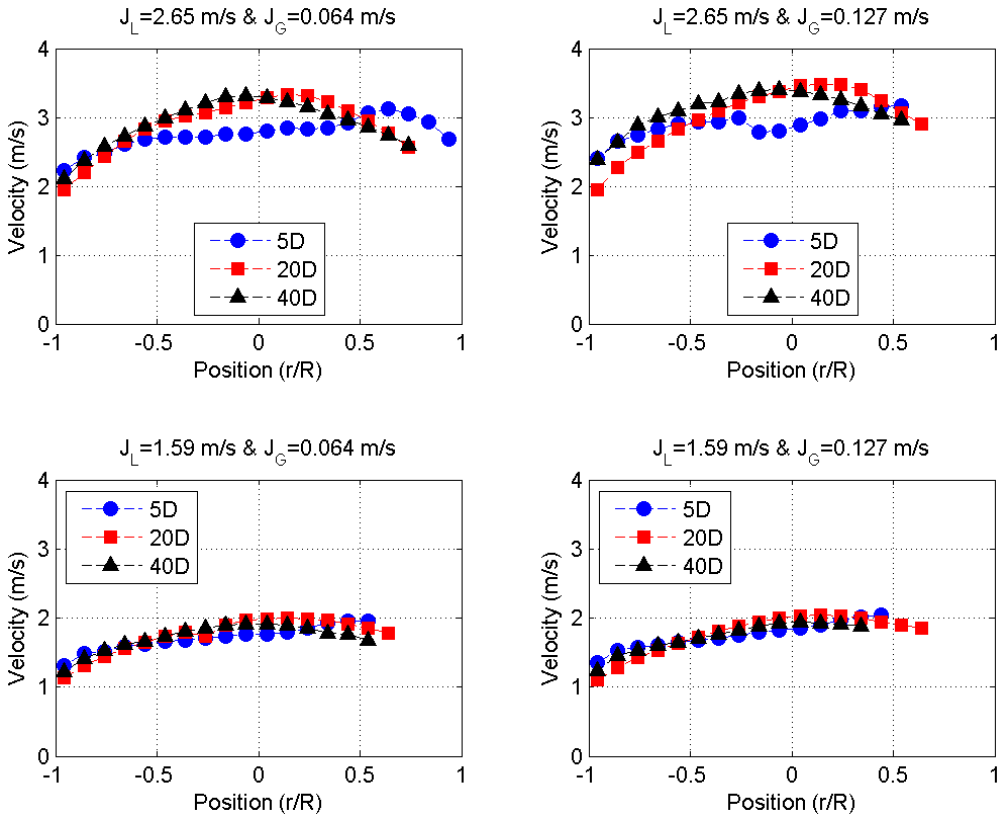

Figure 5.22 - Axial evolution of axial mean liquid velocity profiles for intermittent flows

Concerning the test with J_L=1.59 m/s, the velocity profiles at different axial locations show no significant change with respect to J_L=1.59 m/s case. The profiles of bubbles and liquid phase become

flat and it can be concluded that the boundary conditions are not developed in these flows (slug flows). Similar to the test with J_L=2.65 m/s, the average velocity of the bubbles still derived by the liquid phase and the bubble velocities are slower than the liquid ones. In addition, the velocity decreases in the regions close to the pipe walls due to the wall friction.

5.2.5 Turbulent kinetic energy

Axial evolutions of the turbulent kinetic energy (TKE) profiles for various J_L and J_G are represented in Figure 5.23.

As seen from the figure, the TKE profiles of J_L=2.65 m/s and J_G=0.064 m/s are similar to the ones observed for dispersed bubbly flows. At 5D, the profile is more flat compared to the others measured at 20D and 40D and it increases from the positions close to the pipe walls. The major difference from dispersed bubbly flow is the rise of the TKE on the upper part of the test section. It rises after *r/R*=0.5 due to the contribution of the bubble layer to the turbulence. At 20D, boundary conditions started to be developed. As a result, the TKE starts to shape with a high level near the wall where shear stress is significant and a low level at the center where the production is quite low. Due to the presence of the bubble layer at the top of the test section and its mixing effect, TKE increases sharply in the upper part. When approaching 40D, the distribution of the TKE is almost symmetric (maximum at *-0.1<r/R<0*).

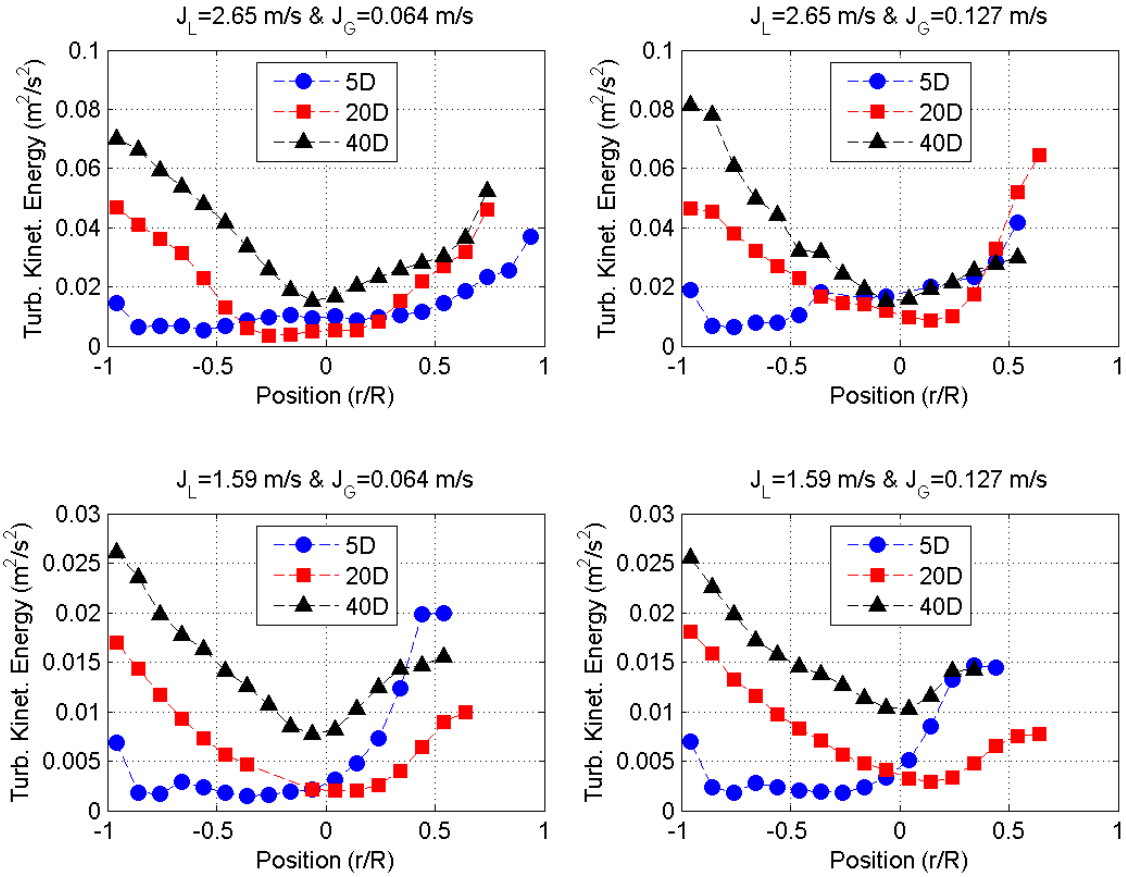

Figure 5.23 - Axial evolution of turbulent kinetic energy profiles for intermittent flows

When the J_G is increased to 0.127 m/s for J_L=2.65 m/s, there are changes in the TKE profiles coming from the plug flow. By increasing the thickness of the bubble layer, the flat part of the profile reduces at 5D and vanishes at 20D. Moreover, because of the existence of greater bubble layer in the flow, the TKE increases sharply at *r/R*=0.34. As a result, the minimum TKE is decentered to *r/R*=0.14. Due to

incapability of hot-film anemometry probes (see Section 3.2.2.1), the TKE could not be measured in the upper part (*0.64<r/R<1*). In the lower part, the TKE increases rapidly since the velocity gradients are increased in this region because of the bubble existence in the upper part which reduces the liquid flow cross section.

Once the liquid flow rate is decreased to 1.59 m/s, the flow enters into the so-called slug flow regime and the TKE profiles have different distributions as seen from Figure 5.23. At 5D, the flow is not established and the TKE is very asymmetric with a very high level near the top where the two-phase flow effect (mixing) is the strongest. From 20D to 40D, the profile keeps a similar shape with high level of energy near the wall where production occurs (wall friction and bubble effect) and a quite lower level near the center where dissipation is only balanced by diffusion from the sides. The profiles rise while the flow and the production of turbulence are establishing.

5.3 Conclusion

Similarly to the previous chapter, the flow quantities are studied locally and axially in this chapter. The results show that the buoyancy force is dominant in the intermittent flows. Furthermore, the turbulent mixing is decreased due to the lower liquid flow rates in this flow regime. Consequently, in the upper part of the test section, the accumulation and coalescence of the bubbles, which generates bigger elongated bubbles, are observed. In the lower part (*-1<r/R<0*), only very small bubbles are captured by turbulent forces and the distributions of void fraction, chord lengths and interfacial area are similar to what is observed in the dispersed bubbly flows. Thus, we could split the flow into two parts such as buoyancy dominant zone and turbulence dominant area. This type of flows has been defined as gas-liquid coordinated flow by Ekambara et al. (2008). The mean velocity profiles indicate that the small bubbles are slower than the liquid phase in intermittent flows. Moreover, the position of the maximum velocity is shifted to the center of the test section because of the higher liquid velocities in the upper part due the acceleration by the faster elongated bubbles. This behavior is also observed in the turbulent kinetic energy profiles as the shift of the minimum TKE position to the center.

Bubble migration toward top, accumulation and coalescence of the bubbles are indicated by the axial evolutions of void fraction, chord length and interfacial area concentration. Furthermore, the high-speed camera visualizations performed for elongated bubbles at 20D and 40D also draw attention to the coalescence. Axial evolution of velocity profiles show that the velocity of the bubbles is determined by the liquid phase; however, bubbles move slower than the liquid phase. For higher J_L, the velocity profiles at 40D are similar to what is observed in the dispersed bubbly flows. In the case of lower J_L, the velocity profiles do not change significantly from 5D to 40D. From the profiles of statistically averaged liquid velocity, we observe an important evolution between 5D and 20D, and then stabilization between 20D and 40D despite the fact that the flow is intermittent. On the other hand, the turbulence field evolves continuously. It can be an effect of the intermittency of the flow.

CHAPTER 6

DIMENSIONLESS FLOW REGIME MAPS

6 DIMENSIONLESS FLOW REGIME MAPS

In Chapter 1, a flow regime map (Figure 1.8) presented in liquid and gas velocity coordinates is given for the METERO experiment. This flow regime map was obtained from high speed camera observations by Bottin (2010). Although this flow regime map is valid for the METERO experiment, it cannot be applied for the other experiments dedicated to the horizontal flow regime studies since it is strongly dependent on the experimental setup configuration (e.g., pipe diameter, pipe cross section, etc.). Thus, the necessity of a flow regime map with dimensionless coordinates is significantly important.

For this purpose, two new flow regime maps with dimensionless coordinates are presented in this chapter. The first flow regime map is derived from the studies of Taitel & Dukler (1976) and Dukler & Taitel (1986). This map has a semi-analytical approach to the horizontal two-phase flow regimes and transitions since the authors couldn't access the local measurements of flow characteristics. The second map is similar to the first one; however, it is derived from the section averaged parameters of the local flow characteristics and it brings a mechanistic approach to the flow regime study. These two-flow regime maps and their transition criteria could contribute to the modeling and simulation of air/water two-phase flows.

6.1 Taitel & Dukler X-T Flow Regime Map

6.1.1 Introduction

In the literature, Taitel & Dukler (1976) and Dukler & Taitel (1986) have investigated flow regimes and transitions for horizontal pipe flows by developing a semi-analytical model. The authors have introduced a generalized flow regime map with dimensionless coordinates for various flows in horizontal pipes, as seen in Figure 6.1.

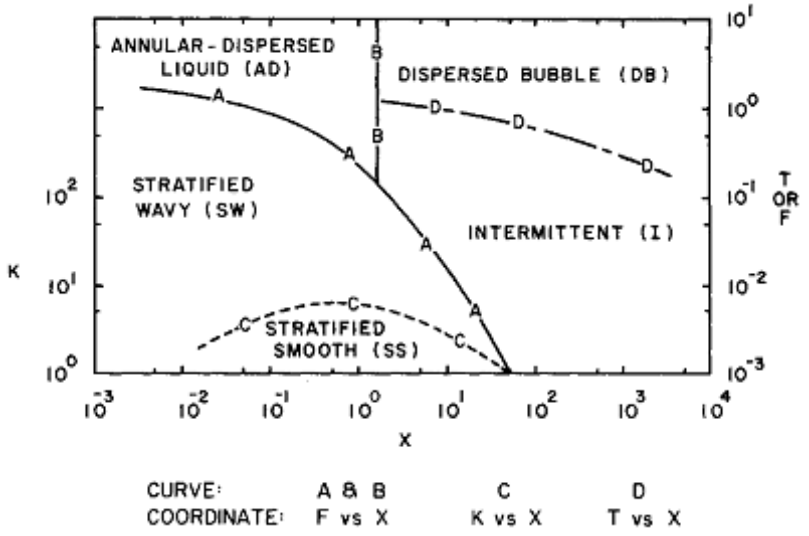

Figure 6.1 - Generalized flow regime map for horizontal two-phase flow (Taitel & Dukler (1976) and Dukler & Taitel (1986))

In the flow regime map of Taitel & Dukler (1976) and Dukler & Taitel (1986), the transitions are represented with different curves and different coordinates. Furthermore, for the *D* curve which represents the transition between the intermittent flows and dispersed bubbly flows, the authors proposed to use the dimensionless coordinates *X* (Lockhart-Martinelli parameter) and *T*

(Dimensionless dispersed bubble flow parameter). In this study, our focus is to investigate the transitions between intermittent flows and dispersed bubbly flows. Thus, these dimensionless coordinates are taken into account in the flow regime map calculations.

6.1.2 Calculation of dimensionless coordinates

The dimensionless coordinates X and T can be calculated by the given formulas where $C_G = C_L = 0.046$ and $n = m = 0.2$ for the turbulent flows:

$$X^2 = \frac{\left(4C_L/D\right)\left(u_{LS}D/\upsilon_L\right)^{-n}\rho_L\frac{u_{LS}^2}{2}}{\left(4C_G/D\right)\left(u_{GS}D/\upsilon_G\right)^{-m}\rho_G\frac{u_{GS}^2}{2}} \tag{18}$$

$$T^2 = \frac{\left(4C_L/D\right)\left(u_{LS}D/\upsilon_L\right)^{-n}\rho_L\frac{u_{LS}^2}{2}}{\left(\rho_L-\rho_G\right)\cos\beta\, g} \tag{19}$$

In addition, the authors stated that the transition from intermittent flows to dispersed bubbly flows occurs when the turbulent fluctuations are superior to the buoyant forces which tend to keep the gas phase at the top of the test section. This phenomenon was formulated in a dimensionless form as Equation (20).

$$T^2 \geq \frac{8\tilde{A}_G}{\tilde{S}_i\tilde{U}_L^2\left(\tilde{U}_L\tilde{D}_L\right)^{-n}} \tag{20}$$

The terms in the right side of Equation (20) are depending only on the ratio of the liquid height to the pipe diameter, h_L/D. The right side of Equation (20) will be called as kappa (κ) in this study hereinafter. The terms of κ can be calculated by the following formulas given by Taitel & Dukler (1976) and Dukler & Taitel (1986):

$$\tilde{h} = h_{Liq}/D \tag{21}$$

$$\tilde{A}_G = 0.25\left[\arccos\left(2\tilde{h}-1\right)-\left(2\tilde{h}-1\right)\left(1-\left(2\tilde{h}-1\right)^2\right)^{0.5}\right] \tag{22}$$

$$\tilde{A} = 0.25\pi \Rightarrow \tilde{A}_L = \tilde{A} - \tilde{A}_G \tag{23}$$

$$\tilde{S}_i = \left(1-\left(2\tilde{h}-1\right)^2\right)^{0.5} \tag{24}$$

$$\tilde{S}_L = \pi - \arccos\left(2\tilde{h}-1\right) \tag{25}$$

$$\tilde{U}_L = \tilde{A}/\tilde{A}_L \tag{26}$$

$$\tilde{D}_L = 4\tilde{A}_L/\tilde{S}_L \tag{27}$$

For the calculation of equations (21) to (27), the height of the liquid phase (h_{Liq}) is required. However, it is not easy to measure the liquid height directly in the test section, i.e. no instrumentation to measure

liquid height is used in the present study. In order to obtain the liquid height, the local void fractions measured by the optical fiber probes at 40D have been taken into account. The test section is split into horizontal layers with equal heights where the radial measurement locations are centered and it is assumed that the measured void fraction is distributed homogeneously in each horizontal layer. Furthermore, these measurement results have been averaged by using Equation (28), each horizontal layer is multiplied by its own void fraction value and their sum is divided by the total area of the test section. A theoretical collapsed liquid height for each test has been calculated trigonometrically as in Figure 6.2.

$$\langle \alpha \rangle = \frac{\sum A_k \alpha_k}{A_T} = \frac{A_G}{A_G + A_L} \tag{28}$$

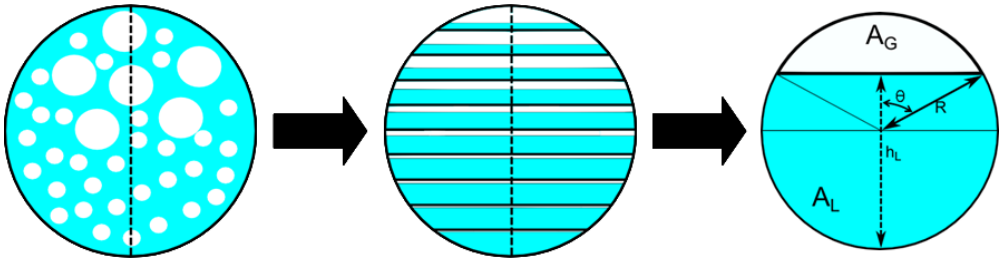

Figure 6.2 - Collapsed liquid height diagram

6.1.3 Results and discussion

The dimensionless coordinate numbers have been calculated by using equations (18) to (28) for each test condition and a new flow map for the METERO experiment has been generated by using these dimensionless coordinates as represented in Figure 6.3.

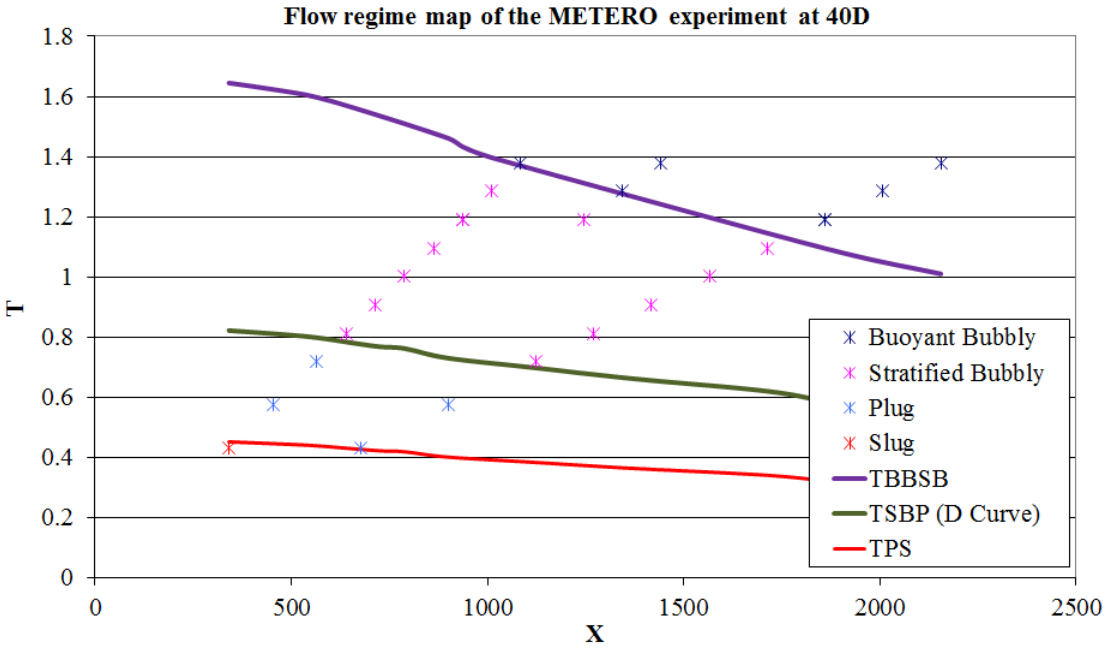

Figure 6.3 - Dimensionless flow regime map of the METERO experiment at 40D

Flow regime transitions have been investigated profoundly to validate Equation (20) (D curve) and this equation can be rewritten as in Equation (29). Furthermore, the left side of Equation (29) has been calculated for each test in a detailed investigation and the following correlations which lead to the new criteria to define flow regime transitions have been pointed out (Equations (30) to (33)).

$$CT = \frac{T}{\sqrt{\kappa}} \geq 1 \quad \rightarrow \quad Dispersion \tag{29}$$

$$\frac{T}{\sqrt{\kappa}} \geq 2 \quad \rightarrow \quad Buoyant \quad Bubbly \quad Flow \tag{30}$$

$$2 > \frac{T}{\sqrt{\kappa}} \geq 1 \quad \rightarrow \quad Stratified \quad Bubbly \quad Flow \tag{31}$$

$$1 > \frac{T}{\sqrt{\kappa}} \geq 0.5 \quad \rightarrow \quad Plug \quad Flow \tag{32}$$

$$0.5 > \frac{T}{\sqrt{\kappa}} \quad \rightarrow \quad Slug \quad Flow \tag{33}$$

In this new flow map, the transitions between flow regimes are represented with three lines derived from high speed camera observations:

- Transition from buoyant bubbly flow to stratified bubbly flow (TBBSB): purple line
- Transition from stratified bubbly flow to plug flow (TSBP): green line
- Transition from plug and slug flow (TPS): red line

In conclusion, a new flow regime map for the METERO experiment at an axial location of 40D has been generated by using dimensionless coordinates proposed by Taitel & Dukler (1976) and Dukler & Taitel (1986). In this map, the experimental points (measurements of velocity, void fraction… by using probes) are represented by stars while the regime transitions (observation with camera) are given by solid lines. This new map is in good agreement with the authors' one in term of the transition from intermittent flows to dispersed bubbly one (D curve, green line). In addition, this new map is independent of the experimental setup conditions. Thus, the flow regimes represented in the new map can be generated in different experimental setups if only the exact dimensionless coordinates for each flow regime are established. Moreover, the flow regime transitions are represented with mechanistic criteria instead of visual observations.

The major drawback of this flow map may be the measurement of the liquid height in the test section which has not been performed directly. Instead of direct measurement of the height, local void fraction values at 40D which include some measurement uncertainties have been used in the liquid height calculations. In addition, a homogeneous distribution of the local void fraction in the horizontal layer has been assumed in the calculations; however, it is distributed heterogeneously in the test section and this is the most important source of error. Furthermore, the liquid height is calculated from the averaged void fraction values which can also introduce error in the calculations.

6.2 A Novel Flow Regime Map

6.2.1 Introduction

As mentioned in the beginning of this chapter, the X-T flow regime map can be used for all horizontal experimental setup. However, this flow regime map was created with limited information since the local flow quantities could not be measured by Taitel & Dukler (1976). Since it is now possible for system code (CATHARE 3) to calculate turbulent kinetic energy, it is worth to generate a flow regime

map based on direct turbulence quantities. Thus, a novel flow regime map for the METERO experiment has been created by taking into account the measured local flow characteristics.

Similar to the general flow map of Taitel & Dukler (1976) and Dukler & Taitel (1986), the new flow regime map has been generated by comparing the turbulent and buoyancy forces affecting on the flow regime and by checking the bubble-bubble interaction. Thus, spatial averages of the following quantities have been chosen to generate the new flow regime map (averaging methods are given in Appendix 3):

1) Void fraction (α), the main two-phase flow parameter
2) Terminal velocity of a rising bubble (V_T) representing the buoyancy force
3) Standard deviation of axial fluctuating velocity (u') as an indicator of turbulence and therefore of mixing and/or of break-up

6.2.2 Calculation of coordinates

Spatial average of void fraction has been calculated by averaging local void fractions measured by our 4-point optical fiber probes. Unfortunately, spatial averaged terminal velocities have not been measured directly in the METERO experiment. Thus, in order to obtain terminal velocities, the spatial averaged Sauter mean diameter of each test has been calculated and the terminal velocity for corresponding bubble size in liquid at rest has been estimated. Spatial average of terminal velocity, which is a function of bubble size (spatial averaged Sauter mean diameter in our case, $<V_T> = f(<d_{32}>)$), has been derived from the information (Figure 6.4) given in the literature (Haberman & Morton, 1953).

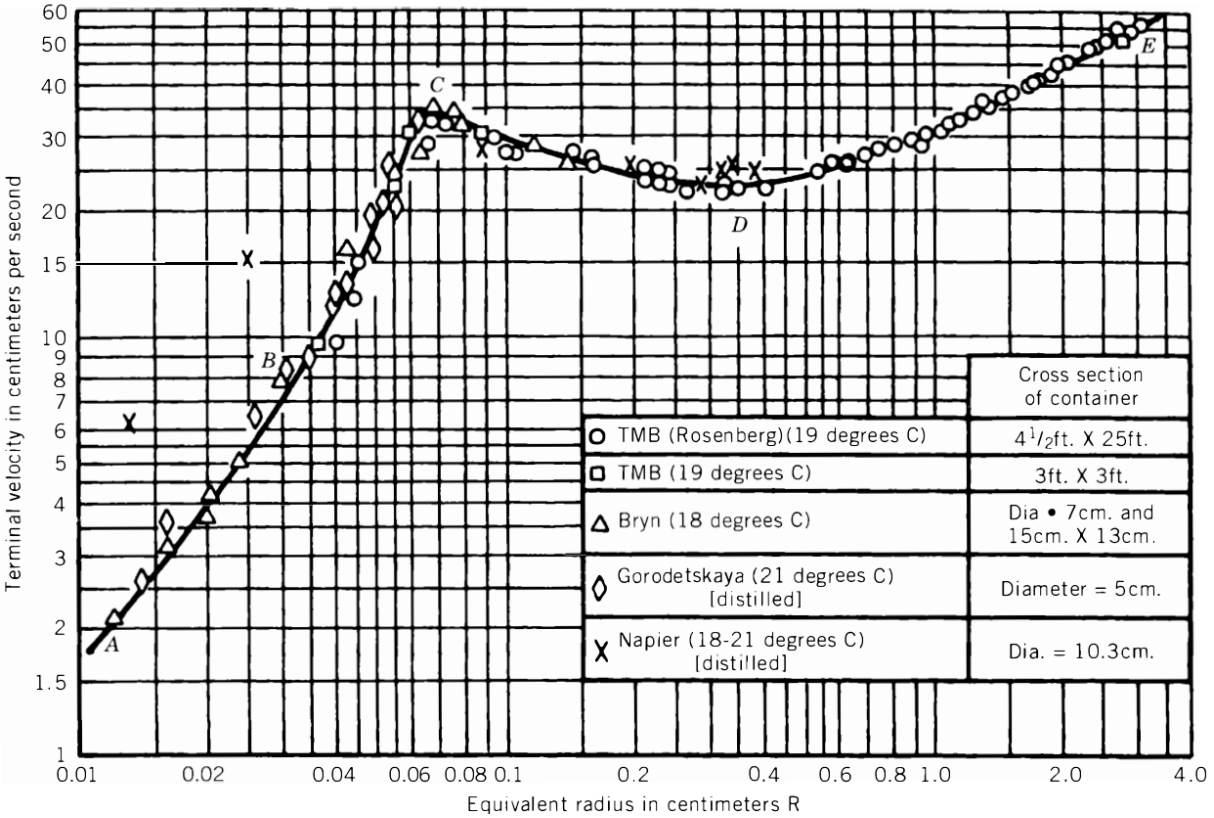

Figure 6.4 - Terminal velocity of air bubbles in liquid (water) at rest as a function of bubble size (Haberman & Morton, 1953)

Standard deviations of local fluctuating velocities cannot be measured for the all tests due to the formation of a wake behind the films in the high liquid flow rates (see section 3.2.2.1). In order to solve the problem, the data used in the study of Bottin (2010) which was acquired for higher liquid flow rates (J_L=4.42 m/s) and the data acquired for the lower liquid flow rates (J_L=3.00, 2.65, 2.12 and 1.59 m/s) at the present study were combined. As seen in Figure 6.5, the combined results show that once the gas flow rate (or superficial velocity) is constant, the spatial averaged standard deviation of axial fluctuating velocity exhibits a linear behavior by changing liquid flow rate (or superficial velocity). With these linear correlations, the missing information for the certain test conditions may be calculated in order to generate the new flow regime map.

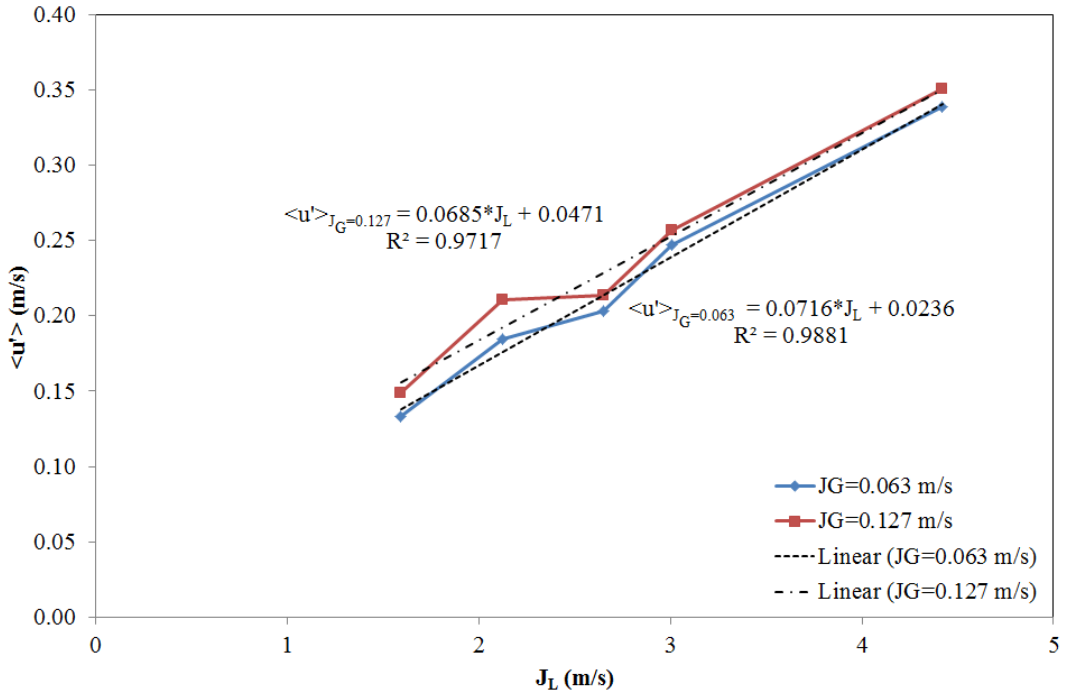

Figure 6.5 - The evolution of <u'> with various liquid and gas superficial velocities

6.2.3 An expected flow map sketch associated with the coordinates

Dimensionless coordinates of the new flow regime map have been calculated from spatial averages of flow quantities (void fraction $<\alpha>$, terminal velocity $<V_T>$ and standard deviation of axial fluctuating velocity $<u'>$) such that:

- $<\alpha>$, which is already dimensionless is given in the horizontal axis of the map.
- $\langle u' \rangle / \langle V_T \rangle$, bringing out a dimensionless coordinate, is represented in the vertical axis. This ratio represents the competition of turbulent and buoyancy forces.

An expected sketch of the new flow regime map is given in Figure 6.6. This map could be categorized in 4 zones such as:

- Zone ① representing low $\langle u' \rangle / \langle V_T \rangle$ and low $\langle \alpha \rangle$
- Zone ② representing high $\langle u' \rangle / \langle V_T \rangle$ and low $\langle \alpha \rangle$
- Zone ③ representing low $\langle u' \rangle / \langle V_T \rangle$ and high $\langle \alpha \rangle$
- Zone ④ representing high $\langle u' \rangle / \langle V_T \rangle$ and high $\langle \alpha \rangle$

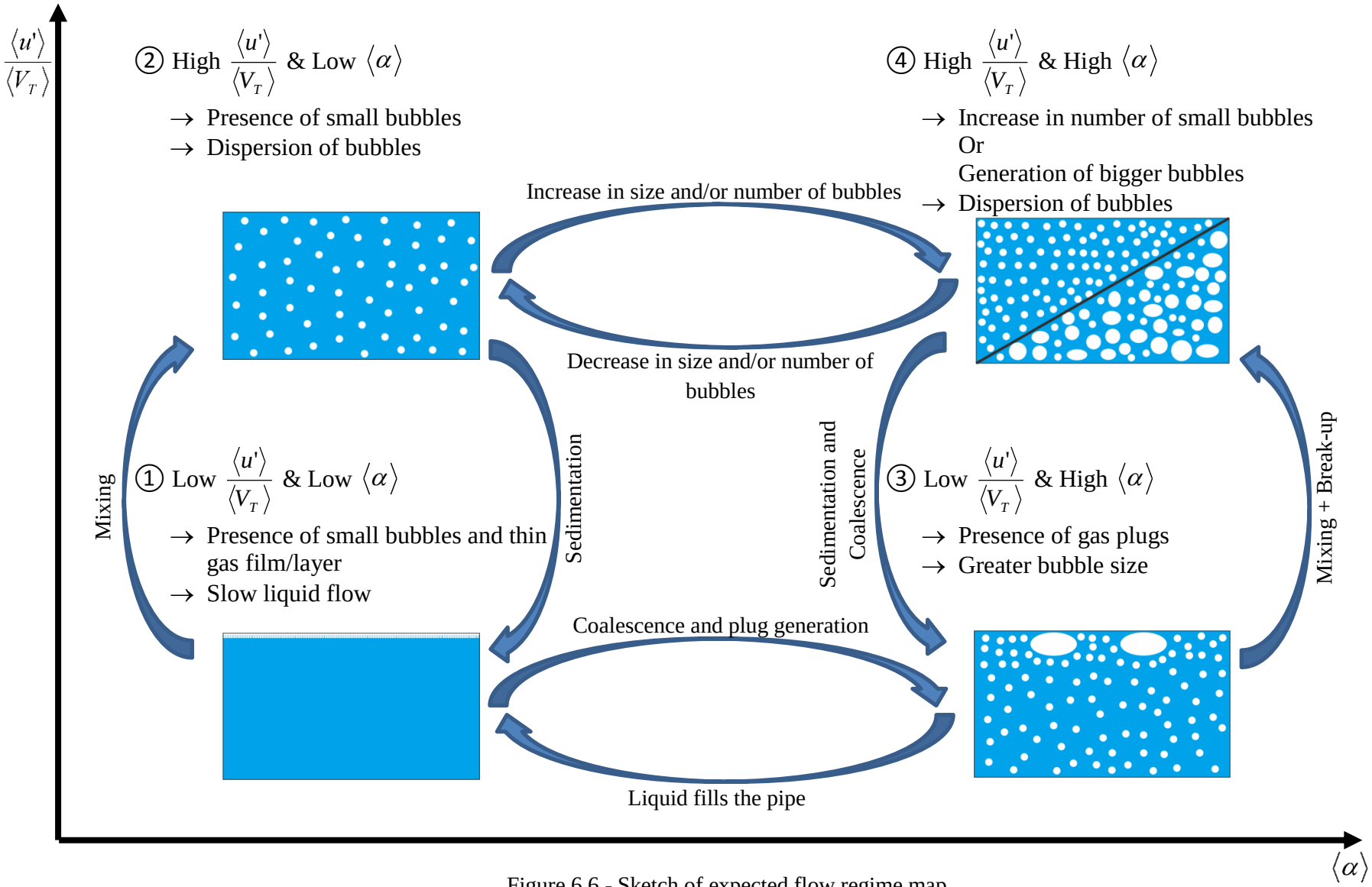

Figure 6.6 - Sketch of expected flow regime map

In Zone ① where the level of turbulence and void fraction are low, it is expected to observe a flow such that the liquid phase fills nearly the entire pipe. In addition, the gas phase (in the form of very small bubbles or thin gas film) takes place at the upper portion of the pipe. These two phases do not mix since the turbulence level in the flow is very low.

If the turbulence level is increased at a low and fixed void fraction, the flow moves from Zone ① to Zone ②. Since turbulence is increased, dispersion of bubbles in the flow is expected due to the mixing effect of turbulence. Thus, dispersed bubbly flow is established in Zone ②. In addition, high level of turbulence and low level of void fraction may not allow the coalescence of bubbles. As a result, the bubble sizes in Zone ② are also very small. When the flow moves from Zone ② to Zone ① by decreasing the turbulence level, the sedimentation of small bubbles at the upper portion of the pipe is expected due to less mixing effect. Moreover, formation of thin gas film is also possible as mentioned before.

If the void fraction is increased at a low and constant turbulence level (moving from Zone ① to Zone ③, coalescence of the bubbles, which increases the bubble size, and plug generation may be observed. As a result, plug flow is expected in Zone ③. In the opposite direction (moving from Zone ③ to Zone ① by decreasing the void fraction), the liquid phase starts to fill the entire pipe and the bubble size diminishes since the bubble-bubble interaction is decreased. Consequently, the expected flow in Zone ① which was mentioned before may be established.

In dispersed bubbly flows where $\langle u' \rangle / \langle V_T \rangle$ is very high, raising void fraction (moving from Zone ② to Zone ④) may bring out two possible results: the number of bubbles may increase or the size of the bubbles may increase depending on the bubble-bubble interactions (break-up and coalescence balance). Moreover, the dispersion of bubbles still remains due to high turbulence level. On the other way round, transition from Zone ④ to Zone ② occurs when the void fraction is decreased. As a result, the number of bubbles and/or the size of bubbles decrease because of less gas. In addition, high turbulence level keeps the dispersion of bubbles in the liquid phase.

If the turbulence level in plug flows (Zone ③) is increased, it is expected to observe dispersion and break-up of bubbles. It can be concluded that the bubble size in Zone ④ is smaller than that in Zone ③ because of break-up. Moreover, the flow becomes dispersed due to the mixing effect of turbulence. In the reverse scenario which is transition from Zone ④ to Zone ③, sedimentation and coalescence of bubbles may be observed due to decrease in turbulence level. As a result, bubble size increases and gas plugs are generated. Moreover, bubbles are accumulated in the upper portion of the pipe.

6.2.4 Application to the METERO experiment, results and discussion

By the help of these hypothetical phase transition approach, we have concluded that this new flow regime map could represent the phase transitions between:

- Buoyant Bubbly Flow (BBF) where turbulence is high while void fraction is low,
- Stratified Bubbly Flow (SBF) where turbulence and void fraction is high,
- Plug Flow (PF) where void fraction is high while turbulence is low.

In other words, BBF, SBF and PF could be presented by Zones ②, ③, and ④, respectively. Zone ① is not presented since this zone requires very low liquid flow rates which are not focused in the present study.

In the light of all the information given above, a new dimensionless flow regime map has been plotted. This map is given in Figure 6.7. It is in a good agreement with our expected map (Figure 6.6). BBF, SBF

and PF regimes take place in the expected zones. This shows that our hypothetical approach of the flow regime transition represents the actual transition mechanisms in a simple manner.

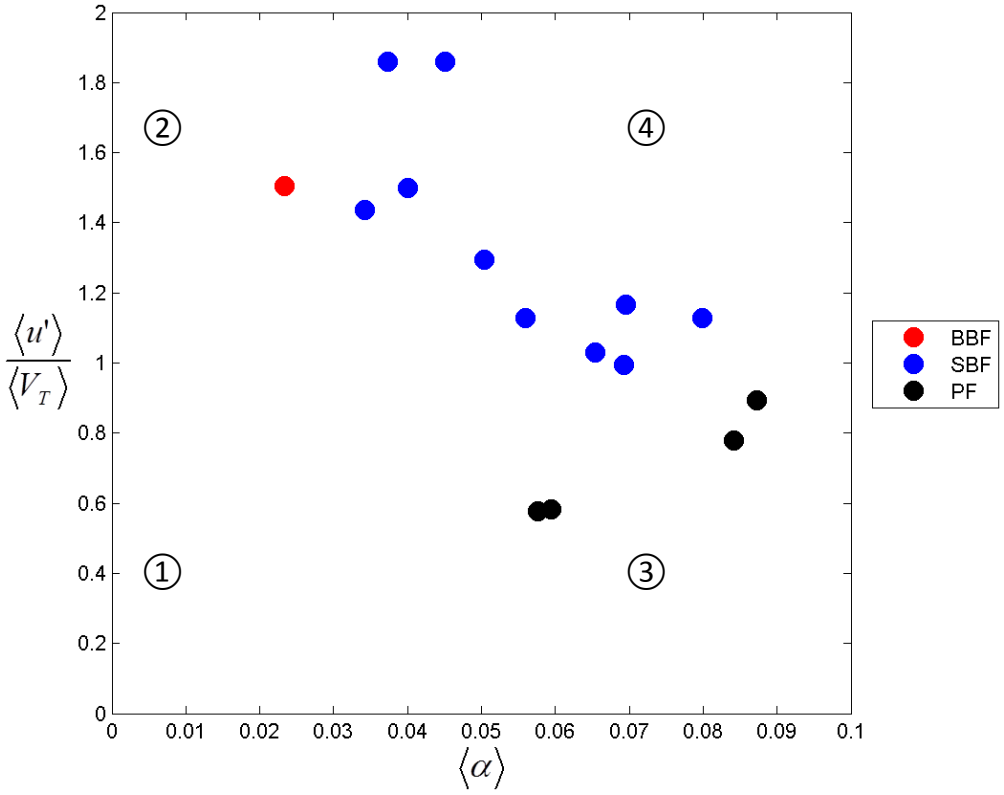

Figure 6.7 - A novel dimensionless flow regime map at 40D

The new flow regime map has several advantages. The first one is that it is based on the measurement of local flow quantities. Thus, this map could represent flow regimes and their transitions more realistically than the maps based on theoretical models. In addition, dimensionless numbers derived from local flow quantities could lead to a better understanding of the mechanism determining the flow regimes (competition of turbulent and buoyancy forces and bubble-bubble interaction). Furthermore, this flow regime map could be used and adopted for other experimental setups dedicated to horizontal flows since it is independent of the experimental setup geometry and dimensionless numbers are used in the map. Although this map successfully represents the flow regimes and transitions of horizontal air-water two-phase flows at atmospheric pressure, further studies and more data are required in order to complete this flow regime map, especially with liquid-vapor and at various pressures.

Nonetheless, the uncertainties in the measurement of local flow quantities and spatial averaging bring out one of the major drawbacks for this flow regime map. In addition, the terminal velocities of bubbles are derived for a single bubble in liquid at rest. However, there exist numerous of bubbles in these flows and they have a cloud effect which is not taken into account in the calculation of the terminal velocity. Thus, if the terminal velocity in the real case is measured, the map may represent the flow regimes and their transitions more precisely. Furthermore, the flow regimes which are observed for high gas flow rates (e.g. annular, stratified and slug flows) could not be represented with this flow regime map since this map represents flows with lower gas flow rates. These flows could be represented by using a third axis (e.g. ratio of liquid-gas interface slip velocity and standard deviation of axial fluctuating velocity. This ratio is very high for annular, stratified and slug flows). However, further studies are essential to define this third axis.

CHAPTER 7

CONCLUSION

7 CONCLUSION

The study presented in this thesis report is original for the following reasons:

1. The horizontal two-phase flows (namely dispersed bubbly and intermittent flows) and their axial development have been investigated in the METERO experiment.
2. Various measurement techniques and instrumentation have been used to measure the flow quantities (void fraction, bubble size, interfacial area, axial mean velocities of bubbles and liquid phase, and turbulent kinetic energy of the liquid phase) in order to describe the axial evolution of the dispersed bubbly and the intermittent flows.
3. The physical mechanisms taking place in both flow regimes are explained by using the experimental results.
4. One improved dimensionless flow regime map (X-T map) flow regime map and one novel dimensionless flow regime map flow regime map have been introduced in order to define the regime transitions for horizontal air-water flows at atmospheric pressure.

After the presentation of the METERO experiment, the instrumentation used in the present study (optical fiber probes, hot-film anemometry and high-speed camera) has been described. Furthermore, detailed information about the instrumentation procedures (settings, calibration, etc.) and data processing methods (e.g., phase discrimination for hot-film anemometry signals and shadowgraphy for high-speed camera images) have been presented.

Afterwards, horizontal dispersed bubbly and intermittent flows have been investigated perpendicularly to the main stream (at 40 pipe diameters downstream) and along the main stream (at 5, 20 and 40 diameters). Thanks to the various instrumentations, the measured flow quantities give access to the description and the analysis of the several flow regimes studied here. Moreover, the mechanisms in each flow regime have been explained in the light of the gathered information.

In dispersed bubbly flows, the competition between turbulent and buoyancy forces determine the distribution of the phase quantities. The balance between these both forces is controlled essentially by the liquid flow rate that drives the turbulence which increases with the liquid flow rate. Consequently, the gas phase quantities (e.g. void fraction, bubble size and interfacial area concentration) are distributed homogeneously and their profiles become more flat when the liquid flow rate increases. On the other hand, a decrease of liquid flow rate and thus of turbulence makes the buoyancy force relatively more important and thus bubbles can accumulate in the upper part of the pipe. The influence of the gas flow rate changes is less significant.

The axial evolutions of void fraction, chord length and interfacial area concentration draw attention to the bubble migration toward the top where the accumulation/coalescence can occur in dispersed bubbly flows. Even though it has not been visualized, the axial evolutions of the flow quantities point out the coalescence of bubbles. It is concluded that the dispersed bubbly flows are partially developed at 40D by checking the axial evolutions of velocity and turbulent kinetic energy profiles.

In intermittent flows, the superiority of buoyancy force on turbulent mixing has been observed due to the lower liquid flow rates. As a result, accumulation and coalescence of the bubbles occur in the upper part of the test section. In the lower part of the pipe, only very small bubbles captured by turbulent forces remain. Moreover, the distribution of the gas phase quantities in the lower part is similar to what is observed in the dispersed bubbly flows. These results show that the flow could be split into two parts: buoyancy dominant zone and turbulent dominant area. This behavior has been described as gas-liquid coordinated flow by Ekambara et al. (2008). In this flow regime, it is observed that the bubbles move slower than the liquid phase which has been also reported in the literature. Furthermore, the position of

the maximum velocity moves to the center of the test section due to the higher liquid flow rates in the upper part of the test section led by faster elongated bubbles while the maximum velocity is observed in the lower part of the test section in the dispersed bubbly flows. This shift of maximum is also observed in the turbulent kinetic energy profiles. The axial evolutions of void fraction, chord length and interfacial profiles draw attention to accumulation and coalescence of the bubbles. In addition, high-speed camera visualizations performed at 20 and 40D for elongated bubbles supports the evidence of coalescence. For lower gas flow rates, the velocity field evolves between 5D and 20D, and stabilizes between 20D and 40D even though the flow is intermittent. The turbulence field evolves continuously from 5D to 40D and this can be an effect of the flow intermittency.

For the METERO experiment, a flow regime map in liquid and gas velocities generated from visual observations was presented. Although this map is valid for the present experimental setup, it cannot be used for other experiments dedicated to horizontal flows. Thus, a significant attention has been paid to create dimensionless flow maps. For this purpose, a flow regime map developed from the generalized flow regime map of Taitel & Dukler (1976) has been introduced. Thanks to it, the flow regime transitions have been described by mechanistic criteria instead of visual observations. In addition to this, a novel dimensionless flow regime map has been generated by the help of the measured local flow quantities. This new flow regime map could represent horizontal air-water flow regimes and their transitions at atmospheric pressure more realistically than the maps based on theoretical models. In addition, the mechanisms determining the flow regimes could be understood better since they are involved directly in the parameters of this map. Finally, this flow regime map is independent from the experimental setup geometry. Thus, it could be applied to other experimental setups studying on horizontal air-water two-phase flows. Although this map presents the flow regimes in the METERO experiment, further studies are essential to extend this flow regime map to the steam-liquid mixture and to higher pressures.

To sum up, dispersed bubbly and intermittent flows have been studied together in the present study. In addition, two dimensionless flow regime maps have been introduced. Since a small fraction of the flow regime map has been investigated, further experimental studies should be performed to investigate the remaining flow regimes (e.g. stratified flows) and to describe the different mechanisms occurring in horizontal two-phase flows.

CHAPTER 8

PROSPECTIVES

8 PROSPECTIVES

As a part of the prospective of this study, the acquired experimental results could be used for the validation of the NEPTUNE code and CATHARE 3. In addition, new physical models, particularly bi-fluid modeling of flows, could be developed by the help of the presented experimental data.

In the Stratified Bubbly Flow (SBF), it was observed that the fluid in the upper region of the test section has a different dynamics than the fluid taking place in the lower part. Thus, the flow could be modeled in two regions which are characterized by two different fluids (Figure 8.1): foam constituted by the mixture of bubbles and liquid film in the upper region and liquid phase in the lower region of the test section.

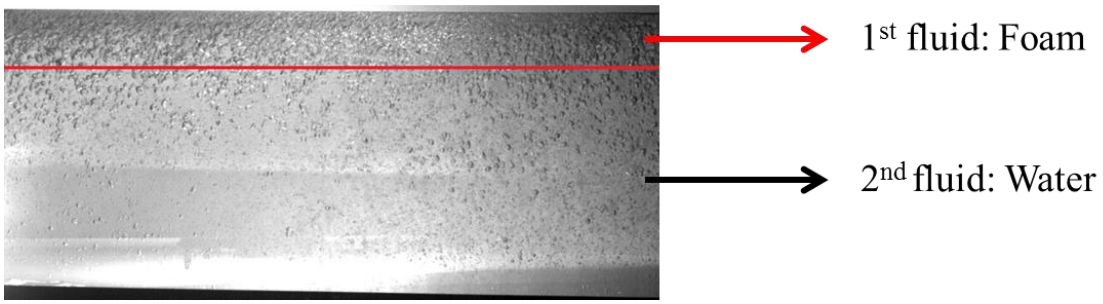

Figure 8.1 - Representation of stratified bubbly flow with two different fluids

Concerning the intermittent flows, an interesting behavior has been observed in the plug flow. When the flow is visualized by high speed camera, it is observed that bubble layer in the upper part of the test section generates pulsations in the flow, as seen in Figure 8.2. It is possible that these pulsations lead to the appearance of the large elongated bubbles. The detection of the boundary between the bubble layer and the liquid phase plays an important role to detect the period (or frequency) of these pulsations. For this reason, a systematic procedure has been developed in the laboratory to detect this boundary. The preliminary results of this procedure are given in Figure 8.3. The physical modeling of this phenomenon for simulations codes is one of the prospective s of the present study.

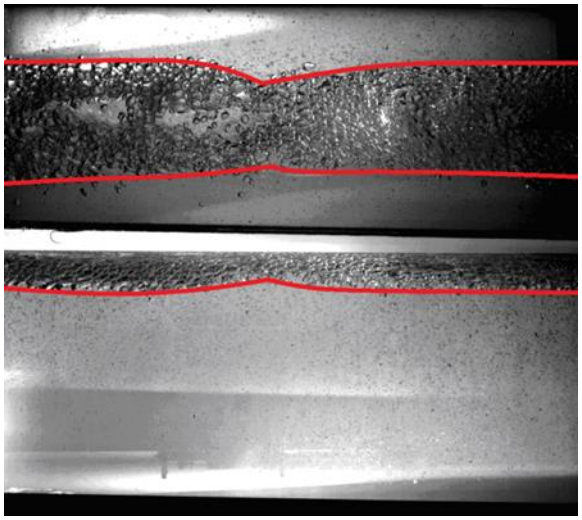

Figure 8.2 - Observation of pulsations in plug flow with high speed camera

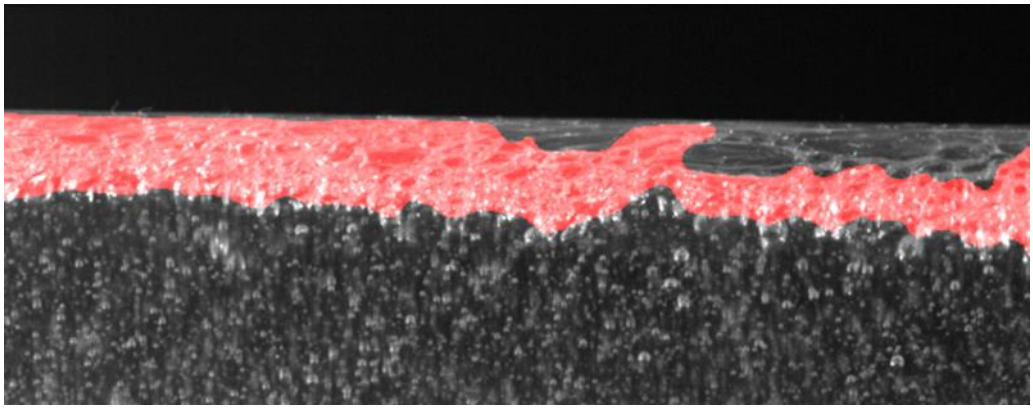

Figure 8.3 - Detection of the boundary between bubble layer and liquid phase in plug flow

APPENDICIES

APPENDIX 1 - CALCULATION OF GAS SUPERFICIAL VELOCITY AS A FUNCTION OF FLOW RATE

The flowmeters measure a mass flow of air in *Nl/min* (Normal liter per minute) or in Nm^3/h. The normal conditions of pressure and temperature can be listed as:

- Pressure = 101325 *Pa* (Sea level standard atmospheric pressure) and,
- Temperature = 0°C or 273.15 °K

The density of air in these conditions is $\rho = 1.293\ Kg/m^3$.

The mass flow of air, $\dot{m}$, is expressed in terms of volumetric flow, Q, such as:

$$\dot{m} = Q \times \rho$$

In the case of normal conditions, the mass flow of air becomes $\dot{m} = Q \times 1.293$

An example: A mass flow of 30 Nl/min represents directly to a volumetric flow rate of 30l/min when the air is in normal conditions (atmospheric pressure and 0°C). If the temperature of air is higher (presenting lower air density), the normal volumetric flow rate corresponds to a greater flow rate. On the contrary, if the temperature of air is lower (higher air density), it will represents a smaller volumetric flow.

In order to calculate the actual volumetric flow rate based on temperature and from the mass flow rate in normal conditions, the following equation is used:

$\dot{m}\left[Kg/s\right] = Q\left[m^3/s\right] \times \rho\left[Kg/m^3\right]$ where ρ is the density of the fluid for the actual pressure and temperature conditions.

The mass flow rate, in S.I. units, is obtained by using the conversion of *Nl/min* into *Kg/s*.

An example: $30\ l/\min = 0.5\ l/s = 0.5 \cdot 10^{-3}\ m^3/s$, thus

$$30\ Nl/\min = 0.5 \cdot 10^{-3} \times 1.293 = 0.647 \cdot 10^{-3}\ Kg/s$$

The superficial velocity of the gas is calculated by using the following formula.

$J_G\left[m/s\right] = \dfrac{Q\left[m^3/s\right]}{S\left[m^2\right]}$ where S is the cross section of the fluid flow.

Even the pressure of the gas is close to the atmospheric pressure in all the tests, the temperature may vary between different tests. For example, the temperature changes around 10 °C between winter and summer such as:

$T_{AIR-WINTER} = 16\ °C$ at maximum

$T_{AIR-WINTER} = 26\ °C$ at maximum

Thus, the density of air is also changing such as:

$\rho = 1.22\ Kg/m^3\ at\ 16\ °C$

$\rho = 1.18\ Kg/m^3\ at\ 26\ °C$

Consequently, the normal mass flow rate of 30 *Nl/min* represents different volumetric flow rates for different temperatures such as:

$Q = 0.647 \cdot 10^{-3}/1.22 = 0.530 \cdot 10^{-3}\ m^3/s\ \ at\ 16\ °C$

$Q = 0.647 \cdot 10^{-3}/1.18 = 0.548 \cdot 10^{-3}\ m^3/s\ \ at\ 26\ °C$

As seen from the results, the change in temperature results in a 3% variation of the volumetric flow rate and superficial velocity for different tests. This 3% variation can be neglected.

APPENDIX 2 - THE LAWS RELATED TO THE USE OF HOT-FILM ANEMOMETRY

A. King's Law Adapted to Hot-Film Anemometry

There are three assumptions to simplify the work such as:

- Hot-film is described as a film or wire with infinite length,
- The probe is placed in an isotropic medium,
- The probe pins are not involved in the behavior of the film.

The assumptions used to obtain the relationship between the terminal voltage of the film and the speed of the liquid are the followings:

- A film with infinite length ($l_{wire} >> d_{wire}$).
- A steady state flow ($\partial/\partial t = 0$).
- Thermally stabilized (No diffusive effects ($\partial^2/\partial x^2 = 0$) and no internal conditions).
- Working with small temperature variations and constant pressure close to atmospheric pressure brings out constant Fourier thermal conduction coefficient of water ($\lambda(T)$), heat transfer coefficient (or Newton convection coefficient) ($h_{Concevtion}(T)$) and kinematic viscosity ($\nu(T)$).
- The probe is oriented in the main flow direction.
- The fluctuating velocity is lower than the average velocity in the flow (non-turbulent flow regime).

T_{ref} is the reference ambient temperature for reference viscosity.

T_a is the actual ambient temperature of the fluid.

d_{wire}, l_{wire}, I and R_{wire} are the diameter of the wire, the length of the wire, the current passing through the wire, the equivalent resistance of the overheated wire respectively.

E_{wire} is the heat energy stored in the wire or film and the power balance on the wire can be written as:

$$\frac{dE_{wire}}{dt} = P_{Joule} - q_{w \to o} \tag{34}$$

$P_{Joule} = R_{wire} \cdot I^2 > 0$ is the power due to Joule effect and $q_{w \to o} > 0$ is heat transfer from the wire to the outside.

The wire is heated to a certain temperature which is calculated from an overheating coefficient and characteristics of the probe, and this temperature is greater than that of surrounding fluid.

Several effects contribute to the heat dissipation such as:

- Conduction to the fluid due to molecular diffusion of the heat in the fluid
- Convection to the fluid where the heat is transferred by the movement of surrounding fluid
- Conduction to the supports due to the diffusion of the heat through the wire
- Thermal radiation: power transfer in the form of electromagnetic radiation

In the METERO experiment, the conduction to the supports and the thermal radiation are considered negligible.

The heat flux through the wire surface ($A_{wire} = \pi \cdot d_{wire} \cdot l_{wire}$) is written as:

$$\frac{q_{w\to o}}{A_{wire}} = h_{Convection}\left(T_{wire} - T_a\right) \tag{35}$$

Nusselt number is introduced as:

$$Nu = \frac{h_{Convection} \cdot d_{wire}}{\lambda} \tag{36}$$

Equation (36) is rewritten as:

$$q_{w\to o} = \pi \cdot l_{wire} \cdot \lambda \cdot \left(T_{wire} - T_a\right) \cdot Nu \tag{37}$$

The variation of the stored energy E in the wire depends on the variation of the wire temperature T_{wire} and it is assumed that the temperature is independent of time. Thus, we have $dE/dt = 0$ and the power balance is written as:

$$R_{wire} \cdot I^2 = \pi \cdot l_{wire} \cdot \lambda \cdot \left(T_{wire} - T_a\right) \cdot Nu \tag{38}$$

From the King's correlation, it is known that:

$$Nu = A_{Nu}\left(\mathrm{Pr}\right) + B_{Nu}\left(\mathrm{Pr}\right) \cdot \mathrm{Re}^{n_K} = \frac{h_{Convection} \cdot d_{wire}}{\lambda} \tag{39}$$

Ohm's law on the film brings out:

$$e^2 = R_{wire}^2 \cdot I^2 = R_{wire} \cdot \pi \cdot l_{wire} \cdot \lambda \cdot \left(T_{wire} - T_a\right) \cdot \left(A_{Nu}\left(\mathrm{Pr}\right) + B_{Nu}\left(\mathrm{Pr}\right) \cdot \mathrm{Re}^{n_K}\right) \tag{40}$$

In the previous formula, *Re* is the Reynolds number of the wire and it is formulated as $\mathrm{Re} = \frac{V_{liq} \cdot d_{wire}}{\upsilon}$

where d_{wire} is the hot wire diameter, V_{liq} is the average velocity of the so-assumed incompressible liquid and V_{liq} is independent of T in the first order (imposed in the our case by selected flow rate), and υ is the kinematic viscosity of the liquid.

By setting $K = R_{wire} \cdot \pi \cdot l_{wire} \cdot \lambda$ independent of the temperature, a relation between the voltage on the hot-film and Reynolds number of the flow is obtained such as:

$$e^2\left(T_a\right) = K \cdot \left(T_{wire} - T_a\right) \cdot \left(A_{Nu} + B_{Nu} \cdot \mathrm{Re}^{n_K}\left(T_a\right)\right) = A\left(T_a\right) + B\left(T_a\right) \cdot \mathrm{Re}^{n_K}\left(T_a\right) \tag{41}$$

Finally, the relation between the voltage on the hot film and the flow velocity, given in 3.2.1, can be written as:

$$e^2\left(T_a\right) = A'\left(T_a\right) + B'\left(T_a\right) \cdot V_{liq}^{n_K} \tag{42}$$

B. Temperature Dependence and Correction

It should be noted that the sensibility of the thermal anemometry measurements are temperature dependent and a temperature correction of the data is essential. In our tests, the classical temperature correction formula given in the literature (Brunn, 1995) has been used.

With the same assumptions given in the previous section, the conversion of voltage and Reynolds number at an ambient and a reference temperature can be written as:

$$e^2(T_a) = K \cdot (T_{wire} - T_a) \cdot \left(A_{Nu} + B_{Nu} \cdot \mathrm{Re}^{n_K}(T_a)\right) = A(T_a) + B(T_a) \cdot \mathrm{Re}^{n_K}(T_a) \tag{43}$$

$$e^2(T_{ref}) = K \cdot (T_{wire} - T_{ref}) \cdot \left(A_{Nu} + B_{Nu} \cdot \mathrm{Re}^{n_K}(T_{ref})\right) = A(T_{ref}) + B(T_{ref}) \cdot \mathrm{Re}^{n_K}(T_{ref}) \tag{44}$$

The temperature variations are small enough to consider a constant kinematic viscosity of the liquid:

$$\upsilon(T_a) \approx \upsilon(T_{ref}) \tag{45}$$

And the liquid velocity is independent of the temperature in the first order. Thus, we can obtain:

$$\mathrm{Re}(T_a) \approx \mathrm{Re}(T_{ref}) \tag{46}$$

Consequently, the coefficients $A(T_a)$ and $B(T_a)$ can be rewritten as:

$$A(T_a) = A(T_{ref}) \cdot \frac{T_{wire} - T_a}{T_{wire} - T_{ref}} \tag{47}$$

$$B(T_a) = B(T_{ref}) \cdot \frac{T_{wire} - T_a}{T_{wire} - T_{ref}} \tag{48}$$

With these corrections, we obtain:

$$e^2(T_a) = \frac{T_{wire} - T_a}{T_{wire} - T_{ref}} \cdot \left(A(T_{ref}) + B(T_{ref}) \cdot \mathrm{Re}^{n_K}(T_{ref})\right) = \frac{T_{wire} - T_a}{T_{wire} - T_{ref}} \cdot e^2(T_{ref}) \tag{49}$$

Finally, a correlation to correct the data measured at an ambient temperature T_a different from the reference temperature T_{ref} is obtained such as:

$$e(T_a) \approx \left(\frac{T_{wire} - T_a}{T_{wire} - T_{ref}}\right)^{0.5} \cdot e(T_{ref}) \tag{50}$$

This correlation has been introduced in many publications and it is commonly recommended to use for the correction (Bearman, 1971 and Brunn, 1995). Therefore, this correlation has been used in our hot-film anemometry measurements to calculate the equivalent voltages for temperatures different from reference temperature and to calculate the effective cooling velocities of the films.

C. Conversion between Effective Velocities and Velocity of the Liquid Phase

The schematics of the geometric path which brings access to the various components of the velocity derived from the effective velocities of two-component hot-film probes (the effective velocity is the cooling velocity of the film) is given in Figure A2.1.

The actual velocity of the liquid flow is considered as $\vec{V}_{liq}$ and the norms of the cooling velocities for two wires or films of the probe are U_{eff1} and U_{eff2}.

Furthermore, $(0, \vec{x}_0, \vec{y}_0, \vec{z}_0)$ represents the laboratory coordinates. $\vec{x}_0$ is collinear with the axis of the pipe and $\vec{y}_0$ is the vertical axis. The probe is placed in the pipe such that the wires/films are arranged along the axis $\vec{i}_1$ and $\vec{i}_2$. The axis of the wires/films form an orthogonal base rotated with an angle of β relative to the laboratory frame $(\beta \approx 45°)$. The actual velocity of the liquid, $\vec{V}_{liq}$, forms an angle of α with pipe axis. Furthermore, $\vec{u}_1$ and $\vec{u}_2$ are the projections of the actual velocity on the wire axes $\vec{i}_1$ and $\vec{i}_2$ respectively.

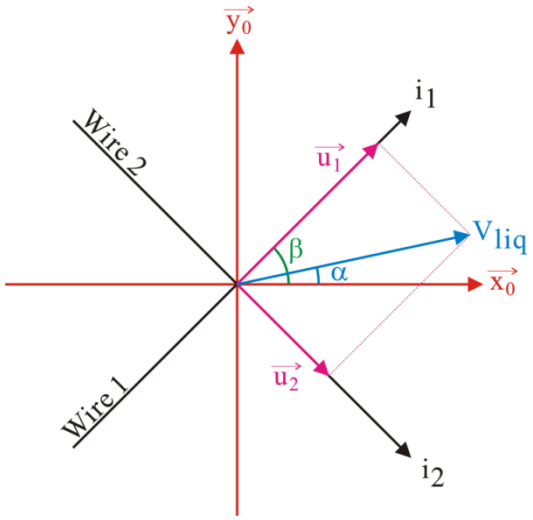

Figure A2.1 - Schematic of fluid velocity with projection on the wire axes

Consequently, we have obtained:

$$\begin{cases} \vec{i}_1 = \vec{x}_0 \cos\beta + \vec{y}_0 \sin\beta \\ \vec{i}_2 = \vec{x}_0 \cos\beta - \vec{y}_0 \sin\beta \end{cases} \quad (51)$$

And

$$V_{liq}^2 = u_1^2 + u_2^2 \quad (52)$$

For each wire/film, the effective cooling velocity U_{eff} is defined as:

$$\begin{aligned} U_{eff\,1}^2 &= u_1^2 + \kappa^2 u_2^2 \\ U_{eff\,2}^2 &= \kappa^2 u_1^2 + u_2^2 \end{aligned} \quad (53)$$

where κ is the inclination factor.

Figure A2.2 represents the decomposition of the effective velocities on the axes of wires/films.

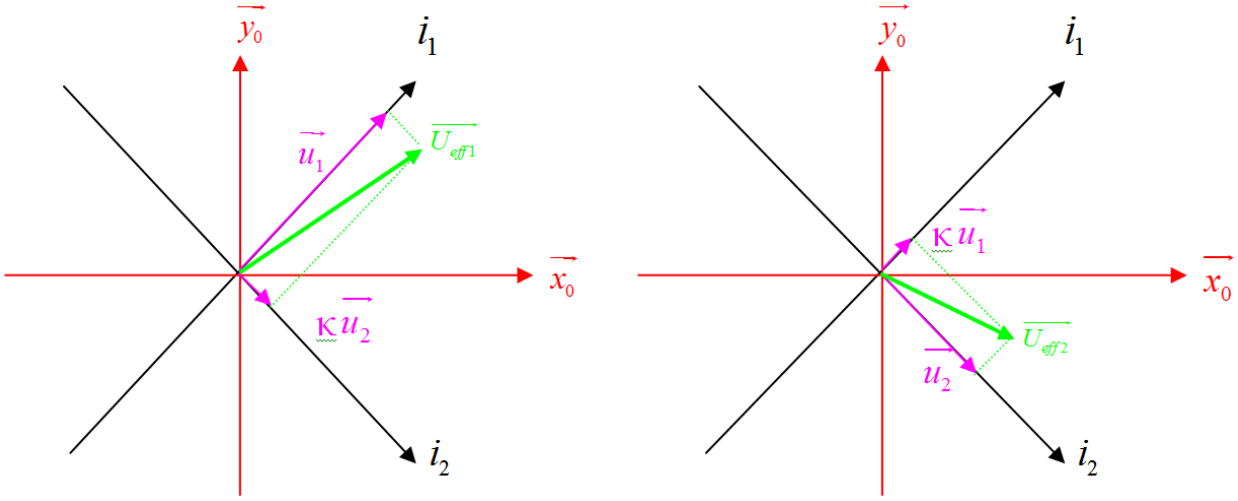

Figure A2.2 - Schematic of effective velocities and their projections on the axes of wires/films

Thus, u_1 and u_2 are written as:

$$u_1 = \sqrt{\frac{1}{1-\kappa^4}\left(U_{eff\,1}^2 - \kappa^2 U_{eff\,2}^2\right)}$$
$$u_2 = \sqrt{\frac{1}{1-\kappa^4}\left(U_{eff\,2}^2 - \kappa^2 U_{eff\,1}^2\right)} \quad (54)$$

The axial and radial components of the liquid velocity $\left(\vec{V}_{liq} = U_L\vec{x}_0 + V_L\vec{y}_0\right)$ are calculated from:

$$U_L = u_1.\cos\beta + u_2.\sin\beta = \cos\beta.\sqrt{\frac{1}{1-\kappa^4}\left(U_{eff\,1}{}^2 - \kappa^2.U_{eff\,2}{}^2\right)} + \sin\beta.\sqrt{\frac{1}{1-\kappa^4}\left(U_{eff\,2}{}^2 - \kappa^2.U_{eff\,1}{}^2\right)}$$
$$V_L = u_1.\cos\beta - u_2.\sin\beta = \cos\beta.\sqrt{\frac{1}{1-\kappa^4}\left(U_{eff\,1}{}^2 - \kappa^2.U_{eff\,2}{}^2\right)} - \sin\beta.\sqrt{\frac{1}{1-\kappa^4}\left(U_{eff\,2}{}^2 - \kappa^2.U_{eff\,1}{}^2\right)} \quad (55)$$

In our study, $\beta = 45°$. Thus, the components are calculated by using the following formulas.

$$U_L = \frac{\sqrt{2}}{2}.\sqrt{\frac{1}{1-\kappa^4}\left(U_{eff\,1}{}^2 - \kappa^2.U_{eff\,2}{}^2\right)} + \frac{\sqrt{2}}{2}.\sqrt{\frac{1}{1-\kappa^4}\left(U_{eff\,2}{}^2 - \kappa^2.U_{eff\,1}{}^2\right)}$$
$$V_L = \frac{\sqrt{2}}{2}.\sqrt{\frac{1}{1-\kappa^4}\left(U_{eff\,1}{}^2 - \kappa^2.U_{eff\,2}{}^2\right)} - \frac{\sqrt{2}}{2}.\sqrt{\frac{1}{1-\kappa^4}\left(U_{eff\,2}{}^2 - \kappa^2.U_{eff\,1}{}^2\right)} \quad (56)$$

APPENDIX 3 - SPATIAL AVERAGES OF KEY VALUES

In our study, certain integration methods have been used in order to obtain an averaged value of the acquired measurements in the test section. The details of these integration methods will be given in the following sections.

A. Integration by Horizontal Layers

This integration method is used for the variables (e.g. void fraction, interfacial area, bubble size, frequency and number of bubbles) whose distribution has a stratified tendency in the test section.

In order to calculate the area of horizontal layers, the area located between r and R (pink zone in Figure A3.1) should be calculated. Afterwards, the area of horizontal layer will be calculated by subtracting the area of the pink zone from the area of the semi-circle. For this purpose, the area of the shaded zone should be calculated in the beginning.

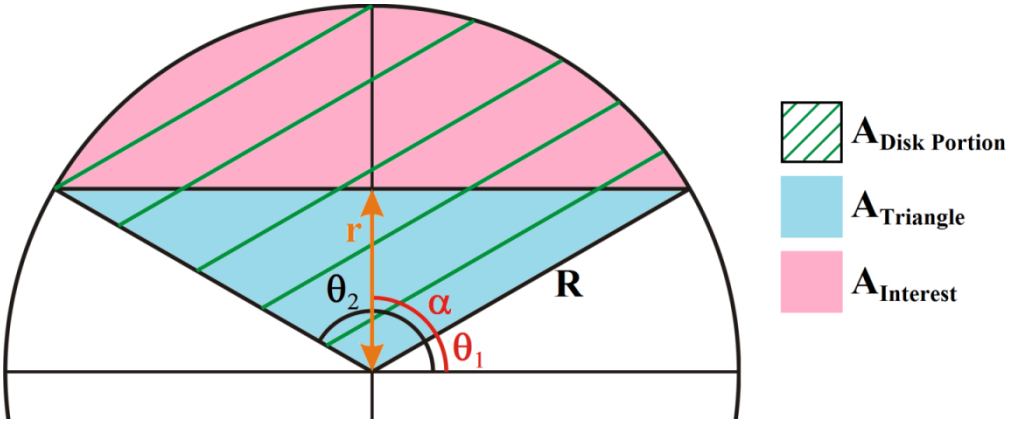

Figure A3.1 - Schematic of the areas in the test section

In order to calculate the area of pink zone, the following formulas are used.

$$\cos(\alpha) = \frac{r}{R} \rightarrow \theta_1 = \frac{\pi}{2} - \alpha = \frac{\pi}{2} - \arccos\left(\frac{r}{R}\right) \tag{57}$$

$$\theta_2 = \frac{\pi}{2} + \arccos\left(\frac{r}{R}\right) \tag{58}$$

Area of the disk portion (shaded zone) which is located between θ_1 and θ_2 is calculated by:

$$A_{Disk\ \ Portion} = \int_0^R r dr \int_{\frac{\pi}{2}-\arccos\left(\frac{r}{R}\right)}^{\frac{\pi}{2}+\arccos\left(\frac{r}{R}\right)} d\theta = R^2 \cdot \arccos\left(\frac{r}{R}\right) \tag{59}$$

Area of the triangle (blue zone) is:

$$A_{Triangle} = r\sqrt{R^2 - r^2} \tag{60}$$

Area of the interest (pink zone) is:

$$A_{Interest} = R^2 \cdot \arccos\left(\frac{r}{R}\right) - r\sqrt{R^2 - r^2} \tag{61}$$

In our study, the test section is discretized in horizontal layers centered at the measurement points with respect to the wall curvature.

The schematic of a horizontal layer centered at radius r_i is given in Figure A3.2.

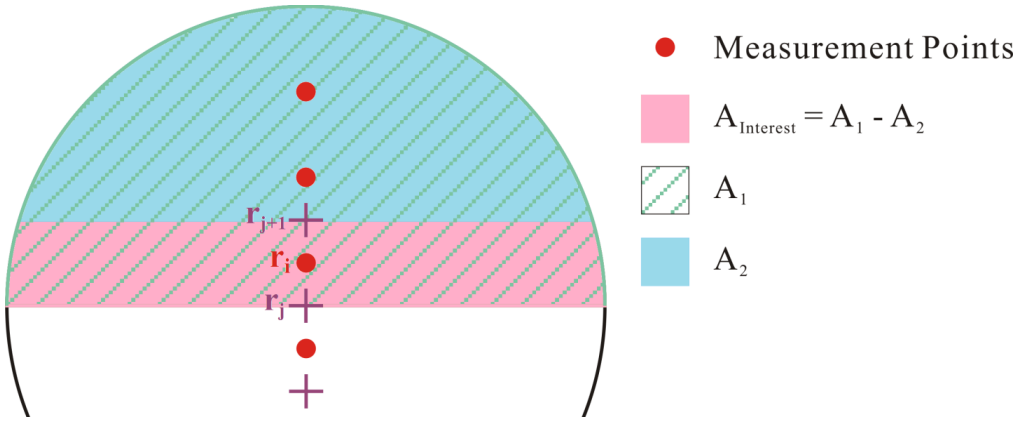

Figure A3.2 - Schematic of the discretization in horizontal layers

The area of the pink zone (area of interest – horizontal layer) is calculated as:

$$A_{Interest} = A_1 - A_2 = R^2 \cdot \arccos\left(\frac{r_j}{R}\right) - r_j\sqrt{R^2 - r_j^2} - R^2 \cdot \arccos\left(\frac{r_{j+1}}{R}\right) + r_{j+1}\sqrt{R^2 - r_{j+1}^2} \tag{62}$$

The average value of a variable *f* measured in a horizontal layer A_i through a test section with an area of S can be calculated as:

$$\langle f \rangle = \frac{\sum f_i \cdot A_i}{S} \tag{63}$$

B. Integration by Semi-Crowns

This integration method used for variables which are distributed semi-axisymmetrically in the test section (e.g. bubble and liquid velocities, turbulent kinetic energy) to calculate the average value of the variables.

In Figure A3.3, the schematic of semi-crown decomposition inside the test section is given. The red points represent the measurement points and surround the semi-crown which is associated with black point.

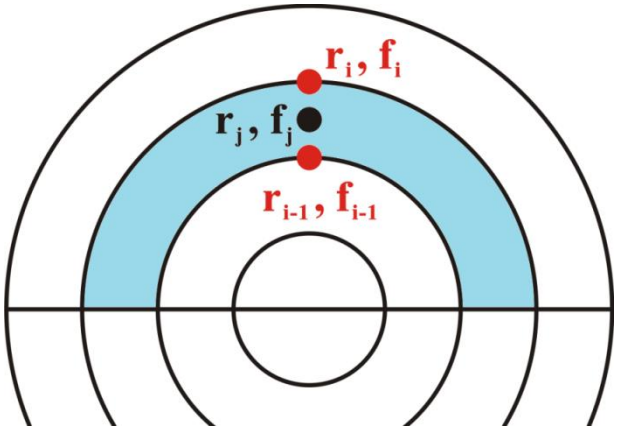

Figure A3.3 - Schematic of semi-crown decomposition

The integral of a variable *f* in a section is formulized as:

$$\langle f \rangle = \frac{1}{S}\int_0^{\pi} d\theta \int_{-R}^{R} f(r)\cdot r \cdot dr = \frac{1}{\pi R^2}\pi \int_{-R}^{R} f(r)\cdot r \cdot dr \tag{64}$$

The discrete form of Equation (64) can be written as:

$$\langle f \rangle = \frac{1}{R^2}\sum f_j \cdot r_j \cdot \Delta r_j \tag{65}$$

where $f_j = f(r_j)$.

In the tests, the variables at r_i and r_{i+1} have been measured. The variable at r_j is generated by applying trapezoidal rule such as:

$$\left.\begin{aligned} f_j \cdot r_j &= \frac{f_i \cdot r_i + f_{i-1}\cdot r_{i-1}}{2} \\ \Delta r_j &= \Delta r_i = r_i - r_{i-1} \end{aligned}\right\} \rightarrow f_j \cdot r_j \cdot \Delta r_j = \frac{\left(f_i \cdot r_i + f_{i-1}\cdot r_{i-1}\right)\cdot \left|r_i - r_{i-1}\right|}{2} \tag{66}$$

By introducing Equation 67, Equation 66 is rewritten as:

$$\langle f \rangle = \sum \frac{\left(f_i \cdot r_i + f_{i-1}\cdot r_{i-1}\right)\cdot \left|r_i - r_{i-1}\right|}{2R^2} \tag{67}$$

If variable f is not attached to the walls of the test section:

$$R = \frac{R_{WallSup} - R_{WallInf}}{2} \tag{68}$$

APPENDIX 4 - INSTRUMENTATION DETAILS

A. Acquisition and Analysis Software of Optical Fiber Probes

In order to calculate intercept lengths, the velocity of each bubble is measured and the individual velocity value is combined with the considered duration of the gas phase. This calculation gives the distribution of intercept lengths ($h_c(l)$) as in Figure A4..

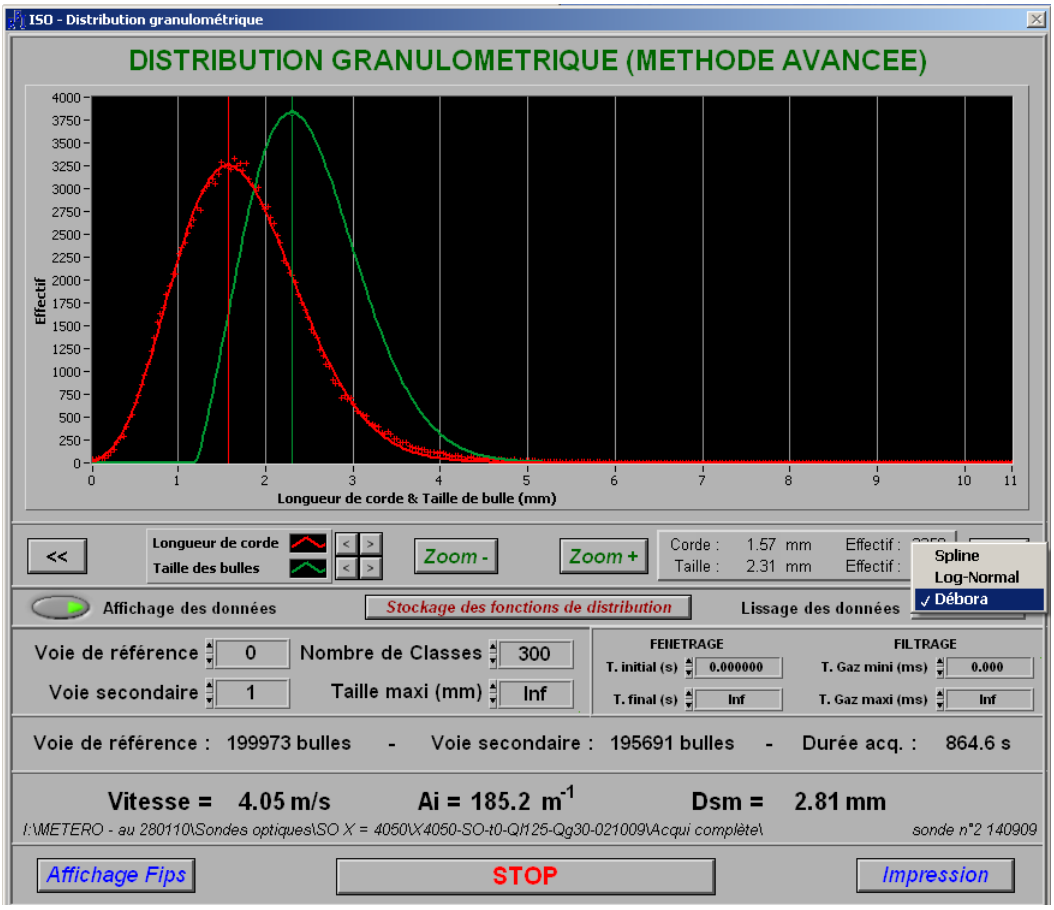

Figure A4.1 - Displaying the bubble size with an improved method in ISO

Equation (3) given in Section 3.1.3.3 is used to calculate the bubble diameter distribution. This equation brings a derivative and assumes that the histogram of intercept length is regular and smooth. On the contrary, the intercept length distribution histograms are often noisy. In ISO software, there exist three methods which can interpolate the best intercept distribution function. These three methods are:

- Spline smoothing
- Log-normal function
- Predefined smoothing function “Debora”.

The Debora function, created for the measurements in the Debora installation at CEA (Garnier (1998)), is the product of a polynomial and exponential functions as:

$$f_{Deb}(x) = x\left[A_2 + x\left(A_2 A_4^2 + xA_1\right)\right]\exp\left(-A_3 x^2 - A_4^2 x\right) \tag{69}$$

where, A_1, A_2, A_3 and A_4 are adjustable constants.

In addition, certain parameters (for instance, maximum bubble diameter to determine number of the classes) are also adjustable in the software. Changing parameters can improve the agreement between experimental data and interpolation function.

Bottin (2010) stated that the interpolation of intercept length distribution function is a time consuming process and none of these three functions (Spline, Log-normal and Debora) represent accurately the intercept length distributions for an entire profile. In addition, heterogeneity of intercept length distribution functions and associated interpolation functions also prevents any automatic process. Thus, the definition of the optimal interpolating curve is user dependent and it is based on visual examination.

In the METERO experiment, it was observed that interpolation of intercept length distribution becomes more difficult for some measurement points located at the center of the test section. This problem was also reported by Bottin (2010). As seen in Figure A4.2 where the histograms of raw intercept lengths, interpolation functions and bubble diameter distributions are given, there exist two peaks in the bubble diameter histogram. The figure shows that only Spline function has the best superimposition of the intercept the intercept length distributions. On the other hand, the deducted bubble diameter histogram is partially deformed and represents a poor bubble size distribution.

It was concluded that the process to calculate the bubble diameter distributions from the intercept length distributions is very sensitive and it should be optimized by finding an interpolation function which can be applied to all intercept length distributions. This will automatize the process.

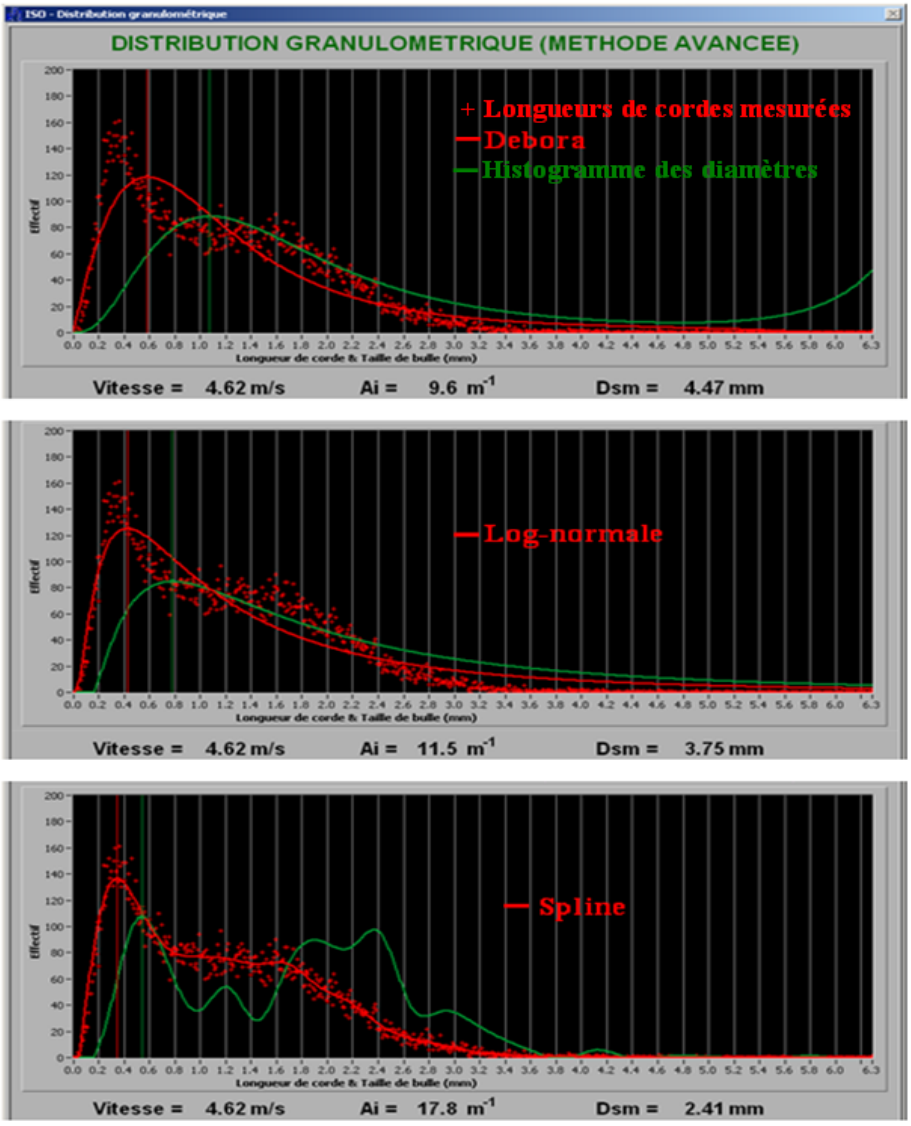

Figure A4.2 - Illustration of the intercept/diameter conversion

B. Uncertainty of Spatial Averaging for Optical Fiber Probes

Bottin (2010) studied the uncertainty of spatial averaging for optical probe measurements. For this purpose, the author averaged the data presented by Andreussi et al. (1999) by using two different averaging methods such as:

- Averaging single vertical profiles by orthoradial layers (a method used for measurements in the METERO experiment) which is presented on the left side of Figure A4.3
- Averaging four profiles in cylindrical coordinates by assuming that the flow is symmetrical with respect to the vertical axis, shown on the right side of Figure A4.3

This uncertainty study showed that the difference between two integration methods is ±6% while averaging four profiles is taken as the reference. Furthermore, after taking into account the measurement uncertainty of the reference data (Andreussi et al., 1999), the estimated maximum uncertainty of averaging is around ±10%.

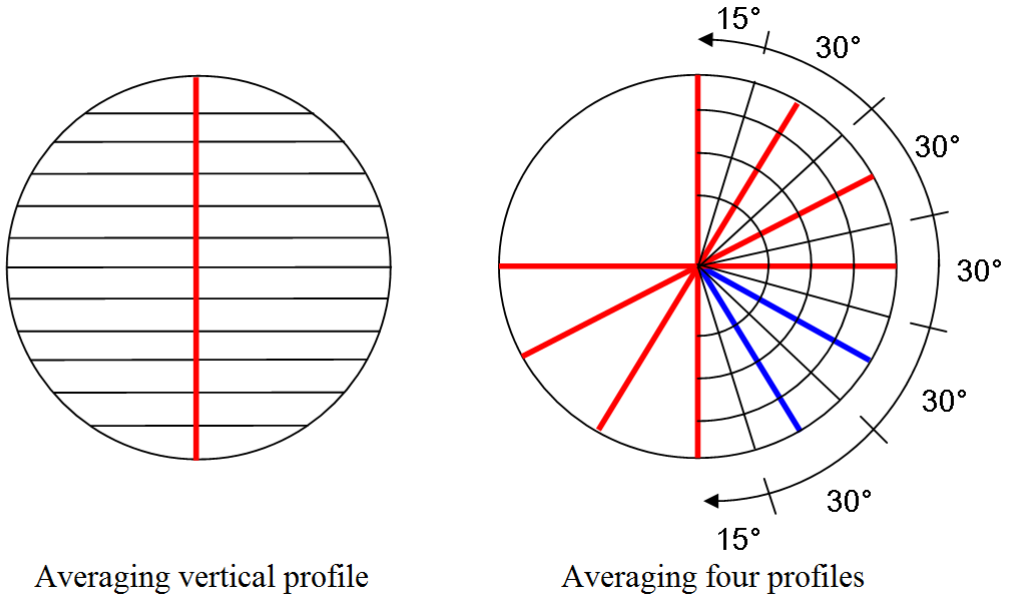

Figure A4.3 - Representation of the averaging methods based on the measurements of Andreussi et al. (1999)

C. Conversion of Voltages into Velocities

The conversion of raw voltages into velocities requires several processing steps. The first step is the calculation of the calibration coefficients. The calibration coefficients are obtained from the voltage signals during the calibration acquisitions with a proper data processing. Afterwards, the calibration coefficients are used for the calculation of velocities.

In the next step, a Labview™ routine, named as “exploitation-donnees-k.vi”, is used to convert the raw voltage signals into the liquid velocities. For the conversion process, the routine requires probe characteristics, acquisition conditions, calibration coefficients and raw voltage signals. Once all the quantities are introduced, the routine calls a Labview™ subroutine (named as “evaluation_k.vi” and seen in Figure A4.4) which concerts voltage signals, calculates liquid velocity and turbulent kinetic energy. In addition, this subroutine records the calculated values into a file.

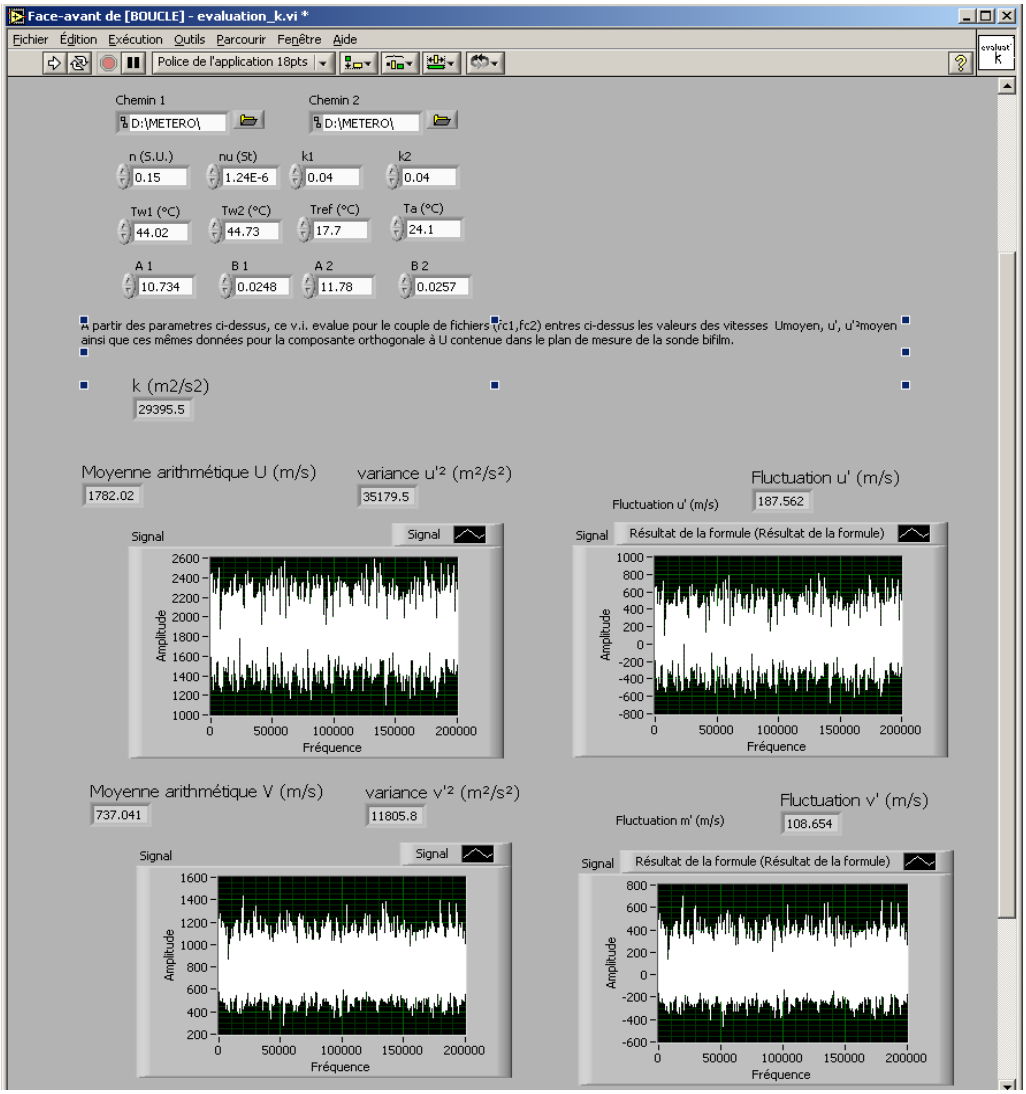

Figure A4.4 - Subroutine of explotation-donnes-k.vi

D. Statistical Test for Measurement Convergence of Hot-film Anemometry

A statistical test of measurement convergence was performed by conical hot-film probes by Bottin (2010). The results showed that acquisition of 200000 samples are sufficient to obtain reliable statistical calculations in single phase flows as see in Figure A4.5. In addition, the author stated that it is not easy to predict the number of samples remaining after the phase discrimination in two-phase flows. Thus, the number of samples acquired in two-phase flows should be greater than in single phase flows in order to ensure statistical converged results. For this reason, the number of samples in two-phase flows has been chosen as 3.6 million.

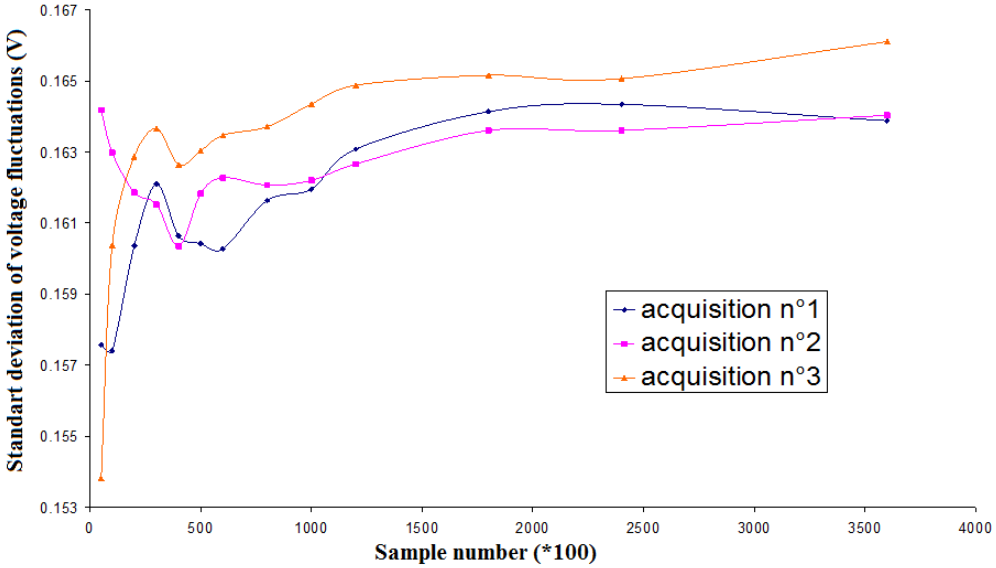

Figure A4.5 - Study of statistical convergence for the conical probe: plot of the standard deviation of the voltage fluctuations depending on the number of samples (Bottin, 2010)

E. Calibration of Hot-film Anemometry Measurements

The calibration measurements are always performed in single phase flow before the acquisitions. The probe is located in the center of the test section where axial component of liquid velocity (U_{axe}) is maximum. The actual velocity of liquid is known by the help of Pitot tube measurements. Calibration measurements are done for various liquid velocities. Afterwards, the voltage across the films (e_i) can be plotted as functions of effective cooling velocities (U_{eff1} and U_{eff2}). The coefficients of the King's law can be calculated by using linear interpolation. The influence of the acquisition condition variations can be minimized by performing a systematic calibration before and after each complete profile acquisitions. The coefficients applied for the conversion are derived from the average of these two coefficient sets, as seen in Figure A4.6.

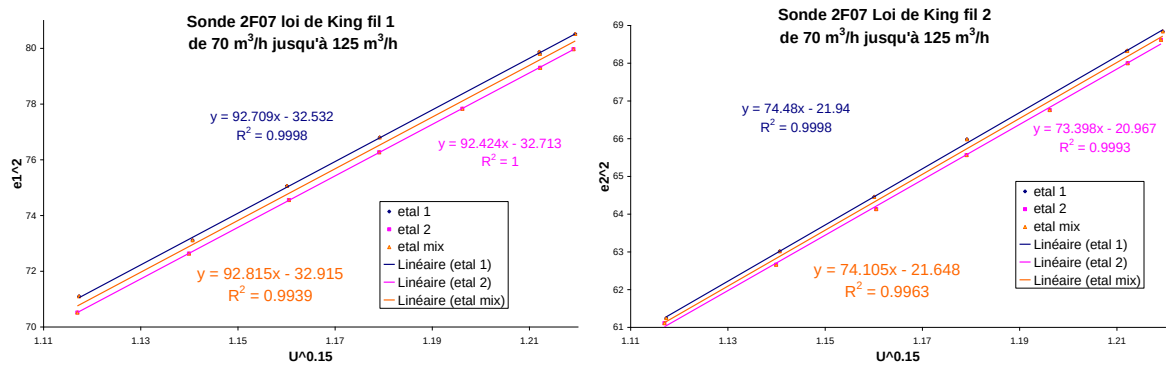

Figure A4.6 - Plot of $e_i^2=f(U_{effi}^n)$ and determination of the calibration constants for a two-component probe (Bottin, 2010)

Bottin (2010) performed several tests at various axial locations (5, 20 and 40 diameters downstream) in order to determine a relationship between axial maximum velocity (U_{axe}) and liquid superficial velocity (V_{deb}) for the METERO experiment by using Pitot tubes. The author has brought up correlations of U_{axe} and V_{deb} for each axial measurement location (as seen in Figure A4.7). These correlations are formulized as:

- at 540 mm from the inlet (5D): $U_{axe} = 1.0339*V_{deb} + 0.0238$ (m/s)
- at 2040 mm from the inlet (20D): $U_{axe} = 1.1193*V_{deb} + 0.0873$ (m/s)

– at 4040 mm from the inlet (40D): U_{axe} = 1.2187*V_{deb} + 0.0387 (m/s)

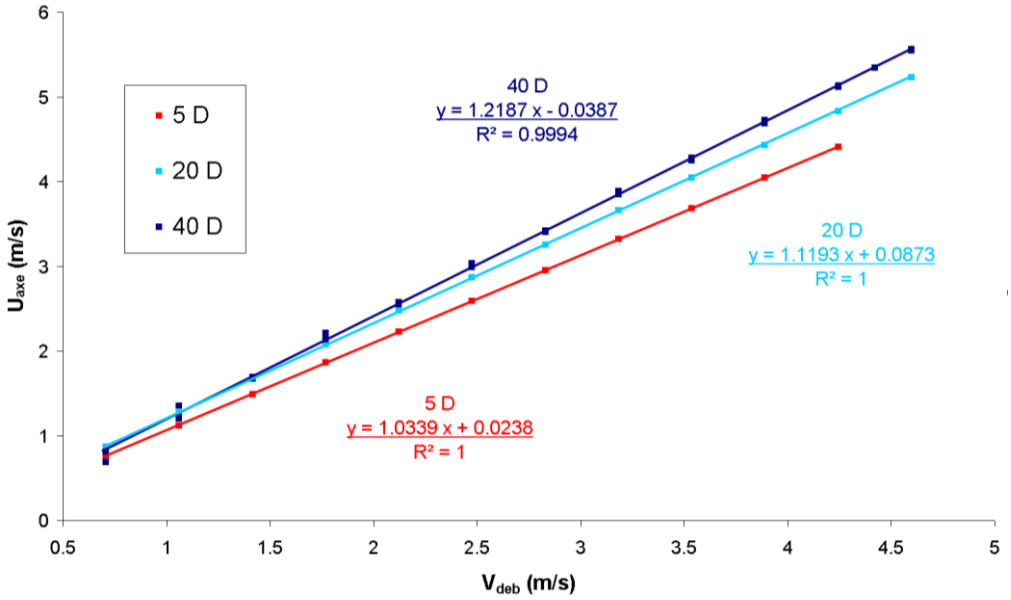

Figure A4.7 - Plot of U_{axe} measured by Pitot tube as a function of V_{deb} (Bottin, 2010)

APPENDIX 5 - DISPERSED BUBBLY FLOWS

A. Local Flow Quantities

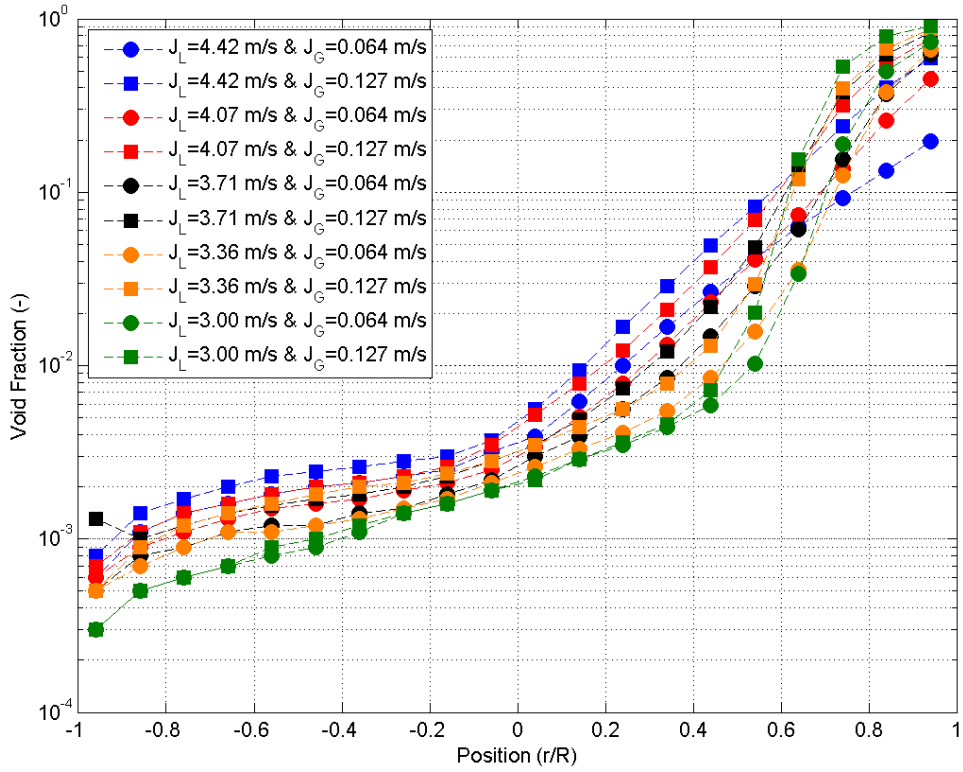

Figure A5.1 - Void fraction profiles measured at 40 diameters for dispersed bubbly flows

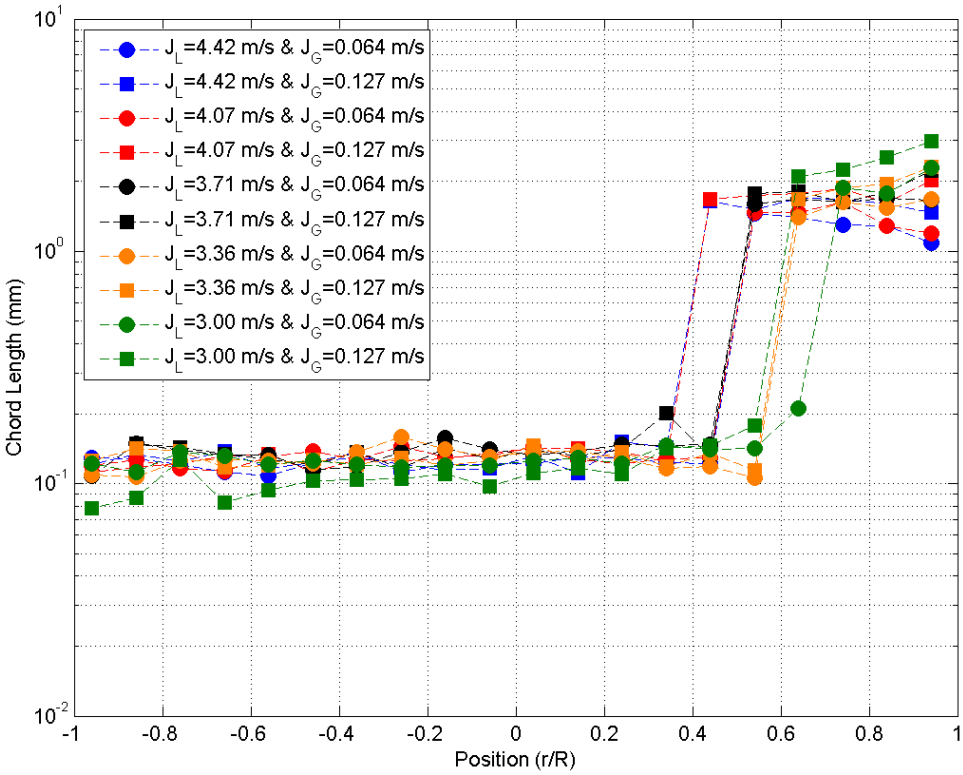

Figure A5.2 - Chord length profiles measured at 40 diameters for dispersed bubbly flows

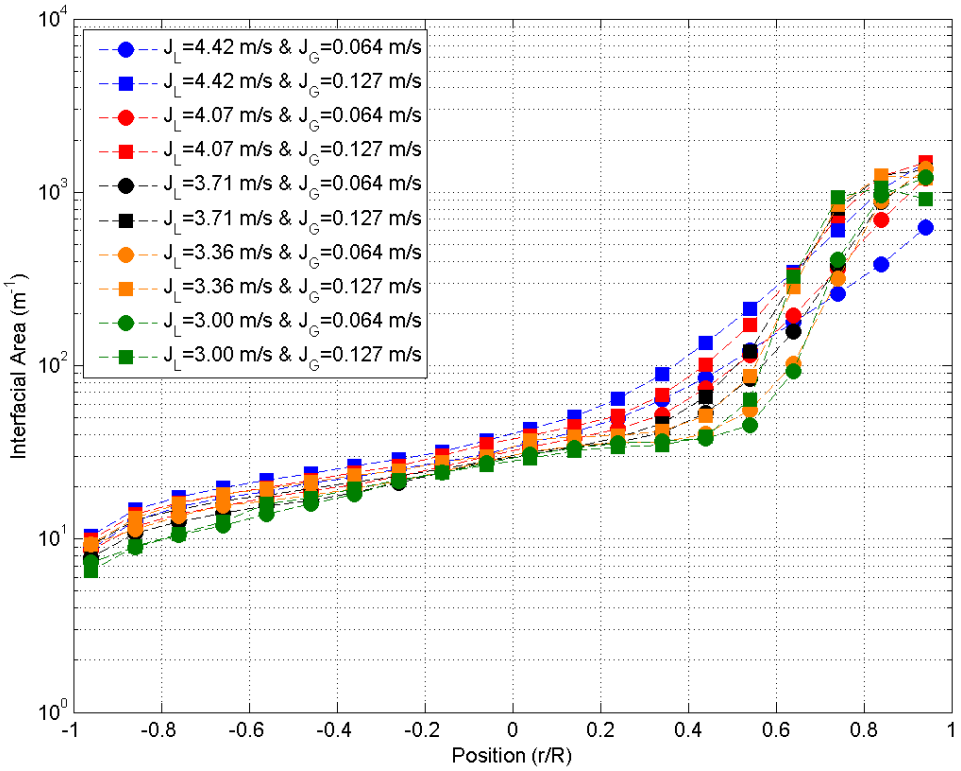

Figure A5.3 - Interfacial area profiles measured at 40 diameters for dispersed bubbly flows

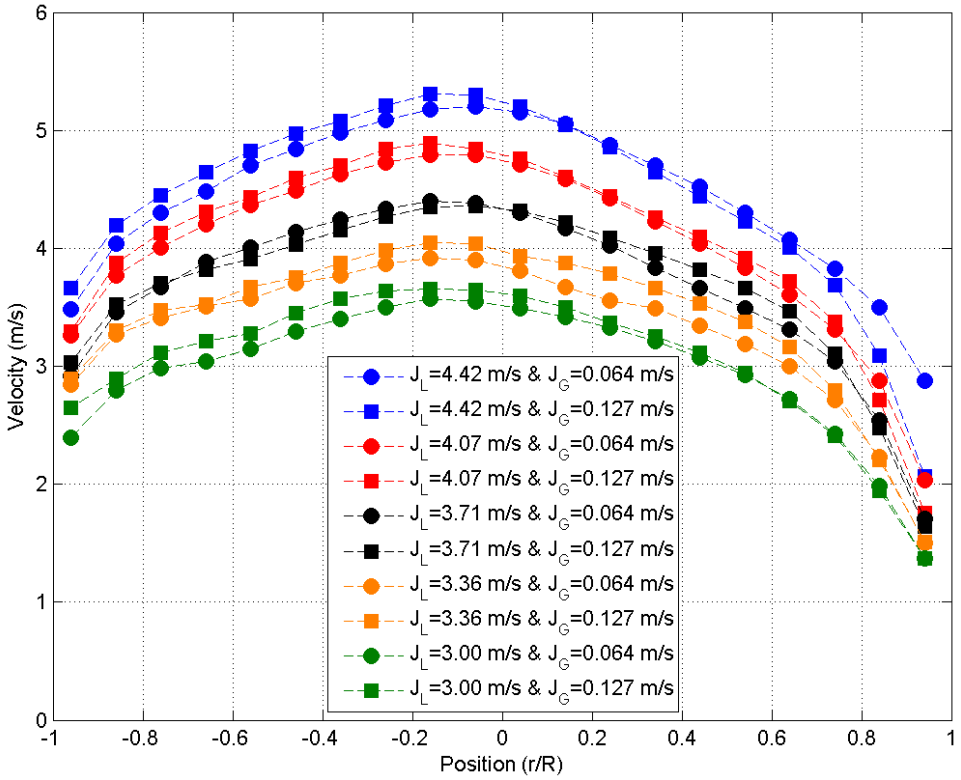

Figure A5.4 - Axial mean bubble velocity profiles measured at 40 diameters for dispersed bubbly flows

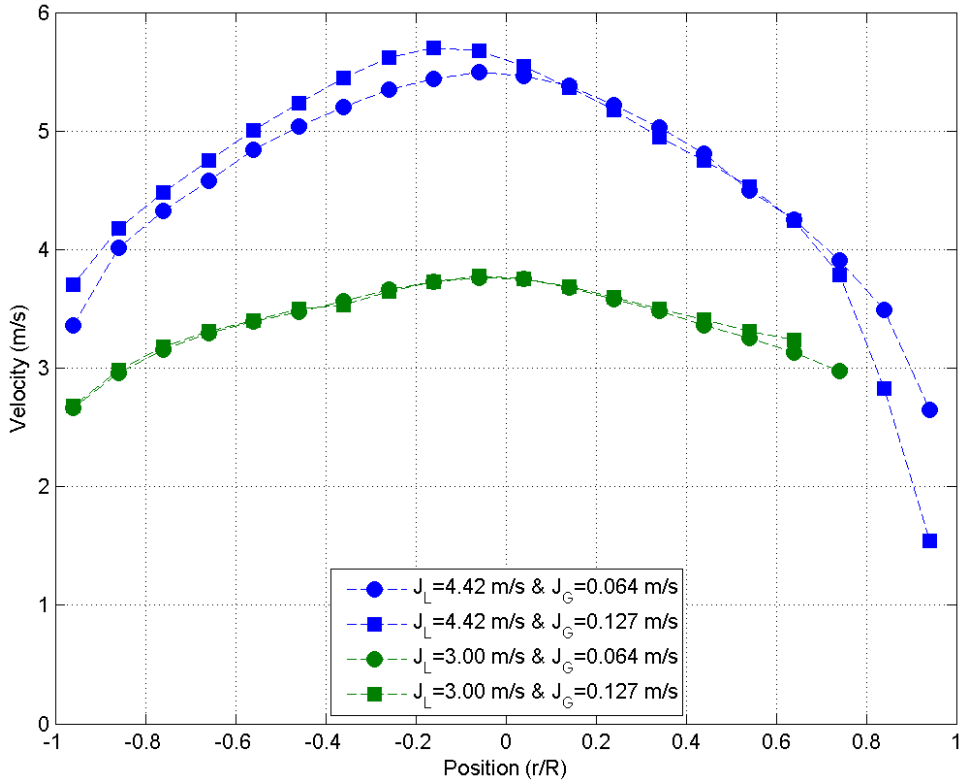

Figure A5.5 - Axial mean liquid velocity profiles measured at 40 diameters

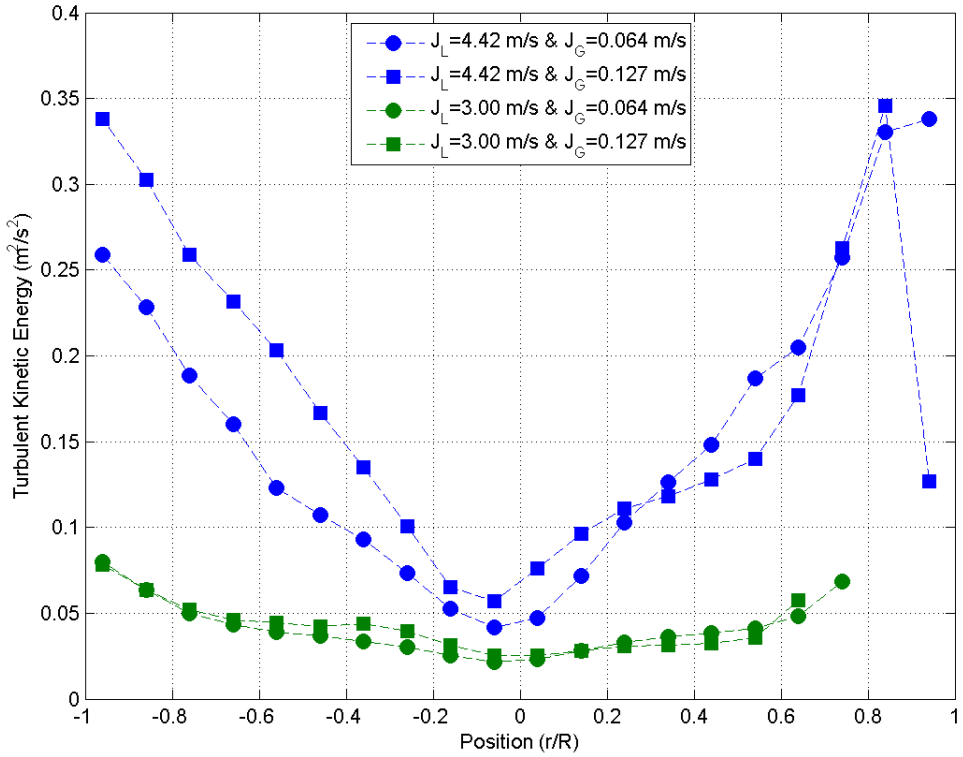

Figure A5.6 - Turbulent kinetic energy profiles measured at 40 diameters for dispersed bubbly flows

B. Axial Evolution of Flow Quantities

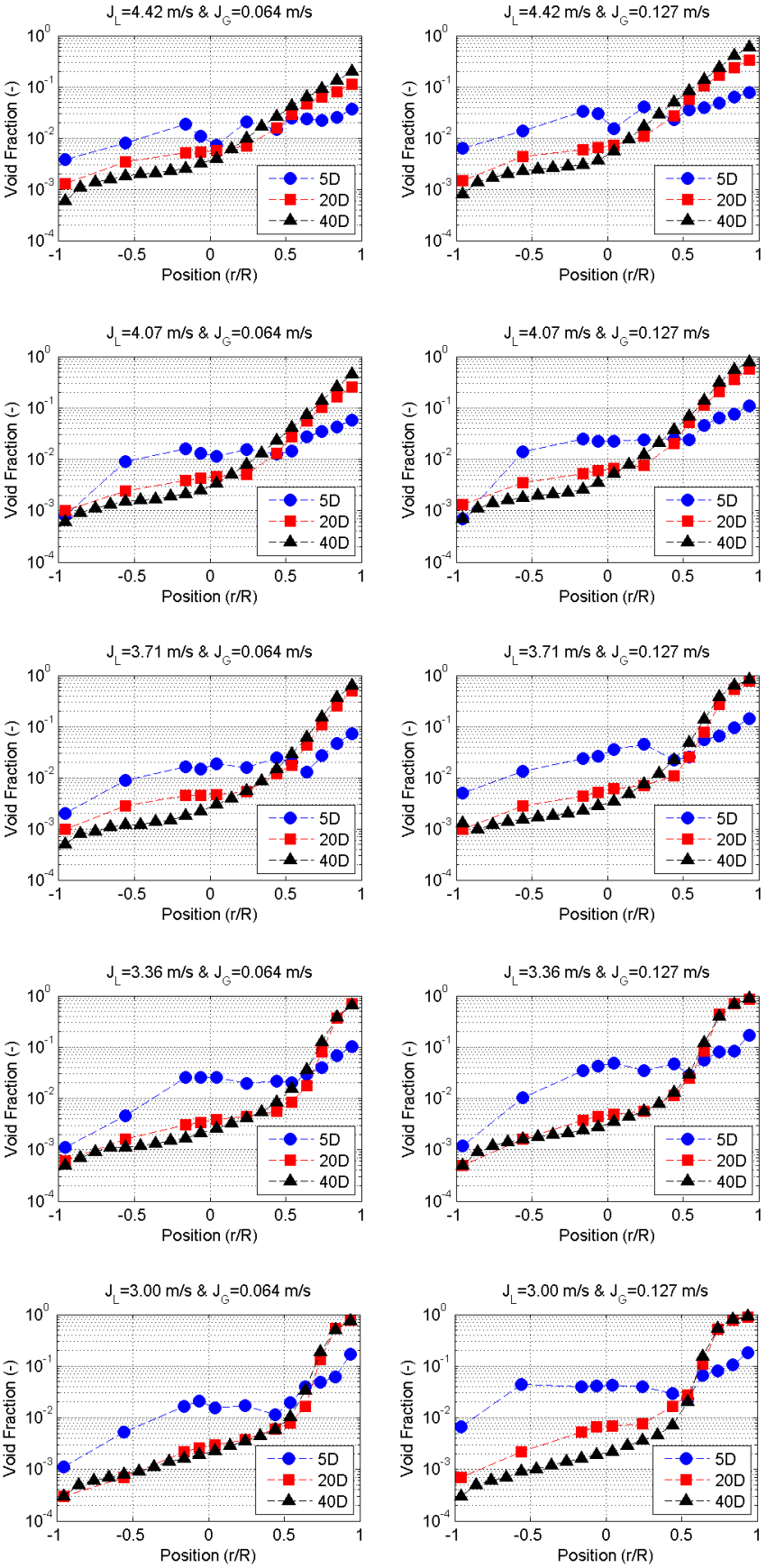

Figure A5.7 - Axial evolution of void fraction for dispersed bubbly flows

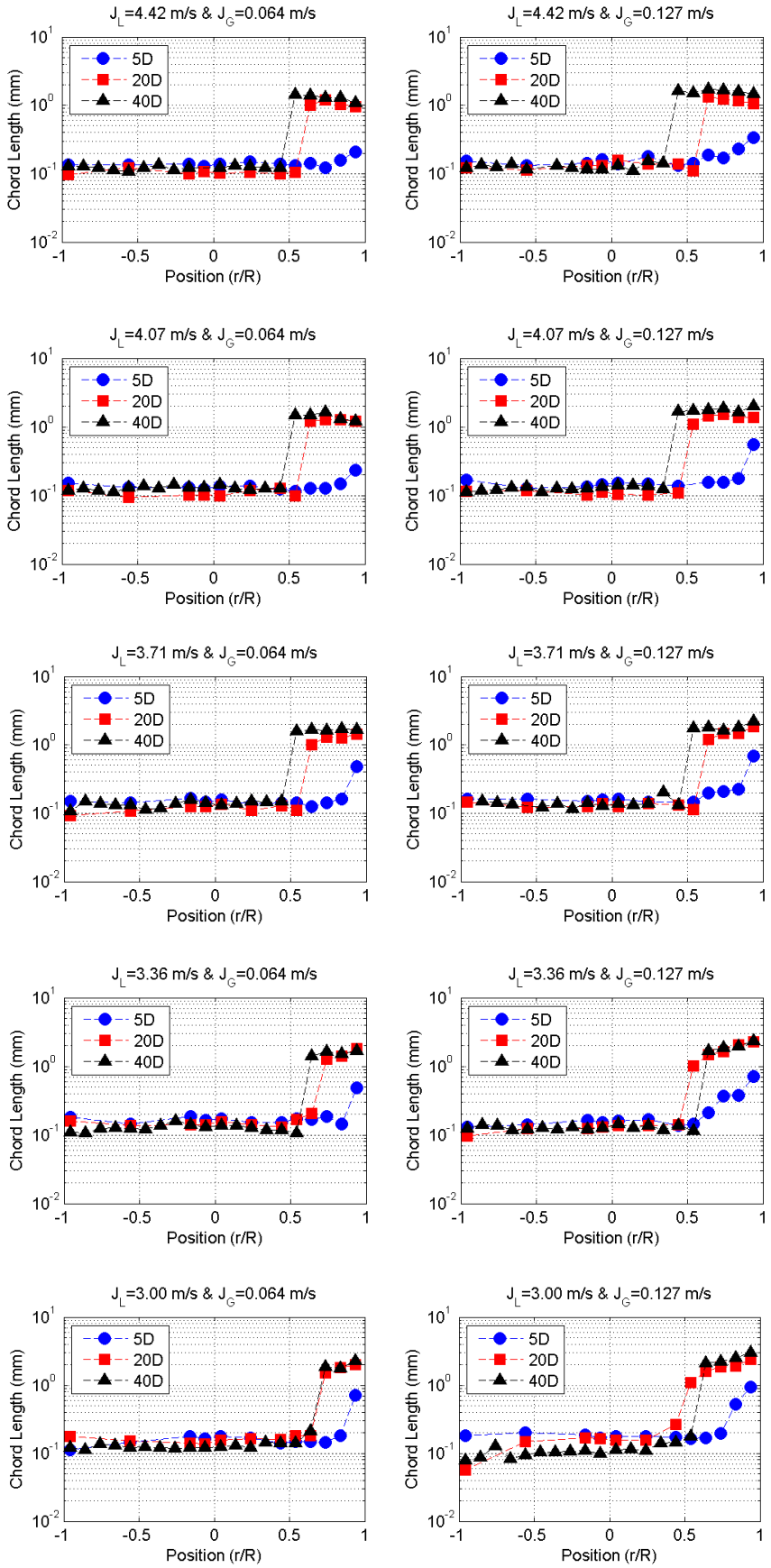

Figure A5.8 - Axial evolution of chord length for dispersed bubbly flows

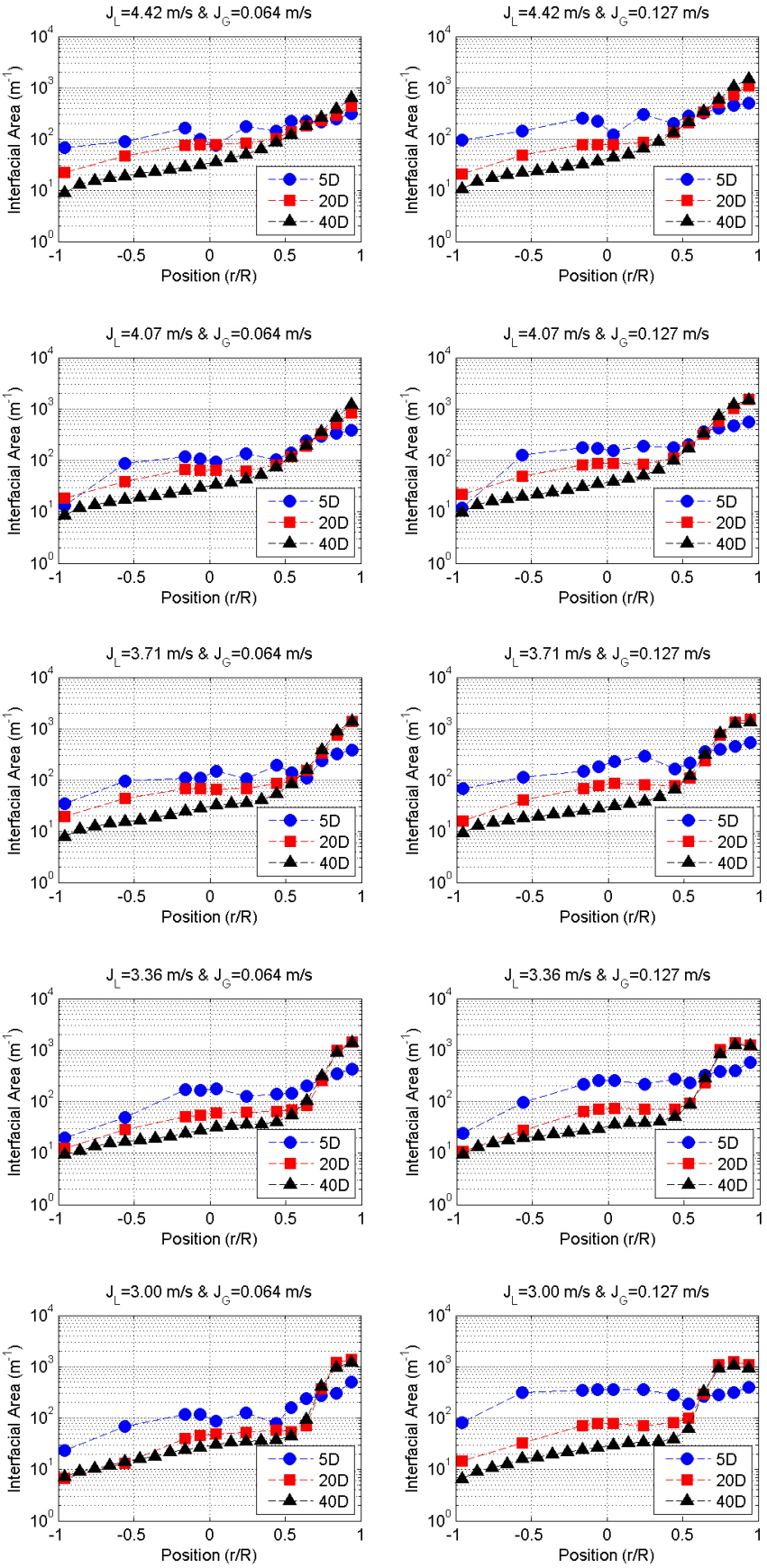

Figure A5.9 - Axial evolution of interfacial area for dispersed bubbly flows

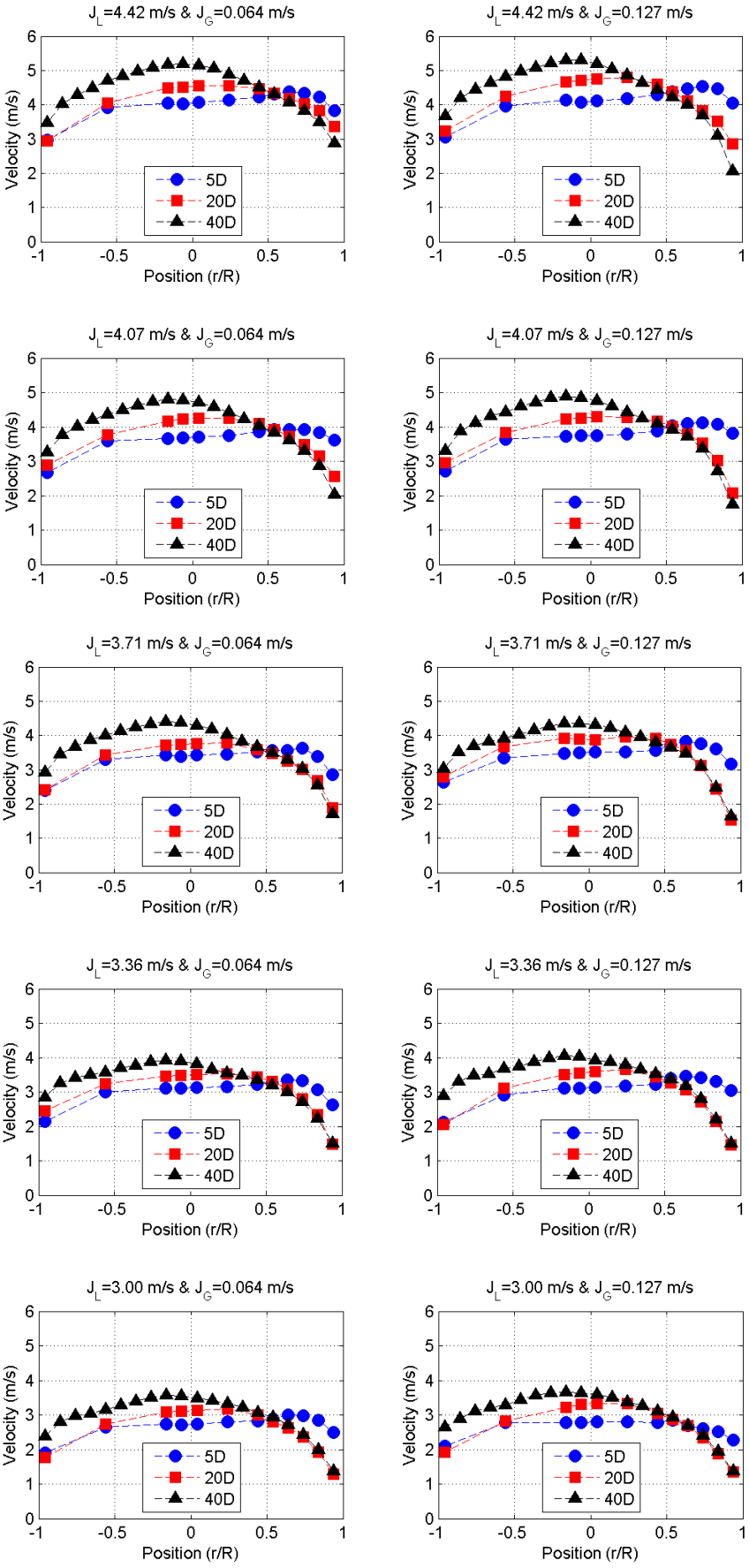

Figure A5.10 - Axial evolution of mean bubble velocity for dispersed bubbly flows

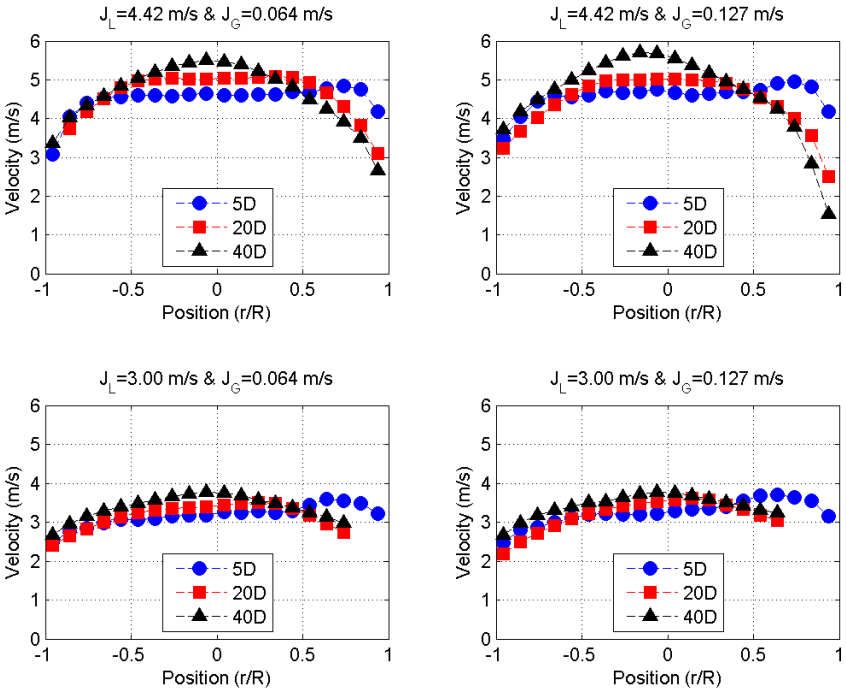

Figure A5.11 - Axial evolution of mean liquid velocity

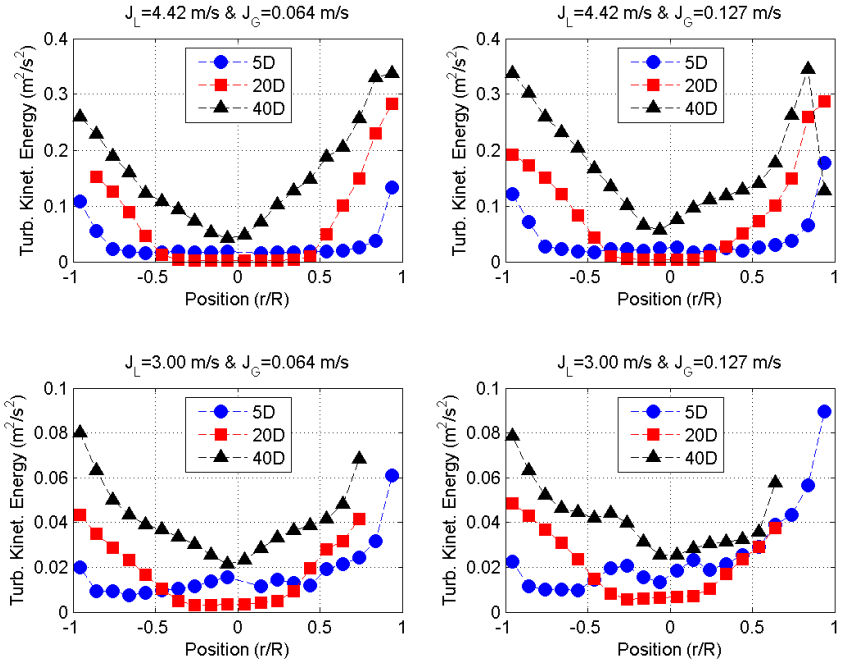

Figure A5.12 - Axial evolution of turbulent kinetic energy for dispersed bubbly flows

APPENDIX 6 - INTERMITTENT FLOWS

A. Local Flow Quantities

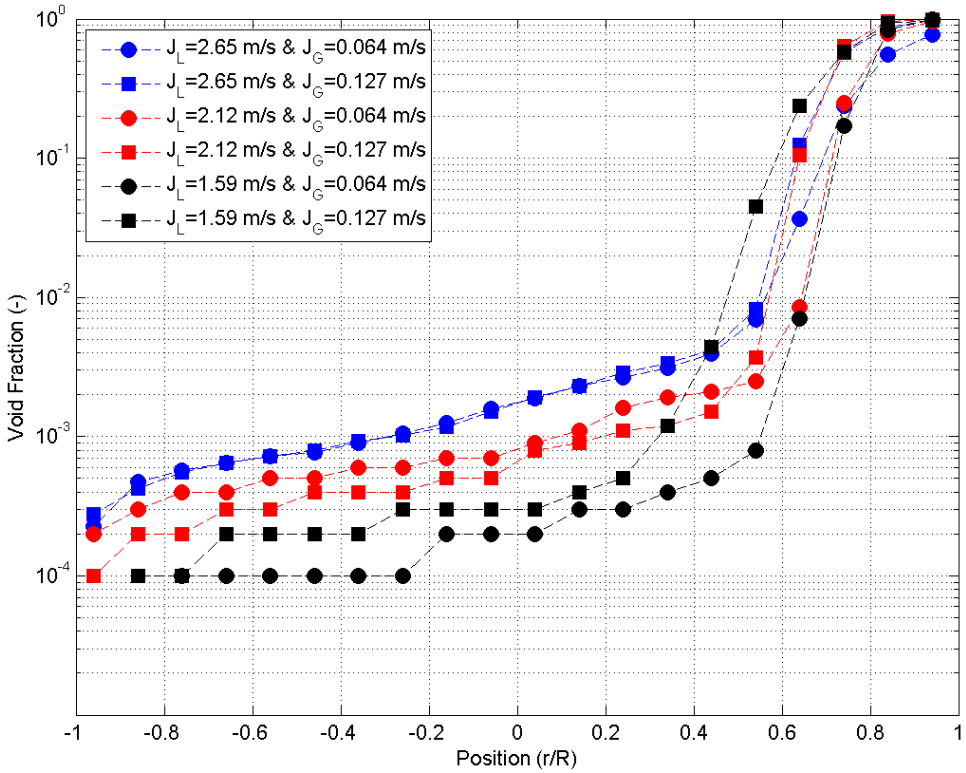

Figure A6.1 - Void fraction profiles measured at 40 diameters for intermittent flows

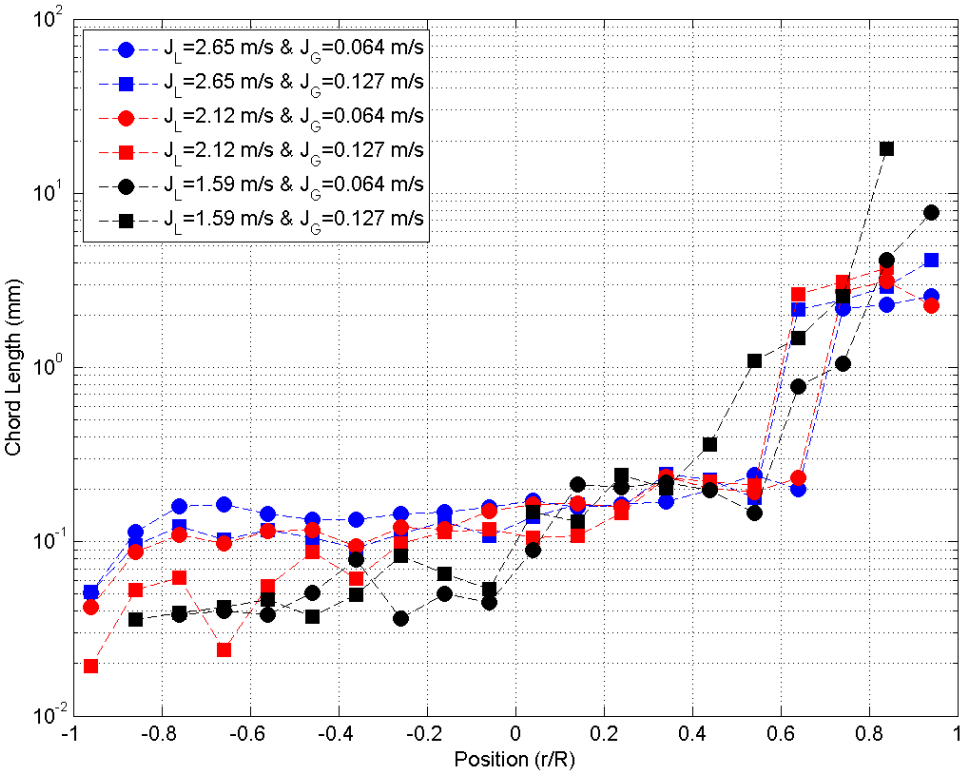

Figure A6.2 - Chord length profiles measured at 40 diameters for intermittent flows

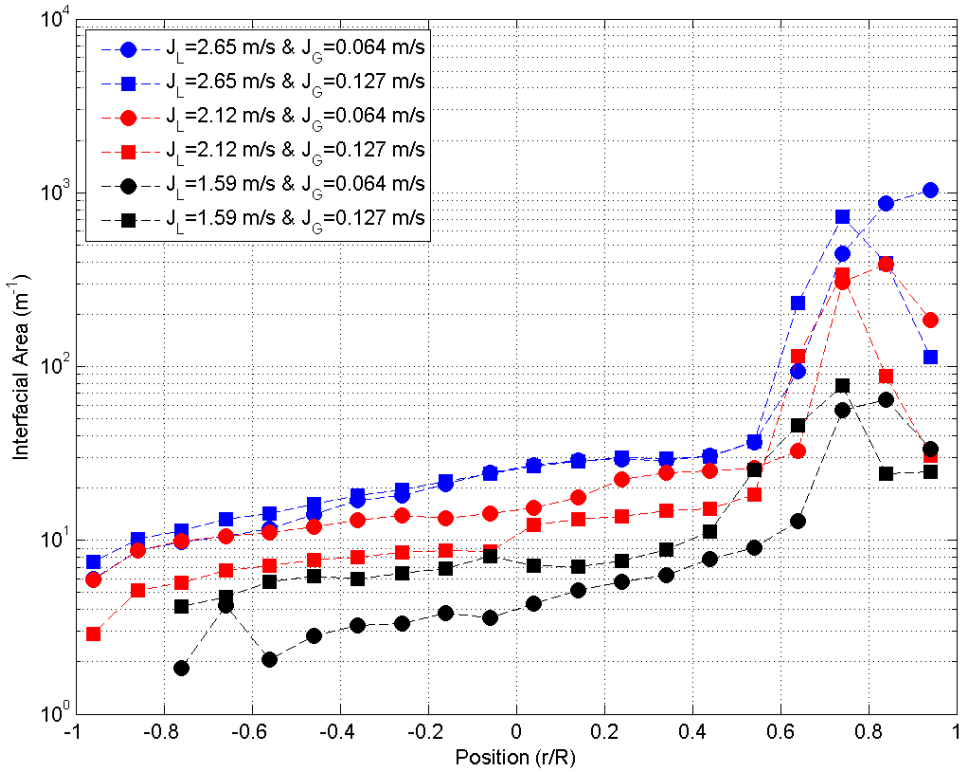

Figure A6.3 - Interfacial area profiles measured at 40 diameters for intermittent flows

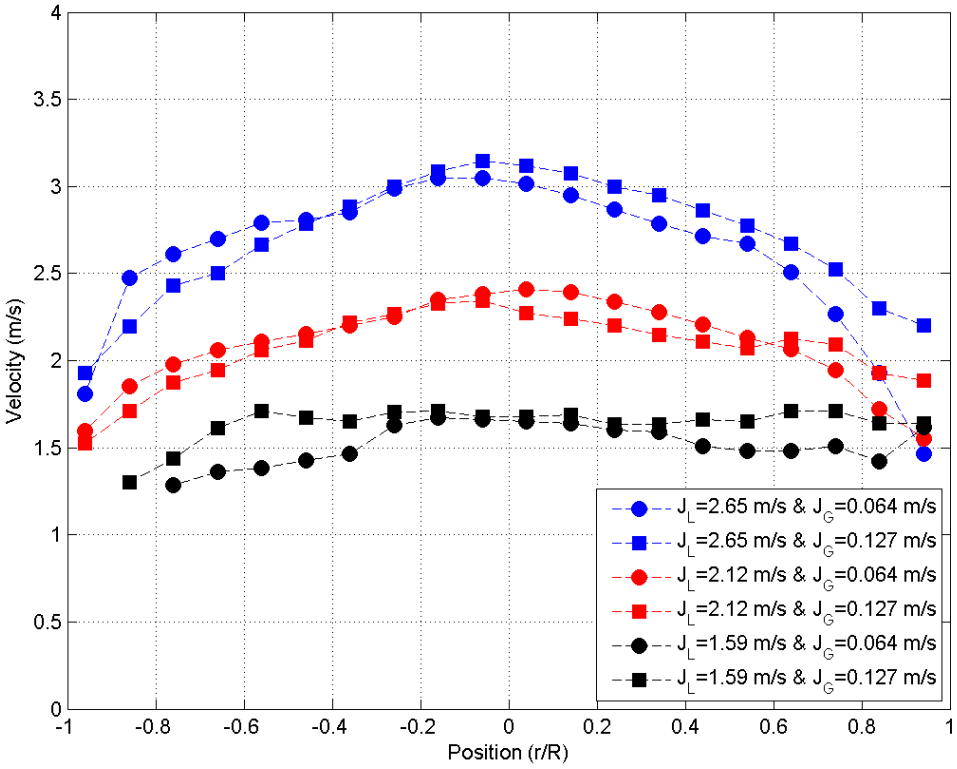

Figure A6.4 - Axial mean bubble velocity profiles measured at 40 diameters for intermittent flows

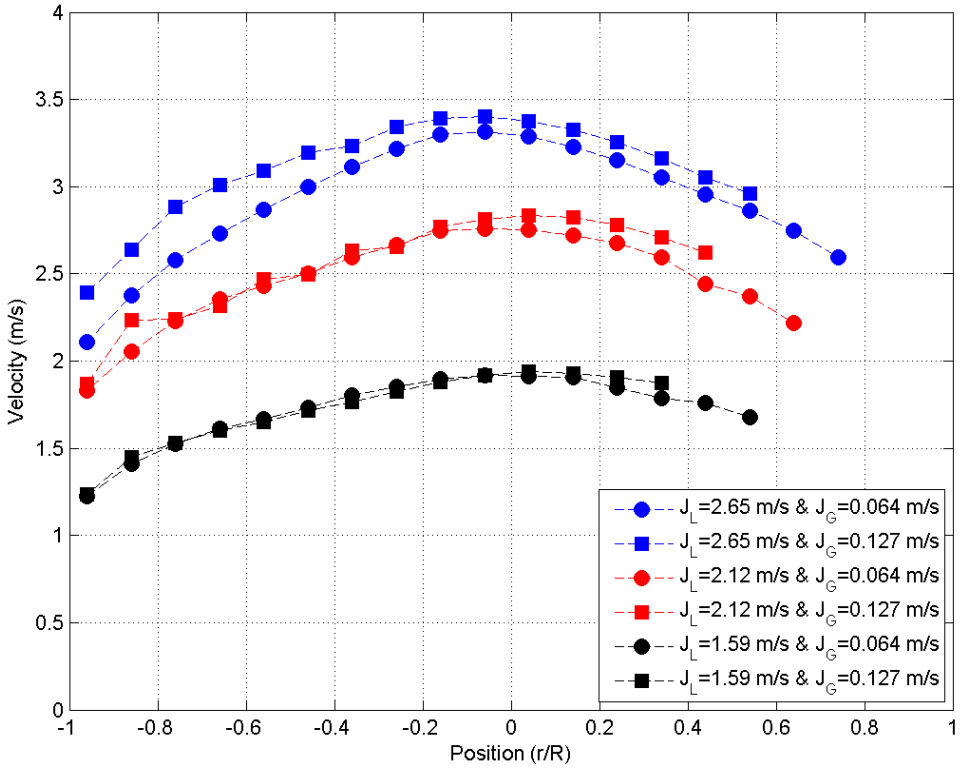

Figure A6.5 - Axial mean liquid velocity profiles measured at 40 diameters for intermittent flows

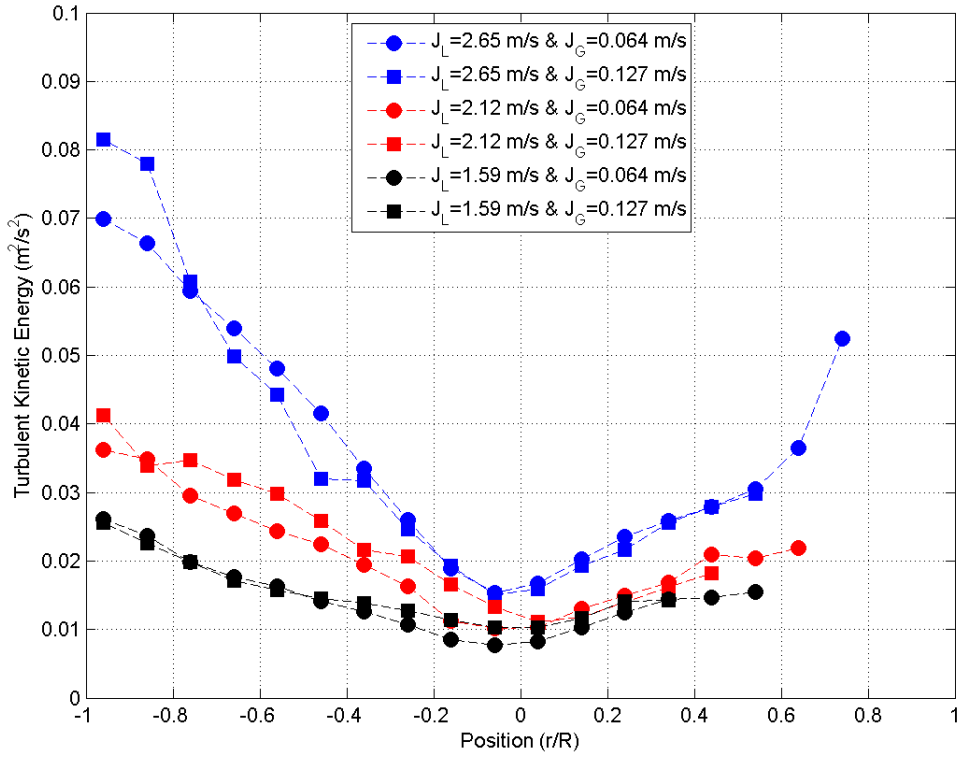

Figure A6.6 - Turbulent kinetic energy profiles measured at 40 diameters for intermittent flows

B. Axial Evolution of Flow Quantities

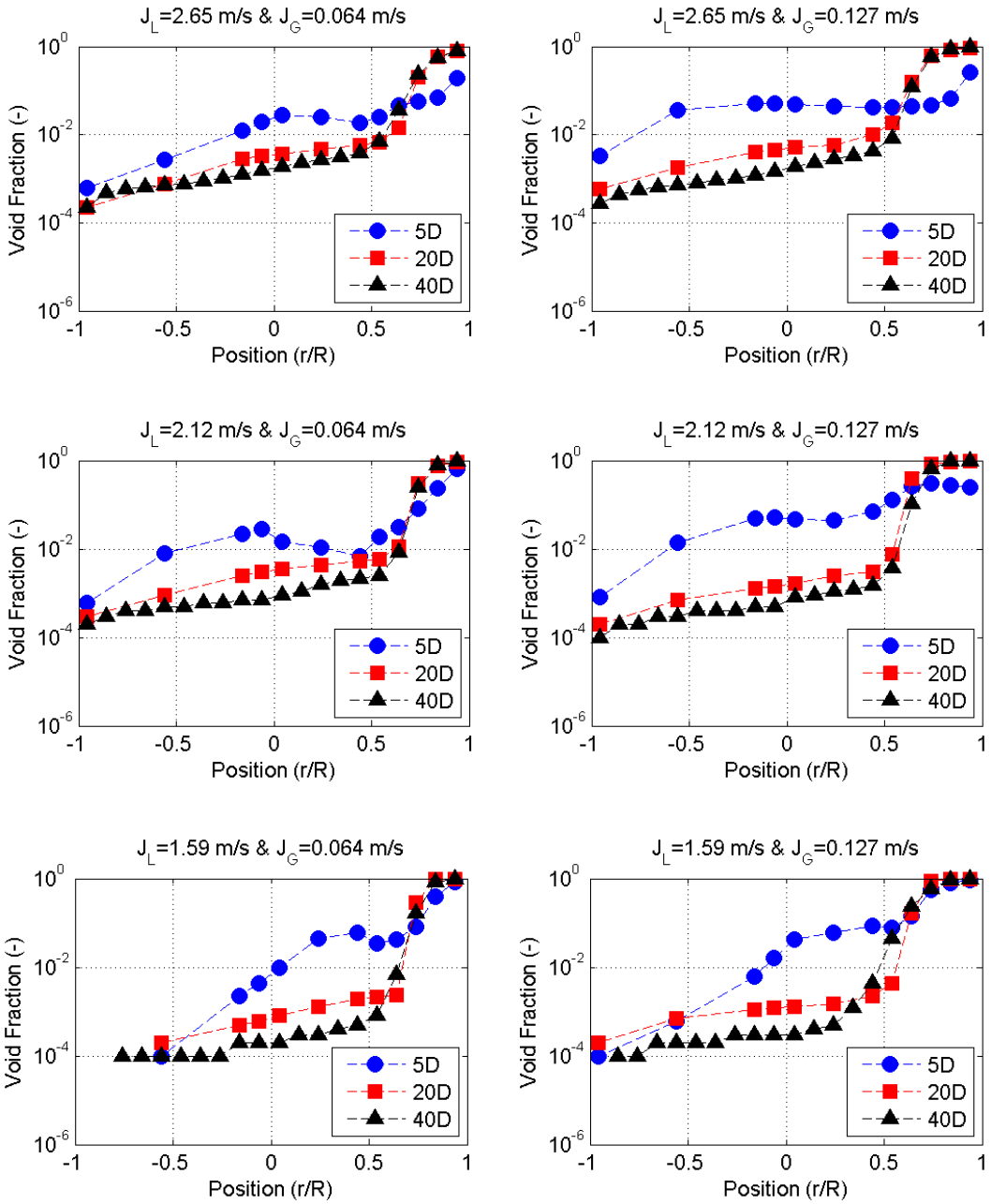

Figure A6.7 - Axial evolution of void fraction for intermittent flows

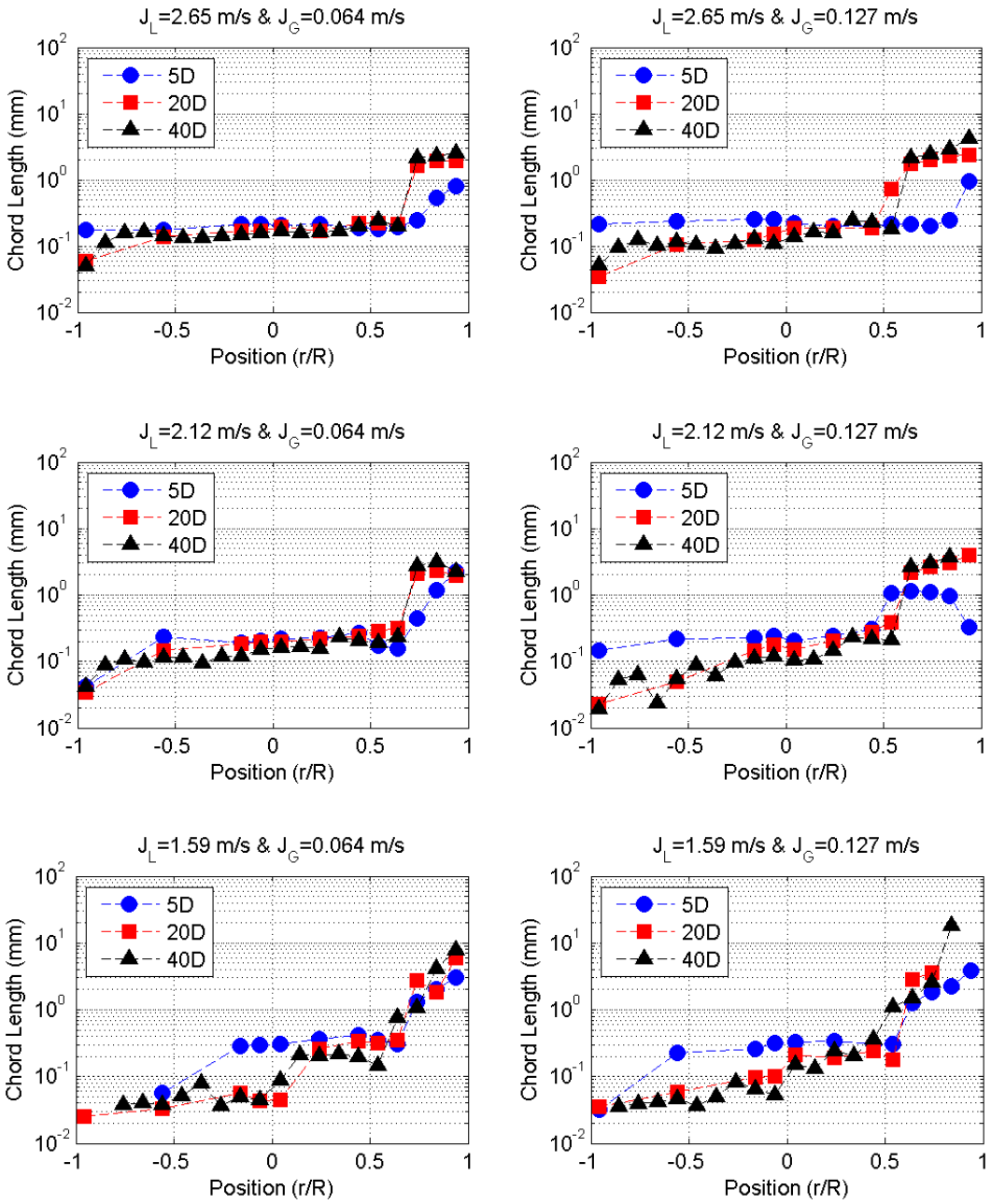

Figure A6.8 - Axial evolution of chord length for intermittent flows

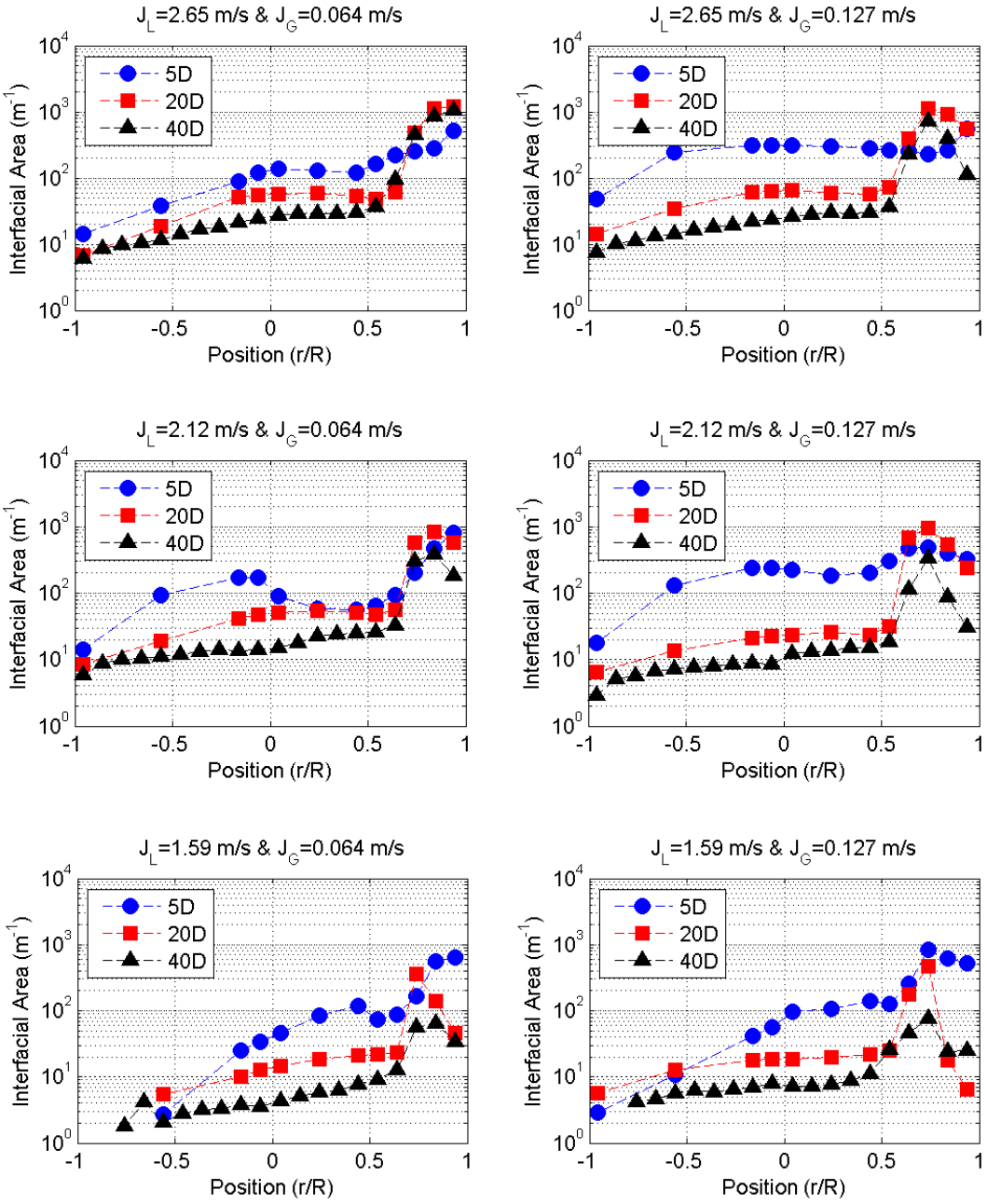

Figure A6.9 - Axial evolution of interfacial area for intermittent flows

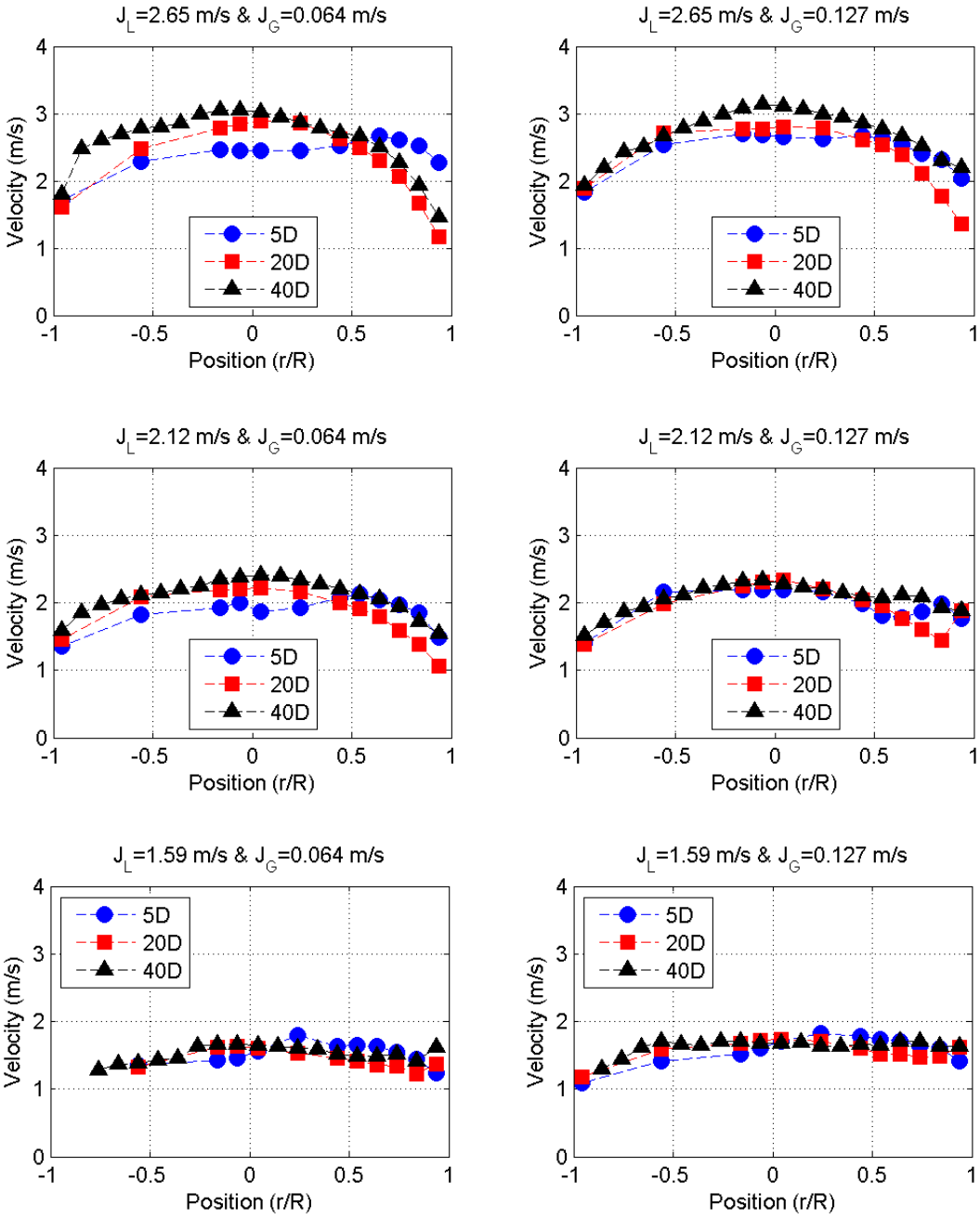

Figure A6.10 - Axial evolution of mean bubble velocity for intermittent flows

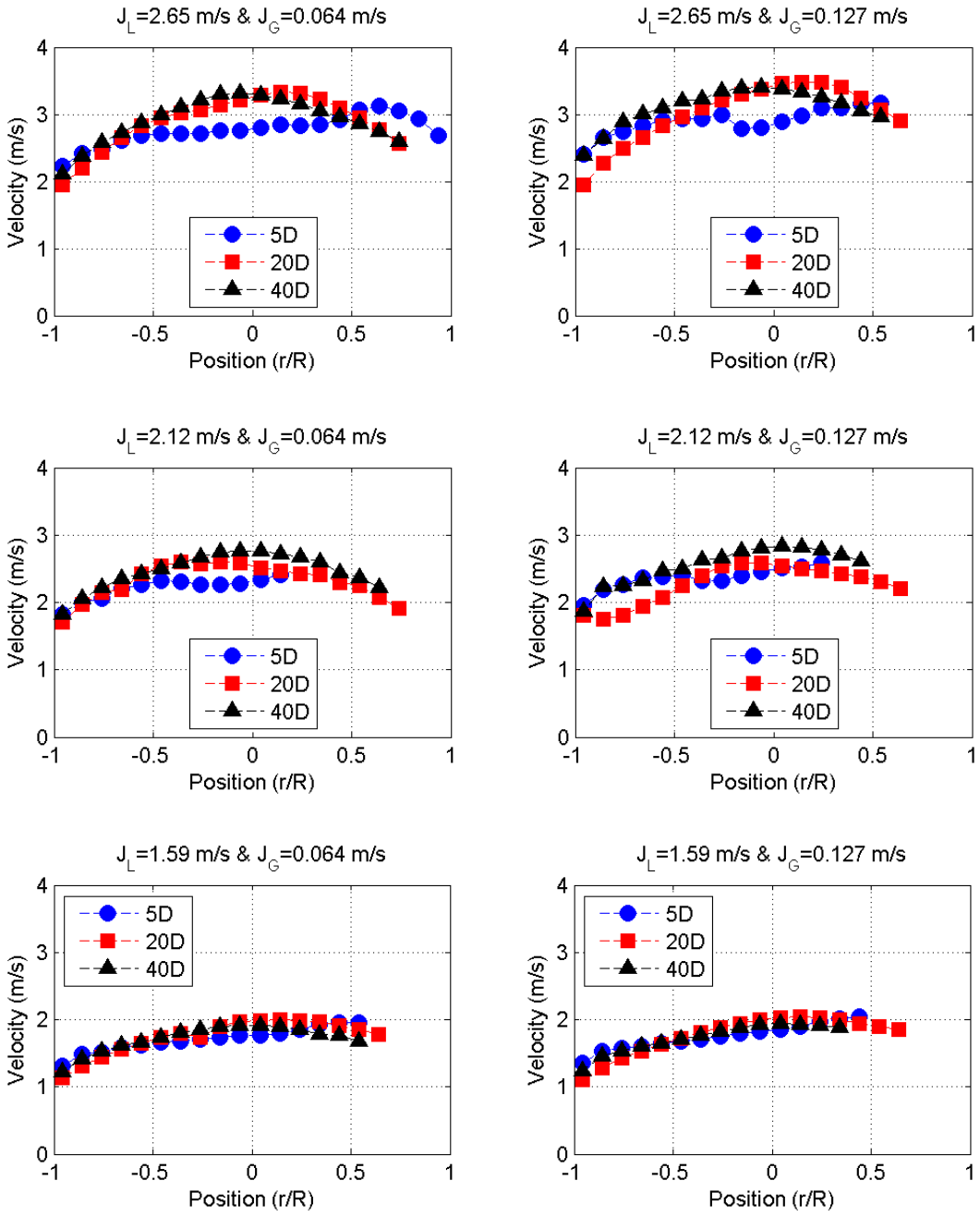

Figure A6.11 - Axial evolution of mean liquid velocity for intermittent flows

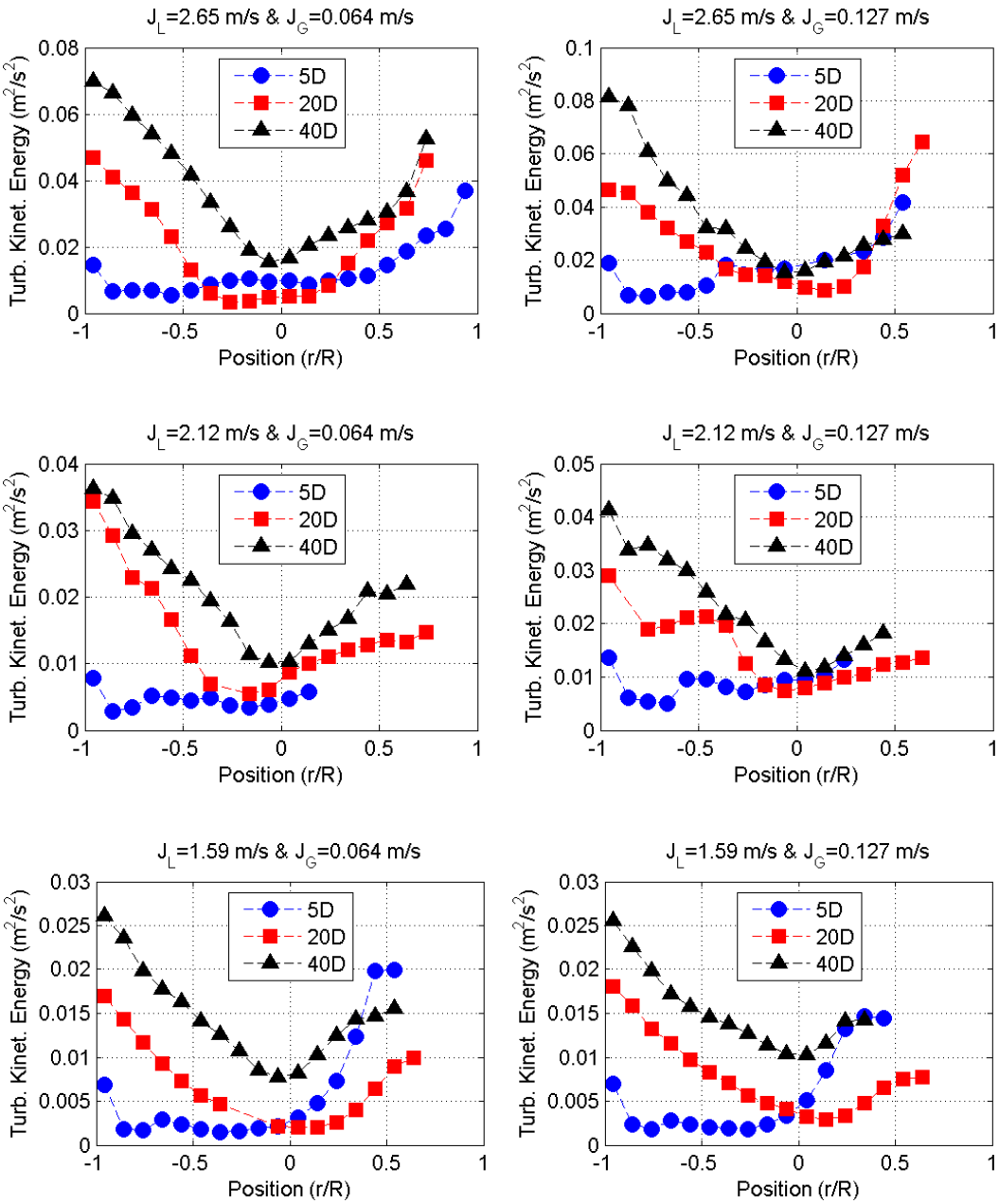

Figure A6.12 - Axial evolution of turbulent kinetic energy

RESUME FRANÇAIS

RESUME FRANÇAIS

1. Introduction

Le propos de cette thèse est d'étudier les évolutions des écoulements diphasiques en conduite horizontale pour comprendre la physique du développement axial des écoulements. De plus, ces études expérimentales permettront d'améliorer les modèles existants dans le code CMFD NEPTUNE et le code système CATHARE 3.

1.1. Contexte Industriel

Les écoulements diphasiques peuvent être rencontrés durant les phases accidentelles dans une centrale nucléaire. Une *brèche* sur le circuit primaire peut causer *une vaporisation violente appelée flashing*. Cela entraine la création d'écoulements diphasiques dans le circuit primaire (Figure R.1).

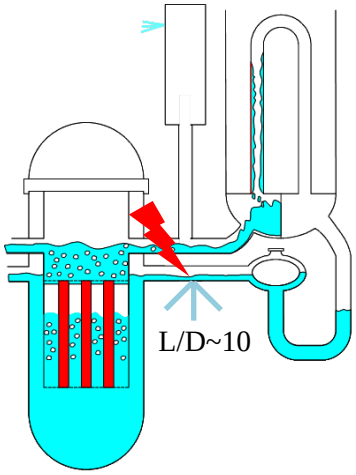

Figure R.1 - La phase accidentelle dans une centrale nucléaire

L'importance du débit brèche et du titre dépend très fortement du régime d'écoulements dans le tuyau où est située cette brèche. La vitesse de dépressurisation du circuit et son refroidissement en dépendent fortement. Ainsi une fuite en vapeur permettra l'évacuation efficace d'énergie et une dépressurisation rapide permettant des injections de sûreté rapides tandis qu'une fuite liquide conduira à une dépressurisation lente et une perte de masse importante. Entre ces 2 cas extrêmes, les conditions à la brèche seront déterminantes pour l'évolution de l'accident et sont donc importantes à calculer.

Pour connaître le régime d'écoulement dans un tuyau on utilise des cartes d'écoulement. Elles ont été établies sur des géométries très élancées où les mesures sont effectuées très loin de l'entrée pour s'affranchir des conditions aux limites du système et obtenir ainsi des cartes universelles. Dans un circuit de réacteur nucléaire, les rapports d'allongement sont très petits, de l'ordre de dix. Par conséquent, les écoulements ne sont jamais développés ce qui nécessite d'étudier leur établissement à partir de l'entrée.

Les nouveaux codes des calculs développés dans projet *NEPTUNE* pour *la sûreté nucléaire* : Neptune CMFD et CATHARE 3, ont besoin de plus de données expérimentales pour valider les modèles de turbulence et d'aire interfaciale d'une part et les critères de transition de régimes d'écoulements d'autre part.

1.2. Contexte Académique

En ce qui concerne la recherche académique, les écoulements diphasiques sont documentés en détails dans la littérature (Figure R.2 et Figure R.3). Par exemple, il existe de beaucoup des travaux sur les écoulements diphasiques en conduite verticale, mais assez peu en conduite horizontale pour lesquels il n'existe pas de représentation axiale détaillée des grandeurs caractéristiques. Pour finir, toutes les recherches ont été faites pour des écoulements développées et il y a donc des lacunes dans la connaissance de l'évolution axiale des écoulements horizontaux.

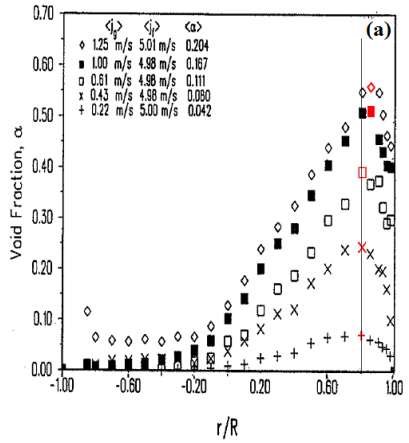

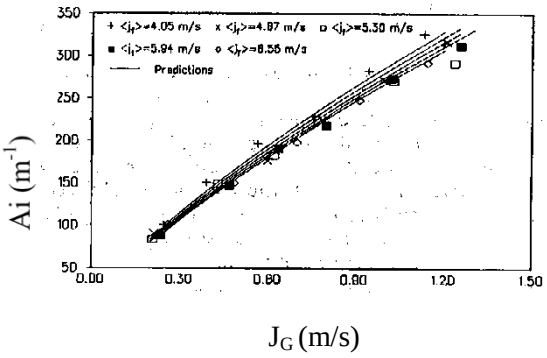

(b)

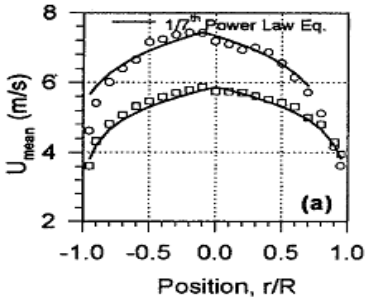

(c)

Figure R.2 - Les profils des grandeurs caractéristiques d'écoulement en écoulements dispersés : (a) Taux de vide (Kocamustafaogullari et al, 1994), (b) la concentration d'aire interfaciale (Kocamustafaogullari et al, 1994), (c) la vitesse axiale moyenne du liquide (Iskandrani & Kojasoy, 2001)

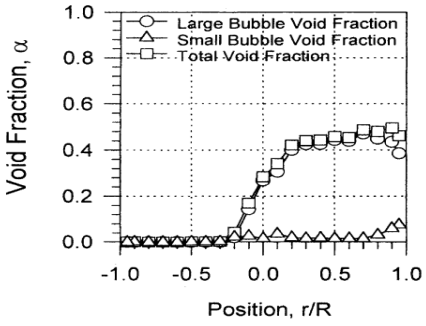

(a)

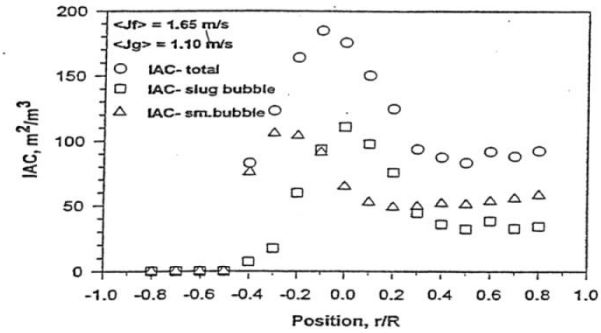

(b)

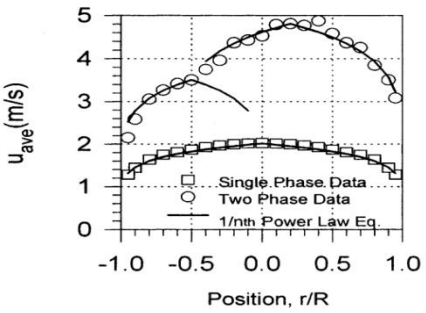

(c)

Figure R.3 - Les profils des grandeurs caractéristiques d'écoulement en écoulements intermittent : (a) Taux de vide (Lewis et al, 2002), (b) la concentration d'aire interfaciale (Riznic & Kojasoy, 1997), (c) la vitesse axiale moyenne du liquide (Lewis et al, 2002)

2. L'Installation Expérimentale METERO

Pour étudier les écoulements diphasiques horizontaux, l'installation expérimentale METERO a été construite. METERO (Figure R.4) est une conduite horizontale de section circulaire de 5 mètre de long, faite en plexiglass et de diamètre intérieur 10 centimètres. Les écoulements diphasiques peuvent être générés en faisant varier les vitesses superficielles d'eau et d'air à une température de 18 dégrées Celsius pour une pression proche de la pression atmosphérique.

Figure R.4 - Installation METERO

Pour mesurer les grandeurs caractéristiques d'écoulement, trois principaux moyens mesure sont utilisés : l'anémométrie à film chaud, la sonde optique et la vidéo-rapide. L'instrumentation peut être positionnée à 5, 20 et 40 diamètres à l'aval de l'entrée de la veine (Figure R.5). De plus, les sondes peuvent être déplacées sur un axe vertical central à l'aide d'un système de déplacement.

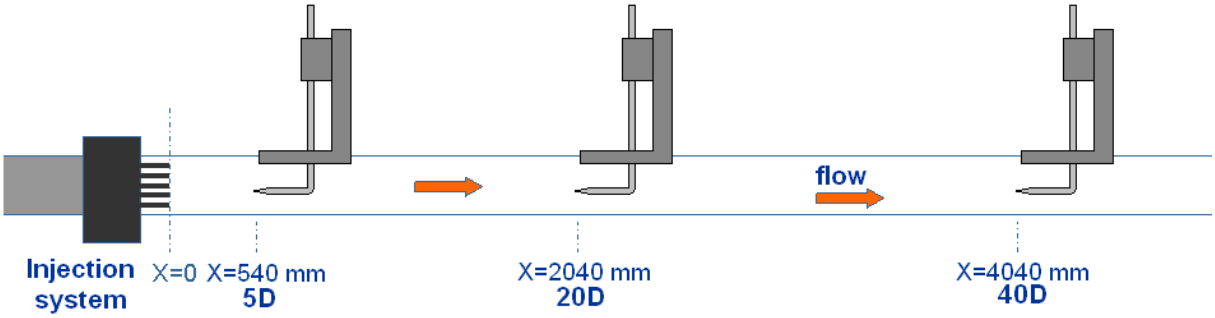

Figure R.5 - Position de mesure axiaux

3. Instrumentation

3.1. L'anémométrie à film chaud

Dans l'expérience METERO, l'anémométrie à film chaud à température constante a été utilisée. Le system d'anémométrie est connecté à une sonde croisée DANTEC (Figure R.6). A l'aide de cette sonde, deux composantes, notamment axiale et radiale de la vitesse instantanée de la phase liquide peuvent être mesurées. Les vitesses moyennes et l'énergie cinétique turbulente sont déduites de ces mesures.

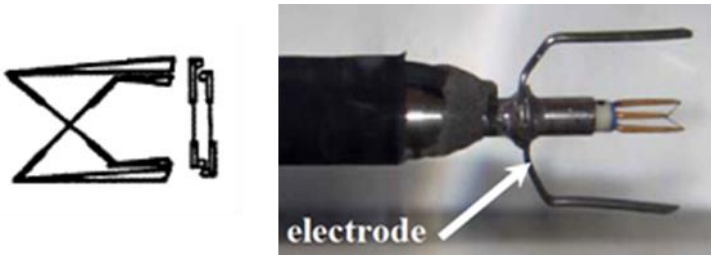

Figure R.6 - La sonde croisée connectée au système d'anémométrie

Le principal inconvénient de l'anémométrie à film chaud en écoulement diphasique est la chute de la tension lors du passage des bulles (Figure R.7). Par conséquent, il est nécessaire d'avoir un système pour discriminer les phases avant le post-traitement. Pour cette raison, un logiciel a été développé par Bottin (2010) pour les sondes mono-composant. Pour l'utilisation de la sonde à deux-composantes, le logiciel existant a été modifié. Que ce soit pour une sonde mono-composant ou deux-composantes, le fonctionnement du logiciel est le même et il est basé sur un principe de seuillage.

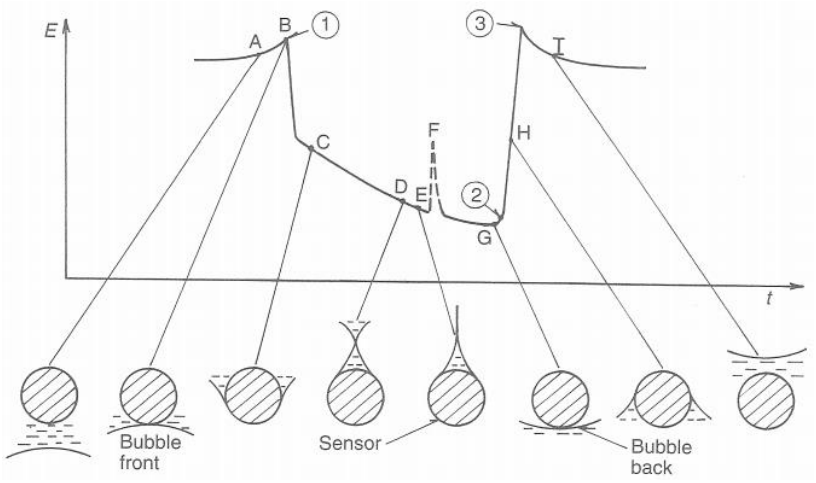

Figure R.7 - La chute de la tension lors du passage des bulles

Les signaux de tension sont lus échantillon par échantillon jusqu'à avoir une différence entre la tension du point et la tension maximale qui soit supérieure à une valeur seuil. Si cette condition est satisfaite, la portion du signal correspondant au passage d'une bulle est supprimée et les deux parties restantes du signal sont jointes. Au finale, les signaux sont alors prêts pour le post-traitement. Le processus de discrimination des signaux est représenté en détail sur la Figure R.8.

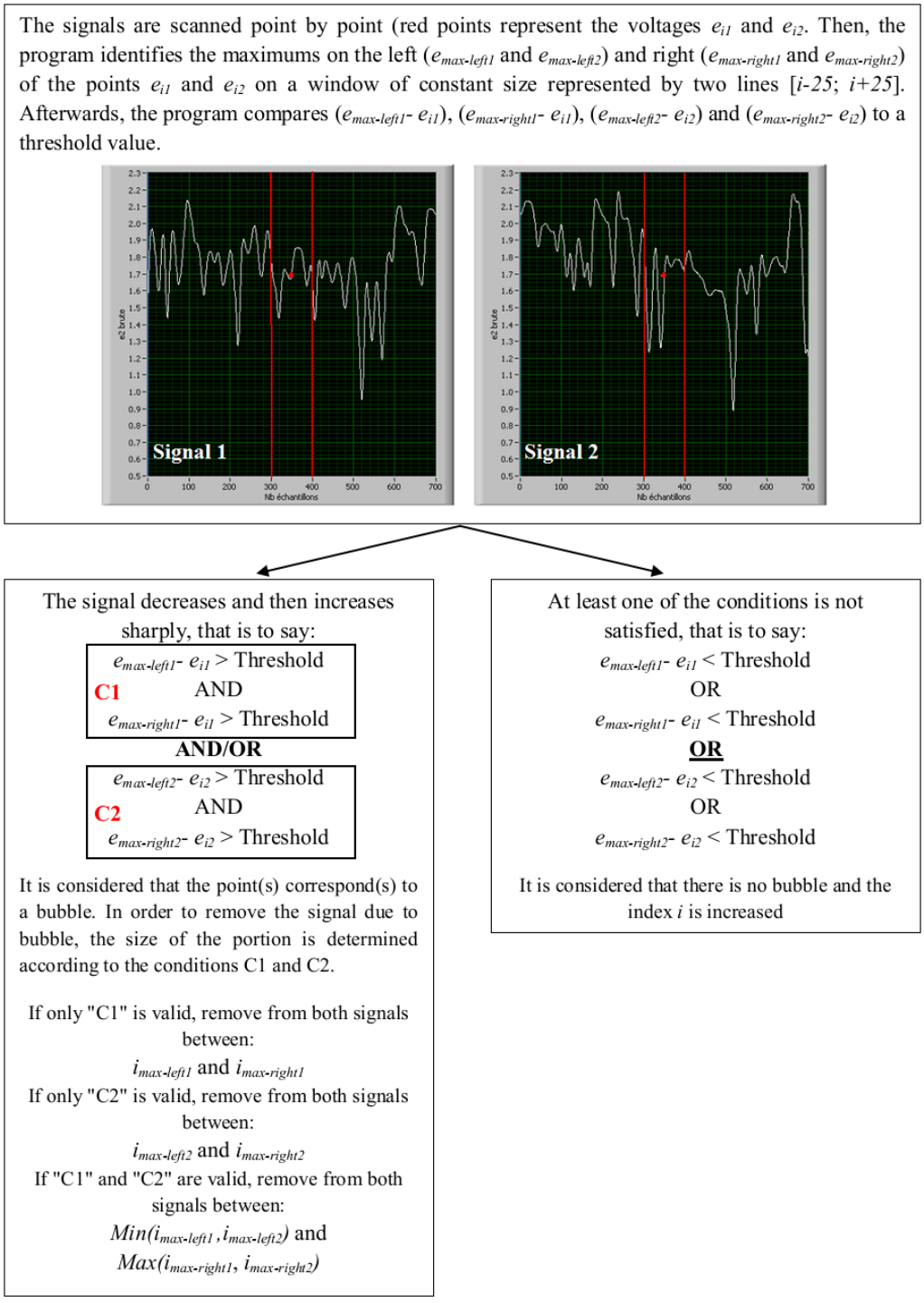

Figure R.8 - Les détails du processus de discrimination des phases

3.2. La sonde optique

Un autre moyen mesure est la sonde optique fabriquée au laboratoire. Elle est composée d'une fibre optique centrale et de trois fibres optiques latérales (Figure R.9). La distance axiale entre la fibre centrale et les trois autres est d'environ de 500 microns. La distance radiale est d'environ de 200 microns (Figure R.10). Cet écartement fixe la taille minimum des bulles qui peut être mesuré avec cette sonde.

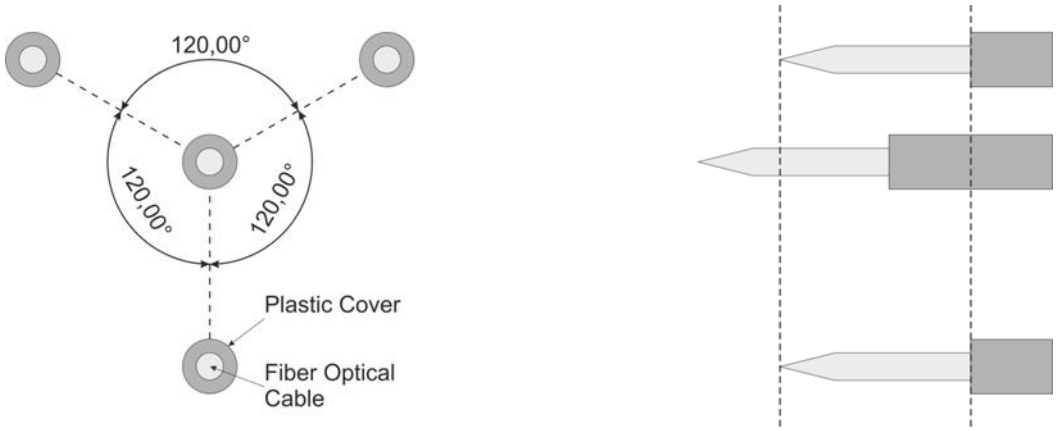

(a) Vue de face (b) Vue de côté

Figure R.9 - Schéma d'une quadri-sonde optique

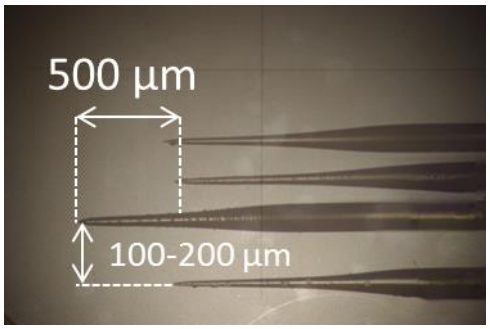

Figure R.10 - La géométrie de la quadri-sonde optique

Le fonctionnement de cette sonde est basé sur les lois de la diffraction. Elle fournit la fonction indicatrice de phase qui donne accès au taux de vide, à la concentration d'aire interfaciale, à la vitesse et à la taille des bulles.

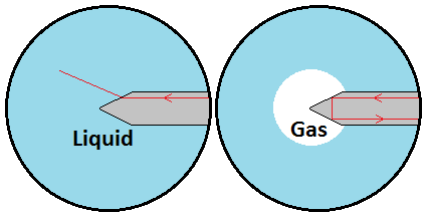

3.3. La vidéo rapide et l'ombroscopie

Le dernier moyen d'instrumentation est la vidéo rapide associée à la technique d'ombroscopie. Cette technique est utilisée pour mesurer des vitesses axiales et radiales de bulles. Nous utilisons une puissante source lumineuse placée derrière la section d'essai et une caméra rapide capture les images des bulles (Figure R.11). Les images acquises sont converties en image noir et blanc (Figure R.12). En utilisant les bulles comme traceur, les vitesses sont calculées par l'utilisation d'un logiciel de PIV.

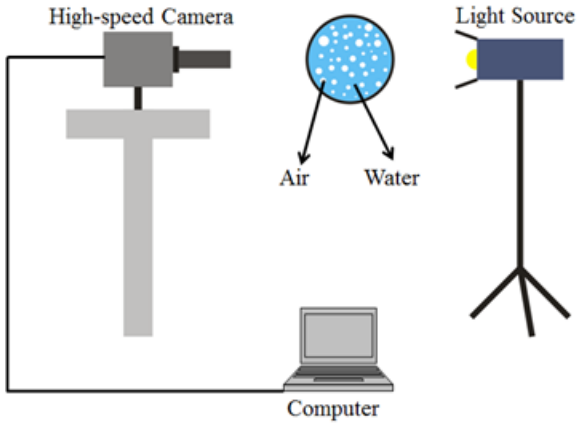

Figure R.11 - Schématique de la technique d'ombroscopie

(a) Grayscale (b) Subtracted (c) BW without filter (d) Filtered BW

Figure R.12 - Les étapes de génération d'image blanc-et-noir

3.4. Validation de la sonde optique

Avant de commencer les principaux tests, les résultats obtenus par bi-sonde et quadri-sonde optique ont été comparé en écoulement dispersé avec la technique d'ombroscopie pour vérifier la validité des mesures de vitesse axiale des bulles (Figure R.13). La thèse de Bottin a montré que la bi-sonde optique sous-estime la vitesse des bulles de l'ordre de 10%. Ce problème pourrait venir de la déformation des bulles par la sonde au moment du contact comme nous l'avons observé avec la camera rapide (Figure R.14). Cette déformation entraine d'une décélération des bulles.

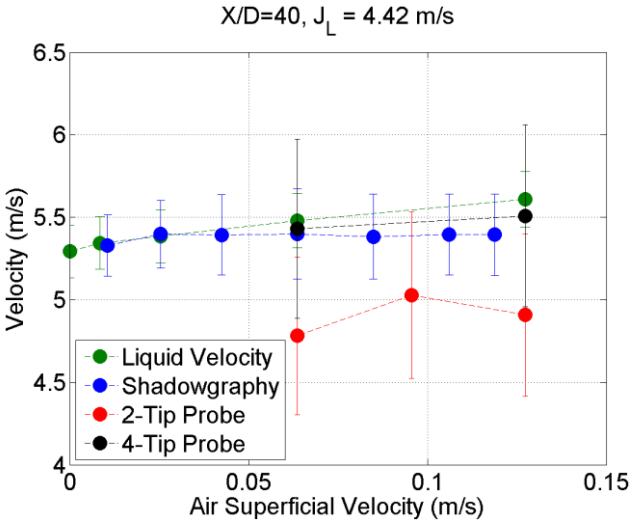

Figure R.13 - Vitesse axiale des bulles pour J_L=4.42 m/s et de divers J_G au centre de la section d'essai et à 40D

Les mesures par quadri-sonde optique montrent un bon accord avec celles réalisées par ombroscopie qui a été choisi comme référence. Pour la suite de la thèse, nous avons donc décidé d'utiliser des quadri-sondes optiques du fait de leur meilleure performance. D'autre part, l'utilisation des quadri-sonde optiques ne repose pas sur l'hypothèse de bulle sphérique. Cette hypothèse est invalide en écoulement intermittent.

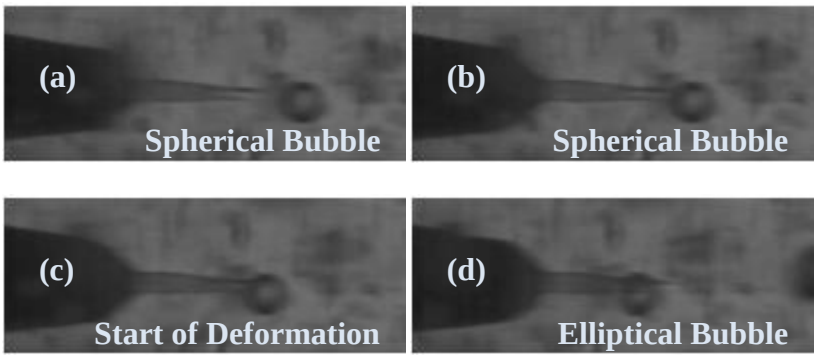

Figure R.14 - L'interaction d'une bulle sphérique avec une bi-sonde optique

4. Carte de Régime d'Ecoulement

La carte de régime d'écoulement, réalisée à 40D à l'aval de l'entrée de la veine, pour l'installation METERO est représentée sur la Figure R.15. Cette carte montre les différents écoulements en utilisant des vitesses superficielles d'air et d'eau comme variables. Dans cette thèse, nous avons travaillé sur les deux principaux régimes d'écoulements qui sont l'écoulement dispersé et l'écoulement intermittent.

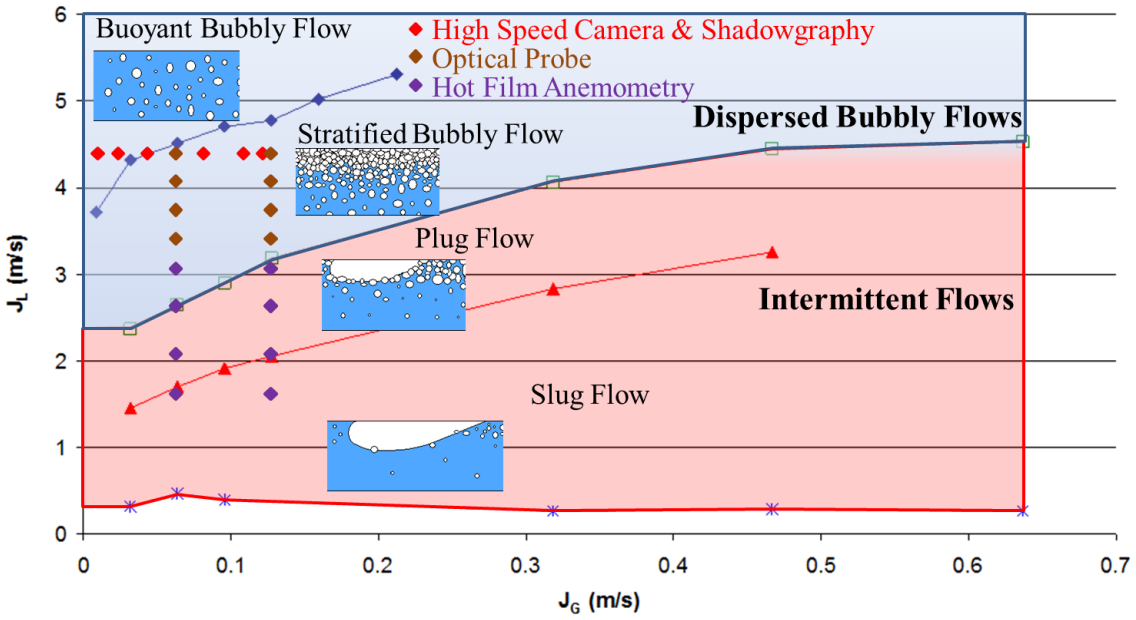

Figure R.15 - La carte de régimes d'écoulements pour l'installation METERO

Dans l'écoulement dispersé, il existe deux sous régimes d'écoulements. Le premier sous régime que nous avons étudié est le régime dispersé gravitaire. Les bulles sont relativement bien dispersées du fait du mélange par la turbulence. Cependant même pour taux de turbulence élevé à grande vitesse liquide, nous pouvons constater l'effet non négligeable de la flottabilité par une légère accumulation des bulles au sommet de la conduite.

Le deuxième sous régime d'écoulement est le régime à bulles stratifiées. L'accumulation des bulles à la paroi est plus importante du fait de la décroissance du mélange.

Dans les écoulements intermittents, nous avons également deux sous régimes. Le premier est le régime à poches dans lequel la migration des bulles est quasiment terminée. On observe des bulles allongées générées par la coalescence du fait du débit liquide plus faible.

Le régime à bouchons est le deuxième sous régime d'écoulement dans les écoulements intermittents. Dans ce régime, de très grosses bulles allongées qui se déplacent plus vite que la phase liquide sont observées.

En ce qui concerne les acquisitions des grandeurs caractéristiques d'écoulements, nous avons utilisé la vidéo rapide et la technique d'ombroscopie dans les régimes dispersés. A l'aide de la sonde optique, nous avons réalisé 16 tests pour chaque position axiale à 5, 20 et 40 diamètres. En ce qui concerne l'anémométrie a film chaud, 8 tests pour chaque position axiale ont été réalisés.

5. Les Etudes sur les Ecoulement Dispersés

5.1. La vitesse axiales et l'énergie cinétique turbulente de la phase liquide à 40D

Les profils de la vitesse axiale moyenne de la phase liquide sont représentés sur la Figure R.16 (a). Les profils montrent que l'augmentation du débit liquide entraine celle de la vitesse liquide. Les vitesses de la phase liquide augmentent également quand le débit gaz augmente mais cet effet est plus faible.

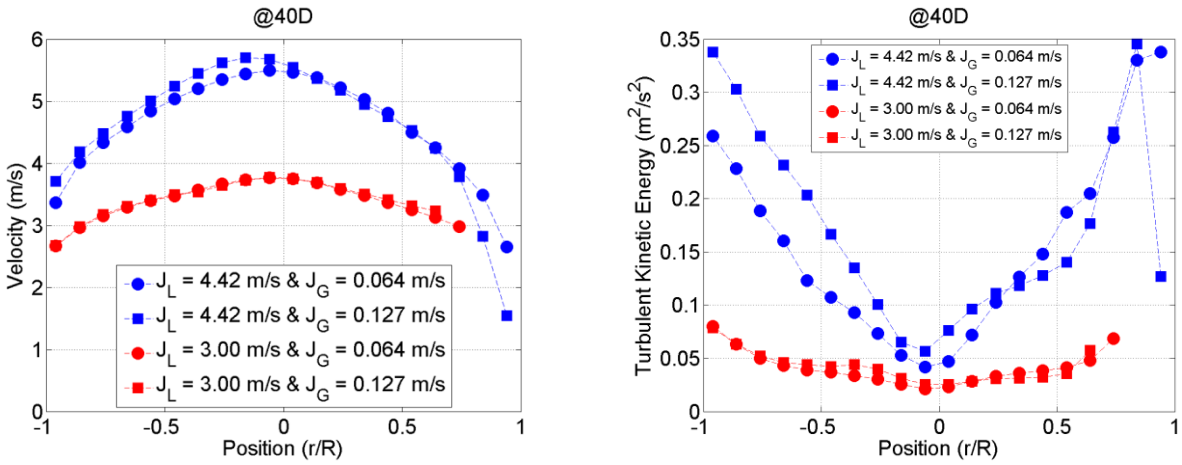

(a) (b)

Figure R.16 - Les profils de la vitesse axiale moyenne (a) et de l'énergie cinétique turbulente (b) de la phase liquide mesurés en écoulement dispersé à 40D

En ce qui concerne les profils d'énergie cinétique turbulente (Figure R.16 (b)), nous voyons que le fait d'augmenter le débit liquide augmente l'énergie cinétique turbulente. De manière similaire aux profils de vitesse, l'ajout de gaz dans l'écoulement augmente l'énergie cinétique turbulente, mais cet effet est plus faible.

5.2. La distribution de la phase gazeuse à 40D

Des changements dans les débits liquides et gaz affectent la distribution de la phase gazeuse.

5.2.1. L'effet du changement du débit liquide

Les résultats expérimentaux (Figure R.17) montrent que si on fixe le débit gaz et qu'on augmente le débit liquide, alors la distribution du taux de vide s'homogénéise du fait de l'augmentation du mélange turbulent. De façon similaire, nous avons observé le même effet sur les profils de la concentration d'aire interfaciale. Les profils de longueur de corde illustrent le processus de fragmentation accrue lorsque la vitesse liquide augmente.

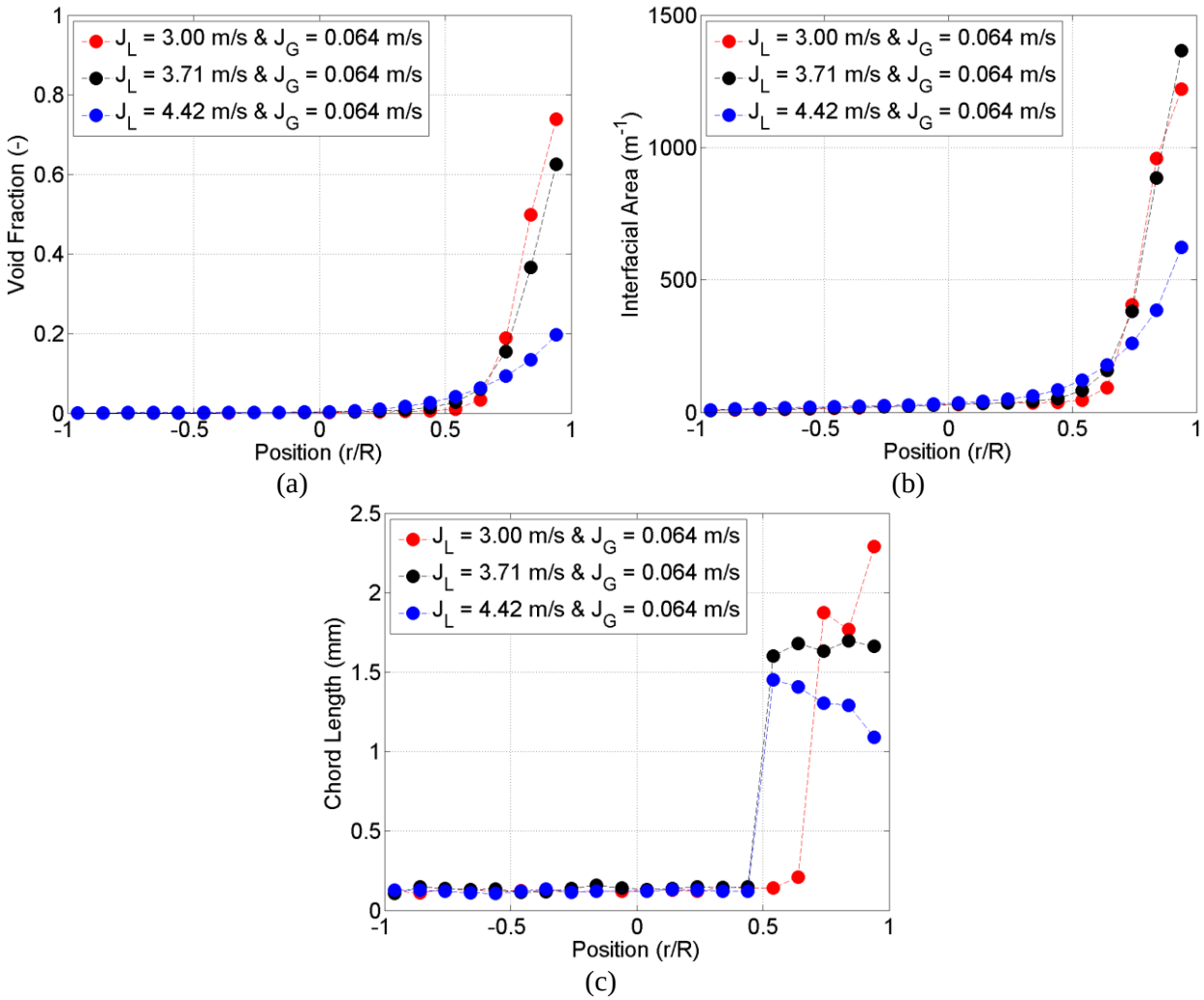

Figure R.17 - Les profils du taux de vide (a), de la concentration d'aire interfaciale (b) et de longueur de cordes (c) mesurés à 40D pour divers J_L et J_G fixé

5.2.2. L'effet du changement du débit gaz

Les profils du taux de vide (Figure R.18 (a)) montrent que le taux de vide augmente au sommet, mais pas au bas de la conduite.

Les profils de longueur de cordes (Figure R.18 (b)) montrent que la taille de bulles augmente au sommet de la conduite.

De façon similaire au taux de vide, les profils de la concentration d'aire interfaciale (Figure R.18 (c)) dans la région supérieure montrent l'accumulation des bulles au sommet.

Tout cela résulte de l'augmentation des forces de flottabilité et de la coalescence induites par l'augmentation de débit gaz.

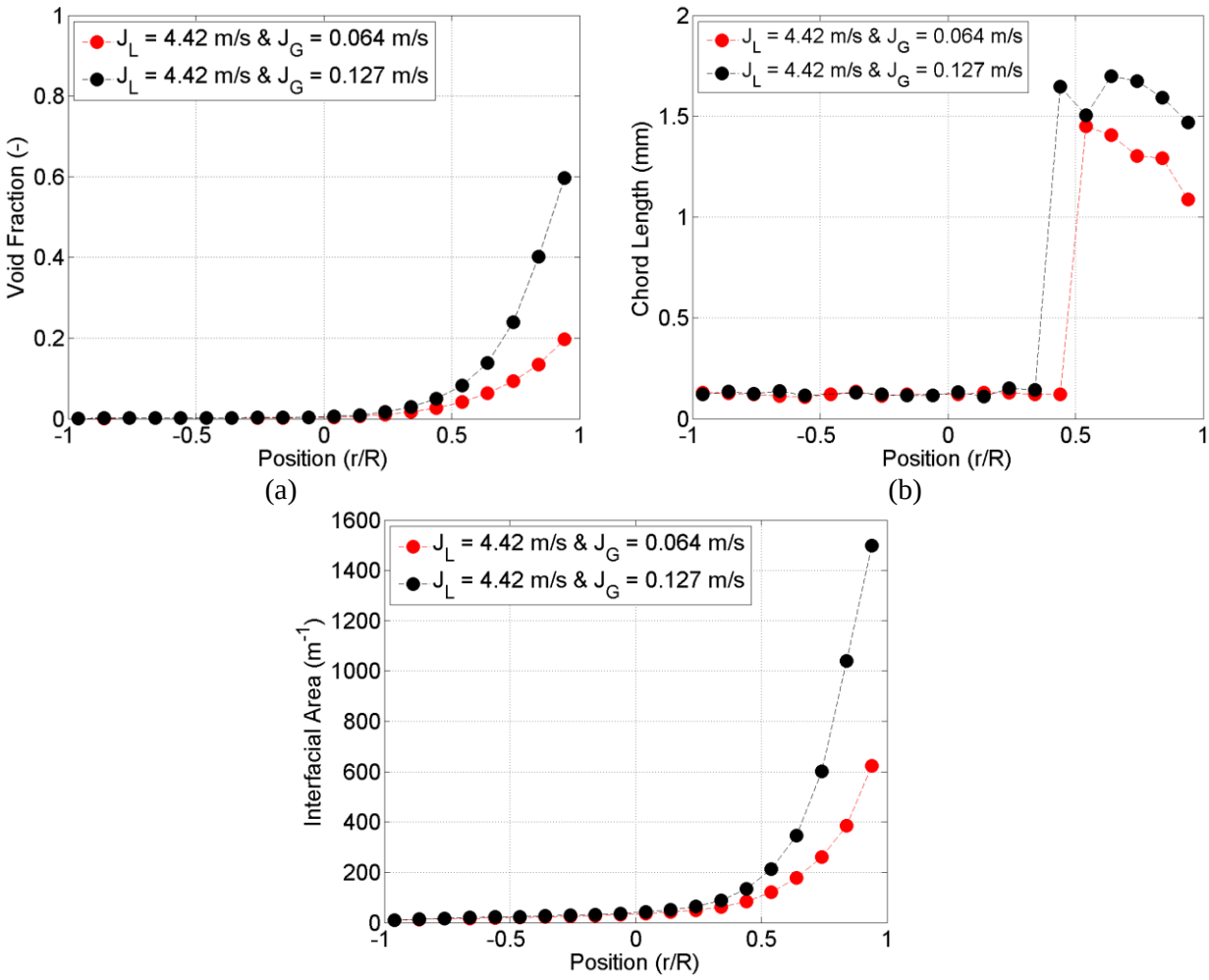

Figure R.18 - Les profils du taux de vide (a), de longueur de cordes (b) et de la concentration d'aire interfaciale (c) mesurés à 40D pour divers J_G et J_L fixé

5.3. L'évolution axiale du taux de vide, de la concentration d'aire interfaciale et de longueur de cordes

Les évolutions axiales du taux de vide, de la concentration d'aire interfaciale et de longueur de cordes sont représentées sur la Figure R.19.

Les profils du taux de vide (Figure R.19 (a)) montrent que le taux de vide dans la région supérieure de la conduite augmente continument, alors qu'il décroit dans la région basse. Ce comportement est aussi observé pour la concentration d'aire interfaciale (Figure R.19 (b)). Ces deux résultats illustrent l'évolution axiale de la sédimentation et de l'accumulation des bulles en partie haute de la conduite. L'analyse des profils de longueur de cordes (Figure R.19 (c)) montre la coalescence des bulles au sommet de la conduite entre 5 et 20 diamètres.

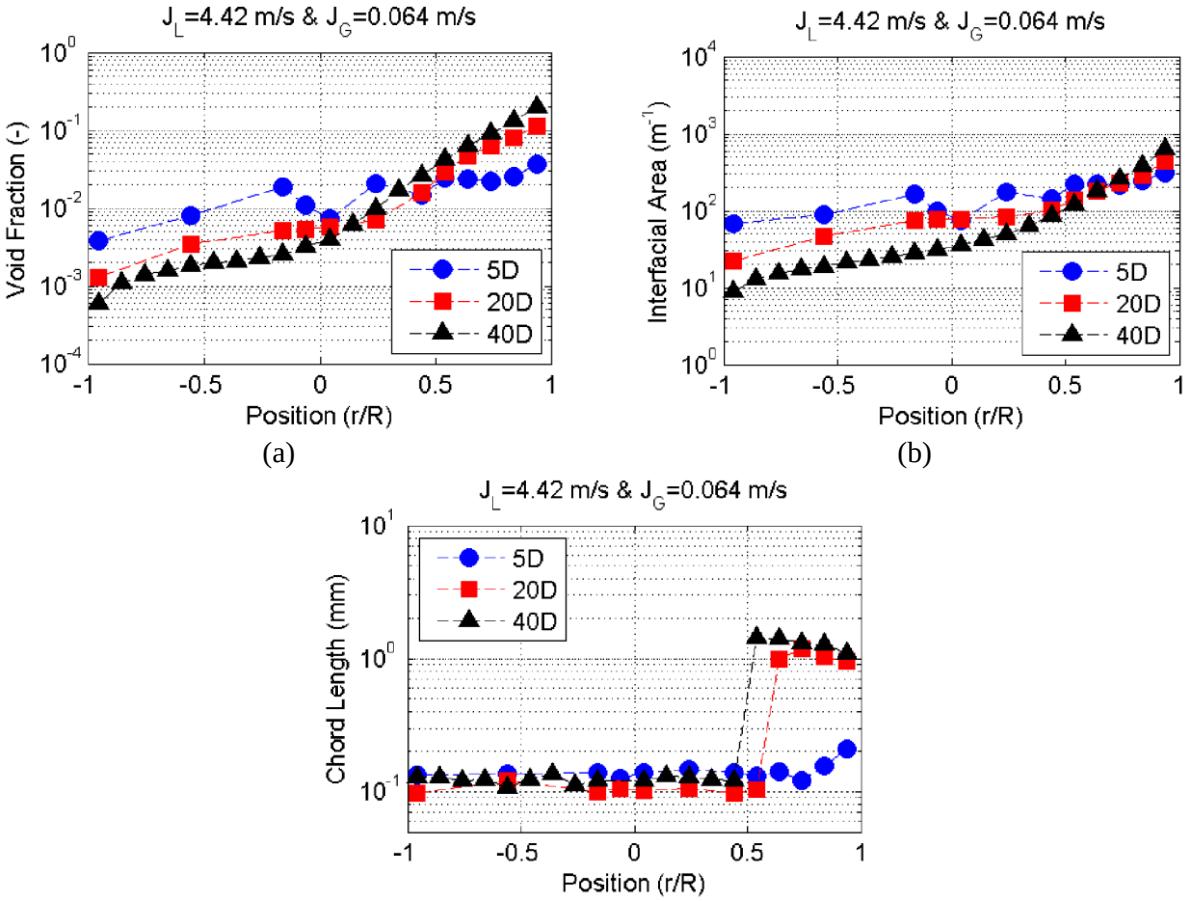

Figure R.19 - Les évolutions axiales du taux de vide (a), de la concentration d'aire interfaciale (b) et de longueur de cordes (c) en écoulements dispersés

5.4. L'évolution axiale de la vitesse des bulles et de la phase liquide

Les évolutions des vitesses des bulles et du liquide sont illustrées sur la Figure R.20. L'évolution continue des profils de vitesse montre que l'écoulement se développe essentiellement entre 5 et 20 diamètres. Entre 20 et 40D, l'évolution est moins importante. Un résultat intéressant concerne les profils à 40 diamètres de vitesse des bulles et du liquide lorsqu'ils sont tracés ensemble (Figure R.21). Leur similarité montre que le glissement est négligeable. Les bulles sont transportées par la phase liquide un peu à la façon d'un scalaire passif.

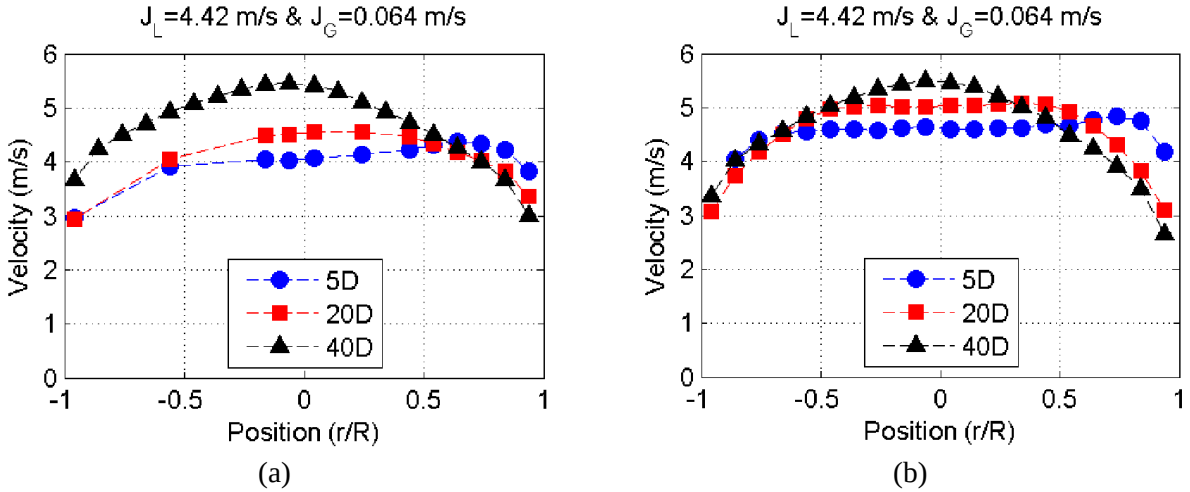

Figure R.20 - Les évolutions axiales des vitesses des bulles (a) et du liquide (b)

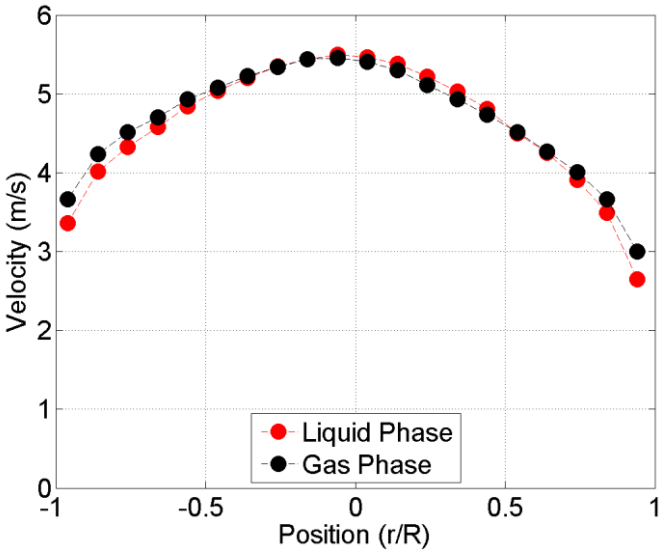

Figure R.21 - Les profils des vitesses des bulles et du liquide à 40D

5.5. Conclusion

Les résultats en régime dispersé ont montré que le mélange turbulent pilote l'écoulement. De plus, les bulles commencent à s'accumuler au sommet en régime à bulles stratifié ce qui préfigure les écoulements intermittents

6. Les Etudes sur les Ecoulement Intermittent

6.1. L'énergie cinétique turbulente de la phase liquide à 40D

La comparaison de l'énergie cinétique turbulente de la phase liquide en écoulement à bulles dispersées avec l'écoulement intermittent est illustrée sur la Figure R.22. La diminution du débit liquide entraine celle de l'énergie cinétique turbulente et du mélange. En conséquence, la force de flottabilité devient dominante dans l'écoulement intermittent et de grosses bulles allongées apparaissent (Figure R.23).

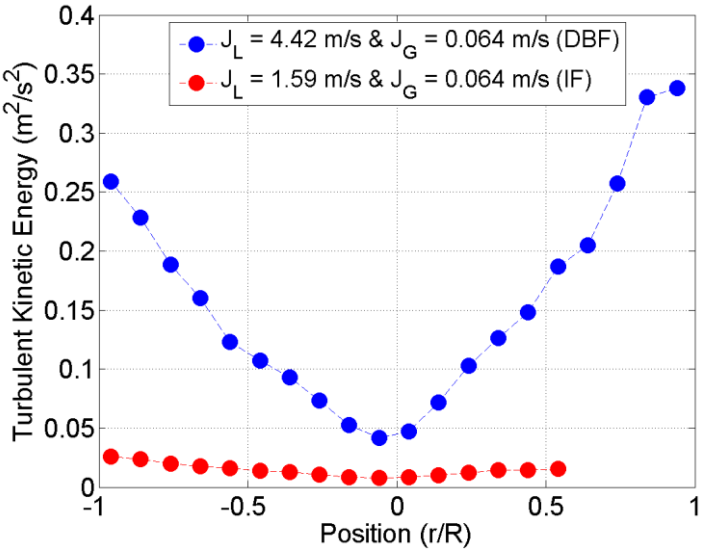

Figure R.22 - La comparaison de l'énergie cinétique turbulente

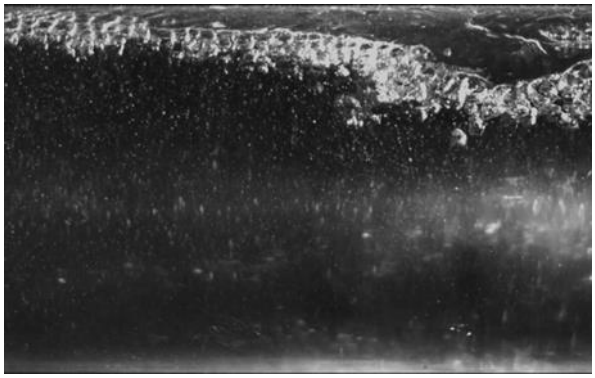

Figure R.23 - Une bulle allongée observée à l'aide de la vidéo rapide en écoulement intermittent

6.2. La distribution de la phase gazeuse à 40D

Les mesures des profils du taux de vide, de la concentration d'aire interfaciale et de longueur de cordes apportent une information détaillée sur la structure d'écoulement.

Le profil du taux de vide à 40D (Figure R.24 (a)) peut être séparé en deux zones. La première zone est occupée essentiellement par la phase gazeuse. La seconde zone est dominée par la phase liquide et montre un taux de vide quasiment nul.

Ces deux zones peuvent être également observées sur les profils de la concentration d'aire interfaciale (Figure R.24 (b)) et de longueur de cordes (Figure R.24 (c)).

A la lumière de cette information, nous pouvons partager les écoulements intermittents en deux zones. Dans la première zone située au sommet, la dynamique de l'écoulement est dominée par la phase gazeuse. Dans la seconde zone en partie basse de la conduite, l'écoulement est piloté par la phase liquide. Ce comportement a été rapporté par Ekambara et al. (2008).

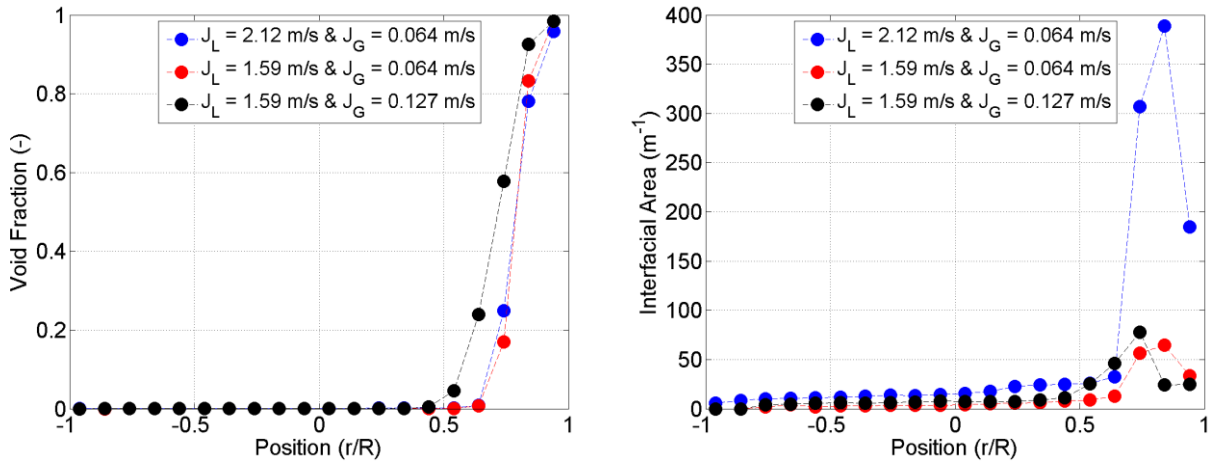

(a) (b)

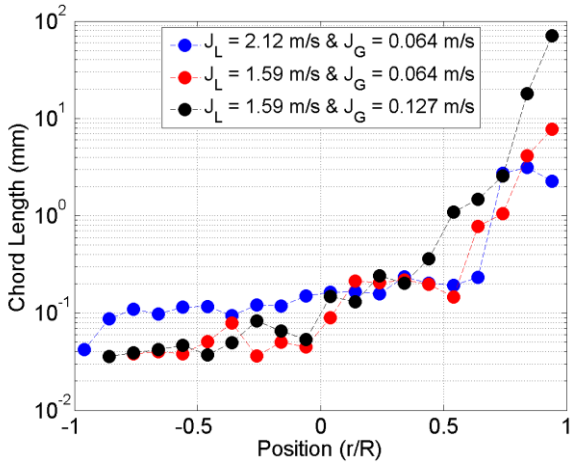

(c)

Figure R.24 - Les profils du taux de vide (a), de la concentration d'aire interfaciale (b) et de longueur de cordes (c) mesurés à 40D en écoulement intermittent

6.3. La vitesse axiale des bulles et de la phase liquide à 40D

Les vitesses des bulles et de la phase liquide mesurées à 40 diamètres pour différents conditions d'essai sont représentées sur la Figure R.25. Pour toutes les conditions d'essai en écoulement intermittent, nous avons observé que la vitesse axiale des bulles est plus faible que celle de la phase liquide. Donc, nous pouvons dire les bulles se déplacent plus lentement que le liquide dans les écoulements intermittents.

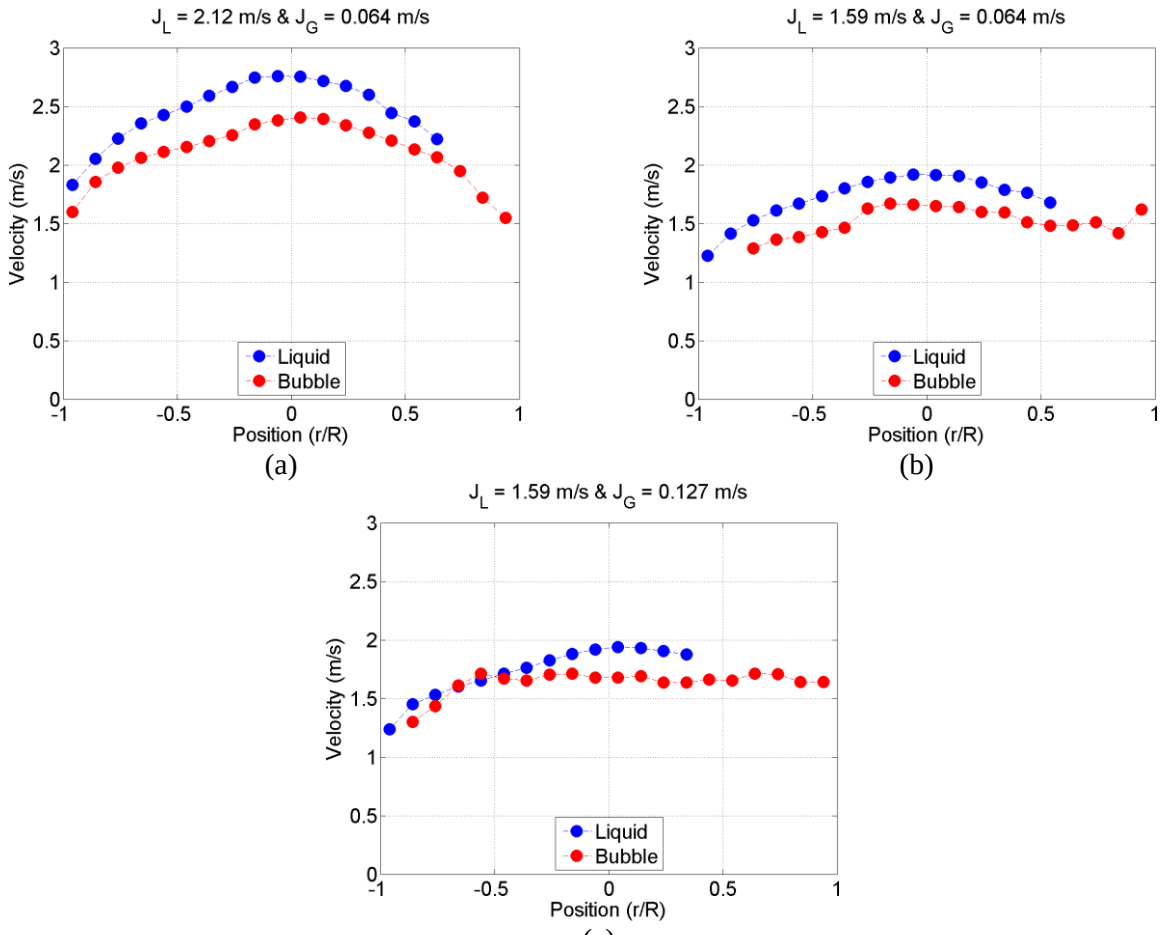

(a) (b)

(c)

Figure R.25 - Les vitesses des bulles et de la phase liquide mesurées à 40 diamètres pour différents conditions d'essai

Les vitesses axiales du liquide mesurées en écoulement dispersé et en écoulement intermittent sont comparées sur la Figure R.26. Un décalage du profil de vitesse liquide vers le haut de la conduite est observé. Ce comportement est également rapporté par Taitel et Barnea (1990). Ce décalage peut s'expliquer par l'accélération horizontale du liquide dans la partie supérieure de la conduite par les bouchons de gaz (Figure R.27).

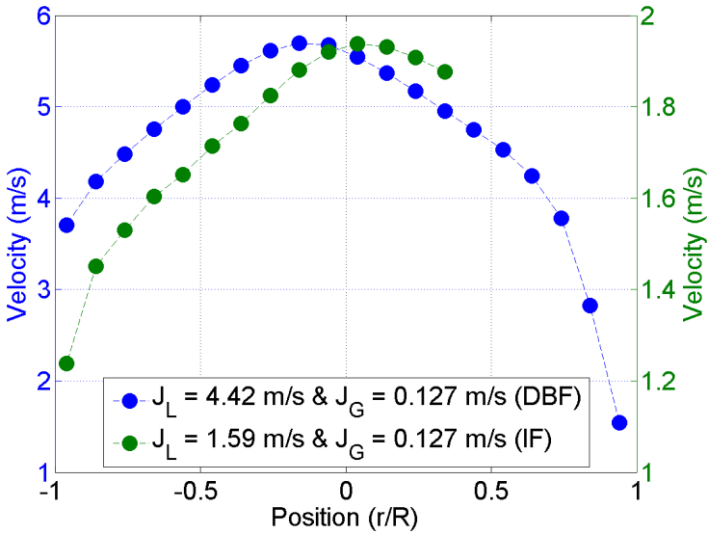

Figure R.26 - La comparaison des vitesses axiales du liquide en écoulement disperse (bleu) et en écoulement intermittent (vert) a 40D

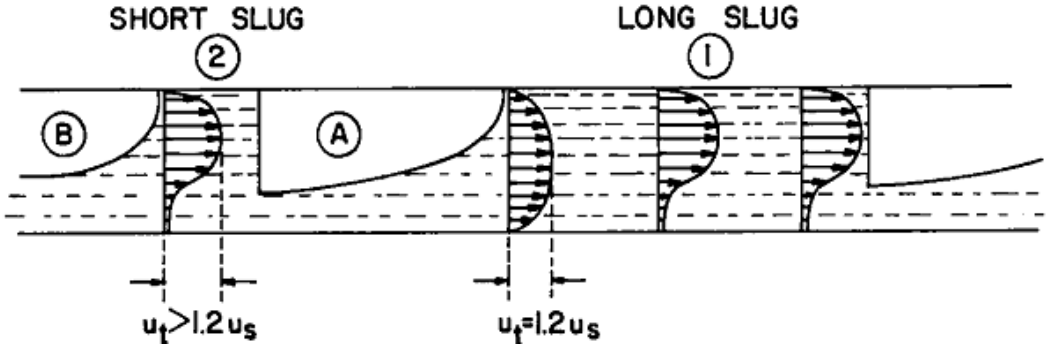

Figure R.27 - Les profils de la vitesse du liquide en écoulement intermittent (Taitel & Barnea, 1990)

6.4. L'évolution axiale du taux de vide, de la concentration d'aire interfaciale et de longueur de cordes

Les évolutions du taux de vide, de la concentration d'aire interfaciale et de longueur de cordes sont illustrées sur la Figure R.28.

Les profils du taux de vide (Figure R.28 (a)) montrent que le taux de vide augmente au sommet de la conduite, alors qu'il décroit dans la partie basse. Cela traduit une accumulation des bulles vers le sommet de la conduite. La concentration d'aire interfaciale (Figure R.28 (b)) décroit également de 5 à 40 diamètres ce qui traduit de la coalescence. L'évolution axiale des longueurs de corde (Figure R.28 (c)) confirme cette coalescence.

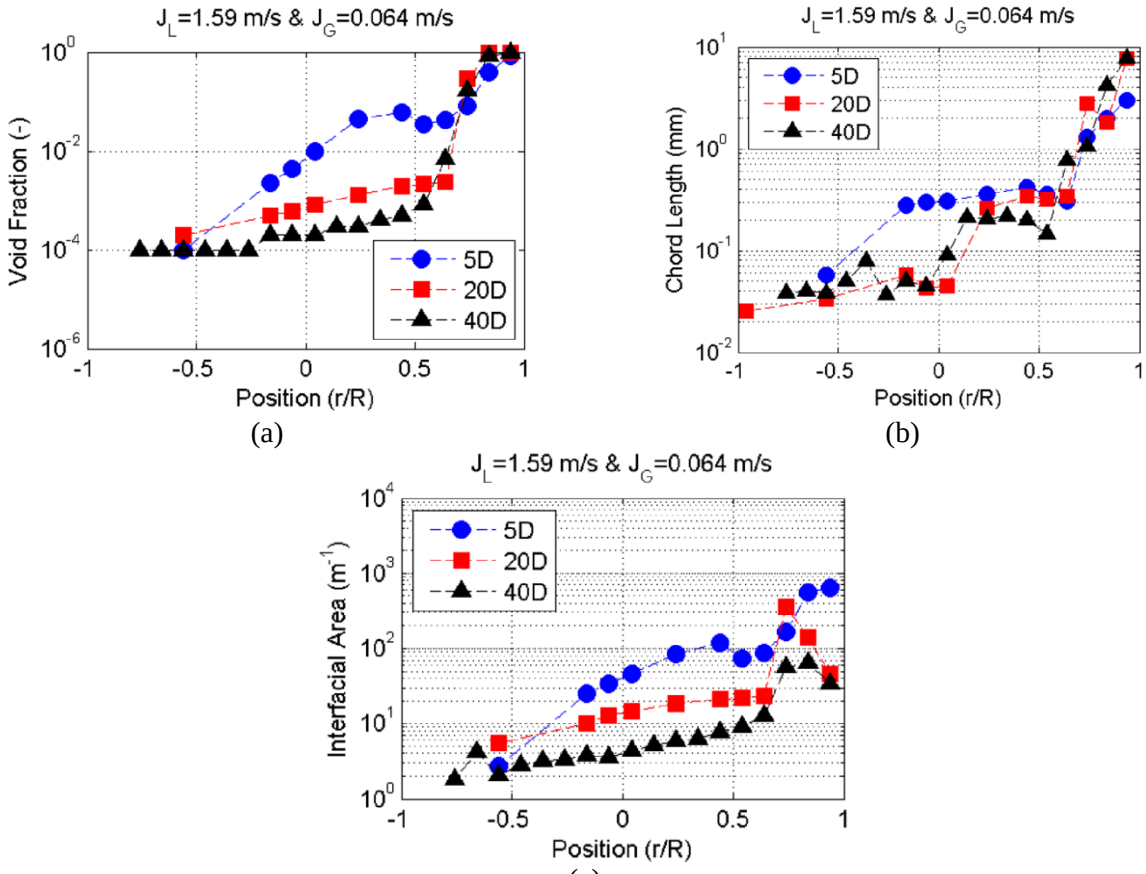

Figure R.28 - Les évolutions axiales du taux de vide (a), de la concentration d'aire interfaciale (b) et de longueur de cordes (c) en écoulements intermittent

Des tests avec la vidéo rapide ont permis de visualiser la coalescence en écoulement intermittent. En passant de 20D à 40D (Figure R.29), les images montrent que la taille des bulles augmente et que l'épaisseur de la mousse diminue.

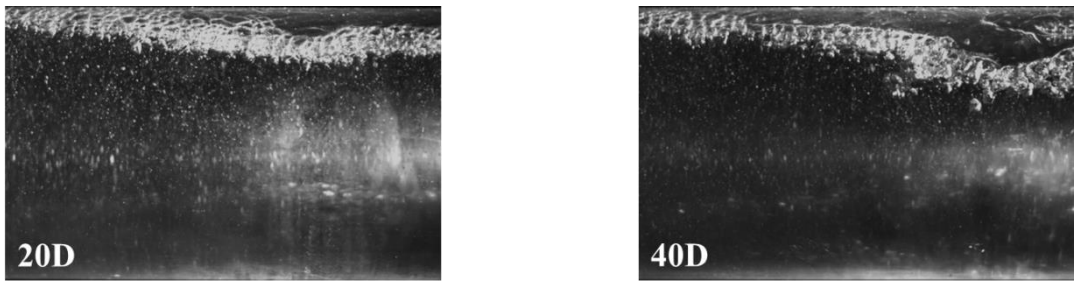

Figure R.29 - Changement de la taille des bulles entrée 20D et 40D en écoulement intermittent

6.5. L'évolution axiale de la vitesse et l'énergie cinétique turbulente de la phase liquide

Les évolutions axiales de la vitesse et l'énergie cinétique turbulente de la phase liquide sont représentées sur la Figure R.30. Pour les profils de vitesse (Figure R.30 (a)), il n'y a pas de changement significatif entre 5D et 40D.

L'énergie cinétique turbulente (Figure R.30 (b)) évolue différemment dans les parties haute et basse. En partie basse, le profil s'établit progressivement comme pour les écoulements dispersés. En partie haute, l'intermittence associée au passage intermittent des bouchons empêche l'établissement de la turbulence.

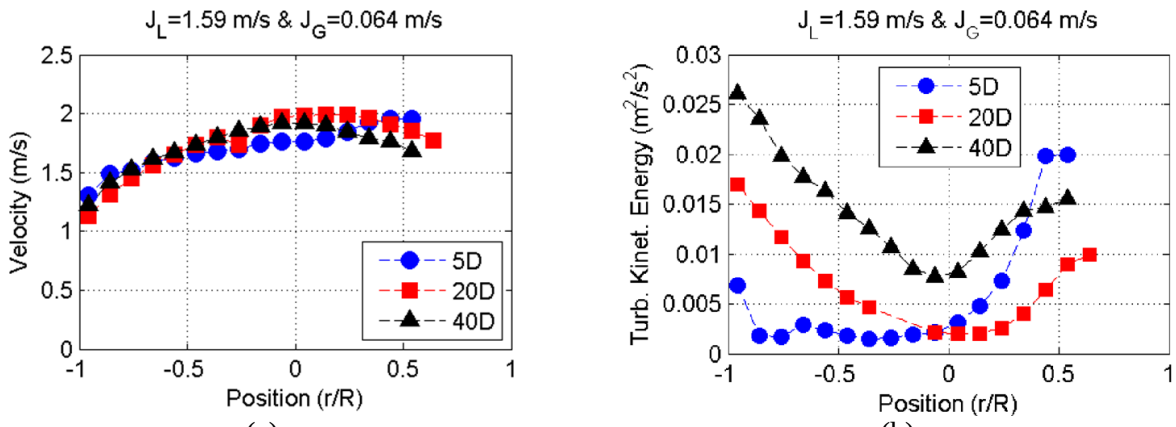

(a) (b)

Figure R.30 - Les évolutions axiales de la vitesse (a) et l'énergie cinétique turbulente (b) en écoulement intermittent

6.6. Conclusion

En régime intermittent, le passage des bouchons de gaz en partie supérieure dissymétrise l'écoulement. En partie basse, la vitesse moyenne et la turbulence s'établissent comme pour les écoulements dispersés. En partie haute, les bouchons de gaz accélèrent le liquide et empêchent l'établissement de la turbulence.

7. Les Cartes de Régime d'Ecoulement Adimensionnelles

La carte de régime d'écoulement créée pour l'expérience METERO (Figure R.15) est représentée en coordonnées dimensionnelles. Ce qui rend difficile son utilisation pour d'autres installations. Pour cette raison, il est nécessaire d'utiliser des coordonnées adimensionnelles pour dessiner une nouvelle carte.

7.1. La carte X-T de Taitel & Dukler

Pour notre nouvelle carte, nous avons choisi d'utiliser une carte de régime d'écoulement généralisée pour les écoulements diphasiques horizontaux, présentée par Taitel et Dukler (1976) (Figure R.31). Les auteurs ont utilisé des coordonnées adimensionnelles et représenté les transitions. Dans cette thèse, nous nous sommes concentrés sur les écoulements dispersés et intermittents. Pour ces deux régimes, Taitel & Dukler ont suggéré d'utiliser les paramétres X et T comme variables d'entrée. X est le paramètre de Lockhart-Martinelli et T est le rapport entre la force turbulente et la force de flottabilité agissant sur la phase gazeuse. Les paramètres sont calculés à l'aide de la formule 1 et de la formule 2. La transition entre l'écoulement dispersé et l'écoulement intermittent est représentée à l'aide de la ligne D.

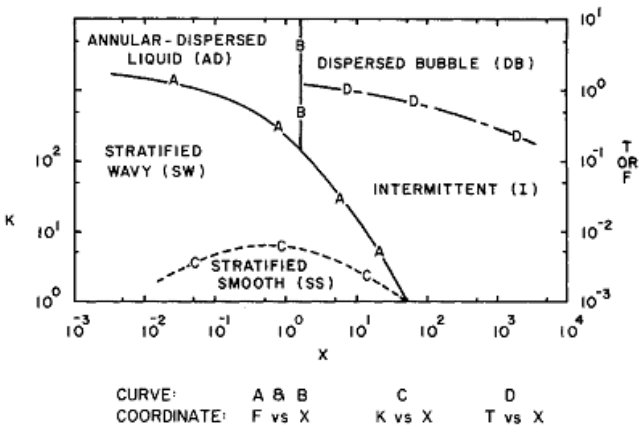

Figure R.31 - La carte de régime d'écoulement généralisée pour les écoulements diphasiques horizontaux

$$X^2 = \frac{\left(4C_L/D\right)\left(u_{LS}D/\upsilon_L\right)^{-n}\rho_L\frac{u_{LS}^2}{2}}{\left(4C_G/D\right)\left(u_{GS}D/\upsilon_G\right)^{-m}\rho_G\frac{u_{GS}^2}{2}} \tag{70}$$

$$T^2 = \frac{\left(4C_L/D\right)\left(u_{LS}D/\upsilon_L\right)^{-n}\rho_L\frac{u_{LS}^2}{2}}{\left(\rho_L-\rho_G\right)\cos\beta\, g} \tag{71}$$

Les auteurs ont rapporté que la dispersion prend place quand la force turbulente est supérieure à la force de flottabilité. Ceci est traduit par la formule 3 que l'on peut réécrire sous la forme d'un critère CT (Formule 4) dans lequel κ représente le terme de droite de la formule 3.

$$T^2 \geq \frac{8\tilde{A}_G}{\tilde{S}_i\tilde{U}_L^2\left(\tilde{U}_L\tilde{D}_L\right)^{-n}} \tag{72}$$

$$CT = \frac{T}{\sqrt{\kappa}} \geq 1 \tag{73}$$

Si CT est plus grand que 1, le régime est dispersé. Sinon, il est intermittent. Il est très important de noter que κ dépend du rapport entre la hauteur du liquide et le diamètre de la conduite.

Les valeurs de CT calculées pour toutes nos conditions expérimentales donnent les résultats suivants :

$$\frac{T}{\sqrt{\kappa}} \geq 2 \quad \rightarrow \quad Buoyant \quad Bubbly \quad Flow \tag{74}$$

$$2 > \frac{T}{\sqrt{\kappa}} \geq 1 \quad \rightarrow \quad Stratified \quad Bubbly \quad Flow \tag{75}$$

$$1 > \frac{T}{\sqrt{\kappa}} \geq 0.5 \quad \rightarrow \quad Plug \quad Flow \tag{76}$$

$$0.5 > \frac{T}{\sqrt{\kappa}} \quad \rightarrow \quad Slug \quad Flow \tag{77}$$

Avec les paramètres calculés et les critères de transition, une nouvelle carte pour l'expérience METERO a été dessinée (Figure R.32). Elle est en bon accord avec la littérature. La ligne de transition D s'accorde parfaitement avec nos points expérimentaux. De plus, nous avons présenté un critère mécaniste pour définir les transitions entre les régimes. Cependant, cette carte présente deux inconvénients : d'une part, les paramètres X et T ont été calculés et non pas mesurés. D'autre part, le critère de transition est impacté par toutes les incertitudes de mesure du taux de vide utilisé pour calculer la hauteur du liquide.

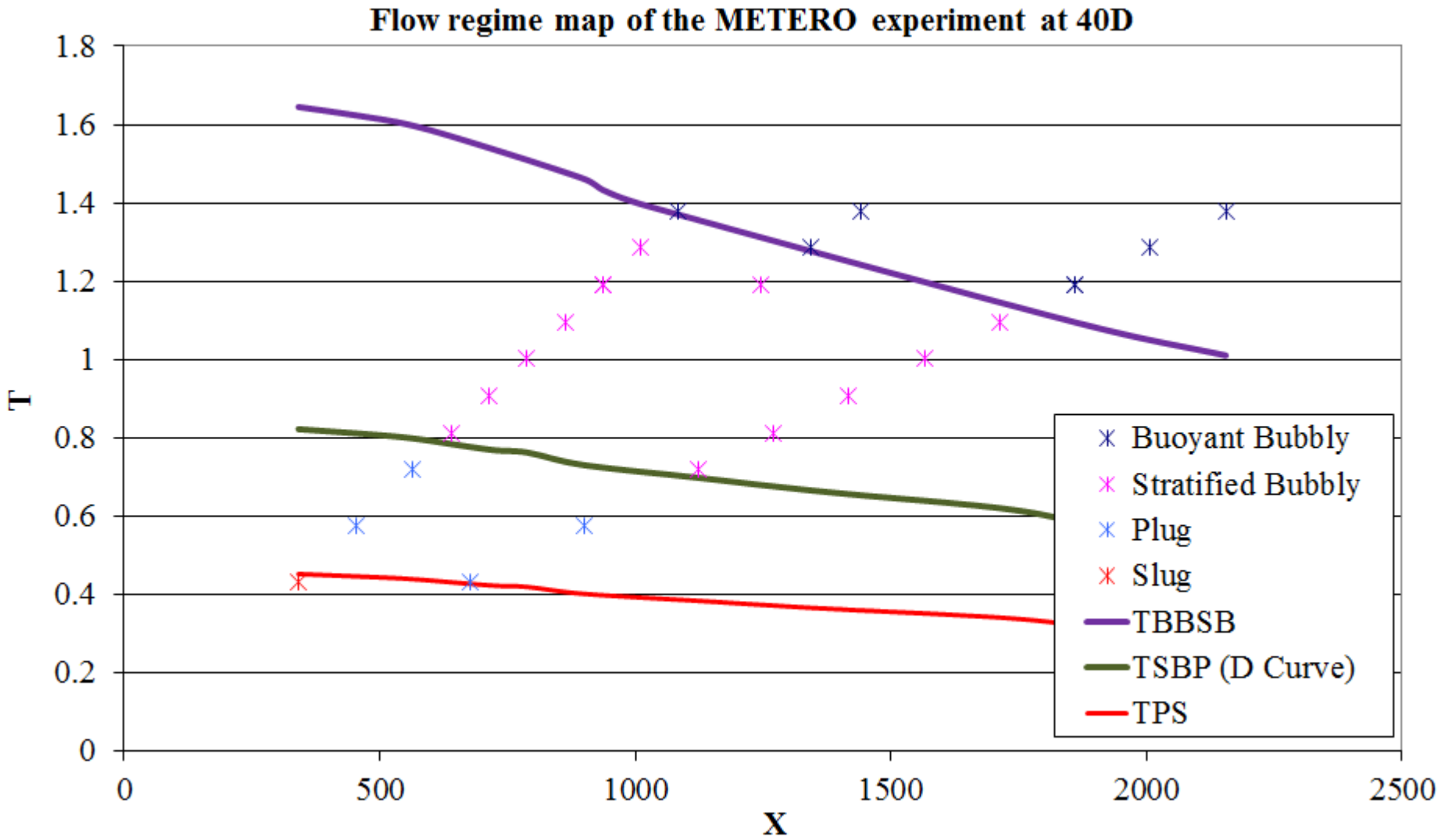

Figure R.32 - La carte X-T pour l'expérience METERO

7.2. Une nouvelle carte de régime d'écoulement adimensionnelle

Pour dessiner une nouvelle carte adimensionnelle, trois paramètres ont été choisis. Ces paramètres sont :

1) Le taux de vide (α) mesuré par sonde optique
2) La vitesse terminale (V_T) d'une bulle montante dérivée des mesures de la sonde optique et des informations de la littérature
3) La vitesse turbulente axiale liquide (u') mesurée par l'anémométrie a film chaud

Les deux paramètres adimensionnels de la carte sont :

1) Le taux de vide moyen dans la section
2) Le rapport entre u' moyen et V_T moyenne qui traduit la compétition entre les forces turbulente et de flottabilité.

La carte simplifiée de régimes d'écoulements pour l'expérience METERO est représentée sur la Figure 6.6. En abscisse nous avons le taux de vide et en ordonnée le rapport de la vitesse turbulente à la vitesse terminale.

Cette carte est classifiée en 4 régions.

Dans la région 1, nous avons peu de turbulence et peu de gaz. Nous pouvons donc nous attendre à la présence de petites bulles ou d'un film de gaz en partie supérieure de la conduite.

Pour le même taux de vide, l'augmentation relative de turbulence conduit à la région 2 où les bulles sont mélangées.

En partant de la région 1 et en augmentant le taux de vide à turbulence constante, nous arrivons dans la région 3 caractérisée par des grosses poches de gaz en partie supérieure.

Si maintenant, le taux de turbulence est augmenté en partant de la région 3, nous arrivons la région 4. En région 4, nous avons à la fois la dispersion et un grand nombre ou de grosses bulles suivant l'importance de la fragmentation turbulente.

Les mécanismes de transition sont la turbulence responsable du mélange et de la fragmentation d'une part et la flottabilité qui stratifie les bulles entrainant la coalescence à fort taux de d'autre part.

La carte de régime d'écoulement de METERO dans le nouveau système de coordonnées est illustrée sur la Figure 6.7. Les régions 2, 3 et 4 prévues sont retrouvées dans cette carte. Nous n'avons pas fait de mesures ni d'observation en région 1. Cette carte confirme notre approche mécaniste des transitions qui sont représenté de manière simple. Cette carte est utilisable pour d'autres installations expérimentales en faisant toutefois attention aux différences de condition d'entrée avec METERO.

Pour être plus générale, cette carte aurait besoin d'être complétée par des essais supplémentaires, notamment pour d'autres pressions, d'autres températures et d'autres conditions d'entrée.

Le calcul des paramètres constituent un inconvénient de cette carte. D'autre part, cette carte ne représente pas les régimes à bouchons et stratifies associes à de forts débits gaz.

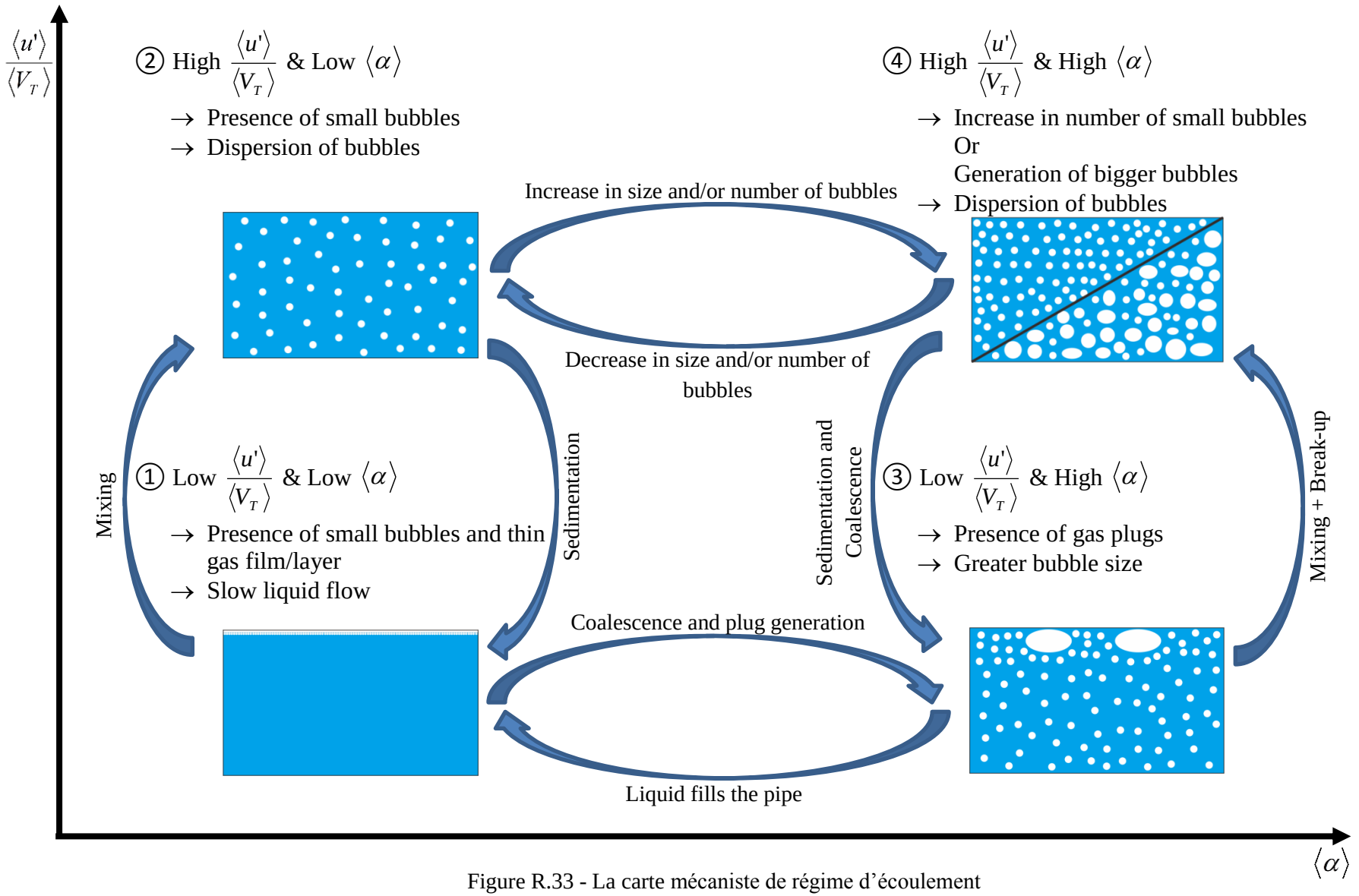

Figure R.33 - La carte mécaniste de régime d'écoulement

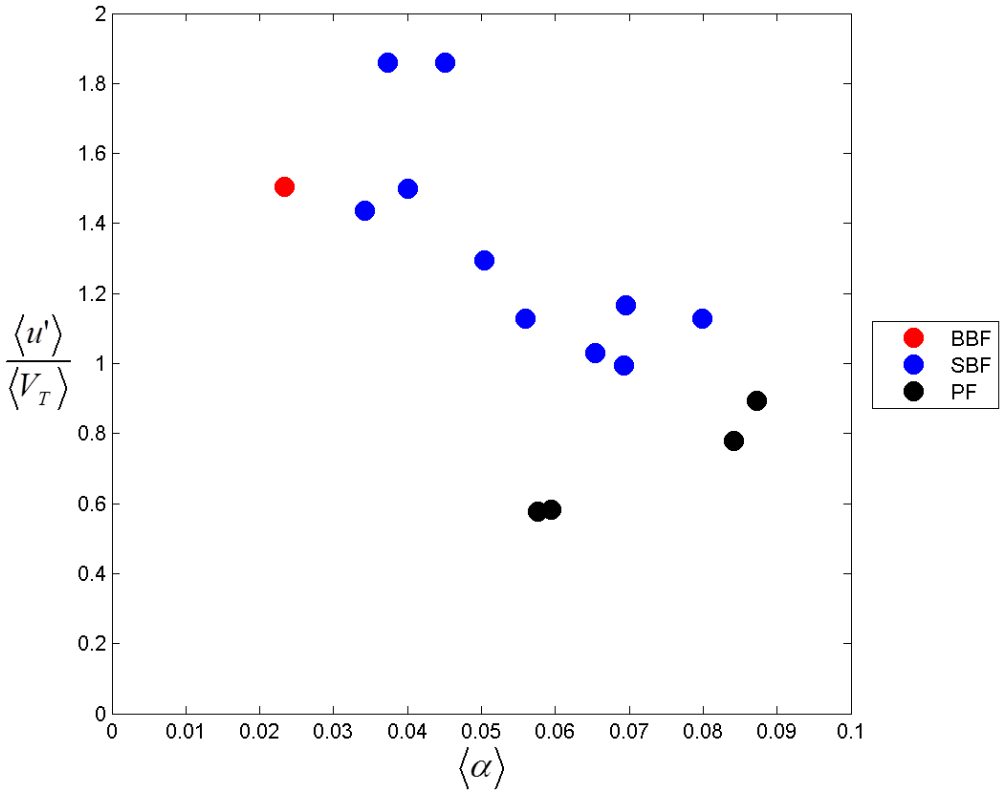

Figure R.34 - La carte de régime d'écoulement dans le nouveau système de coordonnées à 40D

8. Conclusion

Pour résumer cette thèse, les nouveaux moyens de mesure pour l'installation METERO ont été présentés. Les mesures par quadri-sonde optique ont été validées par la technique d'ombroscopie. Différents tests ont été réalisés pour mesurer les grandeurs caractéristiques des écoulements. De plus, les descriptions locale et axiale des différents régimes d'écoulements ont été faites.

Finalement, deux systèmes de coordonnées pour la carte de régime d'écoulement ont été présentés.

Pour la première carte, basée sur l'étude de Taitel et Dukler, le critère de transition de régime a été amélioré. La deuxième carte, adaptée à représentation des écoulements diphasiques horizontaux eau-air, représente les transitions de régime à l'aide d'une approche mécanistique.

BIBLIOGRAPHY

Abuaf, N., Jones Jr., O., & Zimmer, G. (1978). Optical Probe for Local Void Fraction and Interface Velocity Measurements. *Review of Scientific Instruments, 49*, 1090-1094.

Al-Turaihi, R. (2013). Experimental study and CFD simulation of two-phase flow around square-section obstavle in enlarging channel. *International Journal of Science and Engineering Investigations*, 148-160.

Andreussi, P., Paglianti, A., & Silva, F. (1999). Dispersed Bubble Flow in Horizontal Pipes. *Chemical Engineering Science, 54*, 1101-1107.

Bearman, P. (1971). Corrections for the Effect of Ambient Temperature Drift on Hot-Wire Measurements in Incompressible Flows. *DISA Information No. 11*.

Bel Fdhila, R., Suzanne, C., & Masbernat, L. (1993). Local measurements and Eulerian prediction of a bubbly flow downstream of a sudden pipe expansion. *3rd World Conf. Exp. Heat Trans., Fluid Mech. Therm.*, 1393-1401.

Bottin, M. (2010). *Stratification d'un Ecoulement Diphasique Horizontal: Modelisation et Validation Experimental*. Grenoble: Universite de Grenoble Institut Polytechnique de Grenoble.

Bröder, D., & Sommerfeld, M. (2002). An advanced LIF-PLV system for analysing the hydrodynamics in a laboratory bubble column at higher void fractions. *Experiments in Fluids, 33*, 826-837.

Brunn, H. (1995). *Hot-Wire Anemometry. Principles and Signal Analysis.* Oxford Science Publications.

Collis, D., & Williams, M. (1959). Two-dimensional Convection from Heated Wires at Low Reynolds Numbers. *J. Fluid Mech., 6/3*, 357-384.

Comte-Bellot, G., & Corrsin, S. (1966). The Use of a Contraction to Improve the Isotropy of Grid-Generated Turbulence. *J. Fluid Mech., 25*, 657-682.

Cubizolles, G. (1996). *Etude Stéréologique de la Topologie des Écoulements Diphasiques à Haute Pression.* Lyon: thèse de l'Ecole Centrale de Lyon.

Danel, F., & Delhaye, J. (1971). Sonde Optique pour Mesure du Taux de Présence Local en Écoulement Diphasique. *Mesure, Regulation, Automatisme*, 99-101.

Ekambara, K., Sander, R., Nandakumar, K., & Masliyah, J. (2008). CFD simulation of bubbly two-phase flow in horizontal pipes. *Chemical Engineering Journal, 144*, 277-288.

Garnier, C. (1998). *DEBORA, Topologie d'Écoulement : Mise en Forme et Description de la Banque Finalisée.* Note Technique SETEX/LTDF/98-65.

Gundersen, H., & Jensen, E. (1983). Particle Size and Their Distributions Estimated from Line-Sampled and Point-Sampled Intercepts. Including graphical Unfolding. *Journal of Microscopy, 131*, 291-310.

Haberman, W., & Morton, R. (1953). *An Experimental Investigation of the Drag and Shape of Air Bubbles Rising in Various Liquids.* David W. Taylor Model Basin Report 802.

Herringe, R., & Davis, M. (1976). Structural Development of Gas-Liquid Mixture Flows. *Journal of Fluid Mechanics, 73*, 97-123.

Iskandrani, A., & Kojasoy, G. (2001). Local void fraction and velocity field description in horizontal bubbly flow. *Nuclear Engineering and Design, 204*, 117-128.

Kamp et al. (2001). Bubble Coalescence in Turbulent Flows: A Mechanistic Model for Turbulence-Induced Coalescence applied to micro gravity bubbly pipe flow. *International Journal of Multiphase Flow, 27*, 1363-1396.

Keane, R., & Adrian, R. (1990). Optimization of Particle Image Velocimeters. Part 1: Double Pulsed Systems. *Measurement Science and Technology, 1*.

King, L. (1914). On the Convection of Feat from Small Cylinders in a Stream of Fluid. *Phil. Trans. Roy. Soc. London, 214*, 373-432.

Kitagawa, A., Fujiwara, A., Hishida, K., Kakugawa, A., & Kodama, Y. (2003). Turbulence structures of microbubble flow measured by PIV/PTV and LIF techniques. *The 4th Symposium on Smart Control of Turbulence.* Tokyo.

Kocamustafaogullari, G., Huang, W., & Razi, J. (1994). Measurement and modeling of average void fraction, bubble size and interfacial area. *Nuclear Engineering and Design, 148*, 437-453.

Langston, P., Burbidge, A., Jones, T., & Simmons, M. (2001). Particle and Droplet Size Analysis from Chord Measurements Using Bayes' Theorem. *Powder Technology, 113*, 33-42.

Laufer, J. (1953). *The structure of turbulence in fully developed pipe flow.* NACA report 1174. NACA report.

Lewis, S., Fu, W., & Kojasoy, G. (2002). Internal flow structure description of slug flow-pattern in a horizonal pipe. *International Journal of Heat and Mass Transfer, 45*, 3897-3910.

Lindken, R., & Merzkirch, W. (2002). A Novel PIV Technique for Measurements in Multiphase Flows and Its Application to Two-phase Bubbly Flows. *Experiments in Fluids, 33*, 814-825.

Moujaes, S. (1990). Testing of a Spherical Dual-Tipped Optical Fibre Probe for Local Measurements of Void Fraction and Gas Velocity in Two-Phase Flows. *The Canadian Journal of Chemical Engineering, 68*, 504-510.

Nogueira, J., Leecuonq, A., & Rodriguez, P. (1999). Local Field Correction PIV: On the Increase of Accuracy of Digital PIV Systems. *Experiments in Fluids, 27*, 107-116.

Nydal, O., & Andreussi, P. (6-11 June, 1993). Gas entrainment in liquid slugs. *The Third International Offshore and Polar Engineering Conference.* Singapore.

Prasad, A., Adrian, R., Landreth, C., & Offutt, P. (1992). Effect of Resolution on the Speed and Accuracy of Particle Image Velocimetry Interrogation. *Experiments in Fluids, 13*, 105-116.

Riznic, J., & Kojasoy, G. (1997). An Experimental Study on Local Interfacial Parameters in Horizontal Slug Flow. *National Heat Transfer Conference.* Baltimore, Maryland, USA: ANS Proceedings.

Sathe, M., Thaker, I., Strand, T., & Joshi, J. (2010). Advanced PIV/LIF and Shadowgraphy System to Visualize Flow Structure in Two-phase Bubbly Flows. *Chemical Engineering Science, 65*, 2431-2442.

Scarano, F., & Reithmuller, M. (1999). Iterative Multigrid Approach in PIV Image Processing with Discrete Window Offset. *Experiments in Fluids, 26*, 513-523.

Sharma, S., Lewis, S., & Kojasoy, G. (1998). Local studies in horizontal gas-liquid slug flow. *Nuclear Engineering and Design, 184*, 305-318.

Suzanne, C., Ellingsen, K., Risso, F., & Roig, V. (1998). Local Measurements in Turbulent Bubbly Flows. *Nuclear Engineering and Design, 184*, 319-327.

Taitel, Y., & Barnea, D. (1990). Two-phase slug flow. *Advances in Heat Transfer, 20*, 83-132.

Westerweel, J., Dabiri, D., & Gharib, M. (1997). The Effect of a Discrete Window Offset on the Accuracy of Cross-correlation Analysis of Digital PIV Recordings. *Experiments in Fluids, 23*, 20-28.

Yang et al. (2004). Quasi 3-D Measurements of Turbulence Structure in Horizontal Air-Water Bubbly Flow. *Nuclear Engineering and Design, 227*, 301-312.

RESUME

Plusieurs régimes d'écoulement diphasiques adiabatiques eau/air horizontaux (écoulements dispersés à bulles et intermittents) et leur développement axial ont été étudiés dans l'expérience METERO, constituée d'une conduite circulaire horizontale de 100 mm de diamètre interne. Différentes techniques d'instrumentation ont été améliorées et utilisées pour mesurer les grandeurs caractéristiques de l'écoulement afin d'apporter une description locale et l'évolution axiale des écoulements. Les mécanismes physiques responsables des régimes d'écoulement et de leurs transitions, notamment la compétition entre forces turbulente et de flottabilité ont été explicités. Les différences entre les régimes à bulles et intermittent ont été mises en évidence et les processus physiques à l'origine de ces différences ont été expliqués. Deux nouvelles cartes de régime d'écoulement adimensionnelles ont été proposées: la première apporte une amélioration à la représentation de Taitel & Dukler (1976) et propose un nouveau critère de transition. La deuxième, novatrice, quantifie les effets des forces de turbulence et de flottabilité en fonction du taux de vide.

Mots-clés: Ecoulements diphasiques horizontaux, expérimentation, quadri-sonde optique, anémométrie à film chaud, ombroscopie, cartes de régime d'écoulement adimensionnelles

ABSTRACT

Several horizontal water-air two-phase adiabatic flows (dispersed bubbly flows and intermittent flows) and their axial evolutions have been studied in the METERO experiment which is consisted of a horizontal circular test section with an internal diameter of 100 mm. Different measurement techniques have been improved and utilized to measure the flow characteristics in order to bring a local description and axial evolution of the flows. The responsible physical mechanisms of the flow regimes and their transitions, particularly the competition between turbulent force and buoyancy force have been explained. The differences between dispersed bubbly flows and intermittent flows have been highlighted and the physical process at the origin of these differences has been explained. Two new dimensionless flow regime maps have been proposed: the first one brings an improvement to the representation of Taitel & Dukler (1976) and proposes new transition criteria. The second novel map takes into account the effects of turbulent and buoyancy forces and the void fraction.

Keywords: Horizontal two-phase flows, experimentation, four-tip optical probes, hot-film anemometry, shadowgraphy, dimensionless flow regime maps